Development and Characterisation of High-entropy Alloys (HEAs)

by

Armin Asghari Alamdari

A Dissertation Submitted to the
Graduate School of Sciences and Engineering
in Partial Fulfillment of the Requirements for
the Degree of

Doctor of Philosophy

in

Materials Science and Engineering

KOÇ ÜNİVERSİTESİ

May 17, 2024

Development and Characterisation of High-entropy Alloys (HEAs)

Koç University

Graduate School of Sciences and Engineering

This is to certify that I have examined this copy of a doctoral dissertation by

Armin Asghari Alamdari

and have found that it is complete and satisfactory in all respects,

and that any and all revisions required by the final

examining committee have been made.

Committee Members:

Assoc. Prof. Uğur Ünal (Advisor)

Assoc. Prof. Umut Aydemir

Prof. Erdem Alaca

Prof. Burç Mısırlıoğlu

Asst. Prof. Nuri Solak

Dr. Amir Motallebzadeh (Co-Advisor)

Date: May 17, 2024

To my parents and my beloved wife, whose unwavering support and love have been my anchor and inspiration throughout this journey.

ABSTRACT

Development and Characterisation of High-entropy Alloys (HEAs)

Armin Asghari Alamdari

Doctor of Philosophy in Materials Science and Engineering

May 17, 2024

This doctoral thesis presents a comprehensive investigation into the potential applications of High Entropy Alloys (HEAs) as protective coatings for biomedical implants and as electrocatalysts for water-splitting applications. The research spans five main chapters, each exploring different facets of HEAs, including their microstructure, mechanical properties, electrochemical behavior, biocompatibility, and catalytic performance.

Chapter three highlights the deposition of $Ti_{1.5}ZrTa_{0.5}Nb_{0.5}Hf_{0.5}$ RHEA films on 316L, CoCrMo, and Ti6Al4V substrates, revealing amorphous, compact structures with superior mechanical properties and adhesion, particularly on the Ti6Al4V substrate, and demonstrating enhanced corrosion resistance in PBS solution. Chapter four focuses on different RHEA films on 316L substrates, identifying potential as protective coatings due to improved hardness, tribological performance, and biocorrosion resistance, with biocompatibility confirmed through in vitro tests. Chapter five discusses both undoped and Ag-doped $Ti_{1.5}ZrTa_{0.5}Nb_{0.5}W_{0.5}$ RHEA films, noting the mechanical and corrosion-resistant benefits of Ag nanoparticle inclusion. Chapter six details the development of antibacterial RHEA films doped with Ag nanoparticles, showing significant antibacterial efficacy against P. Aeruginosa and S. Aureus, and promising biocompatibility with C2C12 myoblast cells. Collectively, these studies underscore the potential of RHEA films as functional coatings for biomedical applications.

The seventh chapter explores the preparation of CoCuFeNi-based HEAs through mechanical alloying (MA) and their evaluation as electrocatalysts for water splitting. The results show that $CoCuFeNiMnMo_{1.5}$ exhibits the best OER performance, while $CoCuFeNiMnMo_{0.5}$ demonstrates the best HER activity with lower overpotentials and excellent stability. The assembled $CoCuFeNiMnMo_{1.5}$ (anode)‖$CoCuFeNiMnMo_{0.5}$

(cathode) couple achieves a current density of 10 mA cm^{-2} at 1.76 V, with a Faradaic efficiency for generated H_2 of more than 80%.

In conclusion, this thesis provides valuable insights into the potential of HEAs as protective coatings for metallic biomaterials and as efficient electrocatalysts for water splitting, contributing to the advancement of HEA research and the development of novel materials with enhanced properties for biomedical and energy-related applications.

.

ÖZETÇE

Yüksek Entropi Alaşımlarının (HEAs) Geliştirilmesi ve Karakterizasyonu

Armin Asghari Alamdari

Malzeme Bilimi ve Mühendisliği, Doktora

17 Mayıs 2024

Bu doktora tezi, Yüksek Entropi Alaşımlarının (HEAs) biyomedikal implantlar için koruyucu kaplamalar ve su ayrıştırma uygulamaları için elektrokatalizörler olarak potansiyel uygulamalarını kapsamlı bir şekilde incelemektedir. Araştırma, HEA'ların mikroyapısı, mekanik özellikleri, elektrokimyasal davranışı, biyouyumluluk ve katalitik performansı dahil olmak üzere farklı yönlerini araştıran beş ana bölümden oluşmaktadır.

Üçüncü bölüm, $Ti_{1.5}ZrTa_{0.5}Nb_{0.5}Hf_{0.5}$ RHEA filmlerinin 316L, CoCrMo ve Ti6Al4V altlıklarına kaplanması üzerine yoğunlaşmakta, amorf ve kompakt yapılar ile özellikle Ti6Al4V altlığında üstün mekanik özellikler ve yapışma göstermekte ve PBS çözeltisinde artırılmış korozyon direnci sergilemektedir. Dördüncü bölüm, 316L altlıklarında farklı RHEA filmlerine odaklanmakta, iyileştirilmiş sertlik, tribolojik performans ve biyokorozyon direnci nedeniyle koruyucu kaplamalar olarak potansiyelini belirlemekte ve biyouyumluluğu in vitro testlerle doğrulamaktadır. Beşinci bölüm, hem saf hem de Ag ile katkılı $Ti_{1.5}ZrTa_{0.5}Nb_{0.5}W_{0.5}$ RHEA filmlerini tartışmakta, Ag nanopartikül katkısının mekanik ve korozyon direncine olan faydalarını not etmektedir. Altıncı bölüm, Ag nanopartikülleri ile katkılı antibakteriyel RHEA filmlerinin geliştirilmesini detaylandırmakta, P. Aeruginosa ve S. Aureus bakterilerine karşı önemli antibakteriyel etkinlik göstermekte ve C2C12 myoblast hücreleri ile yapılan biyouyumluluk değerlendirmesinde umut verici sonuçlar sunmaktadır. Bu çalışmalar topluca, RHEA filmlerinin biyomedikal uygulamalar için fonksiyonel kaplamalar olarak potansiyelini vurgulamaktadır.

Yedinci bölüm, mekanik alaşımlama (MA) yoluyla CoCuFeNi tabanlı HEA'ların hazırlanmasını ve su ayrıştırma için elektrokatalizör olarak değerlendirilmesini

araştırmaktadır. Sonuçlar, $CoCuFeNiMnMo_{1.5}$'ın en iyi OER performansını sergilediğini, $CoCuFeNiMnMo_{0.5}$'ün ise daha düşük aşırı potansiyellerle ve mükemmel stabilite ile en iyi HER aktivitesini gösterdiğini ortaya koymaktadır. Montajlanmış $CoCuFeNiMnMo_{1.5}$ (anot)‖$CoCuFeNiMnMo_{0.5}$ (katot) çifti, 1.76 V'de 10 $mA.cm^{-2}$'lik bir akım yoğunluğu başarırken, üretilen H2 için Faraday verimliliği %80'den fazla olmaktadır.

Sonuç olarak, bu tez, HEA'ların metalik biyomalzemeler için koruyucu kaplamalar ve su ayrıştırma için etkili elektrokatalizörler olarak potansiyelini değerli içgörüler sağlayarak HEA araştırmalarının ilerlemesine ve biyomedikal ve enerji ile ilgili uygulamalar için geliştirilmiş özelliklere sahip yeni malzemelerin geliştirilmesine katkıda bulunmaktadır.

ACKNOWLEDGMENTS

I want to thank several people for helping and supporting me during my research. This thesis would not have been possible without their support in various ways.

First and foremost, I would like to thank my supervisor Assoc. Prof. Dr. Ugur Unal, for all his guidance and endless support. He provided me with opportunities and infinite freedom while encouraging and trusting me in my work.

I am equally thankful to my co-advisor, Dr. Amir Motallebzadeh, for all his support during these years. He was more than an advisor to me. He was present at all the good and hard moments of my Ph.D. journey as well as my personal life.

Also, I would like to thank Dr. Hadi Jahangiri, whose insights and expertise were crucial in shaping the direction and execution of my research.

I want to express my sincere thanks to my thesis committee members, Assoc. Prof. Umut Aydemir, Prof. Erdem Alaca, Asst. Prof. Nuri Solak, and Prof. Burç Mısırlıoğlu for their valuable comments and help on my research.

I would like to thank KUYTAM, Dr. Barış Yağcı, and Dr. Gulsu Şimşek for all their help and support with XPS and ICP-MS experiments.

I am grateful to the various research groups and lab partners, particularly KUTEM and Assoc. Prof. Sarp Kaya for letting us do the corrosion tests, Kavakli lab, and Prof. Ibrahim Halil Kavakli for the antibacterial tests, KUBAM, Assoc. Prof. Umut Aydemir and Dr. Naeimeh Sadat Peighambardoust for their collaborative efforts and shared expertise, Dr. Pinar Tatar Güner for the antibacterial experiment, and Funtech lab, Prof. Havva Funda Yagci Acar and Dr. Mahshid Hashemkhani for the cell-culture test, which has greatly contributed to the success of this thesis.

I need to thank GSSE staffs, Emine Büyükdurmuş, Zehra Puntar Özkonuk, and Meltem Yabacı for all their support during these years.

I really appreciate and acknowledge the financial support from The Scientific and Technological Research Council of Turkey (TÜBİTAK) under the Grant Number of 119R010.

A special thank you goes to all the previous and present members of Unallab for all of their friendship.

On a personal note, I am profoundly grateful to my wife, Aisan, whose love, patience, and support have been my cornerstone. Her unwavering belief in my capabilities has been a constant source of encouragement.

Finally, I owe a heartfelt thank you to my parents, Seyfallah and Zhila, whose endless support and sacrifices have not only paved the way to this achievement but have shaped the person I am today. Their unconditional love and guidance have been my guiding light throughout this journey.

TABLE OF CONTENTS

LIST OF TABLES

LIST OF FIGURES

ABBREVIATIONS

AFM	Atomic Force Microscopy
CV	Cyclic Voltammetry
E_{corr}	Corrosion Potential
EDS	Energy Dispersive X-ray Spectroscopy
EIS	Electrochemical Impedance Spectroscopy
FE	Faradaic Efficiency
GIXRD	Grazing Incidence X-ray Diffraction
GCE	Glassy carbon Electrode
HEAs	High-entropy Alloys
HER	Hydrogen Evolution Reaction
I_{corr}	Corrosion Current
MA	Mechanical Alloying
OER	Oxygen Evolution Reaction
PVD	Physical Vapor Deposition
RDE	Rotating Disk Electrode
RHEAs	Refractory High-entropy Alloys
R_P	Polarization Resistance
SEM	Scanning Electron Microscopy
TEM	Transmission Electron Microscopy
XPS	X-ray Photoelectron Spectroscopy
XRF	X-ray Fluorescence
XRD	X-ray Diffraction

CHAPTER 1

AN INTRODUCTION

The aim of this study is the development and characterization of High-entropy alloys (HEAs) with different producing methods and for different applications. The information and literature review about HEAs were presented in **Chapter 2**, before the detailed experimental studies.

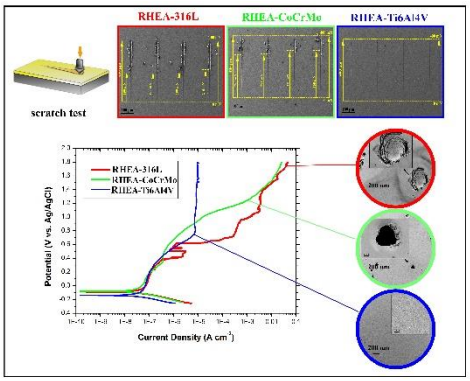

Chapter 3 details A 1.025 µm thick non-equimolar $Ti_{1.5}ZrTa_{0.5}Nb_{0.5}Hf_{0.5}$ RHEA film, deposited on 316L, CoCrMo, and Ti6Al4V substrates using RF magnetron sputtering, exhibited an amorphous and compact morphology. Nanoindentation and scratch tests revealed improved mechanical properties and high adhesion strength on Ti6Al4V, while electrochemical tests indicated remarkable corrosion resistance and a significantly high charge transfer resistance (1.5×10^7 Ω cm^2) due to strong bonding between the RHEA film and Ti6Al4V substrate.

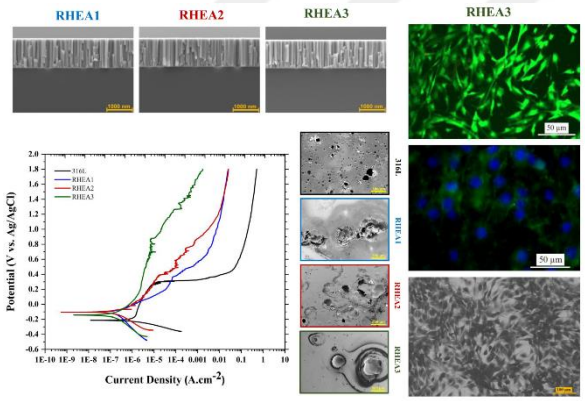

Chapter 4 $Ti_{1.5}ZrTa_{0.5}Nb_{0.5}Hf_{0.5}$, $Ti_{1.5}ZrTa_{0.5}Nb_{0.5}Mo_{0.5}$, and $Ti_{1.5}ZrTa_{0.5}Nb_{0.5}W_{0.5}$ refractory high-entropy alloy (RHEA) films were deposited on 316L using RF-PVD, exhibiting amorphous structures with smooth morphology and granular features. $Ti_{1.5}ZrTa_{0.5}Nb_{0.5}W_{0.5}$ demonstrated enhanced properties, including contact angle, hardness, tribological performance, adhesion, biocorrosion resistance, and low Ni and Cr ion release, making it a promising protective coating for 316L biomaterials, with no cytotoxic response observed in in vitro cytotoxicity assessment using C2C12 muscle myoblast cells.

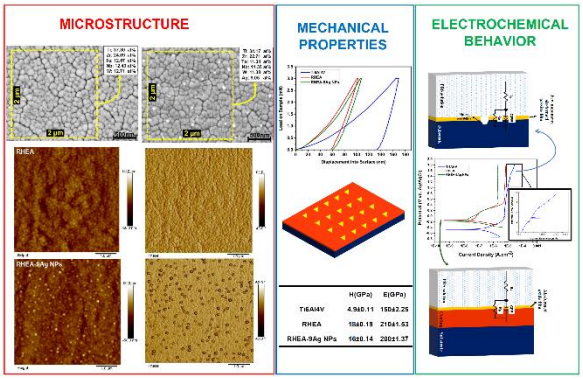

In **Chapter 5**, Surface modification of Ti6Al4V alloys with 1.10 µm thick undoped and Ag-doped $Ti_{1.5}ZrTa_{0.5}Nb_{0.5}W_{0.5}$ refractory high-entropy alloy (RHEA) films was conducted through RF magnetron sputtering, addressing corrosion and bacterial infection issues in metallic biomaterials. The deposited films, exhibiting amorphous structures with cauliflower-like morphology, significantly improved surface mechanical properties, and the addition of Ag nanoparticles further increased corrosion resistance, reducing the corrosion rate by 2.3–2.8 orders of magnitude and enhancing the polarization resistance of the films.

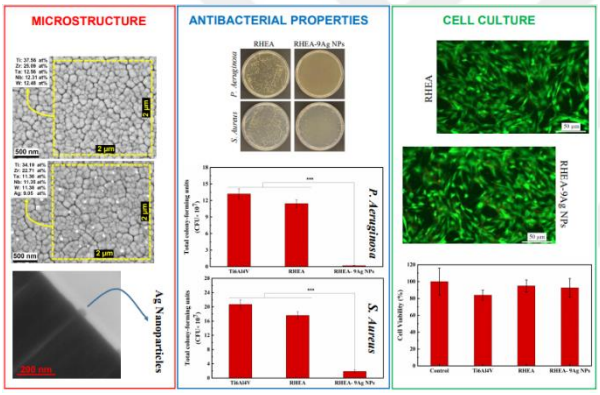

In **Chapter 6**, the study aimed to develop antibacterial and biocompatible $Ti_{1.5}ZrTa_{0.5}Nb_{0.5}W_{0.5}$ RHEA films and their Ag nanoparticle-doped counterparts on Ti6Al4V using RF magnetron sputtering. Microstructural analysis showed homogeneity and amorphous structure, while antibacterial tests demonstrated a significant reduction in bacteria colony forming units, and the films exhibited strong biocompatibility with C2C12 mouse muscle myoblast cells.

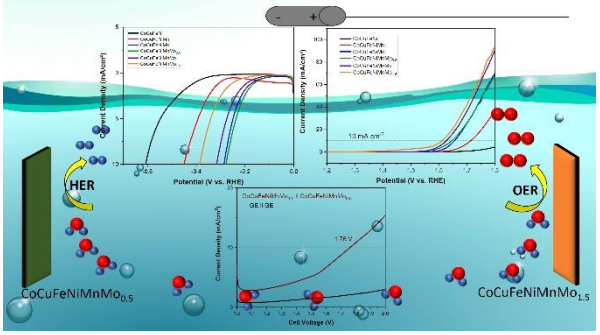

Chapter 7 reports High-entropy alloys (HEAs), composed of solid solutions with five or more elements, have gained attention for water splitting applications. CoCuFeNi-based HEAs, prepared through mechanical alloying, demonstrated promising electrocatalytic performance for Oxygen Evolution Reaction (OER), Hydrogen Evolution Reaction (HER), and overall water splitting, with $CoCuFeNiMnMo_{1.5}$ showing the best OER performance, and $CoCuFeNiMnMo_{0.5}$ exhibiting superior HER activity.

CHAPTER 2

LITERATURE REVIEW

2.1 High-entropy Alloys (HEAs)

Traditional alloys are typically classified as binary, ternary, or multivariate based on the number of principal elements they contain, as depicted in Figure 2. 1[1]. They can also be classified based on their main metallic constituents, such as alloys primarily composed of iron, magnesium, or nickel. In contrast, High Entropy Alloys (HEAs) represent a novel class of alloys characterized by a diverse mix of elements, each contributing similarly to the alloy's properties. This composition defies conventional alloy naming conventions. Yeh et al.[2] initially described HEAs as alloys comprising five or more elements, with each element's atomic fraction being more than 5%. The increased mixing entropy in HEAs aids in inhibiting the development of intermetallic compounds, resulting in a mainly single-phase solid solution structure. It is crucial to grasp the concept of HEAs prior to examining their characteristics and uses [3].

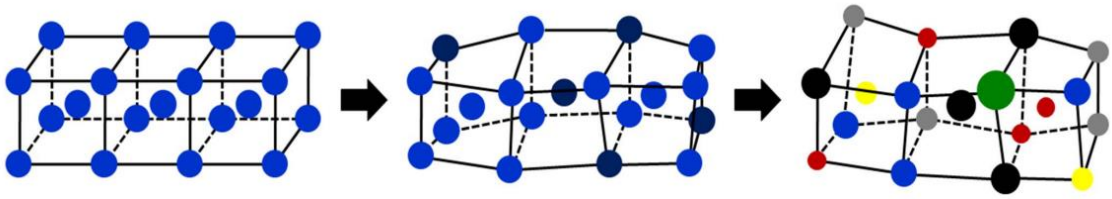

Figure 2. 1. The difference between Pure metal, traditional alloy, and HEA.

Entropy, a core concept in thermodynamics, measures a system's disorder level. Generally, the entropy of a system increases as the disorder grows. Entropy in solid materials mainly originates from different quantum states resulting from lattice vibrations. For solid solutions, combining atoms from various alloying elements with unique configurations enhances the system's entropy, known as configuration entropy or mixing entropy. In HEAs that involve multiple principal elements, the arrangement of atomic configurations plays a substantial role in influencing entropy. Assuming that the impacts of other configurations on entropy are negligible, the mixing entropy from atomic arrangements becomes the primary contributor to the system's overall entropy. Typically, the configuration entropy of a system is well represented by the mixing entropy (ΔSmix) linked to the creation of a solid mixture. This correlation is often quantified mathematically in the following manner:

$$\Delta Smix = -R \sum_{i=1}^{n} C_i \ln C_i$$

For the molar gas constant R and Ci representing the molar content of the ith component, utilizing a mole ratio approach for various elements in alloy design can optimize the mixing entropy [4,5]. From this equation, it becomes clear that in an ideal solid solution, the larger the number of principal elements and the more evenly distributed their proportions, the greater the resulting mixing entropy.

$$\Delta Smix = R\left(\frac{1}{n}\ln\frac{1}{n}+\frac{1}{n}\ln\frac{1}{n}+\frac{1}{n}\ln\frac{1}{n}+\cdots+\frac{1}{n}\ln\frac{1}{n}\right) = R\ln n$$

This equation introduces n as the number of metal atoms in the solid solution, while the mixing entropy (ΔSmix) reflects the count of distinct constituents within the alloy [6]. In a state of random solubility, the alloy behaves similarly to a regular solution. Consequently, the Gibbs free energy (ΔGmix) of the mixture has the potential to be formulated in the following way:

$$\Delta Gmix = \Delta Hmix - T\Delta Smix$$

Where ΔHmix refers to the enthalpy of mixing, representing the energy associated with the bonding between atoms. T denotes the thermodynamic temperature [7]. When ΔHmix is constant, a raise in mixing entropy causes a reduction in the system's free energy, contributing toward the enhanced durability of the alloy system. Consequently, elevating the ΔSmix encourages the formation of a solid solution characterized by uniform element mixing rather than a structured arrangement of intermetallic compounds.

ΔSmix in an alloy can vary based on the equiatomic ratios of its component elements. It has been suggested that for a ΔSmix value of 1.50, a strong interatomic force and high-temperature resistance are necessary. As a result, a threshold for categorizing the entropy levels in an alloy has been established at ΔSmix = 1.50. If the entropy of mixing falls below 1R, it becomes challenging for it to contest against the bonding energy [7,8].

Derived from these considerations, alloys can be classified into three distinct categories as depicted in Figure 2. 2: (1) Low entropy alloys, which primarily consist of one or two elements, characterized by a traditional alloy structure with ΔSconf < 1R; (2) Medium entropy alloys, which contain two to four major elements, with an entropy of mixing range of 1R < ΔSconf < 1.5R; and (3) HEAs, which are composed of multiple elements and exhibit a high entropy of mixing with ΔSconf > 1.5R [8,9].

Figure 2. 2. Different types of entropy alloys based on entropy-based definition.

Just like conventional alloys, the structural makeup of HEAs is capable of being categorized into two main types: crystalline and amorphous. The majority of HEAs are found in a crystalline state, and it is the crystal structure that functions in defining the solid metal's physical, chemical, and mechanical attributes. Among the prevalent crystal structure models observed in HEAs are face-centered cubic (FCC), body-centered cubic (BCC), hexagonal close-packed (HCP), and amorphous structures [3].

2.2 Four Core Effects of HEAs

HEAs, characterized by their composition of five or more primary elements, are distinguished from conventional alloys through four fundamental effects that are thought to influence their microstructure and properties. Of these four effects, three are currently hypothetical in nature, while the cocktail effect stands out as a distinct and exclusive attribute of HEAs [10]. These core effects, as depicted in Figure 2. 3, each playing a critical role in defining the unique aspects of HEAs, are explored in depth in the subsequent sections of the discussion [11].

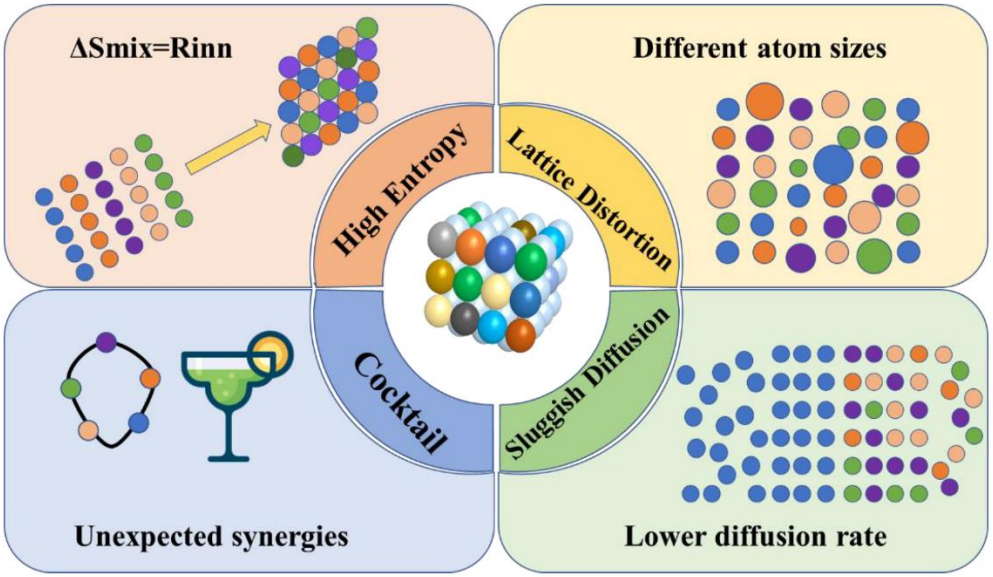

Figure 2. 3. Effects of high-entropy alloys.

2.2.1 High-entropy Effect

The phenomenon initially suggested by Yeh [2] stabilizes high-entropy phases and reduces their variety. Contrary to common assumptions, alloys with equiatomic or nearly equiatomic compositions don't necessarily form intermetallic phases. The Gibbs phase rule explains this: for an alloy in equilibrium, the number of phases (P) is determined by the formula P = C + 1 - F, where C represents the number of components and F is the maximum thermodynamic degrees of freedom.

Under the Gibbs phase rule, a hexanary system (C = 6) can potentially exhibit up to 7 distinct phases when the degrees of freedom (F) is zero. In contrast, observations in quinary systems show a notably smaller number of phases, emphasizing the significant influence of high configurational entropy, as explained in equation (2.2). The Gibbs free energy (ΔG), which represents the thermodynamic potential minimized at chemical equilibrium under constant pressure and temperature, is defined by the equation $\Delta G = \Delta H - T\Delta S$. Here, ΔH is the enthalpy change, and ΔS is the entropy change, which notably increases at elevated temperatures due to the incorporation of more components in the system. This increase in the TΔS term results in a lower Gibbs free energy, thereby facilitating enhanced mutual solubility, crucial for the formation of solid solution phases and limiting the emergence of multiple phases in HEAs. Additionally, other contributing factors like kinetic constraints and low diffusivities, linked to various core effects, also play a significant role in reducing the number of phases in HEAs [10,12].

2.2.2 Severe Lattice Distortion Effect

HEAs contain multiple principal elements, leading to a composition with varied atomic sizes. This necessitates an expansion of the traditional understanding, which primarily focuses on one or two elements, to comprehend lattice formation in HEAs with multiple principal elements. As depicted in Figure 2. 4, the disparate atomic sizes of these multi-principal elements cause significant lattice distortion in the crystal structures of HEAs. Consequently, the lattices in these alloys are typically highly distorted, with each atom acting as a solute and exhibiting considerable variation in atomic size. This distortion is generally more pronounced than in conventional alloys, contributing to an increase in configurational entropy. It is also believed to enhance certain properties of HEAs, such as the strength in BCC-structured HEAs and the tensile brittleness observed in some HEAs. The extent of this distortion, whether in crystalline or amorphous structures, significantly impacts the mechanical, chemical, and other properties of HEAs. This impact, known as the lattice distortion effect, is a key factor in determining the unique characteristics of high entropy alloys [10,12]. Recent research employing advanced techniques such as high-resolution TEM, X-ray diffraction, and neutron scattering has presented substantial evidence supporting the occurrence of severe lattice distortion in HEAs [13,14].

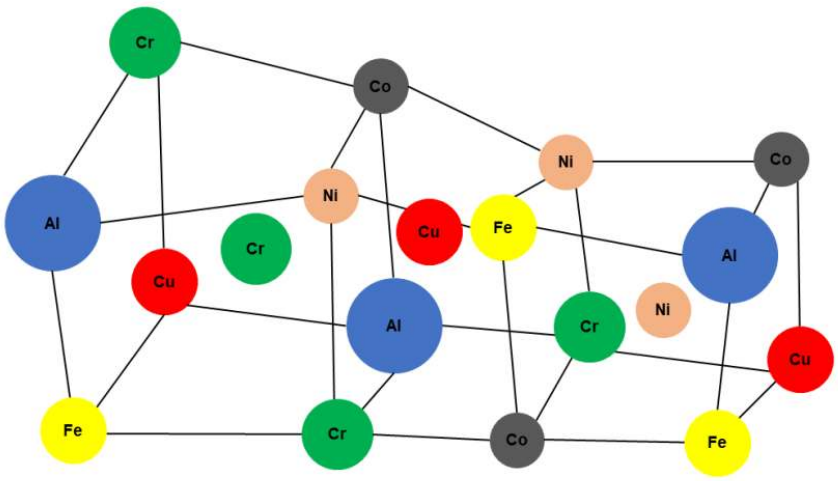

Figure 2. 4. Schematic for Lattice distortion effect.

2.2.3 Sluggish Diffusion Effect

The rate of diffusion and phase transition kinetics in HEAs are typically sluggish compared to traditional alloys due to two primary factors, as shown in Figure 2. 5. Firstly,

in HEAs, each lattice position is surrounded by different neighboring atoms, leading to varied local bonding and energies. This diversity means that an atom moving to a vacancy experiences a different environment, potentially becoming 'trapped' at low-energy sites or easily returning from high-energy sites, both scenarios contributing to reduced diffusion rates. Secondly, the individual diffusion rates of each element in HEAs vary, with some elements being less active and thus less likely to move into vacancies. This variance is critical, as phase transitions often require the co-diffusion of multiple elements for processes like new phase formation or grain growth. Slower-moving elements can become rate-limiting factors, impeding these processes. However, this sluggish diffusion can also confer benefits, including the creation of a supersaturated state, the formation of fine precipitates, an increase in recrystallization temperature, and reduced rates of grain growth and coarsening. These advantages contribute to improved control over the microstructure and its properties, thereby enhancing the overall performance of the alloy [15–17].

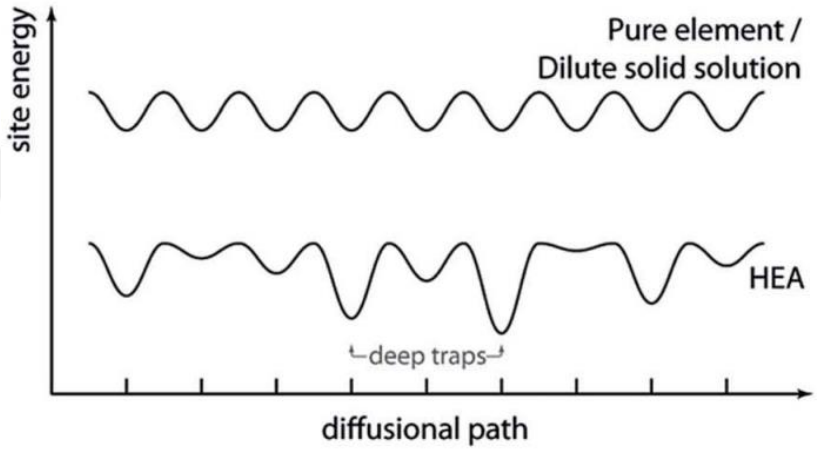

Figure 2. 5. diagram of the difference in the lattice potential energy distribution.

2.2.4 Cocktail Effect

Ranganathan first introduced the concept of "multi-metallic cocktails," highlighting their crucial role in alloy development. The overall properties of these alloys are shaped by the phase shape, distribution, boundary, and the cumulative effect of each phase's properties. These phases, each being a multicomponent solid solution, resemble atomic-scale composites. Their overall performance stems not just from the fundamental characteristics of the constituent components as per the mixing principle but also from the synergy between these elements and the significant lattice distortion they cause. These interactions and distortions add complexity to the predictions made by mixing rules. The

cocktail effect in alloys extends from a multicomponent composite effect at the atomic level to the microscale. Thus, a thorough understanding of these factors is essential for selecting the right composition and process in alloy design. Despite being a relatively new approach, this methodology holds promise for discovering additional potential components in HEAs [17].

2.3 Methods for Creating HEAs

The creation of HEAs is primarily undertaken using three distinct approaches. The first of these is liquid-state synthesis, involving various techniques such as arc melting, electric resistance melting, induction melting, and others like selective laser and electron beam melting [18–21]. These methods are widely used, yet they necessitate extremely high temperatures to achieve the desired material uniformity. This process often results in a dendritic microstructure, necessitating further heat treatment to achieve homogeneity. The second approach encompasses solid-state methods, notably mechanical alloying and spark plasma sintering (SPS) for compaction [22,23]. Although widely employed, these techniques come with drawbacks such as high energy demands and a tendency for the material to oxidize, often leading to roughness that requires additional pressing and sintering processes to rectify.

The third category is gas-state synthesis, incorporating techniques like magnetron sputtering deposition and pulse laser deposition. While effective, these methods involve complex and costly equipment and are not ideally suited for large-scale production [24]. Given these challenges, innovating new methods for synthesizing HEAs with unique characteristics remains crucial for advancing their applications.

2.3.1 Synthesis of Powder HEAs

Vara Lakshmi [25] and colleagues pioneered the use of nanocrystalline AlCrCuFeTiZn HEA in the production of HEAs, sparking a significant increase in research focused on Mechanical Alloying (MA).

The primary objectives of milling in the context of MA include particle size reduction, effective blending and mixing, and particle shape alteration. During milling, a balance is eventually achieved between the rates of welding and fracturing of particles [26–28]. This process is essential for developing supersaturated solid solutions and ensuring a uniform distribution of elements that strengthen the alloy. Subsequently, the

welding process becomes predominant, leading to the formation of equiaxed particles. A schematic diagram of the Mechanical Alloying setup is shown in Figure 2. 6 [29].

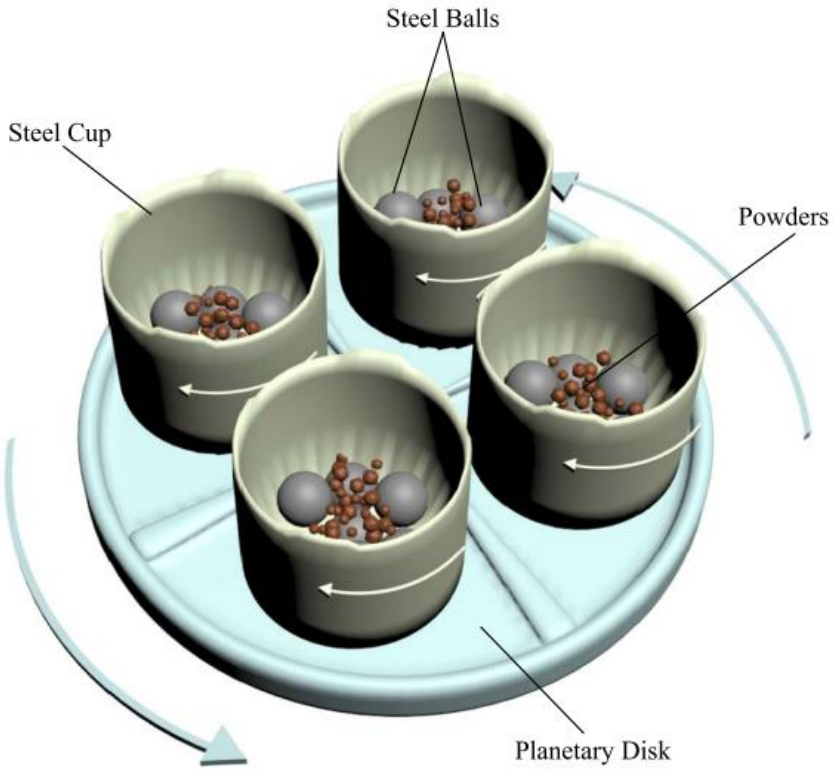

Figure 2. 6. Schematic for Mechanical Alloying system.

Mechanical Alloying is influenced by several key factors that are crucial for the formation of uniform compounds. These factors significantly affect the final characteristics of the product, such as stoichiometry, degree of disorder, and amorphization. Effective management of these variables is paramount for achieving superior particle formation. The challenge lies in achieving fine particles with a specific morphology and microstructure. This can be addressed through the optimization of various process variables. The key process variables and their impacts on MA include the Ball to Powder Weight Ratio (BPR), Rotational Speed, Grinding Duration, and Ambient Conditions. Each of these variables has a critical impact on the effectiveness and quality of the mechanical alloying process [10].

In research, Szklarz et al. [30] investigated the corrosion characteristics of a CoNiFeMnCr alloy in a chloride medium. This alloy was produced through mechanical alloying of pure powders of chromium, manganese, iron, cobalt, and nickel, followed by hot isostatic pressing (1000°C, 15 minutes, 150 bar). Furthermore, the study explored a composite of the initial HEA with SiC nanoparticles, finding that the inclusion of 5 mass% SiC enhanced hardness and the anti-corrosion properties of the material.

Alijani et al. [31] carried out research on the magnetic properties of the FeCoNiMnV HEA, which was synthesized via ball milling. X-ray diffraction data indicated FCC and BCC phases during the milling process. Additionally, a vanadium-enriched sigma-phase was detected in the milled samples, leading to the classification of the obtained powders as semi-hard magnetic materials.

A separate investigation into mechanically alloyed CoFeNi, CoFeNiCr, CoFeNiCrMn, and CoFeNiCrMnAl powders revealed that a rise in the count of components from 3 to 6 resulted in altered sintering kinetics. This change manifested as slow grain growth, a reduction in compaction rate, and an increase in the activation energy required for sintering. These alterations also correlated with an upward trend in microhardness, suggesting improved mechanical properties of these alloys [32].

Also, Murali et al. [33] studied the impact of varying zinc amounts on the crystal structure and phase formation of the $AlCoCrCuFeZn_x$ alloy obtained through mechanical alloying. The research successfully synthesized both crystalline and non-equilibrium nanocrystalline samples with a crystallite size of less than 10 nm.

2.3.2 Synthesis of Bulk HEAs

The predominant method for synthesizing High Entropy Alloys (HEAs) in bulk form is through liquid-state processing, commonly referred to as the melting and casting technique. This approach predominantly utilizes two processes: vacuum arc melting and induction melting. A diagrammatic representation (Figure 2. 7) of the arc melting process highlights its popularity in HEA synthesis, owing to its ability to reach extremely high temperatures by adjusting the electrical power supplied to the electrodes. Temperatures exceeding 3000 °C can be attained, sufficient to melt most metals typically used in HEA production [34].

This method is particularly advantageous for creating HEAs from elements with high melting points, like refractory elements such as Titanium (Ti) and Zirconium (Zr). A notable limitation, however, is the potential evaporation of metals with lower melting points, such as Magnesium (Mg) and Zinc (Zn). To counter this, the resistance and induction heating furnaces are employed, as they offer superior compositional control compared to the arc melting process [12].

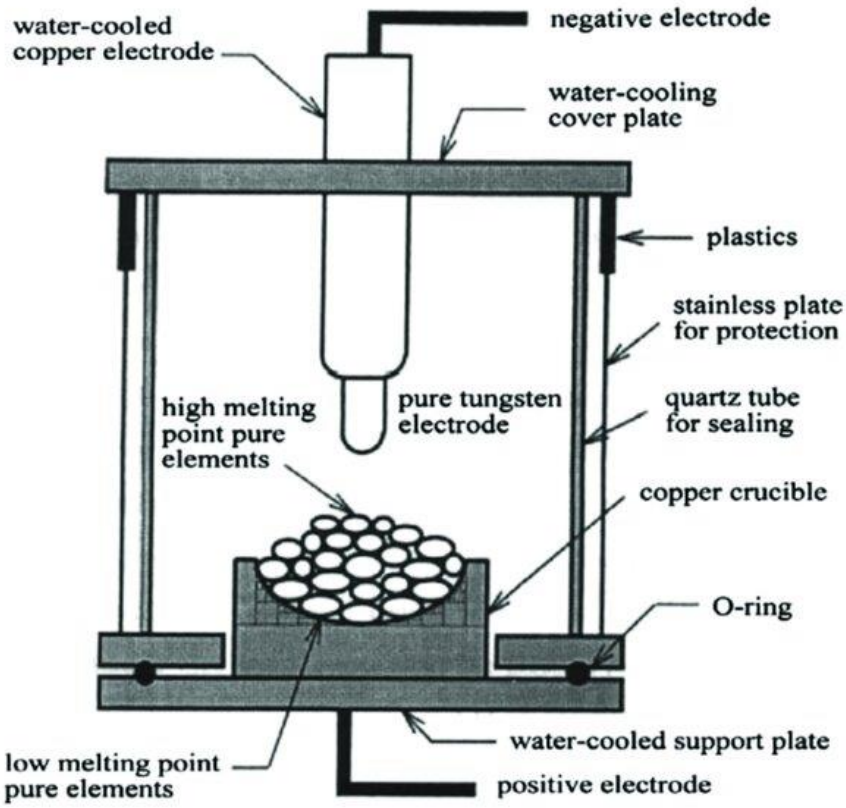

Figure 2. 7. Schematic diagram of the vacuum arc melting process.

Once the melting process is completed, regardless of the method used, the resultant HEAs are quickly cast into various shapes, including rods, which are then utilized for diverse applications. This quick transition from melting to casting is a critical step in ensuring the quality and applicability of the HEAs produced.

Systematic investigations have been conducted on $Al_xFeNiCrCo$ HEAs synthesized through both sintering and arc melting of pure metal powders. These studies have revealed two distinct crystallographic structures within these alloys, encompassing three separate phases with varying stoichiometries. The composition and proportion of these phases have been found to be closely linked to the aluminum content present in the HEA. Although the phase compositions in these alloys are largely similar, their microstructures exhibit notable differences. Samples that underwent the melting process displayed a dendritic structure, whereas those subjected to sintering revealed the formation of large, regular grains. This contrast in microstructural characteristics highlights the influence of the synthesis method on the final properties of the high-entropy alloys [35].

In other research by Chen et al. [36], $Al_{0.4}CoCu_{0.6}NiSi_x$ high-entropy alloys developed with varying silicon content (x=0, 0.05, 0.1, 0.2) employing two distinct methods: Vacuum Arc Melting (VAM) designated as Mx and fast quenching through

copper injection, referred to as Ix. Their study focused on examining the effects of silicon addition and rapid cooling on these alloys. The findings revealed that Mx alloys typically exhibited a face-centered cubic plus L_{12} (FCC+L_{12}) structure. However, when the silicon content was increased to 0.1 and 0.2, the structure evolved to include a minor body-centered cubic (BCC) phase along with the existing FCC and L12 structures. Similarly, the Ix alloys generally displayed an FCC+L12 structure, except for the alloy with a silicon content of x=0.2, which also exhibited a minor BCC phase. A notable increase in hardness was observed with the rise in silicon content for both types of alloys. For Mx, the hardness escalated from 193 HV to 334 HV, whereas for Ix, it increased from 216 HV to 395 HV. This enhancement in strength is ascribed to the development of the BCC phase, solid solution strengthening, and the enhancement of grain size. Among these mechanisms, the formation of the BCC phase had a more significant impact on strengthening compared to fine-grained strengthening, which in turn was more effective than solid solution strengthening. These findings underscore the critical role of silicon content and cooling methods in influencing the microstructure and mechanical properties of HEAs.

The other study focused on NbZrTiCrAl HEA, which was synthesized using the Vacuum Arc Melting (VAM) process. Researchers investigated its microstructure and analyzed the oxidation behavior at 800, 1000, and 1200 °C. The alloy was primarily composed of a single-phase solid solution featuring a BCC structure characterized by a non-uniform microstructure that included both dendritic and interdendritic regions. At temperatures of 800 and 1000 °C, the alloy underwent oxidation following second-order kinetics. This oxidation process led to the formation of a uniform and dense layer of complex oxides, including $CrNbO_4$, ZrO_2, TiO_2, Al_2O_3, and $ZrNb_2O_7$, which were credited with providing protective properties to the alloy. However, a notable change occurred at 1200 °C. At this higher temperature, the oxidation kinetics shifted to a linear pattern, and the oxides developed a layered structure. This structural change in the oxides at 1200 °C is likely a contributing factor to the alloy's reduced stability against prolonged oxidation at elevated temperatures. This research highlights the critical impact of temperature on the oxidation behavior and stability of HEAs [37].

2.3.3 Fabrication of HEA Thin Films

Thin films, which are layers of material applied to a base surface typically known as the substrate, vary in thickness from several nanometers to a few micrometers. Their

primary function in surface engineering is to enhance various attributes of the underlying material, including its mechanical, electrical, optical, chemical, and other properties. This enhancement is achieved by altering the material's interaction with its environment. A diverse array of deposition techniques is employed to fabricate HEA thin films. These include methods like magnetron sputtering, laser cladding, arc cladding, spraying, and pulsed laser deposition. Among these, magnetron sputtering and pulsed laser deposition have gained prominence in recent times. The operating principles of these advanced deposition techniques will be elaborated upon in the subsequent sections, offering insights into their functionality and applications in the creation of HEA thin films [38,39].

Physical Vapor Deposition

For many years, Physical Vapor Deposition (PVD) has stood as the preferred technology for the production of thin films and coatings. This process involves the transformation of material from a condensed state to a vapor phase and subsequently back to a condensed thin film state, as illustrated in Figure 2. 8.

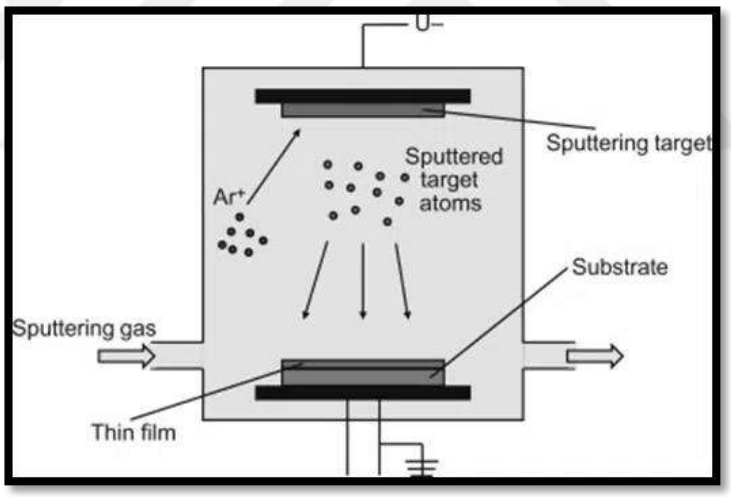

Figure 2. 8. Schematic of PVD process**.**

In this process, the material is initially evaporated from a target source. This evaporation is facilitated by various methods such as arc discharge, sputtering, and the use of electron or laser beams. Once evaporated, the material is accelerated away from the source and then condenses onto a substrate, forming the desired coating [40].

Among the various PVD techniques, magnetron sputtering [41] and pulsed laser deposition [42] have emerged as the most commonly used methods for depositing structural and functional coatings commercially. These techniques have been developed

and refined over time, establishing themselves as critical in the field of thin film and coating fabrication.

Magnetron Sputtering

The process known as sputtering deposition involves ejecting materials from a target source through the assistance of energetic ion bombardment. In this process, atoms or molecules are ejected from the source (target), evaporate, and then condense onto a substrate, resulting in film formation. There are two primary sources for the energetic ions required for this process: direct ion beam and glow plasma. While ion beam sputtering finds more application in surface analysis characterization, plasma-based sputter deposition is more prevalent in industrial applications due to its suitability for thin film deposition.

The plasma-based sputtering process is depicted in Figure 2. 9. In this setup, the cathode target and anode substrate are positioned parallel to each other within a vacuum chamber. This chamber is filled with an inert gas like argon. The application of a high bias, either direct current (DC) or radio frequency (RF), generates a glow discharge, leading to the formation of high-density plasma. The ionized Argon ions (Ar^+) vigorously sputter the target, causing clusters of atoms and molecules to be ejected and then energetically deposited onto the substrate [40].

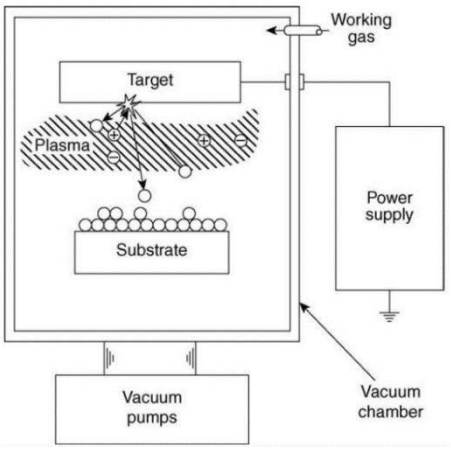

Figure 2. 9. Schematic for Plasma-based sputtering process.

Additionally, by introducing reactive gases such as N_2, O_2, CH_4, etc., it is possible to deposit coatings like nitrides, oxides or carbonitrides. The sputtering deposition process is highly controllable due to the numerous process parameters, allowing precise manipulation of the growth, structure, and properties of the deposited films. However, limitations of this technique include a low deposition rate, inefficiencies in plasma

ionization, and potential excessive heating of the substrate. To overcome these challenges, the technique of magnetron sputtering was developed, enhancing the efficiency and applicability of the sputtering deposition process [43].

In a diode sputtering system, the pattern of electron trajectories is solely influenced by the electrical field established between the target and the substrate. In this setup, electrons are rapidly accelerated across the cathode sheath, moving at high velocities towards the anode. However, this rapid electron movement often results in a quick loss of electrons, leading to an insufficient generation of ions necessary for maintaining the discharge. To counteract this issue, an effective method involves applying a magnetic field parallel to the cathode. This magnetic field creates a situation where electrons are retained near the cathode target, engaging in a more complex, elongated path toward the anode. This extended journey increases the likelihood of collisions with Argon (Ar) atoms, thereby generating an Ar^+ plasma and secondary electrons [44].

The Ar^+ ions are then accelerated to bombard the cathode target. Concurrently, the secondary electrons, influenced by the magnetic field, execute circular movements within the plasma region. These movements lead to further collisions with Argon atoms. The colliding Ar^+ ions undergo intricate scattering and collisions with the target atoms, resulting in their sputtering. The presence of a high-density plasma, a consequence of this process, significantly enhances ionization efficiency. It also reduces the discharge pressure and voltage while improving both the sputtering and deposition rates. This method effectively addresses the limitations inherent in the basic diode sputtering system, ensuring more efficient and controlled sputtering deposition [45].

Xing et al. [46] conducted a study on the $NbTiAlSiZrN_x$ HEA coating prepared under varying nitrogen flow rates. Their research revealed that the corrosion resistance of this coating significantly differs from that of 304 stainless steel. In another study, Lukáč et al. [47] developed an HfNbTaTiZr HEA film using DC magnetron sputtering. This film exhibited a nano-cell structure characterized by a fine surface microstructure and an uneven distribution of defects. Additionally, Chen and colleagues [48] investigated the mechanical properties and tribo-corrosion behavior of a VAlTiCrCu HEA thin film. This film was deposited on the surface of 304 stainless steel using magnetron sputtering at different deposition temperatures. Their findings showed that the film displayed exceptional corrosion resistance when exposed to an H_2SO_4 solution. Moreover, at a deposition temperature of 300 °C, the film's hardness was measured at 10.93 ± 1.07 GPa, and its elastic modulus was found to be 230.04 ± 56.03 GPa. These studies collectively

highlight the advancements in HEA coatings and their significant potential in enhancing the properties of substrates like stainless steel.

Table 2. 1 contains information regarding thin films based on HEA that were produced using the magnetron sputtering technique.

Table 2. 1. The details about HEA-based coatings fabricated using magnetron sputtering.

Coating	Substrate	Phases	Thickness	Hardness	Ref
$Al_{0.3}$CoCrFeNi	Si wafer	FCC	4.0 µm	11.09 GPa	[49]
TiTaHfNbZr	Ti-6-4	Amorphous	0.8 µm	12.51 GPa	[50]
CrNbSiTiZ	SS	Amorphous	1.0 µm	12.4 GPa	[51]
AlCrMoNbZr	N36 Zr alloy	Amorphous + BCC	3.0 µm	11.8 GPa	[52]
AlCrSiTiMoO	Si	Amorphous	3.3-3.8 µm	8.9 GPa	[53]
(CrNbSiTaZr)C	WC	Amorphous	1.2-2.1 µm	6.5-20 GPa	[54]
(AlCrNbSiTiV)N	Si wafer	Amorphous + FCC	≈1.0 µm	≈41 GPa	[55]

Influence of Deposition Parameters

Several factors within the magnetron sputtering deposition process, including the composition of the cathode target, the target's current or power density, the flow or pressure of the reactant gas, and the substrate's bias or temperature, significantly impact the composition, microstructure, and characteristics of the coatings produced [56,57].

Flow rate of Nitrogen (N_2)

In the context of nitride coatings, research has shown that the rate or partial pressure of nitrogen flow directly influences the collision and ionization of sputtered species. This impact is primarily through alterations in plasma density and the number of particles arriving at the substrate. These changes affect various aspects of the deposition process, including the rate of deposition, the chemical composition, and the crystal structure of the

film. Consequently, these factors play a crucial role in determining the mechanical properties of the resulting deposited film [58,59].

Temperature of the Substrate

Thornton's structure zone models (SZMs) [60] provide insight into how substrate temperature affects the morphology and microstructure of as-deposited coatings, as illustrated in Figure 2. 10. This model uses the homologous temperature ratio, Ts/Tm, where Ts is the substrate temperature, and Tm represents melting point of the coated material, to describe different zones.

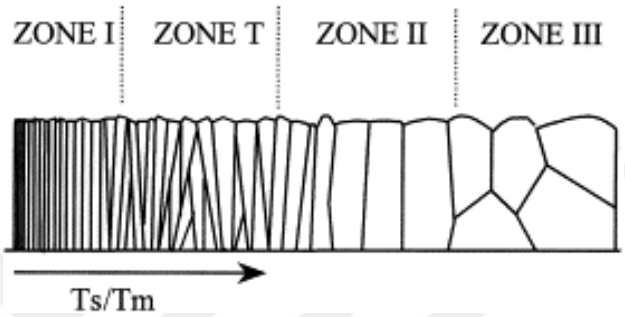

Figure 2. 10. Main characteristics of structure zones as a function of homologous temperature Ts/Tm

In Zone I, characterized by a Ts/Tm ratio of 0 to 0.2, the film is made up of fine fibers with diameters ranging from 1-10 nm. This structure is a result of the nucleation density and statistical fluctuations. Fibrous grains originate from primary nuclei and extend homogeneously along the film's thickness, often accompanied by a high density of defects and porous grain boundaries within the crystals.

Zone T, with a Ts/Tm ratio between 0.2 and 0.4, displays an inhomogeneous structure throughout the film thickness. At the coating/substrate interface, fine crystallites composed of V-shaped grains are evident, transitioning to columnar grains in the upper part of the films. The formation of this structure is governed by self-diffusion mechanisms.

In Zone II, where the Ts/Tm ratio exceeds 0.4, the film typically exhibits a structure of columnar grains that is homogenous through the film thickness. This pattern is more common at higher substrate temperatures.

Zone III is distinct in that it is characterized by equiaxed grains, suggesting periodic interruptions in crystal growth. This structure emerges under certain conditions, reflecting

the complex interplay between substrate temperature and material properties in the coating process [61].

Pulse Laser Deposition

Pulsed laser deposition is a highly effective method for depositing HEA thin films, offering several advantages. One significant benefit is the laser-induced ablation of the target material, forming a plume that allows the stoichiometry of the deposited film to closely match that of the target material, a precision often unattainable with other techniques. Additionally, the laser parameters, such as laser fluence, can be finely adjusted to precisely control the growth rate of the film [62].

However, there are some drawbacks to this method. The high kinetic energy of the plume can lead to re-sputtering from the film's surface, potentially introducing defects. Furthermore, macroscopic fragments may be ejected from the target, potentially degrading the film's properties.

A diagrammatic representation of a pulsed laser deposition system is depicted in Figure 2. 11 and illustrates how a high-power pulsed laser beam is focused onto the target using lenses. The target for this system is typically prepared through a powder metallurgy process involving cold pressing followed by sintering. When the laser beam is focused on the target, the material is vaporized and ejected as a plasma plume, which then deposits onto the substrate, forming a thin film. This process can be carried out either in high vacuum conditions or in an environment with background gases like oxygen or nitrogen, which is essential for forming ceramic thin films [34].

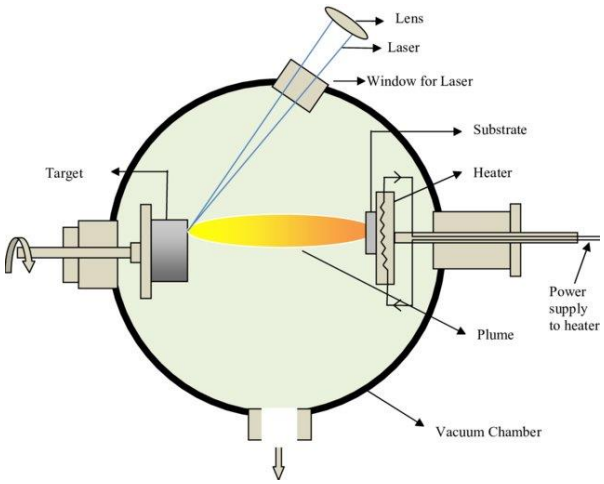

Figure 2. 11. A schematic diagram of the pulsed laser deposition setup**.**

2.4 Refractory High-entropy Alloys (RHEA)

Alloy systems developed and studied can generally be categorized into two types: Transition Metal High-Entropy Alloys (TM HEAs) and Refractory High-Entropy Alloys (RHEAs). TM HEAs primarily consist of Al and IV period 3d transition metals like Fe, Co, Ni, Cr, Cu, Mn, and Ti. On the other hand, RHEAs are based on refractory metals such as Mo, Ti, V, Nb, Hf, Ta, Cr, and W, among others [63].

The exploration into these alloys was largely driven by a desire to investigate the vast central region of complex phase space and to create new high-temperature structural alloys. In this vein, Senkov et al. [64] pioneered the creation of refractory metal high-entropy alloy systems NbTaMoW and VNbTaMoW in 2010. Their research focused on analyzing the crystal structure, lattice parameters, and mechanical properties of these alloys. These studies unveiled that both alloys possessed a simple body-centered cubic (BCC) crystal structure and exhibited Vickers hardness values 2 to 3 times greater than those predicted by theoretical mixing law calculations, marking a significant advancement in the study of refractory metal HEAs. Their capability to retain high strength at temperatures as high as 1600 °C quickly drew widespread attention from the high-temperature research community [65].

The initial RHEAs were composed of a combination of five refractory metals: Mo, Nb, Ta, V, and W. Subsequent iterations of RHEAs expanded to include a broader spectrum of nine refractory metals from groups IV (Ti, Zr, Hf), V (V, Nb, Ta), and VI (Cr, Mo, W). Occasionally, non-refractory metal elements such as Al, Si, Co, or Ni were also incorporated. As research deepened, there has been an increasing focus on alloys that merge non-metallic elements with refractory transition elements, expanding the field from RHEAs containing only transition metals to new systems based on transition metals and supplemented by other elements.

Recent studies highlight the significant role of the "cocktail effect" inherent in HEAs, where the type and amount of alloying elements in RHEAs have profound impacts on phase stability, compositional uniformity, and microstructure. Consequently, these factors greatly influence the comprehensive properties of RHEAs. Additionally, the "lattice distortion effect" in HEAs means that the addition of alloying elements can modify the original lattice of RHEAs in three primary ways: by filling interstitial positions, replacing atoms in the existing lattice, or forming precipitated/dispersed phases. These modifications alter the toughening mechanisms in RHEAs, with alloying

elements acting as key mediators in various properties and mechanical strengths. As a result, many RHEAs exhibit exceptional properties after elemental adjustment, making element regulation an essential and ongoing area of research [63].

2.4.1 Preparation of RHEAs

In the fabrication of RHEAs containing refractory elements with high melting points (typically above 1800 °C) and notable differences in their melting points (ranging from Cr at 1857 °C to W at 3422 °C), various challenges arise. These include macro-segregation often manifested as dendritic structures, the formation of pores, and solidification defects like residual stress, complicating the preparation of RHEAs [66].
Commonly employed methods for producing RHEA include arc melting, induction melting, laser melting, and spark plasma sintering [67–73]. Among these, arc melting is the most prevalent technique for RHEA fabrication, a trend that holds true for HEAs in general. Given the susceptibility of refractory metals to high-temperature oxidation, these melting processes are typically conducted in vacuum conditions or within high-purity inert atmospheres, with vacuum arc melting being particularly prominent [63].
Qiao and colleagues [74] adeptly fabricated the VTaTiMo RHEA utilizing vacuum arc melting, resulting in an alloy with commendable mechanical properties. Similarly, Guo and team [75] employed vacuum-arc melting to synthesize the MoNbHfZrTi RHEA, focusing their research on examining the alloy's thermal deformation and dynamic recrystallization behaviors. In addition, Yi and associates [76] created the CrHfNbTaTi RHEA through vacuum-arc melting, conducting a thorough analysis of the alloy's microstructure and mechanical attributes. Notably, the high-temperature mechanical performance of this alloy was found to surpass that of traditional nickel-base superalloys.

Advancements in preparation methods have led to the increasing use of powder metallurgy (PM) in conjunction with grinding and mechanical alloying (MA) for RHEA production. This approach, noted for its effectiveness, has gained rapid acceptance. Powder metallurgy involves mixing and mechanically grinding elemental or pre-alloyed powders to achieve the desired composition, followed by vacuum spark plasma sintering (SPS) to consolidate these powders into dense products. RHEAs produced via this method tend to exhibit reduced component segregation, limited dendrite formation, and minimal multi-phase precipitation, resulting in bulk high-entropy alloys with finer grains and more

uniform compositions. This results in enhanced performance of the HEAs. Nonetheless, it is crucial to prevent contamination and internal oxidation during the preparation process [72,73,77].

Studies have shown that the sintered TiNbTaZrAl RHEA exhibits a compressive yield strength of 1740 MPa and compressive plasticity of 12%, underscoring how powder metallurgy techniques can significantly enhance the mechanical properties of RHEAs [78]. The VNbMoTaW RHEA, fabricated using the powder metallurgy method, presents a superhard nanocrystalline BCC structure with a hardness value of 16.3 GPa post-sintering [74]. Malek et al. [70], through powder metallurgy, created HfNbTaTiZr samples that achieved high hardness and a fine-grained structure following high-pressure torsional deformation. Additionally, Kang and team [79] developed the $Al_{0.1}$CrNbVMo RHEA via MA and Spark Plasma Sintering SPS. This alloy exhibits a lower density compared to many nickel-based superalloys, with a room temperature compressive strength of 2863 MPa and maintaining over 1400 MPa at 1000 °C. Its specific yield strength, at 176 MPa cm^3/g, stands out among RHEAs, suggesting its potential for future applications in the development of lightweight RHEAs.

Techniques such as magnetron sputtering, plasma spraying, electrochemical deposition, thermal spraying, and laser cladding are commonly used for the fabrication of refractory high-entropy alloy films or coatings. In terms of heat treatment, the most extensively studied processes for HEAs include high-temperature annealing and aging. As research progresses, both the preparation and heat treatment methods for RHEAs will continue to evolve, expanding the potential applications of HEAs [63].

Bachani and colleagues [80] developed a VNbMoTaWAl RHEA coating with exceptional hardness using magnetron sputtering. This coating significantly enhances the corrosion resistance of 304 stainless steel in an H_2SO_4 solution. Similarly, Alvi and team [81] employed magnetron sputtering to apply a BCC-structured CuMoTaW RHEA film onto 304 stainless steel. The findings from this study revealed that the RHEA film possesses nanocrystalline characteristics, with a peak hardness of 21.3 GPa and an elastic modulus of 278.2 GPa, demonstrating notable wear resistance. Such research is pivotal in advancing the commercial application of HEA films. Generally, RHEA thin films produced via magnetron sputtering exhibit superior hardness and wear resistance compared to those that are as-cast or sintered, showcasing their vast potential for applications in surface enhancement technologies.

2.5 Applications of HEAs

Alloys, recognized as one of the three principal material systems globally, have found extensive application across various engineering domains, ranging from high-strength construction materials to corrosion-resistant coatings. The advent of HEAs in the early 21st century, distinguished by their superior mechanical attributes, has led to their widespread exploration and utilization in numerous engineering disciplines. Notably, HEAs exhibit exceptional strength and toughness at elevated temperatures and demonstrate remarkable stability and durability in diverse, challenging conditions.

Over the last decade, the distinct functional properties of HEAs have garnered increasing interest, leading to an expansion in their application across various fields. The forthcoming section will specifically delve into the employment of HEAs in the realms of biomaterials and electrocatalysts, highlighting their pivotal role and the innovative advancements they bring to these areas [17].

2.6 RHEA for biomaterial app

In 2019, the introduction of the term "BioHEA" was reported through the publication of two articles, marking its first documented usage. This designation has been attributed to multi-principal element alloys under consideration for biomedical applications. The goal has been to surpass the performance of traditional alloys such as cp-Ti, Ti6Al4V, 316L, and CoCrMo in terms of overcoming their inherent limitations. Encouraging findings have demonstrated these alloys' potential for offering equal or superior corrosion resistance, stability against implant degradation in physiological conditions, mechanical robustness alongside biocompatibility, controlled ion release, minimal magnetic susceptibility, enhanced wear resistance, and effectiveness against bacterial infections.

When evaluating materials for biomedical use, hardness stands out as a critical property due to its straightforward measurement. Specifically, for applications related to bone tissue, the material's hardness needs to match or exceed that of bone to prevent undesirable penetration. Additionally, a higher hardness level plays a significant role in diminishing wear rates. Another essential property, Young’s modulus, measures material stiffness. For optimal integration with bone tissue, the modulus should closely match that of bone, preventing the stress shielding effect that could lead to biomaterial fracture and failure. Also, it is essential to conduct appropriate in vitro experiments [82].

2.6.1 Electrochemical Test

In recent years, the extensive adoption of metallic implant materials in healthcare has prompted researchers to closely monitor and study patients post-repair surgery. It has been observed that these implant materials are susceptible to corrosion from complex interactions with bodily fluids. Additionally, there is a possibility of stress wear arising from the movement between bones. Such conditions can lead to plastic deformation of the material, ultimately affecting its properties and leading to implant failure, potentially resulting in patients needing multiple surgical interventions in severe cases. Moreover, the wear of implant materials against the surrounding human tissues can lead to the generation of metallic debris, which might provoke tissue infections and allergic reactions. Corrosion and stress wear of the implants may also facilitate the release of toxic metal ions, potentially initiating toxic and allergic responses. Consequently, there is a pressing need for the development of new implant materials that exhibit superior overall performance to mitigate the adverse effects of implants within the human body [83,84]. RHEAs are recognized for their exceptional cytocompatibility, yet the selection of these materials for practical applications must account for their operational environment, particularly their interaction with body fluids. The bodily environment poses a highly aggressive challenge to metals and alloys due to the presence of hydrogen ions, chloride ions, and proteins. When used as metal implants, Bio-HEAs engage in chemical interactions with body fluids, leading to the oxidation of the metal components of the alloy into ionic forms and the reduction of dissolved oxygen into hydroxide ions. This process can result in various types of corrosion damage. To assess the corrosion resistance of Bio-HEAs, researchers commonly employ solutions that simulate the physiological environment. These include saline (a 0.9% NaCl solution), Hank's solution, phosphate buffer saline (PBS), and fetal bovine serum (FBS). These solutions provide a standardized context for evaluating how Bio-HEAs might perform in the human body, highlighting their corrosion behavior in conditions analogous to those within the human body [85–87]. Potentiodynamic polarization curve analysis stands as a cornerstone technique in the study of electrochemical corrosion, offering vital insights into the corrosion rates and mechanisms of bio-alloy materials within a simulated physiological setting. This method is instrumental in assessing the compatibility of Bio-HEAs with biological environments, specifically under conditions of chemical corrosion. Key parameters such as corrosion potential (Ecorr), corrosion current density (Icorr), and AC impedance play crucial roles

in evaluating a material's corrosion resistance. For Bio-HEAs containing elements like Ti and Ta, their lower Ecorr values suggest a propensity to form protective passivation layers, typically oxides, enhancing their durability [88,89].

Remarkably, most Bio-HEAs exhibit no pitting reaction up to 1.8-2V, indicating their robust performance in the human body's potential range of 0–0.2 V. This absence of pitting and localized corrosion, due to the stability of the protective passivation films, significantly extends the lifespan of alloy implants. The corrosion current density, Icorr, serves as an indicator of the material's corrosion rate; a lower Icorr value denotes a reduced rate of corrosion. The favorable Icorr values associated with Bio-HEAs underscore their suitability for use in medical alloy implant applications, promising enhanced longevity and reliability [87,90].

The Ti-Zr-Ta-Hf-Nb Bio-HEAs system emerges as an advanced metallic biomaterial, showcasing an optimal mix of properties such as wear resistance, wettability, pitting resistance, and general corrosion resistance. These characteristics surpass those of traditional metallic biomaterials like 316L stainless steel, CoCrMo alloys, and Ti-6Al-4V [87]. Song and Xu [91] delved into the electrochemical behaviors of $(TiZrNbTa)_{90}Mo_{10}$ HEA in Ringer's solution and utilized XPS for analyzing the passive film formation on the $(TiZrNbTa)_{90}Mo_{10}$ HEA surface. Their findings reveal that $(TiZrNbTa)_{90}Mo_{10}$ HEA demonstrates considerably enhanced corrosion resistance compared to CoCrMo alloys and stainless steel. Furthermore, Aksoy et al. [92] explored the application of TiTaHfNbZr HEA films on NiTi shape memory alloys through RF magnetron sputtering. The subsequent immersion of these films in artificial saliva (AS) and gastric fluid (GF) highlighted the TiTaHfNbZr HEA coatings' significant role in curbing the release of Ni ions. Thus, TiTaHfNbZr HEA thin films have been identified as promising biomedical coatings for NiTi implants aimed at preventing Ni ion release.

Wang and Xu [93], as shown in Figure 2. 12, conducted a study on the electrochemical behavior of HEA in PBS through kinetic potential polarization tests. They aimed to assess the corrosion resistance of the HEA in a physiological setting and compared its performance with that of Ti6Al4V, 316L, and CoCrMo alloys. Their findings revealed that the TiZrNbTaMo HEA demonstrated a wide passive range in the polarization curve up to 1.2 V SCE without any signs of pitting or breakdown of passivation. This behavior closely resembled that of the Ti-6Al-4V alloy, although the HEA showed a more positive Ecorr and a marginally higher passive current density than Ti-6Al-4V. In the simulated physiological environment of PBS media, the TiZrNbTaMo HEA displayed remarkable

corrosion resistance comparable to that of the Ti6Al4V alloy. Furthermore, it exhibited superior pitting resistance compared to both 316L SS and CoCrMo alloys, indicating its potential suitability for biomedical applications.

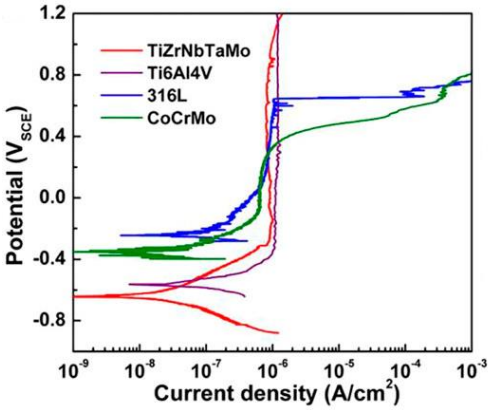

Figure 2. 12. Potentiodynamic polarization curves of arc-melted TiZrNbTaMo HEA, as well as Ti-6Al-4V, 316L, and CoCrMo alloys in PBS for comparison of biocompatibility

2.6.2 Cell Adhesion and Cytotoxicity

Cell adhesion plays a crucial role in the stability of tissue structures and acts as a significant regulator of cell movement and functionality, impacting cell proliferation and differentiation significantly [94]. The cytotoxicity assay is commonly employed to assess an alloy's impact on cellular growth activity, serving as a vital metric in vitro evaluations [95]. Cytotoxicity encompasses the actions of chemical substances, drugs, or physiological impacts on cells, affecting fundamental structures and processes. These include alterations to the cell membrane or cytoskeleton, cellular metabolism, synthesis, degradation, or release of cellular components or products, ion regulation, and cell division. These actions can disrupt cell survival, proliferation, or functionality, leading to adverse effects [84].

In recent investigations, follow-up studies of patients post-implant surgery have revealed that long-term implantation of metal materials can lead to various biological issues. Notably, elements like Co and Ni in cobalt-based alloys pose serious sensitization concerns, while the prolonged presence of Al and V in widely used Ti-6Al-4V implants can impact human organs and functions. Thus, evaluating the cytotoxicity and activity of metal implant materials holds paramount importance prior to their surgical implantation in humans [84].

Cytotoxicity and cell activity assessments primarily focus on the responses of individual cells, including changes in cell membrane permeability. Based on prior research, methods

for detecting cytotoxicity and cell activity are categorized into dye exclusion assays, colorimetric assays, fluorometric assays, and luminometric assays. Within these, colorimetric assays such as MTT, XTT, and LDP are frequently utilized for cellular analyses, underscoring their significance in the examination of cell interactions with implant materials.

Hori et al. [96] developed a collection of innovative Ti-Nb-Ta-Zr-Mo HEAs, revealing their efficacy in enhancing the maturation of local adhesion spots in osteoblasts. Comparative analyses, as shown in Figure 2. 13, indicated a higher adhesion of osteoblasts on these HEAs, specifically $Ti_{1.4}Zr_{1.4}Nb_{0.6}Ta_{0.6}Mo_{0.6}$ and $Ti_{0.6}Zr_{0.6}Nb_{1.4}Ta_{1.4}Mo_{1.4}$, in comparison to SUS316L stainless steel. Notably, the $Ti_{1.4}Zr_{1.4}Nb_{0.6}Ta_{0.6}Mo_{0.6}$ alloy demonstrated exceptional biocompatibility, underscored by significantly longer adhesion structures compared to its $Ti_{0.6}Zr_{0.6}Nb_{1.4}Ta_{1.4}Mo_{1.4}$ counterpart.

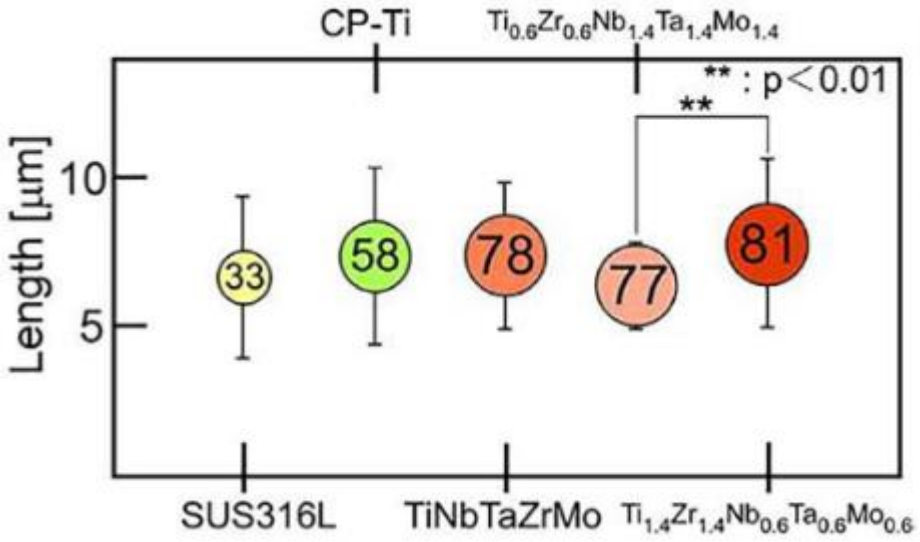

Figure 2. 13. quantitative analysis of size regulation of fibrillar adhesions (longer than 5 μm) in osteoblasts cultured on the fabricated specimens.

In separate research, Nagase et al. [97] observed that the Ti-Zr-Hf-Cr-Mo and Ti-Zr-Hf-Co-Cr-Mo HEAs exhibited superior biocompatibility relative to commercially pure titanium (CP-Ti). Similarly, Edalati et al. [98] assessed the TiAlFeCoNi HEA, which displayed ultra-high hardness and promising cellular activity, as confirmed through MTT assays and microhardness tests. Todai and his team [99] introduced a TiNbTaZrMo HEA, noting its commendable biocompatibility in comparison to CP-Ti. The morphology of osteoblasts on both as-cast and annealed surfaces of this HEA was observed to closely resemble that on CP-Ti surfaces. In contrast, osteoblasts on 316L stainless steel exhibited

a limited variety of morphologies. The findings suggest that osteoblasts on TiNbTaZrMo HEAs and CP-Ti are significantly beneficial for bone matrix formation.

Yang et al. [100] conducted an experiment to assess the biocompatibility of Titanium-Zirconium-Hafnium-Niobium-Tantalum High Entropy Alloys (Ti-Zr-Hf-Nb-Ta HEAs) using MC3T3-E1 cells. The cells were cultured on four different substrates: $Ti_{20}Zr_{20}Hf_{20}Nb_{20}Ta_{20}$ named Alloy-I, $Ti_{25}Zr_{25}Hf_{25}Nb_{12.5}Ta_{12.5}$ named Alloy-II, $Ti_{27.78}Zr_{27.78}Hf_{27.78}Nb_{8.33}Ta_{8.33}$ named Alloy-III, and Ti6Al4V, a widely used titanium alloy. After 72 hours of incubation, the cellular activity on these substrates was visualized through fluorescence staining.

The results in Figure 2. 14 showed that a considerable number of MC3T3-E1 cells adhered well to both the HEA and Ti6Al4V surfaces, demonstrating a high survival rate of the attached cells. This suggests that the HEA provides a favorable environment for cell survival and initial adhesion. Moreover, cell survival counts conducted over three consecutive days revealed no significant differences between the HEA and Ti6Al4V substrates. This finding indicates that the Ti-Zr-Hf-Nb-Ta HEA exhibits a level of biocompatibility comparable to that of the Ti6Al4V alloy.

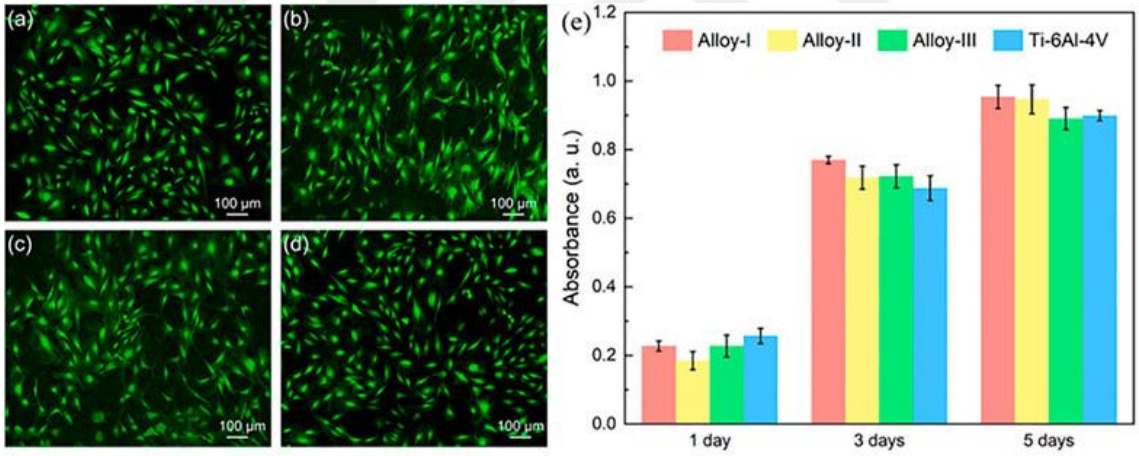

Figure 2. 14. Live/dead staining of MC3T3-E1 cells on (a) Alloy-I, (b) Alloy-II, (c) Alloy-III, and (d) Ti64 after 72 h of incubation. (3) The proliferation of MC3T3-E1 cells on Alloy-I, Alloy-II, Alloy-III, and Ti64 after 1, 3, and 5 days of cell culture, respectively

2.6.3 Antibacterial

Titanium alloys and other metallic materials used for implants are known to be vulnerable to bacterial infections post-surgery within the human body. To mitigate the incidence of such infections during the implantation process, the current strategy extends beyond merely relying on antibiotics; it includes employing implants imbued with antibacterial properties. Should an infection arise, the implant risks becoming dislodged

or failing altogether, necessitating prolonged antibiotic treatment or even multiple surgical interventions for the patient. This situation escalates the psychological and financial strain on both the patients and the healthcare infrastructure.

Consequently, there is a dedicated effort within biomedical research to innovate materials endowed with antibacterial capabilities. The medical sector is in pressing need of novel biomedical materials capable of sustaining long-term anti-infection roles, aiming to diminish infection rates and curb antibiotic overuse. The development of such materials holds profound implications for easing patient suffering and enhancing the quality of life. In foundational research conducted by Wu et al. [101], the antibacterial efficacy of HEA coatings was evaluated by exposing them to bacteria such as Staphylococcus aureus, Escherichia coli, Klebsiella pneumoniae, and Pseudomonas aeruginosa [84]. Observations after 24 hours revealed that HEA coatings markedly inhibited bacterial colony growth, achieving an antibacterial efficiency exceeding 95%, thus confirming their potent antibacterial properties.

To bolster both the mechanical and antibacterial performance of these materials, it is common practice to integrate trace amounts of antibacterial elements like Cu and Ag into the metallic composition. Recent scholarly investigations have delved into the antibacterial attributes of copper-enriched Ti-based HEAs and copper-inclusive HEAs. For instance, Ke et al. [102] developed a Ti-13Nb-13Zr-10Cu medical alloy, which not only exhibited a significantly reduced elastic modulus compared to CP-Ti but also demonstrated pronounced antibacterial activity against S. aureus cultures after 24 hours. HEAs that possess antibacterial properties not only exhibit robust and enduring bactericidal capabilities but also demonstrate commendable corrosion resistance and mechanical strengths. This suggests that Bio-HEAs hold significant promise for use in medical device applications. Bio-HEAs enriched with Cu or Ag ions are particularly noted for their enhanced antibacterial effectiveness. However, the liberation of Cu^{2+} and Ag^{+} ions can potentially harm the human body, necessitating a careful selection of elemental compositions. The objective is to design Bio-HEAs that effectively balance antibacterial functionality with minimal adverse effects on human health [87].

2.7 HEA for electrocatalyst app

Currently, HEAs have found applications across various domains, with their use in electrocatalysis emerging as particularly promising. A growing body of research has

focused on the application of HEAs in electrocatalytic reactions [103]. Investigators have found that HEA catalysts serve as multifunctional electrode materials, offering optimized performance across a wide range of compositions. To advance the utilization of HEAs in electrocatalysis, researchers have explored the nanostructures of different HEA series and their catalytic properties in reactions such as the oxygen reduction reaction (ORR), nitrogen reduction reaction (NRR), oxygen evolution reaction (OER), hydrogen evolution reaction (HER), ethanol oxidation reaction (EOR), and methanol oxidation reaction (MOR) [104–109]. The findings suggest that HEAs hold significant potential in the field of electrocatalysis and could serve as a viable alternative to conventional catalysts.

2.7.1 HEAs for OER

The Oxygen Evolution Reaction (OER) is a critical electrochemical reaction with both fundamental and technological significance in the field of renewable energy production. It plays a vital role in water splitting, fuel cells, metal-air batteries, and other sustainable energy systems [110,111]. OER represents the half-reaction of water splitting, where water molecules are oxidized to produce oxygen gas. It involves a four-electron transfer process, making its reaction mechanism more intricate compared to the Hydrogen Evolution Reaction (HER). Furthermore, the behavior of OER varies under acidic and alkaline conditions, impacting its efficiency and applicability in different energy systems [112].

For acidic solution:

$2H_2O \rightarrow O_2 + 4H^+ + 4e^-$

For alkaline solution:

$4OH^- \rightarrow O_2 + 2H_2O + 4e^-$

For the OER, two primary mechanisms exist: the adsorbate evolution process and the lattice oxygen oxidation process. In the adsorbate evolution mechanism, depicted in Figure 2. 15a, OER involves several adsorption-related intermediates. The catalytic activity can be enhanced by modulating the binding strength of these intermediates. On the other hand, the lattice oxygen oxidation mechanism, illustrated in Figure 2. 15b, encompasses the adsorption of hydroxide ions (OH^-), the formation of O-O bonds and *OOH, the release of water (H_2O), and the reaction of *OOH with OH^- to produce molecular oxygen (O_2). In this mechanism, the creation of O-O bonds facilitate the

generation of oxygen vacancies, which promotes the adsorption of OH^- and the surface reconstruction of oxyhydroxide [113,114].

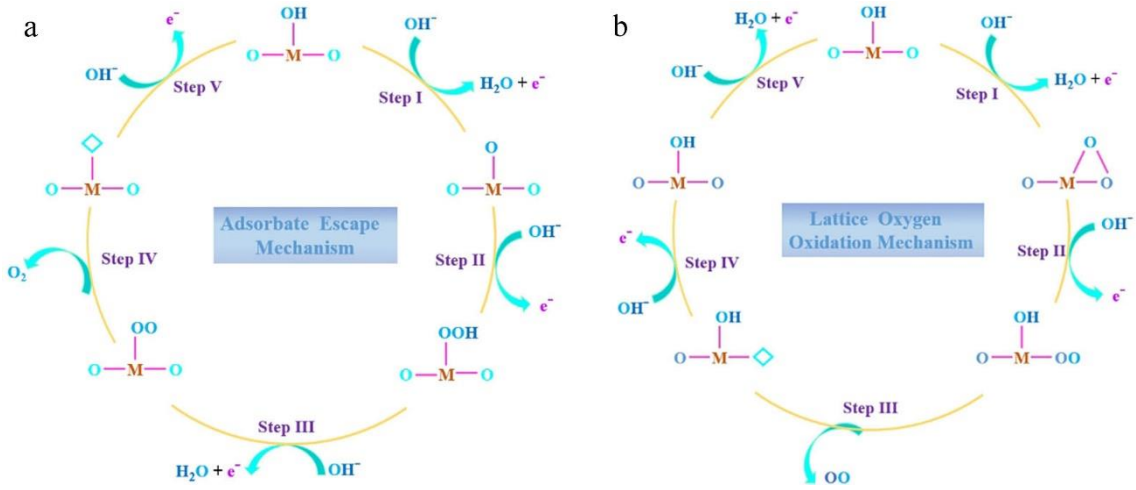

Figure 2. 15. Mechanism of oxygen evolution reaction process a. OER mechanisms plots of adsorbate escape mechanism. b. Lattice oxygen oxidation mechanism (M represents metallic electrode material).

It should be highlighted that the emergence of an O-O bond in the lattice oxygen oxidation mechanism is contingent upon the ability of two adjacent oxidized oxygen atoms to rotate and hybridize with an oxygen vacancy without compromising the metal-oxygen hybridization.

However, the anodic OER typically necessitates high overpotentials due to its complex four-electron transfer process. The slow kinetics at the anode often require a large thermodynamic potential (1.23 V vs. RHE) to drive the reaction. Precious metals and metal oxides, such as ruthenium and iridium oxides (Ru/Ir oxides), have been employed in practical applications to enhance OER efficiency. Nevertheless, their limited availability, poor stability, low selectivity, and high cost pose challenges to their widespread use [115].

The distinctive high entropy effect and cocktail effect inherent in HEAs contribute to their exceptional stability and versatility, particularly in terms of electrochemical behavior. The synergistic interaction among various elements in HEAs results in heightened chemical reactivity. The specialized chemical sites on the surface of HEAs enhance adsorption capabilities and binding efficiency, substantially lowering the energy barrier in catalytic processes. Consequently, HEAs are extensively utilized in catalysis, with notable applications in water splitting [116].

Qiu et al. [117] successfully synthesized various nano-porous High Entropy Alloy (np-HEA) structures with a controlled size range of 2–3 nm using a top-down dealloying

method. The modified AlNiCuMoCoFe np-HEA exhibited high activity in Oxygen Reduction Reaction (ORR) tests, suggesting that np-HEAs prepared via this method could potentially replace noble metal-based electrocatalysts. Further, Qiu et al. [118] investigated the OER performance of AlNiCoFeX (X=Mo, Nb, Cr) np-HEA electrocatalysts, also prepared by the dealloying method. After substantial Al removal from the precursor, the resulting alloy exhibited a fine metallic sheet structure with numerous nanopores, as shown in Figure 2. 16a. XPS analysis revealed a consistent +6 valence state for Mo ions in the catalyst. Linear Sweep Voltammetry (LSV) tests identified np-AlNiCoFeMo as exhibiting superior OER activity, as depicted in Figure 2. 16b,c. These results indicate that Mo's high oxidation state, detected by XPS, aligns with its inherent activity. The lattice distortion-induced compressive strain further diminishes Ni chemisorption, favoring proton migration. This underscores the inherent activity of HEA catalysts based on Electrochemical Surface Area (ECSA) and highlights the synergistic effect among elements in HEA catalysts.

Using a similar synthesis process, Jin's team [119] synthesized AlNiCoIrMo np-HEA with a nano-bimodal porous structure (Figure 2. 16d), showcasing an FCC structure with two nanopore size levels and excellent OER catalytic activity under acidic conditions. Experimental analyses revealed enhanced oxygen evolution performance under acidic conditions, which was attributed to the increased number of Ir-O active sites in the catalyst. The high entropy system studied by Jin, akin to the previous one, demonstrates that a change in a single component can alter the activity source, highlighting the diversity and different activity mechanisms of high entropy materials.

Contrasting with the FCC-structured HEA systems, Ding et al. [120] developed a $FeCoCrNb_{0.5}Ni$ HEA with an intermetallic compound Laves phase, as shown in Figure 2. 16e. After surface etching, this alloy formed an oxide-alloy core-shell junction. Electrochemical measurements revealed an overpotential value of only 288 mV at a current density of 10 mA cm^{-2}, showcasing its catalytic efficiency.

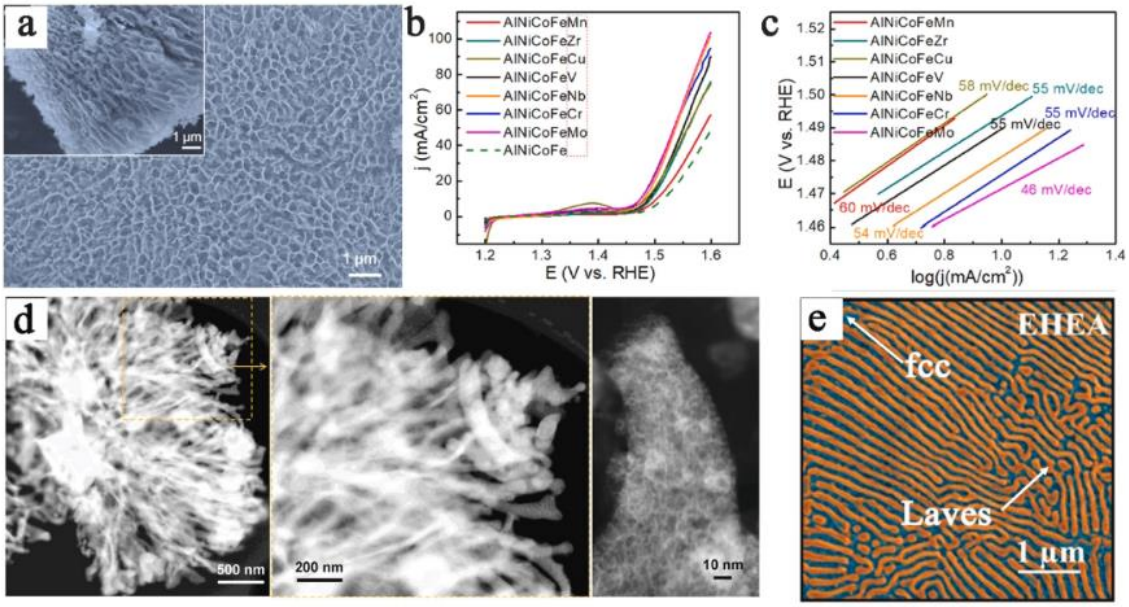

Figure 2. 16. a) SEM image of nanoporous AlNiCoFeMo. b) LSV curve of np-AlNiCoFeMo and its control group. c) Tafel slope of np-AlNiCoFeMo and its control group. d) STEM images of the dealloyed np-AlNiCoIrMo at different magnifications. e) SEM image of porous HEA before dealloying

Tang et al. [121] successfully synthesized a HEA catalyst using powder compaction and microwave sintering, with magnesium powder serving as a structural proppant in the catalyst design—a rare approach. Intriguingly, magnesium completely evaporated during microwave heating and sintering, facilitating the formation of a porous structure in the CoCrFeNiMo HEA catalyst. The surface of the electrochemically activated CoCrFeNiMo-20Mg sample exhibited numerous fluffy nanosheets, along with abundant stacking faults and twin defects, which could potentially act as active centers for reactions. Furthermore, the elements in CoCrFeNiMo-20Mg-HEA remained mostly in a metallic state, with only a minor portion undergoing oxidation. After electrochemical testing in a 1.0 M KOH solution, all metallic states and low-valent oxides were converted into high-valent oxides and hydroxides, indicating their role as truly active species. This transformation suggests that intermetallic synergy is fundamental to the formation of catalytically active sites.

In the realm of special metal materials, amorphous alloys also exhibit catalytic activity for the OER under alkaline conditions. Recently, Wang et al. [122] prepared nano-amorphous $Fe_{29}Co_{27}Ni_{23}Si_9B_{12}$ with high entropy as an OER electrocatalyst through melt spinning and etching. Experiments demonstrated that after $Fe_{29}Co_{27}Ni_{23}Si_9B_{12}$ underwent corrosion by hydrochloric acid (HCl) and potassium chloride (KCl) for 1 hour, the surface of the corroded HEA (A-HEA) exhibited a concave-convex morphology with randomly

distributed pits ranging from 30 to 300 nm in diameter. Prolonged etching for 3 hours resulted in larger, interconnected pits, creating a staggered surface morphology while preserving the amorphous structure. Further characterization revealed that the shallow pores consisted of nanometer-sized dots, providing a larger specific surface area and more catalytic active centers.

2.7.2 HEA for HER

Electrocatalytic Hydrogen Evolution Reaction (HER) stands as one of the most promising methods for artificial hydrogen production and has been extensively researched [123]. As a crucial half-reaction in electrocatalytic water splitting, HER involves two proton-coupled electron transfers, encompassing the adsorption and desorption of hydrogen atoms, with only one H^* playing a role in the rate-determining step. The behavior of HER varies under acidic and alkaline conditions [124,125].

For acidic solution:

$2H^+ + e^- \rightarrow H_2$

For alkaline solution:

$2H_2O + 2e^- \rightarrow H_2 + 2OH^-$

As illustrated in Figure 2. 17, the initial phase is the Volmer reaction, where a proton combines with an electron to form an adsorbed hydrogen atom (H^*) on the electrode material's surface. In acidic electrolytes, the proton source is the hydronium ion (H_3O^+), while in alkaline electrolytes, water molecules serve as the proton source. Following this, molecular hydrogen (H_2) can be produced through either the Heyrovsky reaction, the Tafel reaction, or a combination of both. In the Heyrovsky step, an additional proton merges with H^* and reacts with a second electron to form H_2. In the Tafel step, two neighboring H^* entities on the electrode surface come together to create H_2.

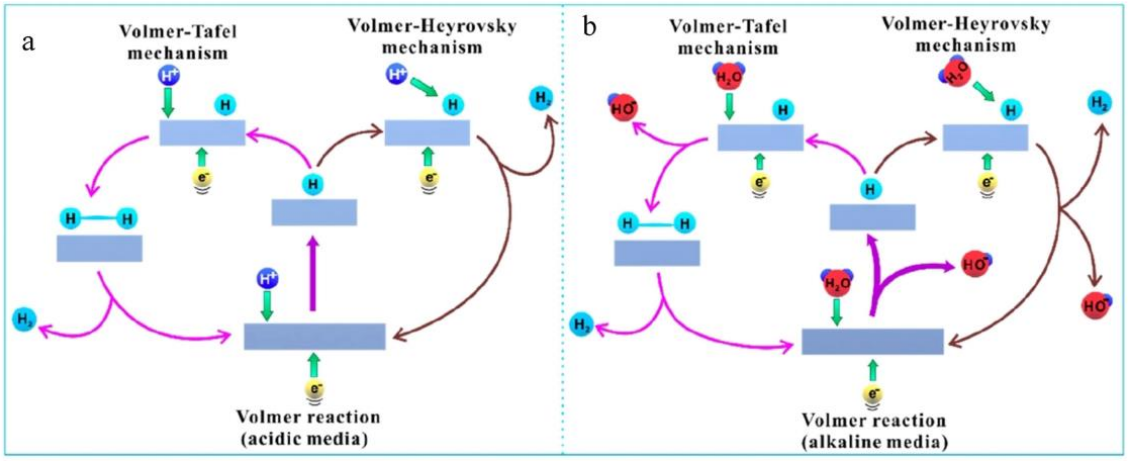

Figure 2. 17. Mechanism of hydrogen evolution reaction process. a. HERmechanismin acidic electrolyte. b. HERmechanismin alkaline electrolyte.

Transition metals and alloys like Ni, Co, Mo, and Fe are known for their catalytic activity in the HER. Integrating these transition metals with precious metals into single nanoparticles (NPs) can offer adjustable catalytic properties. Glasscott and colleagues [126] synthesized CoFeLaNiPt high-entropy metallic glass nanoparticles (HEMG-NPs) using the nanodroplet-mediated electrodeposition method, which exhibited excellent HER activity in electrocatalytic hydrolysis. The HEMG-NPs outperformed individual components with an overpotential of 555±2 mV, showing better performance than Fe, Pt, and Co NPs. This suggests synergistic effects between Pt and other elements in the alloy, enhancing the catalytic activity. The CoFeLaNiPt HEMG-NP system combines the electrocatalytic properties of transition and noble metals, offering a versatile approach for various reactions.

Despite significant advancements in electrocatalytic hydrogen evolution, developing alternatives to Pt and efficient synthesis strategies remains crucial. PdFeCoNiCu HEA nanoparticles have emerged as an efficient HER electrocatalyst prepared in the oil phase under facile conditions. This method increases the specific surface area and exposes more active sites. PdFeCoNiCu/C shows excellent alkaline HER performance, with a Tafel slope of 39 $mVdec^{-1}$ and an overpotential of 18 mV, significantly better than Pt/C. DFT calculations indicate Pd and Co as dominant electroactive sites, with Ni, Fe, and Cu enhancing electron transfer and optimizing hydrogen binding energy. Efficient p-d coupling of *OH with Co and Ni sites suggests stable water-splitting and adsorption, contributing to superior HER performance [127].

Reducing the cost of HEAs, particularly by minimizing the use of precious metals, is an ongoing goal. Wang and colleagues [128] employed confinement-assisted arc and plasma

shock (APS) to prepare high-entropy alloy nanocomposites (HEA-NPs) with improved catalytic performance. TiNbTaCrMo HEA-NPs showed a Tafel slope of 96.33 $mVdec^{-1}$, indicating enhanced catalytic activity. Alloying changes the rate-determining step to the Heyrovsky reaction, accelerating water adsorption and dissociation. The d-band center of HEA-NPs is closer to the Fermi level, enhancing adsorption and providing more active sites for HER activity.

Lai and colleagues [129] proposed a low-temperature sol-gel strategy to synthesize high-entropy metal phosphide NiCoFeMnCrP nanoparticles (HEMP NiCoFeMnCrP NPs) on a carbon matrix. This method allows for the synthesis of monometallic, bimetallic, trimetallic, tetrametallic, and even high-entropy phosphides with a single phase, offering a versatile approach for HER catalysis without precious metals. The synergistic interaction among metal elements in NiCoFeMnCrP nanoparticles (NPs) has led to an exceptional catalytic performance in the HER. These NPs demonstrated significant enhancements in HER activity, achieving a low overpotential of 220 mV at a current density of 10 mA/cm^2, surpassing the performance of other metal phosphides such as NiP, NiCoP, NiCoFeP, and NiCoFeMnP. Additionally, the Tafel slope of NiCoFeMnCrP NPs was measured at 94.5 mV/dec, indicating faster HER kinetics compared to other metal phosphides. After a 24-hour stability test, the current density of NiCoFeMnCrP NPs remained stable, showing minimal potential fluctuation. This stability suggests that the incremental addition of different metal elements can enhance HER activity. Furthermore, the amalgamation of metals and transition metal phosphides modifies the electronic structure between metals, leading to an increase in active sites. This change fosters a synergistic effect between the metals, which is advantageous for electrocatalysis.

CHAPTER 3

IN VITRO BIOCOMPATIBILITY EVALUATION OF $Ti_{1.5}ZrTa_{0.5}Nb_{0.5}Hf_{0.5}$ REFRACTORY HIGH-ENTROPY ALLOY FILM FOR ORTHOPEDIC IMPLANTS: MICROSTRUCTURAL, MECHANICAL PROPERTIES AND CORROSION BEHAVIOR

The majority of this chapter has been published in *the Journal of Alloys and Compounds 883 (2021) 160786*. The original manuscript has been rearranged to conform to the format requirements of the dissertation.

3.1 Introduction

The superior mechanical properties of metallic biomaterials have made them an ideal candidate for load-bearing orthopedic implants such as hip joint and knee joint replacement and dental roots [130,131]. Despite many metallic materials being produced in industry, 316L, CoCrMo, and Ti6Al4V are the most commonly used alloys that exhibit biocompatibility and capable of long-term success as an implant material [132]. However, the highly corrosive media of the biological environments and susceptibility of the metallic biomaterials to degradation induced by the electrochemical destructive attack can lead to the leaching of metal ions such as Cr, Ni, Co, Al, and V from the implants into the surrounding tissue [133,134]. Clinical evaluations demonstrated that the release of cytotoxic metal ions over time causes inflammation, osteolysis, and adverse psychological reactions in the neighboring biological tissues leading to shortening the lifetime of the implants [131,132,135].

Even though spontaneously formed passive oxide films on bare metallic biomaterials may have a positive effect on their corrosion resistance, cyclic loadings and sliding movement of the implant against a counter body can locally remove these passive oxide films (depassivated zone) and expose their surface to the biological media [136,137]. As a result, the galvanic coupling established between depassivated and still passive zone can lead to the acceleration of corrosion and subsequent release of toxic metal ions [131,136]. Therefore, applying a protective and durable coating on metallic biomaterials is essential in order to enhance their biocompatibility and longevity after being inserted into the human body [137]. Ceramic coatings such as aluminium oxide, zirconium oxide, and hydroxyapatite are commonly employed on the surface of metallic implants to enhance their biocompatibility and corrosion resistance [138–140]. However, the mechanical durability provided by the ceramic coatings is the most prominent concern in their long-term applications. Mismatch in mechanical properties of brittle ceramic coatings and deformable metallic implants subjected to multi-axial loadings may result in the formation and propagation of cracks leading to delamination and spallation of coating and consequently failure of the implant [131,140,141]. Thus, exploring a new class of coating materials that simultaneously satisfies the biocompatibility, corrosion resistance, and, most importantly, ensure good mechanical properties and adhesion has been attracted significant attention in biomedical applications.

In recent years, high-entropy alloys (HEAs), consist of at least five principal elements with equimolar or non-equimolar compositions, have been introduced as a new category of metallic materials [12,142,143]. Due to unique features, including superior mechanical properties, high hardness, good tribological properties, and excellent corrosion resistance, HEAs have shown great potential in a wide variety of applications [143–148]. Exploring the biomedical applications for HEAs mainly focuses on developing the allergy-free and non-toxic refractory HEAs (RHEAs), including transition metals such as Ti, Zr, Mo, Nb, Hf, and Ta, by using the arc-melting technique [93,99,149–153]. Even though the versatile properties of RHEAs render them as a promising material for biomedical applications, inferior castability and compositional inhomogeneity, mainly attributed to the high melting point of constituent elements, are the major drawbacks of these alloys in utilizing them as actual implants [93,154,155]. Therefore, using RHEAs as a coating material seems quite attractive from a technical and economic point of view. Up until now, numerous RHEAs films have been successfully deposited using DC and RF magnetron sputtering techniques. The reported results in literature have revealed that these films display remarkable mechanical properties such as high hardness and elastic modulus and wear resistance along with outstanding corrosion and oxidation behavior [156–159].

In our previous research, microstructure, mechanical properties, and electrochemical behavior of non-equimolar $Ti_{1.5}ZrTa_{0.5}Nb_{0.5}Hf_{0.5}$ RHEAs were studied, and the excellent corrosion resistance of this alloy compared to that of 316L stainless steel, CoCrMo, and Ti6Al4V has been demonstrated [151]. Thus, achieved promising results motivated the authors to initiate this investigation to study the microstructure, mechanical properties, adhesion, and corrosion behavior of non-equimolar $Ti_{1.5}ZrTa_{0.5}Nb_{0.5}Hf_{0.5}$ RHEAs film deposited onto the different biomedical substrates by magnetron sputtering technique.

3.2 Materials and Methods

3.2.1 Target and Substrate preparation

In this work, $Ti_{1.5}ZrTa_{0.5}Nb_{0.5}Hf_{0.5}$ RHEA target was fabricated through arc-melting of 99.99% pure constituent elements in an argon (Ar) atmosphere, followed by re-melting five times to improve the homogeneity; then, a disk with the diameter of 50.8 mm and

thickness of 6.3 mm was shaped. The nominal and actual chemical composition of the target analyzed using X-ray fluorescence (XRF, Brucker S8 Tiger) is given in Table 3.1.

Table 3.1. The nominal and actual chemical composition of the target (wt% and at%).

	Ti		Zr		Ta		Nb		Hf	
	wt%	at%	wt%	at%	wt%	at%	wt%	at%	wt%	at%
Nominal	18.46	37.50	23.43	25.00	23.25	12.50	11.93	12.50	22.93	12.50
Actual	18.31	37.37	23.29	24.76	23.80	12.97	11.84	12.52	22.76	12.38

Commercially available 316L stainless steel, CoCrMo, and Ti6Al4V rods were cut to disc-shaped specimens (diameter of 8 mm) using electro-discharge machining and used as substrates. Before the deposition process, the surface of substrates was prepared by standard metallographic techniques using a series of SiC emery papers up to 2500 grit followed by cloth polishing with 0.3 µm alumina suspension. Finally, substrates were ultrasonically cleaned with acetone and ethanol then rinsed with de-ionized water.

3.2.2 Film Deposition Process

$Ti_{1.5}ZrTa_{0.5}Nb_{0.5}Hf_{0.5}$ RHEA film with a thickness of about 1 µm was deposited on different substrates of 316L, CoCrMo, and Ti6Al4V (designated as RHEA-316L, RHEA-CoCrMo, and RHEA-Ti6Al4V) and silicon wafer by radio frequency (RF) magnetron sputtering. RHEA deposited silicon wafer was used for cross-sectional investigation because of convenience in preparing. The deposition process using the RF magnetron sputtering (Nanovak NVTS-400) machine was performed in an Ar atmosphere without substrate bias. The chamber base pressure was below 1×10^{-5} Pa, and the Ar flow was kept at 10 standard cubic centimeters per minute (SCCM) at the power of 100 W. For the sake of having a clean surface, the target was first pre-sputtered by Ar plasma for 20 minutes, and then the specimen shutter was opened.

3.2.3 Microstructural Characterization

The phase structure of the substrates and deposited RHEA films were characterized by an X-ray diffractometer (XRD, Bruker D8 Advance) and grazing incidence X-ray diffraction (GIXRD) with the use of Cu Kα radiation. In the GIXRD method, the data were collected at the incidence angle of 4° and an acquisition angle ranging from 10° to 90°. The cross-sectional and surface microstructure of deposited films were studied using a field-emission scanning electron microscope (FESEM, Zeiss, Ultra Plus) equipped with the energy dispersive spectrometer (EDS). The composition of air-formed oxide layer developed on RHEA films was characterized by X-ray photoelectron spectroscopy (XPS, Thermo Fisher Scientific K-Alpha) employing monochromatic Al Kα (1486.6 eV) source. The surface topography and roughness of the uncoated substrates and RHEA-coated specimens were examined by atomic force microscopy (AFM, Brucker, Dimension Icon) in the tapping mode.

3.2.4 Nanoindentation and scratch testing

The hardness (H) and elastic modulus (E) of the deposited film on different substrates were measured using a nanoindentation tester (Agilent G200) with a Berkovich diamond indenter tip from the loading and unloading curves based on the Oliver-Pharr analysis model. The maximum load of 3 mN with a loading and unloading rate of 0.3 mN/s was applied. The penetration depth of the indenter was controlled at about 1/10 of the film thickness, and thus, the substrate effect could be neglected. At least 20 measurements were performed on each specimen, and the average values of H and E with respective standard deviations were reported.

The scratch tests were also conducted by utilizing the nanoindentation (Agilent G200) instrument with a 5 mm end radius sphero-conical diamond indenter. The scratch test was carried out in a single-pass 400 µm length using the normal load force with values increasing progressively from 0 to 400 mN at a constant loading rate of 10 mN/sec.

3.2.5 Electrochemical Test

Electrochemical measurements were performed in phosphate buffer saline (PBS) solution (8 g/L NaCl, 0.24 g/L KH_2PO_4, 0.20 g/L KCl and 2.19 g/L Na_2HPO_4, pH 7.40 ±

0.05) at 37±1 ℃ using an electrochemical workstation (Biologic Science Instrument, VSP-300) with a standard three-electrode system. The cylindrical sample holder with a constant exposed area, $Ag/AgCl_2$ (3M KCl) electrode, and platinum wire were used as the working electrode, reference electrode, and counter electrode, respectively. High-purity N2 flow was used to deoxygenize the PBS electrolyte before the electrochemical tests. All samples were immersed in the electrolyte for 1 h to stabilize open circuit potential (OCP) at the equilibrium state. The temperature of the electrolyte was kept at 37±1 ℃ by using a thermostatic bath during all tests. Corrosion tests were carried out from 0.30 V versus EOCP till the final potential of 1.80 V versus ERef at a scan rate of 1 mV/s. Electrochemical impedance spectroscopy (EIS) tests were also carried out in PBS solution at 37±1 ℃ at OCP with a sinusoidal potential amplitude of 10 mV, running from 100 kHz to 10 mHz.

3.3 Results and Discussion

3.3.1 Crystal Structure Analysis

XRD patterns of the substrates are presented in Figure 3.1 right. As can be seen, an FCC structure can be generally seen in 316L substrate. In the CoCrMo substrate, the structure appears to be a mixture of α-(CoCr) with FCC and ε-(CoCr) with HCP structure. Also, Ti6Al4V is mainly composed of α-HCP and minority β-BCC phase. Figure 3.1 left shows GIXRD patterns of RHEA film deposited on different substrates of 316L, CoCrMo, and Ti6Al4V. For the RHEA films, broad peaks indicating an amorphous structure were observed. According to the literature, the amorphous nature of the deposited films can be attributed to the high mixing entropy, low enthalpy, the large atomic size difference, and long-range diffusion [160–163]. Besides, the rapid quenching effect of the magnetron sputtering method on the deposited constituent elements, which results from the large thermal gradian at substrate/film interface, can suppress the crystallization of the films [157,164].

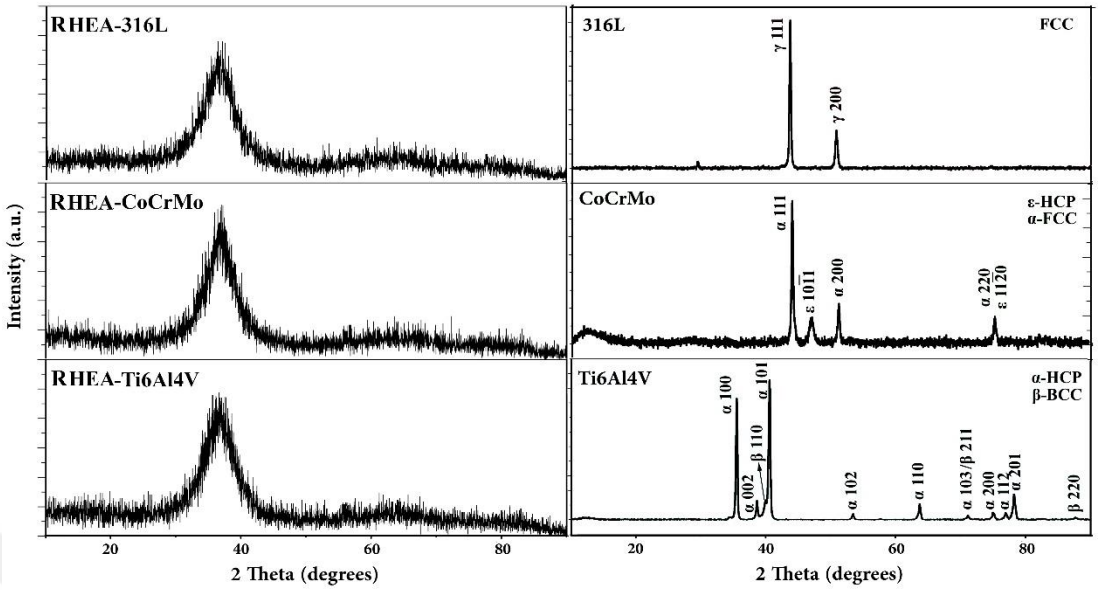

Figure 3.1. Left: GIXRD pattern of RHEA film deposited on different substrates Right: XRD pattern of the 316L, CoCrMo, and Ti6Al4V substrates.

Figure 3.2 shows the FESEM micrograph of the cross-sectional view of deposited RHEA film on the silicon wafer and its surface morphology on different substrates. As seen from Figure 3.2a, a compact RHEA film with a thickness of 1.025 µm was deposited. Also, from the surface images (Figure 3.2b-d), a continuous and cauliflower-like structure of the film is evident for all specimens with no difference in surface morphologies. The development of the cauliflower-like grains composed of many clusters with a size that differs from tens to hundreds of nanometers has been reported in most metallic films [160,162]. Even though the deposited films consist of an amorphous phase, grain boundaries are seen in their surface views. These intrinsic grain boundaries in the amorphous films are density-deficient regions that form due to the growth of the void network in the structure [165,166]. Additionally, as seen in Figure 3.2, cracks can be observed along the grain boundaries. Developing cracks in the deposited film can be attributed to the internal stresses that arise during the deposition process [166].

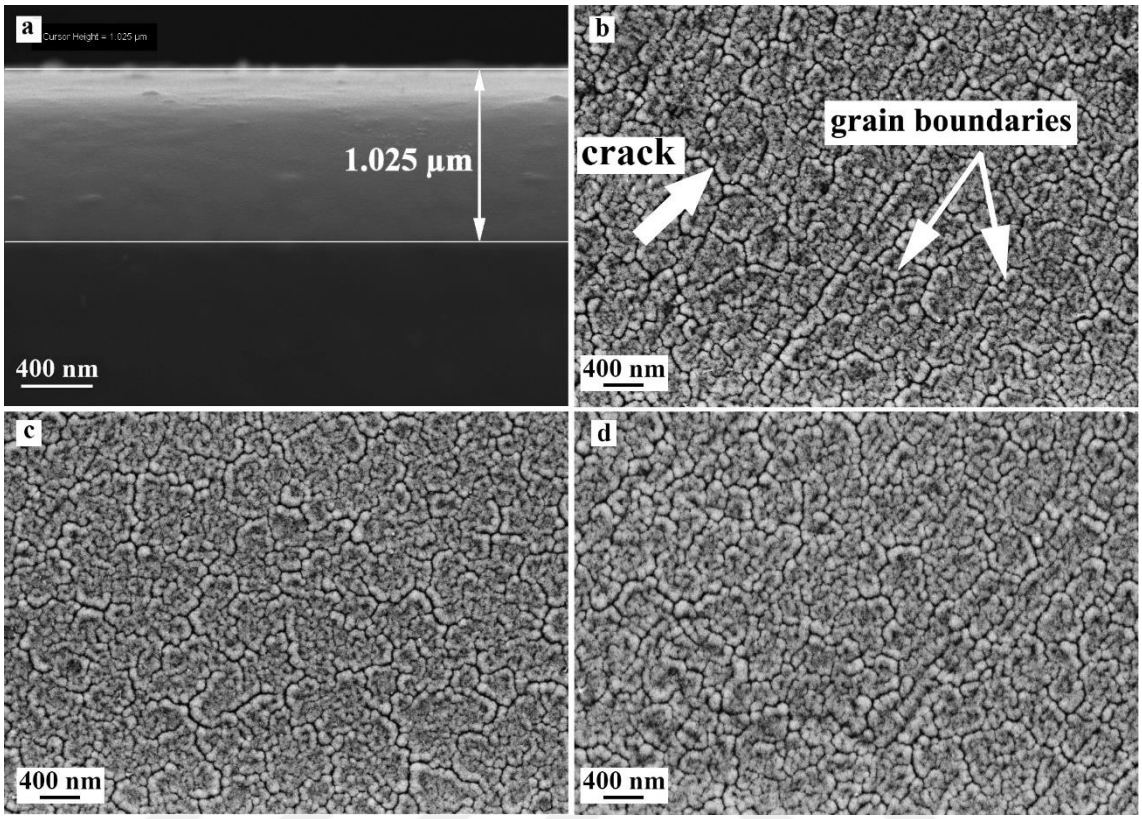

Figure 3.2. a) Cross-sectional FESEM micrograph of the RHEA film deposited on a silicon wafer and surface view FESEM micrographs of the RHEA film deposited on b) 316L, c) CoCrMo, and d) Ti6Al4V substrates.

EDS measurements were carried out at the different regions of the surface of the RHEA-coated silicon wafer. The collected spectrum and corresponding chemical composition of each measurement are presented in Figure 3.3. In addition, EDX elemental mapping displayed in Figure 3.4 was used to study the distribution of individual constituent elements in the microstructure of the deposited films. The results revealed that the uniform RHEAs films were developed, and constituent elements were homogeneously distributed in its microstructure. Neither significant difference from the nominal chemical composition nor segregation or second phases were observed in the studies.

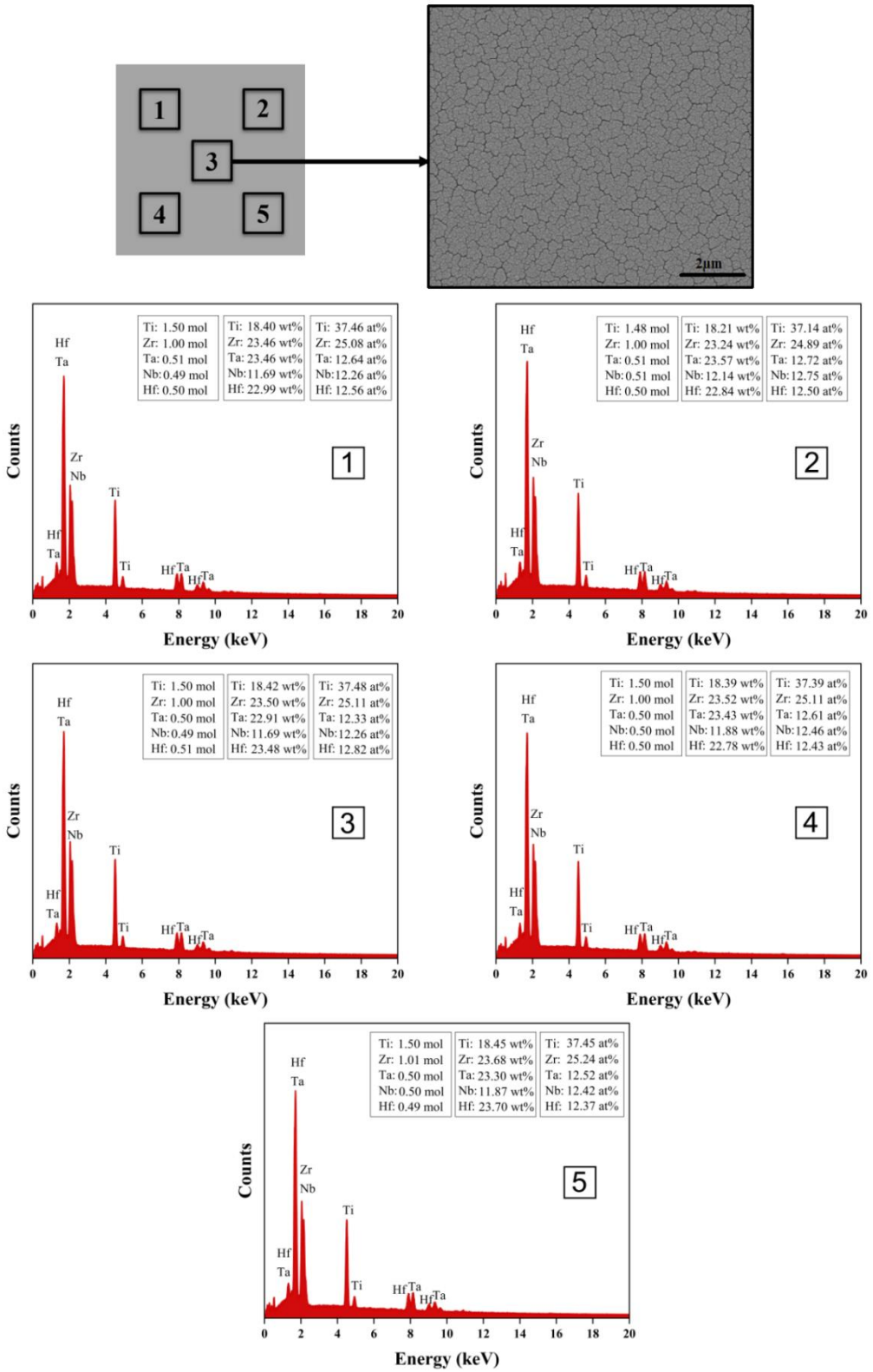

Figure 3.3. Schematic representation of EDS measurements carried out on the surface of RHEAs-coated silicon wafers at the different regions.

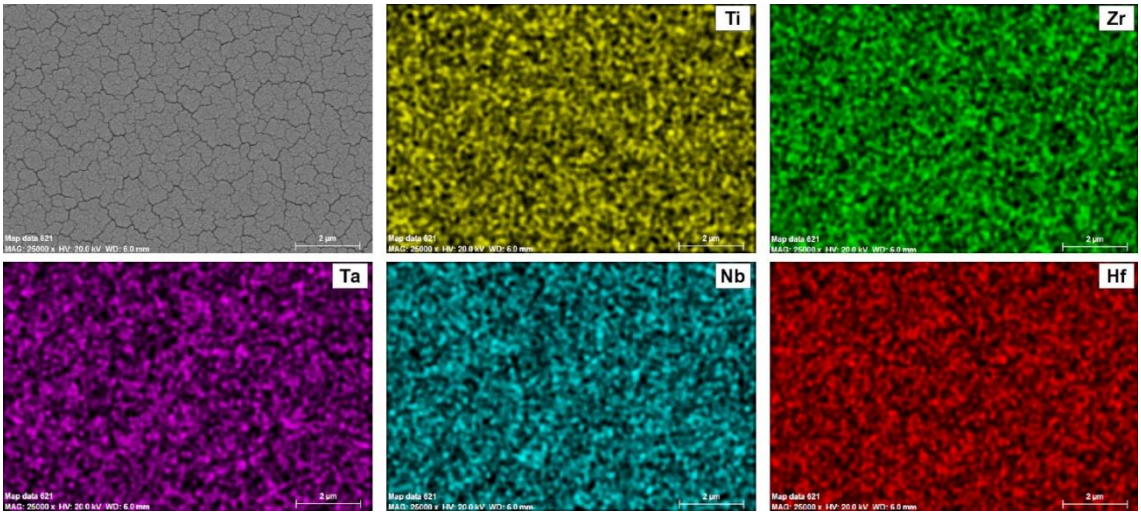

Figure 3.4. EDS elemental mapping of RHEA film deposited on the silicon wafer.

The 3-dimensional AFM images of uncoated 316L, CoCrMo, and Ti6Al4V substrates and RHEA-coated specimens acquired from an area of 5 μm×5 μm are depicted in Figure 3.5. On the surface of uncoated substrates, scratch marks formed during mechanical polishing are present, and the mean surface roughness value, Ra, was measured 1.63, 1.71, and 1.92 nm for 316L, CoCrMo, and Ti6Al4V, respectively. While substrate surfaces exhibited a smooth morphology, the deposition of the RHEA film with the nature of cauliflower-like structure slightly increases the surface roughness. The roughness of RHEA-316, RHEA-CoCrMo, and RHEA-Ti6Al4V specimens was measured as 2.05, 2.11, and 2.27 nm, respectively.

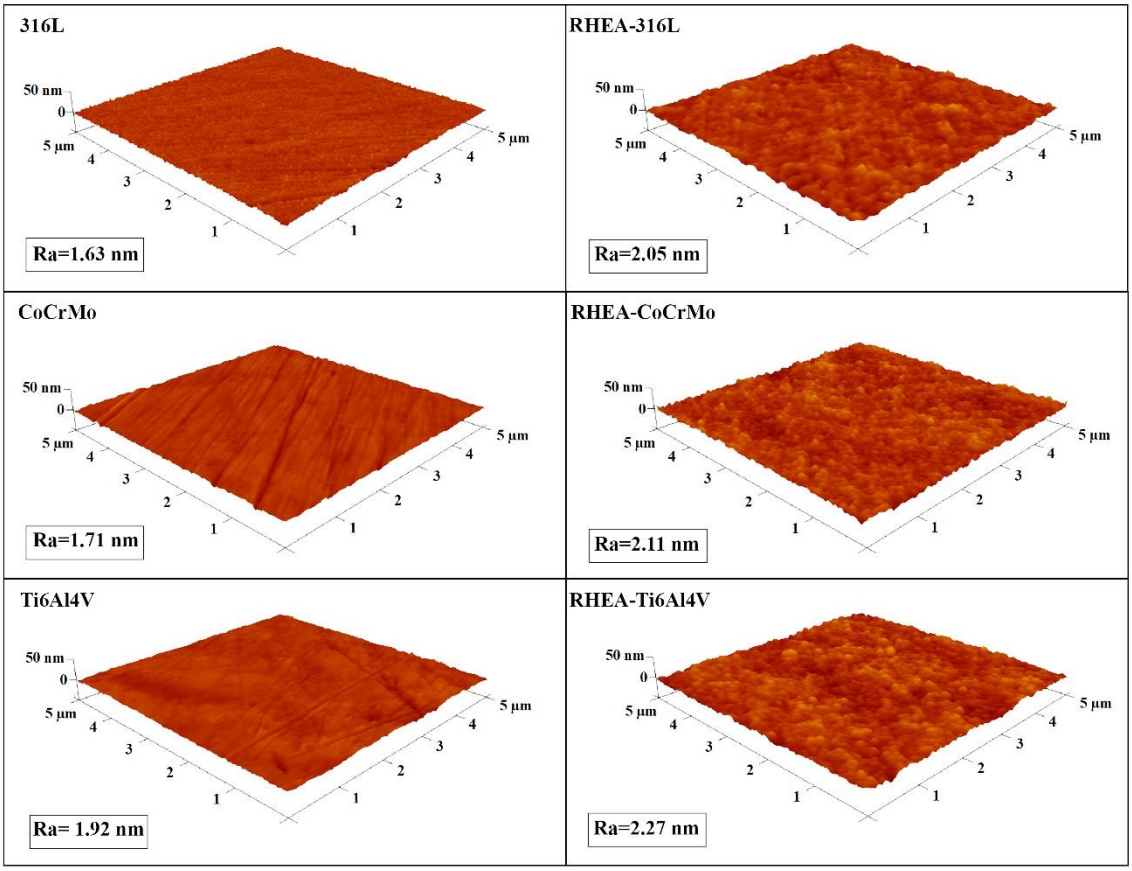

Figure 3.5. AFM images and surface roughness values of uncoated substrates and RHEA-coated specimens.

Mechanical Properties

Table 3.2 presents the H and E values of deposited RHEA film on the different substrates measured using the loading and unloading curves and employing Oliver-Phar methods. The measured H values of the deposited film are 11.43 ± 0.15, 11.49 ± 0.12, and 11.45 ± 0.15 GPa for RHEA-316, RHEA-CoCrMo, and RHEA-Ti6Al4V, respectively. Also, the obtained E values are very close and vary between 180±1.5 GPa and 185±1.7 GPa. In our previous study, the H values of 316L, CoCrMo and Ti6Al4V substrates after pile-up correction were reported as 2.44 ± 0.18, 4.21 ± 0.15, and 3.32 ± 0.15 GPa, respectively [151]. It can be concluded that the deposition of RHEA film on the examined substrates significantly enhances their surface hardness. It is believed that the higher hardness of RHEA film originates from its dense, amorphous nature and fine grain structure, which impedes the dislocation motion by reducing their movement [160,167–169].

Table 3.2. H and E values of the RHEA film deposited on different substrates.

	H (GPa)	E (GPa)
RHEA-316L	11.43±0.15	180±1.5
RHEA-CoCrMo	11.49±0.12	185±1.7
RHEA-Ti6Al4V	11.45±0.15	183±2.1

The adhesion between the RHEA film and 316L, CoCrMo, and Ti6Al4V substrates were measured using a scratch test with a 5 mm end radius sphero-conical diamond indenter. At this test, the load was ramped from 0 to 400 mN in 40 s, and the scratch length was set as 400 μm at a scratching speed of 10 μm/s. The critical load, defined as the load in which film flaking and delamination starts, was determined from the SEM examination of the scratch tracks and load-scratch depth curves. The abrupt change along the profile indicates the critical loads on the scratch track where the delamination of the film takes place. Figure 3.6 shows FESEM images of the surface topography after scratch tests and related load-scratch depth curves. As seen from Figure 3.6, the critical load between 190-210 mN corresponds to the cracking and delamination of RHEA film deposited on the 316L substrate. Fluctuations in load-scratch depth curves of RHEA film on CoCrMo start between 280-310 mN that denotes the initiation of films' cracking and peeling from the substrate. In contrast, the RHEA film deposited on Ti6Al4V substrate exhibited superior adhesion strength and good scratch resistance without any delamination. Excellent adhesion properties of the RHEA film on Ti6Al4V can be related to good bonding between the deposited film and Ti6Al4V substrate due to the presence of Ti atoms in the film [55,170]. It has been demonstrated that chemical coherency between the deposited film and substrate plays a crucial role in enhancing the adhesion strength of film/substrate.

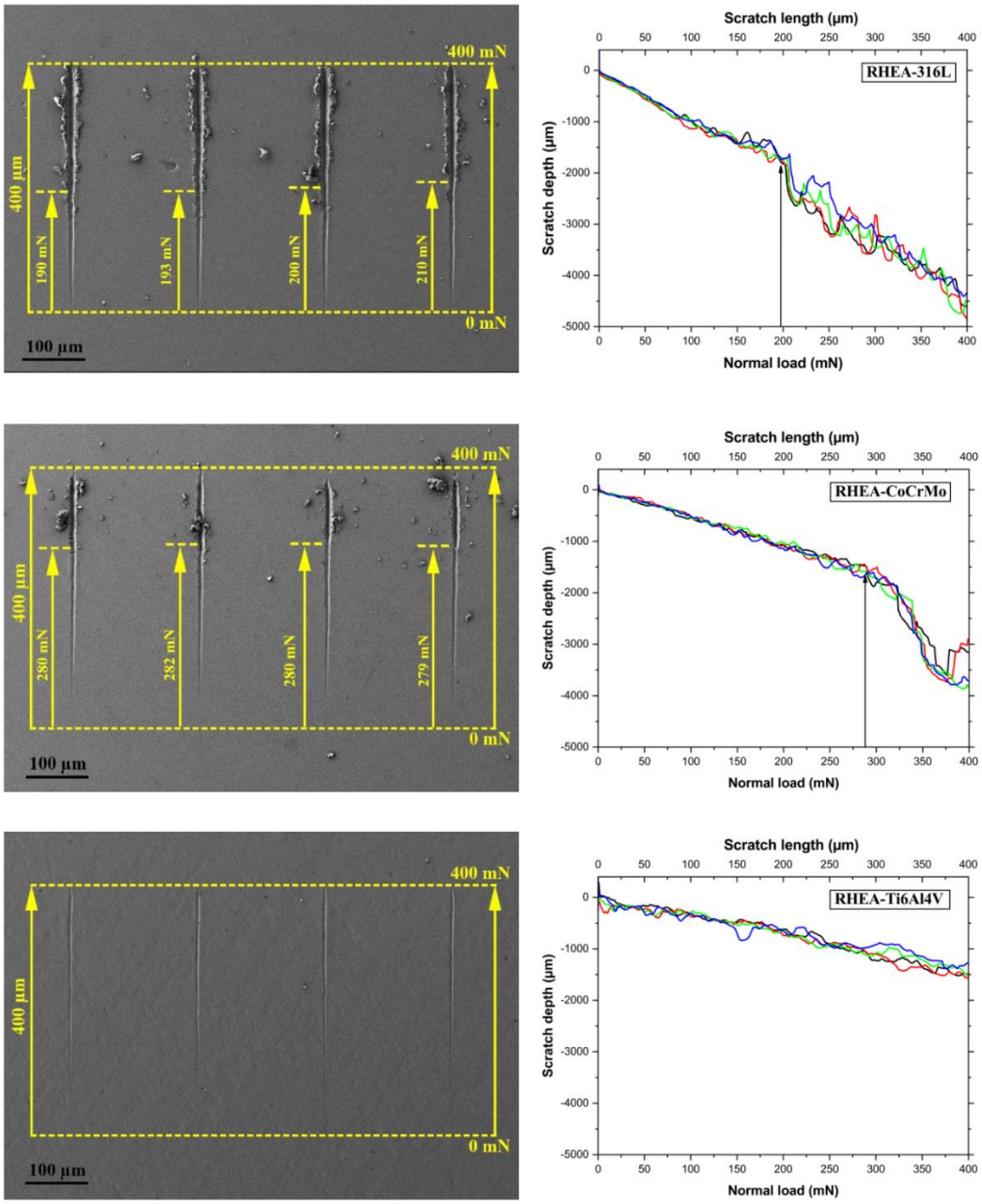

Figure 3.6. Left: FESEM micrograph of RHEA-coated specimens after scratch tests and Right: the related load-scratch depth curves.

3.3.2 Corrosion behavior

Potentiodynamic polarization behavior in PBS

The potentiodynamic polarization curves of RHEA-coated specimens are shown in Figure 3.7. All tests were performed in the PBS solution with the scan rate of 1 mV/s at the temperature of 37±1 ℃ to simulate the biological environment. The corrosion parameters were extracted from the curves and listed in Table 3.3. E_{corr}, I_{corr}, E_{pit}, and I_{pass}

represent the corrosion potential, the corrosion current density, the pitting potential, and the passive current density, respectively. E_{corr} is acquired by the potential in open circuit, and I_{corr} indicating the corrosion rate calculated by extrapolating the linear zone of the Tafel plot near E_{corr}. In addition, E_{pit}, which demonstrates the corrosion resistance, can be determined from the curves where the current increases suddenly.

As seen from Figure 3.7, the RHEA-316L and RHEA-CoCrMo specimens show pitting behavior, as the current density increases around pitting potential of 0.40 V. In contrast, although the I_{corr} of RHEA-Ti6Al4V specimen is slightly higher than those of the RHEA-coated 316L and CoCrMo specimens, it reveals a continuous passive plateau without pitting effect. However, at potentials higher than 1.4 V, current fluctuations emerged. These fluctuations represent the ultimate surface pitting resistance, as they called metastable pitting [171]. Since a remarkable difference between I_{corr} and I_{pass} values (extracted at the 0 V Ag/AgCl) of examined specimens is not observed, polarization resistance (R_p) was calculated for determining their corrosion resistance performance. The R_p values (listed in Table 3.3) were calculated by the Stren-Geary equation as follow:

$$I_{corr} = (\beta_a \cdot \beta_c)/(R_p 2.303(\beta_a + \beta_c)) \quad (1)$$

where β_a and β_c are calculated from the Tafel branch slopes and called anodic and cathodic slopes, respectively. From Table 3.3, it is evident that the R_p of RHEA-Ti6Al4V is higher than RHEA-coated 316L and CoCrMo specimens. The increment in corrosion resistance of RHEA- Ti6Al4V can be attributed to the excellent adhesion strength between RHEA film and Ti6Al4V compared to the 316L and CoCrMo substrates that were confirmed by the scratch test conducted in this research. In accordance with our previous work [151] the results of the current work indicate that RHEA-coated specimens have a higher corrosion potential than the uncoated substrate, stating their nobler properties. Besides, the I_{corr} values of the coated specimens are less than that of the uncoated substrates, which indicates that the deposition of RHEA film can diminish the corrosion rate of examined substrates.

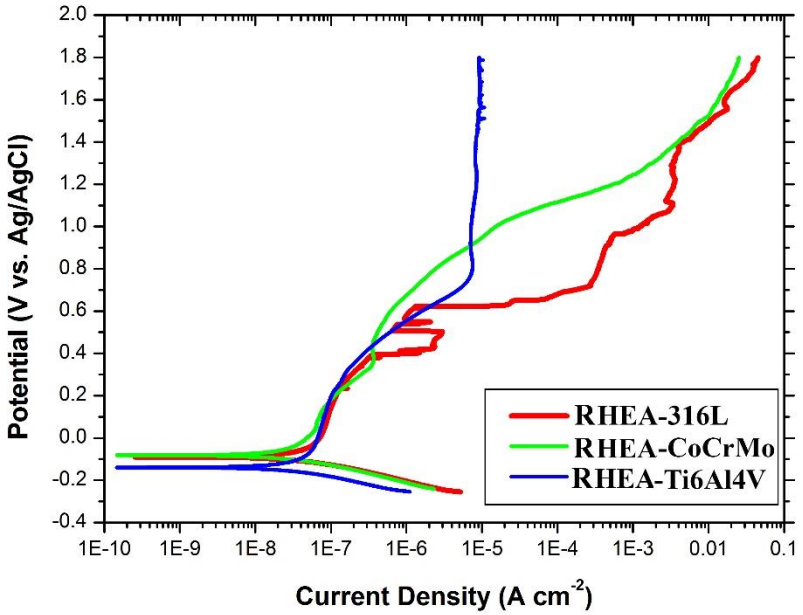

Figure 3.7. Potentiodynamic curves of RHEA-coated 316L, CoCrMo, and Ti6Al4V substrates in PBS electrolyte at 37±1 ºC with a scan rate of 1 mV/s.

Table 3.3. Electrochemical parameters of the RHEA-coated 316L, CoCrMo, and Ti6Al4V substrates in PBS electrolyte with a scan rate of 1 mV/s at 37±1 ºC.

Alloys	E_{corr} (mV)	I_{corr} (μA/cm^2)	E_{pit} (mV)	I_{pass} (μA/cm^2)	β_a (mV)	β_c (mV)	R_p (Ωcm^2)
RHEA-316L	-100.2	0.040	391.4	0.071	758.6	79.7	78.2E4
RHEA-CoCrMo	-87.8	0.039	460.1	0.048	773.2	81.2	81.8E4
RHEA-Ti6Al4V	-167.5	0.042	-	0.067	943.1	87.8	83.0E4

FESEM surface images of RHEA-coated specimens subjected to the corrosion test are shown in Figure 3.8. The images were taken to evaluate the film stability and the pitting effect on the examined specimens. It is obvious from Figure 3.8a and b that the pitting traces are detected on the surface of RHEA-coated 316L and CoCrMo substrates after the corrosion test. In the RHEA-316L specimen, a couple of wide cavities with a diameter of about 450 μm are seen. In contrast, in the RHEA-CoCrMo specimens, the number of cavities was increased, and their size was reduced down to about 70 μm. As it was demonstrated from the scratch tests (Figure 3.8), the RHEA film on the 316L and CoCrMo substrates has weak adhesion strength, and thus delamination occurs under the applied load. Conversely, from Figure 3.8c, it can be seen that there are no pits on the surface of the RHEA-Ti6Al4V specimen. In this case, the chemical attack resulting in the

deterioration of the metals did not occur due to excellent adhesion strength between the deposited film and Ti6Al4V substrate.

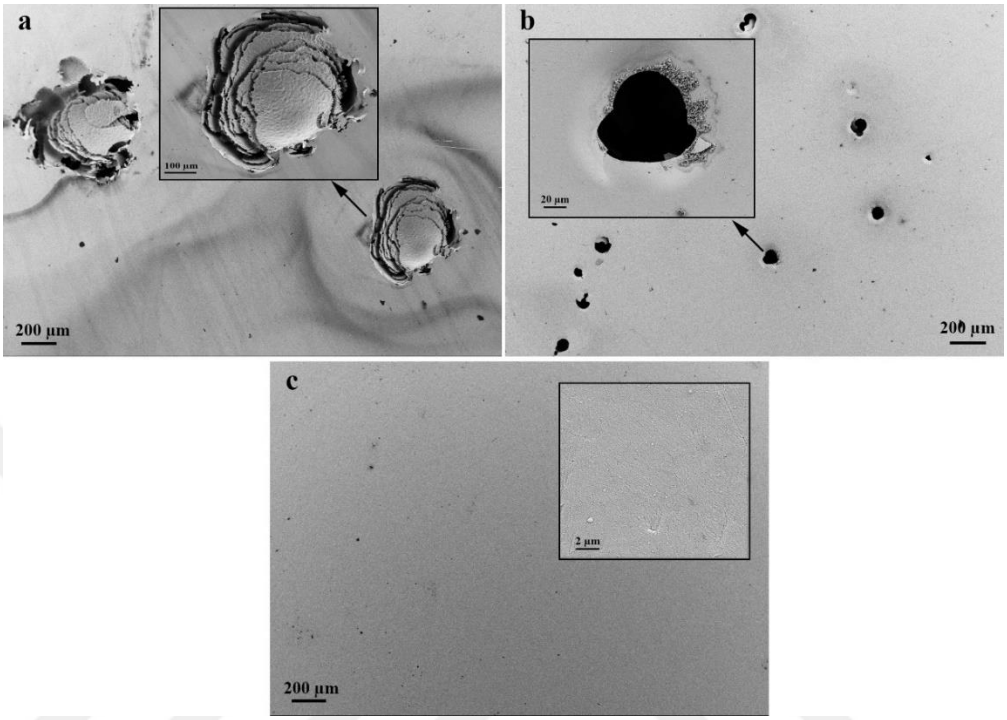

Figure 3.8. FESEM images of the RHEA-coated 316L, CoCrMo, and Ti6Al4V substrates after the corrosion tests in PBS electrolyte at the temperature of 37±1 ℃**.**

EIS study

Figure 3.9 shows the EIS results of the RHEA-coated specimens. According to Figure 3.7, because the examined specimens exhibited different corrosion performances, distinct mechanisms should be considered for the electrochemical behavior. Figure 3.8 shows that the RHEA-coated 316L and CoCrMo specimens possess pitting traces, while no pitting was detected on the RHEA-Ti6Al4V. Therefore, two different equivalent electrical circuits should be considered as presented in Figure 3.10: the surface with pitting cavities (Figure 3.10a) and the surface with the continuous coating without any pitting trace (Figure 3.10b). Accordingly, the EIS results of RHEA-316L and RHEA-CoCrMo specimens were fitted based on the equivalent electrical circuit of Figure 3.10a, and the EIS data of RHEA-Ti6Al4V were simulated using equivalent electrical circuit in Figure 3.10b. The models presented in Figure 3.10 are designed as a substrate with a deposited film on it and an air-formed oxide film upon the film, which protects its surface.

XPS results given in Figure 3.11 confirm the development of an air-formed oxide film at the outermost surface of the specimens. Based on the results, the air-formed oxide film mainly consists of TiO_2, ZrO_2, Nb_2O_5, Ta_2O_5, and HfO_2, and minor Nb, Zr, Ta, and Hf sub-oxides are detected. After carrying out XPS analyses from the surface of the specimen, the etching process was accomplished by ion bombardment (4 keV Ar+) in 1 cycle with an etching time of 200 sec. AFM studies revealed that the etching rate was 0.25 nm/s, so the investigated region was approximately 50 nm below the film surface. After etching, the XPS studies demonstrated that the majority of the constituent elements were found in the metal state in the film's structure. Despite using high purity argon and decreasing pressure of PVD chamber to the desired level, incorporation of oxygen impurity due to the residual gas in the deposition chamber and high affinity of Zr and Hf to form oxides, very small amount of their sub-oxides were detected within the deposited films [172].

In the equivalent electrical model (Figure 3.10), Re is the electrolyte resistance, CPEfilm and Rfilm are capacitance and resistance of RHEA film with an air-formed oxide film on it, respectively. The double-layer capacitance (CPE_{dl}) is generated in the metal/solution interface beneath the deposited film through the pitting in the examined specimens. The Faradic corrosion reaction is also represented by charge transfer resistance (Rct). When delamination or peeling of the RHEA film from the 316L and CoCrMo substrates occurs, the solution can penetrate under the film. In this situation, the impedance is considered as a transmission line [173]. In the case of the RHEA-Ti6Al4V specimen (Figure 3.10b), an electrolyte-specimens system represented by an equivalent circuit consisting of a parallel CPE_{film}-R_{film} merged in series with parallel CPE_{dl}- Rct combination [173]. This electrochemical behavior of the RHEA-Ti6Al4V specimen can be associated with the excellent adhesion of the deposited film and Ti6Al4V substrate.

The fitting results of Nyquist and Bode-Phase curves (Figure 3.9) based on the presented models in Figure 3.10 with the chi-square values ($\chi 2$) in order of 10^{-4} are listed in Table 3.4. As seen from Table 3.4, R_{film} and Rct of the RHEA-CoCrMo specimen are higher than the RHEA-316L. The Rct value is directly related to the adhesion of the deposited film on the substrate; therefore, increasing the bonding strength between the film and substrate can lead to the increment of Rct value. In contrast, the mechanism of electrochemical behavior in the RHEA-Ti6Al4V, which poses enhanced film/substate bonding strength, is completely different, and no pitting cavity is observed. Table 3.4

shows that the Rct value of the deposited film is enormously high, about 1.5×10^7 Ωcm^2, indicating excellent bonding between RHEA film and the Ti6Al4V substrate. This finding is consistent with the scratch test results presented in Figure 3.6.

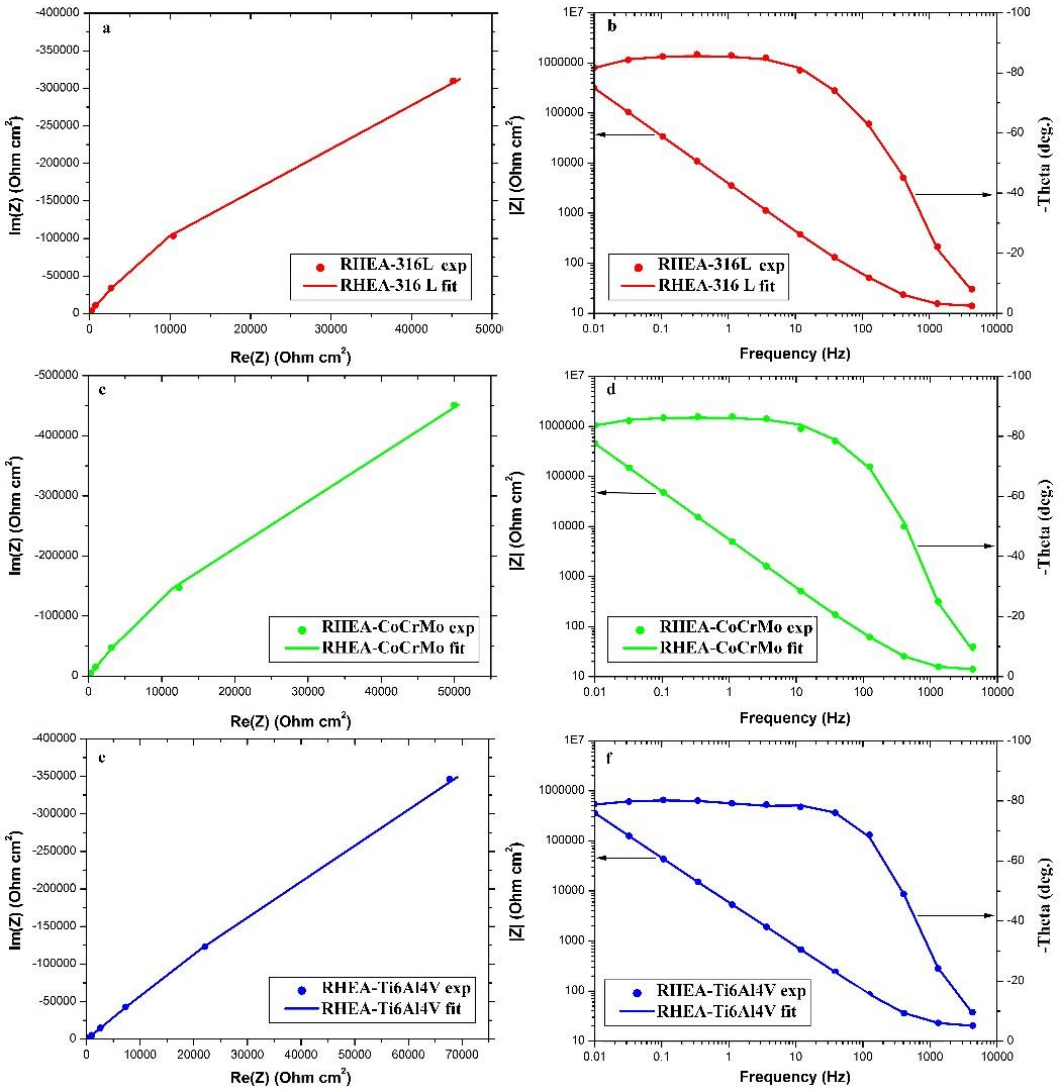

Figure 3.9. Nyquist plots (a, c and e) and Bode-Phase plots (b, d and f) of RHEA-coated specimens obtained from the EIS test at open circuit potential with a sinusoidal potential amplitude of 10 mV, running from 100 kHz to 10 mHz, in PBS electrolyte at 37±1 ºC.

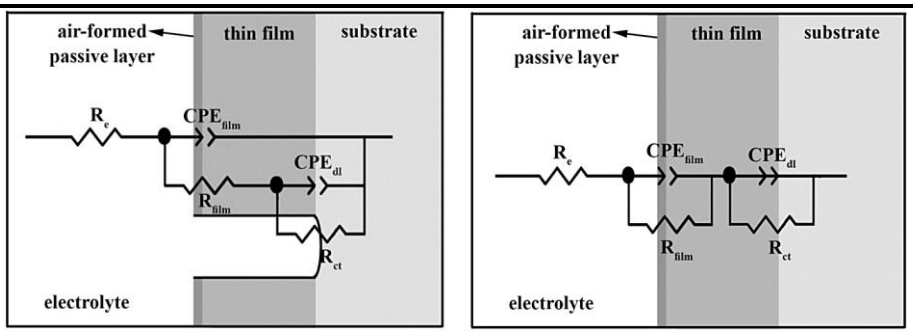

Figure 3.10. Equivalent electrical circuit representative of the RHEA film interfaces on a) 316L and CoCrMo substrates and b) Ti6Al4V substrate in the PBS electrolyte.

Table 3.4. Equivalent-circuit parameter values for EIS data in the PBS electrolyte.

Sample	Re (Ωcm^2)	CPE_{film} ($\mu\Omega^{-1}S^n cm^{-2}$)	n_{film}	R_{film} (Ωcm^2)	CPE_{dl} ($\mu\Omega^{-1}S^n cm^{-2}$)	n_{dl}	R_{ct} (Ωcm^2)	$\chi^2 \times 10^{-4}$
RHEA-316L	13.79	3.25E-5	0.95	5.10E04	1.15E-5	0.96	4.25E6	6E-4
RHEA-CoCrMo	13.75	2.70E-5	0.96	6.10E04	0.60E-5	0.97	6.95E6	1E-4
RHEA-Ti6Al4V	19.40	3.49E-4	0.98	8.43E04	2.33E-6	0.90	1.54E7	0.4E-4

Overall, the outcomes of this investigation demonstrate that non-equimolar $Ti_{1.5}Ta_{0.5}Hf_{0.5}Nb_{0.5}Zr$ RHEA film consists of allergy-free and non-toxic refractory elements can be considered as a promising and protective coating on the metallic biomaterials. The combination of their unique microstructure and superior mechanical properties as well as their noble electrochemical behavior in the simulated biological environments makes them the proper choice of metallic coatings suitable for a wide range of biomedical applications.

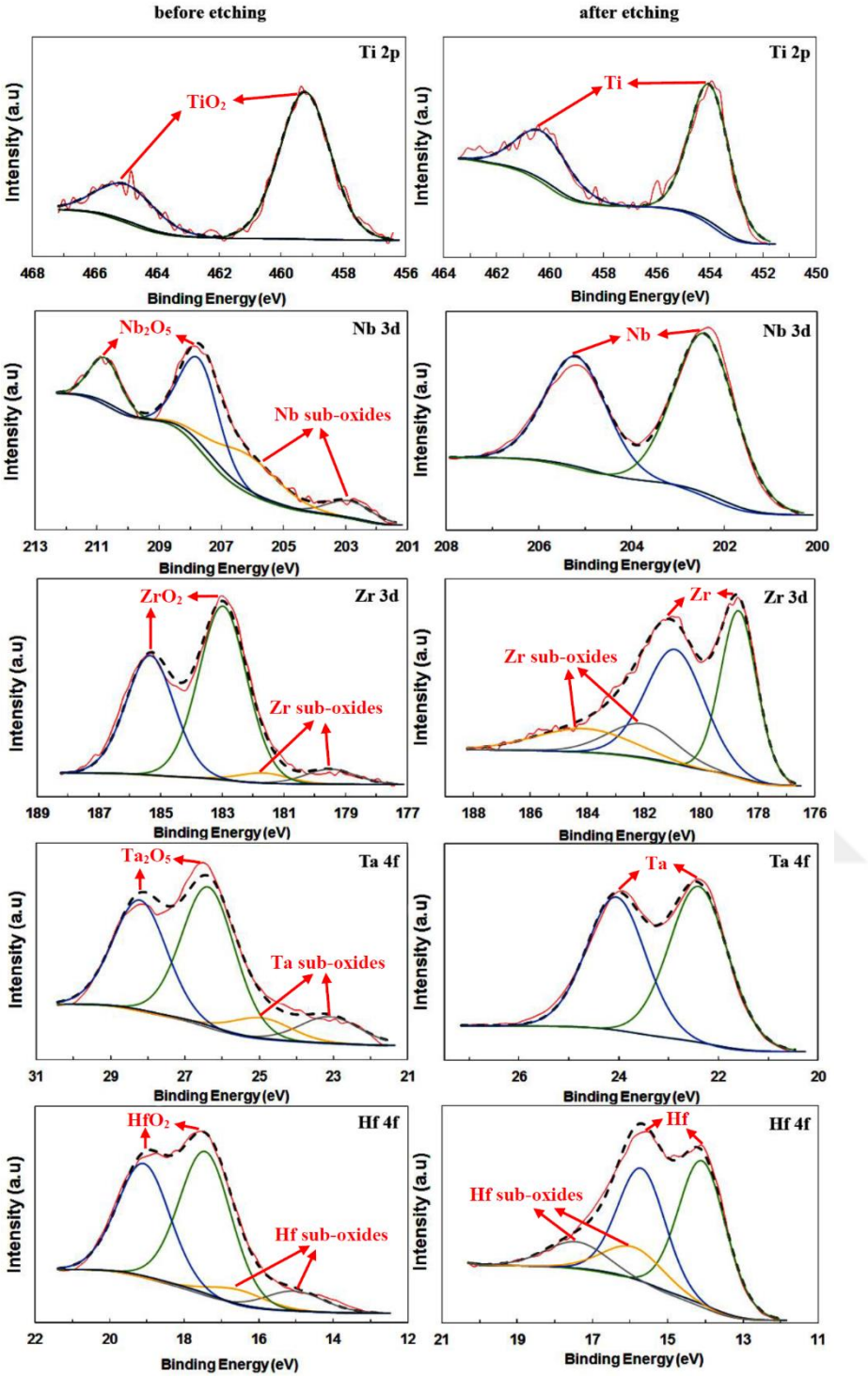

Figure 3.11. XPS spectra of the deposited RHEA film before and after etching.

3.4 Conclusion

The microstructure, mechanical properties, and electrochemical behavior of the non-equimolar $Ti_{1.5}Ta_{0.5}Hf_{0.5}Nb_{0.5}Zr$ RHEA film deposited on 316L, CoCrMo, and Ti6Al4V substrates by RF magnetron sputtering was investigated and compared with uncoated substrates. The results showed that the RHEA could be prosperously used as an alternative coating on metallic biomaterials. Particularly, the obtained results in this study can be summarized as follows:

1. Microstructural characterizations revealed that compact, smooth, and cauliflower-like morphology RHEA film with the amorphous structure was developed on the different substrates. Despite its amorphous state, the deposited film exhibited grain boundaries formed due to the growth of the void network in the structure.
2. The surface mechanical properties of the substrates were enhanced after applying the RHEA films on them. The hardness values of 2.44, 4.11, and 3.32 GPa of 316L, CoCrMo, and Ti6Al4V substrates, respectively, were increased to 11.43, 11.49 and 11.45 GPa for the RHEA-coated 316L, CoCrMo, and Ti6Al4V, respectively. The dense, smooth, and compact structure of the deposited RHEA film as well as its fine-grained amorphous nature, could provide a significant enhancement of the mechanical properties.
3. The scratch test results showed that while the deposited RHEA film on the 316L started to crack and delamination at the loads between 190-210 mN, cracking and peeling of the RHEA-coated CoCrMo began between 280-310 mN. In contrast, the RHEA film deposited on Ti6Al4V exhibited superior adhesion without any delamination.
4. According to potentiodynamic polarization tests performed in PBS solution, the RHEA-coated 316L and CoCrMo substrates show pitting behavior, whereas the RHEA-Ti6Al4V specimen reveals a continuous passive plateau without any pitting traces. Besides, the Rp value of the RHEA-Ti6Al4V is higher than those of the RHEA-coated 316L and CoCrMo specimens.
5. The EIS results showed that the highest Rct value (about $1.5 \times 10^7\ \Omega\ cm^2$) was achieved in the RHEA-Ti6Al4V specimen. It is likely the excellent adhesion generated in the film/substrate interface contributed to the increment of charge transfer resistance of the RHEA-Ti6Al4V specimen in PBS solution.

CHAPTER 4

A COMPREHENSIVE STUDY OF MICROSTRUCTURE, MECHANICAL BEHAVIOR, BIOCORROSION, AND CYTOTOXICITY OF RF-PVD DEPOSITED $Ti_{1.5}ZrTa_{0.5}Nb_{0.5}X_{0.5}$ (X: Hf, Mo, AND W) REFRACTORY HIGH-ENTROPY ALLOY FILMS ON 316L

The majority of this chapter has been published *in Intermetallics 162 (2023) 108003*. The original manuscript has been rearranged to conform to the format requirements of the dissertation.

4.1 Introduction

316L stainless steel is a widely used material for medical implants due to its mechanical strength, formability, and relatively low cost compared to other metallic implants such as Ti- and Co-based alloys [174]. As a result of these beneficial characteristics, 316L is a commonly chosen material for plates, pins, screws, wire, and stents [175]. Although 316L is known as corrosion resistant material due to the presence of a protective chromium-rich oxide layer on its surface, it can still be vulnerable to pitting and crevice corrosion when exposed to a biological environment [176,177]. Prolonged contact with the body fluid medium can cause corrosion of the 316L material leading to the release of chromium and nickel ions [177,178]. The release of these hazardous ions not only triggers the mechanical failure of the implant but also results in histopathological changes in the patient's detoxification organs, including the liver, kidney, and spleen, and may even lead to the development of tumors [177,179,180]. It has been reported that corrosion was the main cause of the nearly 25% of the premature removal of the 316L implants [151,181].

Thus the use of coatings on implants has gained significant attention from researchers in recent years. The purpose of applying these coatings is not only to improve the corrosion resistance of 316L implants but also to enhance their biocompatibility, lifespan, and tissue integration [175,182]. It is important to note that the coatings used on implants should also be cost-effective and able to be consistently reproduced [174]. In this regard, researchers are actively working to improve the design and functionality of these coatings with enhanced properties to meet the demand for such specifications.

High-entropy alloys (HEAs) deviating from the conventional alloy design concepts possess unique characteristics such as excellent mechanical properties and corrosion resistance, making them promising for use in various applications [151,183–187]. The tunability of HEAs in terms of properties allows for attaining desired characteristics by altering the type and content of constituent elements [188–191]. Research into the biomedical applications of HEAs has primarily focused on the development of allergy-free and non-toxic refractory HEAs (RHEAs) made up of transition metals such as Ti, Zr, Ta, Mo, Nb, Hf, and W [151,192–194]. While the bulk RHEAs have been explored as a promising material for biomedical applications in literature, their use has been limited

due to difficulties in production and compositional inhomogeneity resulting from the high melting point of the constituent elements [93,97,184].

Therefore, applying RHEA coatings could be a promising solution for enhancing the surface properties of commercially available metallic implants and serve as a new generation protective coating for biomedical applications [183,192]. However, it is essential to accurately analyze and understand the relationship between the chemical composition of RHEA and desired characteristics, as the physical and chemical properties of the deposited coatings or films significantly impact biocompatibility, successful osteointegration, and the long-term use of the implant. With this in mind, this study focuses on evaluating the microstructure, mechanical properties, corrosion resistance, and cytotoxicity of $Ti_{1.5}ZrTa_{0.5}Nb_{0.5}X_{0.5}$ high-entropy alloy (RHEA) films with X being Hf, Mo, or W, deposited onto 316L stainless steel using a radio-frequency physical vapor deposition (RF-PVD) machine.

4.2 Materials and Methods

4.2.1 Targets and Subsrtate Preparation

The targets of $Ti_{1.5}ZrTa_{0.5}Nb_{0.5}Hf_{0.5}$, $Ti_{1.5}ZrTa_{0.5}Nb_{0.5}Mo_{0.5}$, and $Ti_{1.5}ZrTa_{0.5}Nb_{0.5}W_{0.5}$ RHEA were prepared by arc-melting of principle elements (at least 99.9% purity) under Argon (Ar) atmosphere, followed by remelting at least four times to enhance the uniformity and homogeneity. Before the preparation of the target, the remaining oxygen was removed from the furnace chamber through the remelting of 50 grams of commercially pure titanium three times. The produced targets were subsequently heated at 1000 °C for a 12-hour period in a vacuum to ensure homogenization. The nominal and actual chemical composition of the manufactured targets quantitatively examined by an X-ray fluorescence analyzer (XRF, Bruker S8 Tiger) are listed in Table 4.1.

Table 4.1. The nominal and actual chemical composition of the prepared targets (wt% and at%).

	Nominal Chemical composition													
	Ti		Zr		Ta		Nb		Hf		Mo		W	
	wt%	at%	wt%	at%	wt%	at%	wt%	at%	wt%	at%	wt%	at%	wt%	at%
$Ti_{1.5}ZrTa_{0.5}Nb_{0.5}Hf_{0.5}$	18.46	37.5	23.43	25	23.25	12.5	11.93	12.5	22.93	12.5	---	---	---	---
$Ti_{1.5}ZrTa_{0.5}Nb_{0.5}Mo_{0.5}$	20.65	37.5	26.21	25	26.00	12.5	13.35	12.5	---	---	13.79	12.5	---	---
$Ti_{1.5}ZrTa_{0.5}Nb_{0.5}W_{0.5}$	18.33	37.5	23.27	25	23.09	12.5	11.85	12.5	---	---	---	---	23.46	12.5
	Actual													
$Ti_{1.5}ZrTa_{0.5}Nb_{0.5}Hf_{0.5}$	18.21	37.14	23.24	24.89	23.57	12.72	12.14	12.75	22.84	12.50	---	---	---	---
$Ti_{1.5}ZrTa_{0.5}Nb_{0.5}Mo_{0.5}$	20.79	37.66	26.62	25.33	25.77	12.36	13.18	12.31	---	---	13.64	12.34	---	---
$Ti_{1.5}ZrTa_{0.5}Nb_{0.5}W_{0.5}$	18.28	37.43	23.43	25.19	23.33	12.64	11.57	12.32	---	---	---	---	23.29	12.42

Disc-shaped 316L stainless steel substrates with a dimension of 4 mm radius and 1 mm thick were sliced using electro-discharge wire cutting followed by mechanical grinding and surface polishing to a mirror finish. After ultrasonically cleaning the substrates with acetone and ethanol, the specimens were rinsed in deionized water before depositing the films.

4.2.2 Film Deposition Procedure

$Ti_{1.5}ZrTa_{0.5}Nb_{0.5}Hf_{0.5}$, $Ti_{1.5}ZrTa_{0.5}Nb_{0.5}Mo_{0.5}$, and $Ti_{1.5}ZrTa_{0.5}Nb_{0.5}W_{0.5}$ RHEA films designated as RHEA1, RHEA2, and RHEA3, respectively, with an approximate thickness of 1-1.2 µm were deposited on 316L substrates and silicon wafers by RF-PVD machine (Nanovak NVTS-400). The substrates were heated to 200 °C prior to the deposition process, which was carried out in an Ar atmosphere using a power of 120 W without applying the bias to the substrate. Prior to the sputtering process, the base pressure was kept lower than 1×10^{-5} Pa, and then the flow of Ar gas was controlled at 10 standard cubic centimeters per minute (SCCM). A pre-sputtering with Ar plasma is performed for 20 minutes on the target surface before opening the specimen shutter to achieve a fresh surface.

Coated silicon wafers were used in grazing incidence X-ray diffraction (GIXRD) and field-emission scanning electron microscope (FESEM) cross-sectional investigations due to the improved signal-to-noise ratio and the ease of specimen preparation.

4.2.3 Microstructural Characterisation

An X-ray diffractometer (XRD, Bruker D8 Advance) and grazing incidence X-ray diffraction (GIXRD) were used to characterize the phase structures of the substrate and deposited films, respectively. By utilizing the GIXRD method, measurements were taken at an angle of incidence of 4° with a scanning rate of 0.6°/min, using increments of 0.02°. The coated specimens' surface characteristics and cross-sectional investigations were conducted using an energy-dispersive X-ray spectrometer (EDS) equipped field-emission scanning electron microscope (FESEM, Zeiss, Ultra Plus).

The outermost surface chemical composition of the deposited films was investigated by X-ray photoelectron spectroscopy (XPS, Thermo Fisher Scientific K-Alpha) equipped with a monochromatic Al Kα (1486.6 eV) source.

To determine the surface characteristics of the specimens, including topography and roughness, atomic force microscopy (AFM, Brucker Dimension Icon) was utilized in tapping mode. The analysis was conducted using a silicon cantilever probe with a tip radius of 8 nanometers (RTESPA-525).

The sessile drop testing (DataPhysics, OCA 20) was used to measure the uncoated and coated surface wettability by dropping a PBS droplet. The test was repeated three times, and the static angles between the droplet and the surface of the specimens were recorded and measured using a digital camera. The composition of the PBS solution and its pH value is given in Table 4.2.

Table 4.2. The ingredients of the PBS solution and its pH value used in sessile drop testing.

Ingredients	Amounts (g/l)	pH
NaCl	8.00	7.4±0.05
KH_2PO_4	0.24	
KCl	0.20	
$Na_2HPO_4.7H_2O$	2.19	

4.2.4 Mechanical and Adhesion Tests

The hardness (H) and elastic modulus (E) of the deposited RHEA films were measured by a load-controlled nanoindentation machine (Agilent G200) by employing a Berkovich diamond tip performing in continuous stiffness measurement (CSM) mode. The experimental parameters of the strain rate and displacement amplitude were set at 0.05 s^{-1} and 2 nm, respectively. In this research, the indenter penetrated less than 10% of the thickness of the films to remove the substrate's influence on the mechanical properties. At least 20 indents were carried out on both the RHEA coated specimens, and the Oliver-Pharr method was applied to determine the H and E. In addition, scratch tests were performed on the nanoindentation instrument (Agilent G200) using a diamond stylus with a 5 µm end radius. Parallel single-pass scratches with a length of 400 µm were made using the normal load, increasing from 0 to 400 mN at a loading rate of 10 mN/sec. In order to determine the critical load at which the cracking and delamination initiate, the scratch tracks were individually studied using FESEM.

4.2.5 Biocorrosion Test

The biocorrosion behaviors of the uncoated 316L substrate and RHEA coated specimens in PBS solution were assessed using a potentiodynamic polarization measurement (Biological Science Instrument, VSP-300). In this study, an Ag/AgCl electrode, a platinum sheet, and a sample holder with a constant contact area were used as the reference electrode, the counter electrode, and the working electrode, respectively. The open circuit potential (OCP) was stabilized after soaking the specimens in the PBS electrolyte for 1 hour. The temperature of the PBS remained constant at 37 ± 1 °C using the thermostatic bath during the tests. From 0.30 V versus E_{OCP} to 1.80 V versus ERef, corrosion tests are conducted at a scan rate of 10 mV/s. Anodic and cathodic slopes were extrapolated to determine the corrosion current density (I_{corr}), corrosion potential (E_{corr}), and corrosion resistance (R_p) of each specimen.

At the end of the corrosion tests, the used PBS electrolyte was analyzed by inductively coupled plasma mass spectrometry (ICP-MS, Agilent 7700x) to identify the concentration of released chromium (Cr), and nickel (Ni) ions in the solution.

4.2.6 Cytotoxicity and Cell Attachment

Cytotoxicity of specimens on healthy muscle cells (C2C12) was tested by standard MTT assay (3-(4,5-dimethyl-thiazol-2yl)-2,5-diphenyltetrazolium bromide). For sterilization, specimens were washed three times with EtOH and then exposed to UV light for 4 h. After seeding the cells onto the sterilized specimens in complete DMEM media supplemented with 10% FBS and 1% penicillin-streptomycin (5×105 cells/well), they were incubated at 37 ± 1 °C and 5% CO_2 atmosphere for 72 h. The specimens were then washed with PBS 1X, and the cytotoxicity was measured using an MTT assay as described previously [193]. Data were analyzed by one-way ANOVA using Tukey's comparison test, and the results were shown as mean ± standard deviation (SD), and $p < 0.05$ was considered statistically significant.

Live/dead assay (Abcam, UK) was used to confirm the viability of C2C12 cells on the specimens. Cells were stained after 72 h of incubation on specimens according to the manufacturer's protocol, and then the fluorescence images were collected using a fluorescence microscope (Zeiss Axio observer Z1).

The attachment and spread of cells on the specimens were studied by confocal microscopy and SEM. Cells were again seeded on specimens and washed with PBS 1X after 72 h incubation, then were fixed with 4% paraformaldehyde for 20 min for SEM. To monitor the cell attachment using confocal microscopy, the nuclei and actin filaments were stained using 4',6-diamidino-2-phenylindole (DAPI), and Phalloidine, respectively. Each dye was added at 2 μg/mL concentration for 15 min in the dark, cells were washed with PBS 1X three times to remove the unbounded dyes, and then, the cell adhesion was studied using a confocal microscope (Leica dmi8/SP8) with two different filters: DAPI (λex: 325–375 nm and λem: 435–485 nm) and FITC (λex: 495 nm and λem: 516 nm). ImageJ software was used to process and merge the images.

4.3 Results and Discussion

4.3.1 Microstructural Characterisation

XRD and GIXRD patterns of the 316L substrate and deposited films are presented in Figure 4. 1. It is obvious that the substrate has a typical microstructure feature of the stainless steel composed of FCC phase. For all deposited RHEA films presented in Figure 4. 1, a broad GIXRD peak was detected in their pattern, implying their amorphous structure. The resulting amorphous features of the deposited RHEA films are attributed to the constituent elements' large atomic size, long-range diffusion, high mixing entropy as well as the quenching-like phenomenon commonly occurring in the PVD technique [157,160].

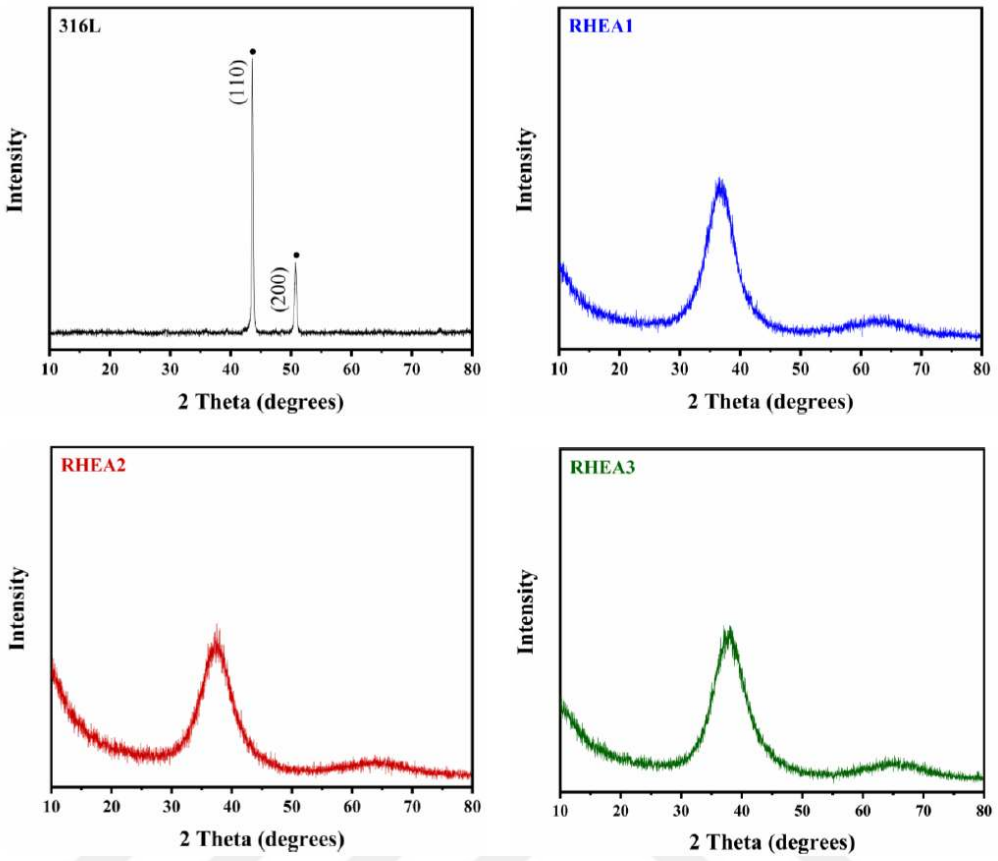

Figure 4. 1. XRD peaks of 316L and GIXRD patterns of the RHEA films.

Figure 4. 2 shows the cross-sectional FESEM micrograph, surface morphology, and EDS spectra of RHEA films deposited on the silicon wafer and 316L substrates. As shown in Figure 4. 2a, dense RHEA films with a thickness of around 1.075±0.025 µm were deposited on the substrates. Additionally, the surface images (Figure 4. 2b) depict a continuous and granular morphology for all specimens without macro defects and delamination. Granular featured grains have been reported in many magnetron sputtered metallic films having a size ranging from a few to several hundreds of nanometers [162,184]. In spite of the amorphous features of synthesized PVD films, grain boundaries (GBs) can be observed on their surfaces. Intrinsic GBs within amorphous films are density-deficient zones formed as a result of the growth of void networks within the structure, resulting in the formation of superficial microcracks along their length [165,193]. Figure 4. 2c shows the spectra and chemical composition of RHEA1, RHEA2, and RHEA3 specimens measured by EDS at the surface of deposited films on silicon wafers. The measurements were repeated at least five different locations, and the average values were reported. The EDS spectra exhibited signals of constituent elements and

stated that the chemical compositions of deposited films and relevant targets did not differ significantly.

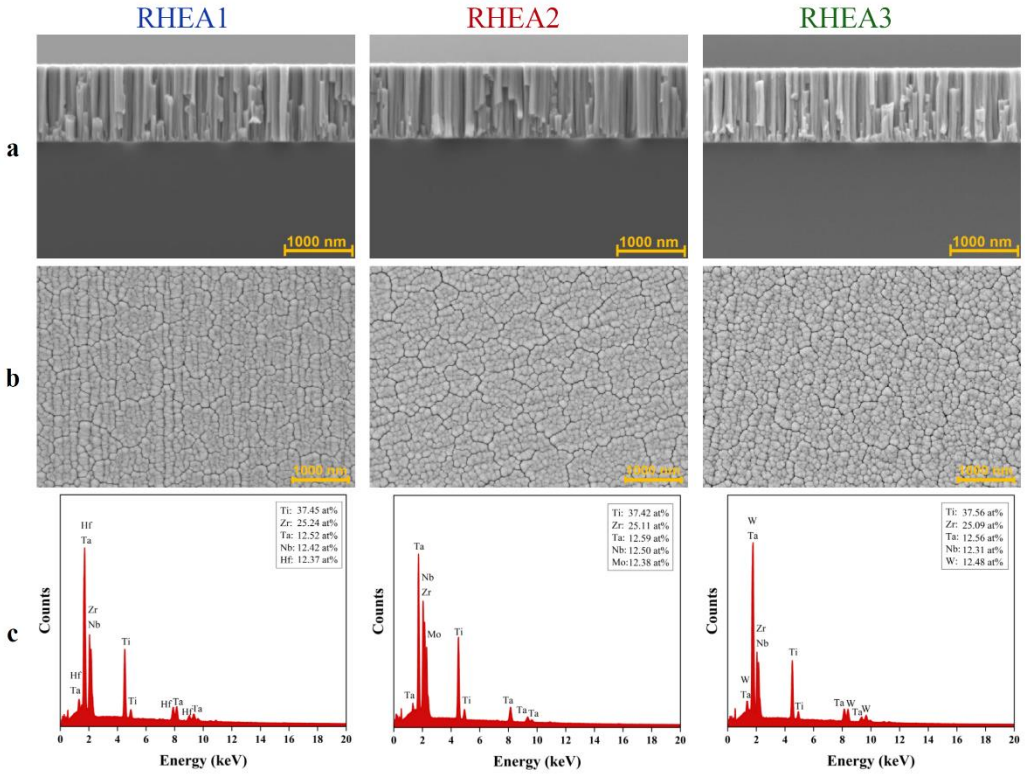

Figure 4. 2. (a) Cross-sectional FESEM image of RHEA films deposited on the silicon wafer, (b) surface FESEM micrographs of the deposited film on the 316L substrate, and (c) EDS spectra obtained from the surface of RHEA films deposited on the silicon wafer**.**

The chemical states of the elements presented at the outermost surface of the deposited RHEA films were investigated through the XPS, and the results are depicted in Figure 4. 3. By referencing the binding energy of hydrocarbons at 284.6 eV as measured by the C1s peak, the spectra were corrected for charging shifts, and the relevant peaks were then identified using standard reference spectra. The XPS spectra indicated that the superficial surfaces of deposited films were composed of elements in their oxide and/or sub-oxide forms as a result of spontaneous oxidation when exposed to the open environment. Based on the obtained XPS spectrum given in Figure 4. 3 for all deposited specimens, observed Ti peaks at 458.2±0.2 eV and 464.2±0.2 eV are related to TiO_2. Also, as it is obvious from Figure 4. 3, for other common elements presented in all deposited films (Zr, Ta, and Nb), the detected peaks are related to their oxides and sub-oxides discussed in our previous studies in detail [184,193]. In addition, the XPS survey spectrum of the variable elements (X: Hf, Mo, and W) indicated that oxide and/or

suboxide of Hf, Mo, and W developed at the surface of the examined specimens. For Hf, peaks at 16.6 eV and 18.2 eV are related to HfO_2, whereas peaks at 13.9 eV and 15.6 eV reflect its sub-oxide. The Mo XPS spectrum revealed that peaks at 228.6 and 231.6 eV coincide with MoO_2. XPS analysis of W showed that peaks at 34.9 eV and 37.1 eV are associated with WO_3, and peaks at 30.7 eV and 32.5 eV are linked to the sub-oxide form of W. The development of oxide and/or suboxide of the constituent elements at the topmost layer of the deposited films subjected to the open atmosphere can be related to their high chemical reactivity with oxygen.

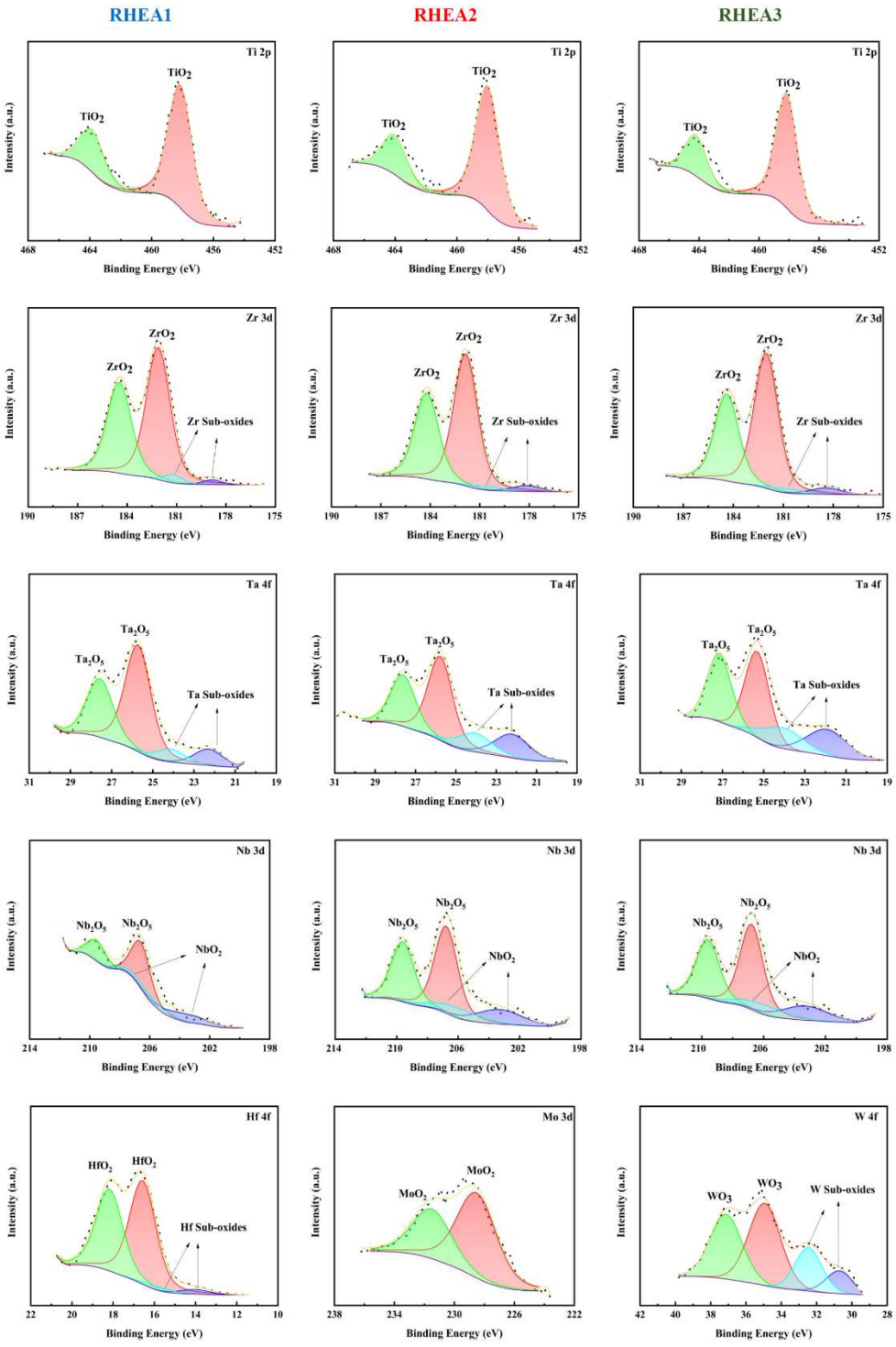

Figure 4. 3. The obtained XPS spectra from the outermost surface of deposited RHEA films.

Figure 4. 4 shows AFM images of uncoated, and RHEA coated specimens in three-dimensional form, obtained from a 5 μm×5 μm scanning area. The scratches on the surface of the uncoated specimen are the result of mechanical polishing while preparing

the specimens. Average roughness (Ra) values for 316L, RHEA1, RHEA2, and RHEA3 specimens were reported 3.24±0.20 nm, 3.63±0.30 nm, 3.64±0.03, and 3.33±0.42 nm, respectively. The slight increase in coated specimens can be attributed to the deposition of RHEAs films with granular characteristics [192]. However, the obtained roughness values in the same range and lower than 4 nm indicate that the surface of all examined specimens is smooth, and the deposited films possess uniform features.

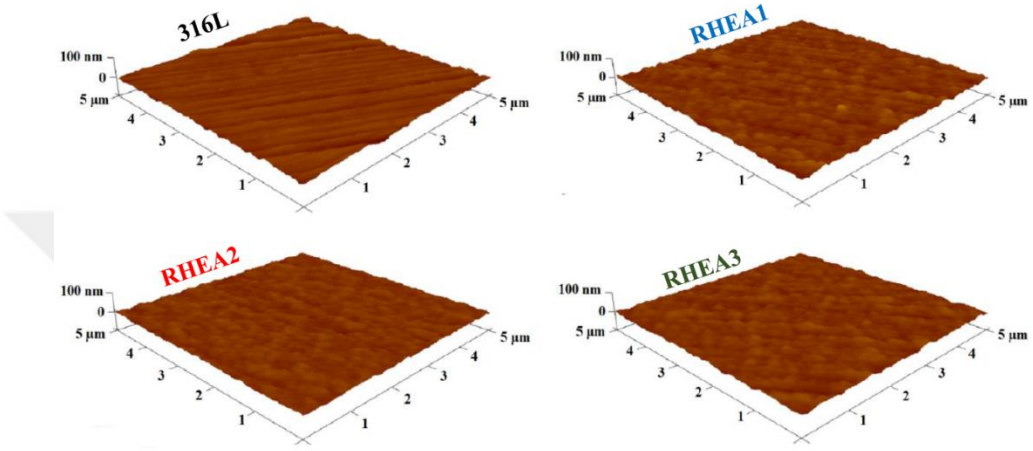

Figure 4. 4. AFM surface topography of uncoated and coated specimens.

Using the sessile drop methodology, PBS is injected into a syringe and dropped on specimen surfaces; the droplet image shows the contact angle (CA) and the solid-liquid-air interface. PBS droplet states as well as the CAs for all specimens can be seen in Figure 4. 5. The CA values were reported 70.99 °, 52.91 °, 48.93 °, and 40.33 ° for for 316L, RHEA1, RHEA2, and RHEA3, respectively. As it is obvious, the deposition of RHEA films reduces the CA of 316L substrate. On hydrophobic surfaces, liquid droplets tend to remain spherical rather than spread over the surface to minimize their surface area. Alternatively, a surface with a low interfacial tension allows droplets to spread over its surface because of the strong attraction between solid and liquid [195]. The surface wettability of implanted metallic prostheses, such as load-bearing joints, bone plates, stents, and wires, significantly impacts implant-tissue interaction since it stimulates the growth of cells. For tissue regeneration, the optimal CAs values are recommended to fall within the range of 35° and 80° [183,193,196].

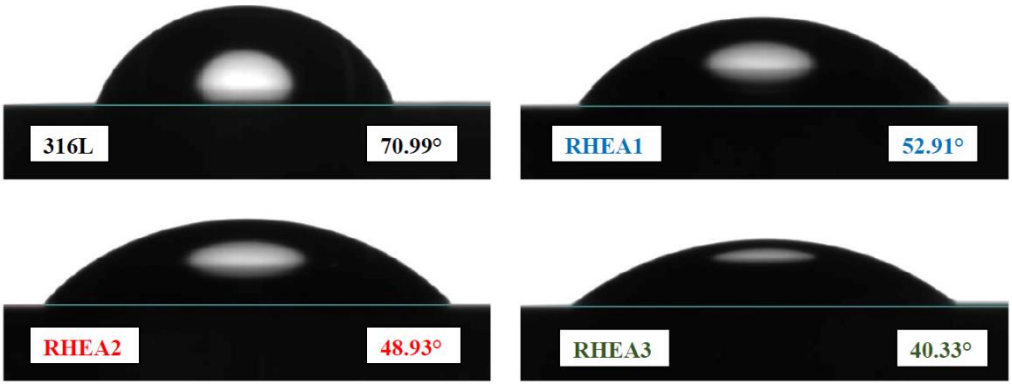

Figure 4. 5. Photographs of PBS drops on the surface of uncoated substrates and RHEA-coated specimens.

4.3.2 Mechanical Properties

A nanoindentation tester and the Oliver-Pharr method were used to measure the mechanical properties of RHEA1, RHEA2, and RHEA3 specimens in terms of the H and E. Previous work reported the H and E values of 316L substrate after pile-up correction [8]. As shown in Table 4.3, the measured results revealed that the H values of the 316L, RHEA1, RHEA2, and RHEA3 specimens are 3.54 ± 0.21GPa, 12.23 ± 0.17 GPa, 17.29 ± 0.12, and 17.25 ± 0.14 GPa, respectively. In addition, E values for specimens are reported 195.62 ± 9.32 GPa, 181.18 ± 1.3 GPa, 216.25 ± 1.9, and 200.72 ± 1.2 GPa for uncoated 316L, RHEA1, RHEA2, and RHEA3, respectively. In general, RHEAs films exhibit superior improvements in H values due to their fine and dense amorphous structure [167]. This dense structure impedes shear band motion because of slip toward different grain orientations [169]. As it is obvious from Table 4.3, the hardness of RHEA2 and RHEA3 is remarkably enhanced compared to RHEA1. It has been reported that stress induced within the film due to the large atomic size difference (δ) of the constituent elements plays an important role in the hardness of the RHEA films [197]. Increasing δ and consequently greater induced stress could enhance the thin films' mechanical properties. The atomic size difference (δ) could be calculated by [198]:

$$\delta = 100\sqrt{\sum_{i=1}^{n} C_i(1 - r_i/r)^2} \qquad \text{(Eq. 1)}$$

According to Eq. 1, δ the values of the RHEA1, RHEA2, and RHEA3 films were computed as 4.77, 5.37, and 5.28, respectively. Thus it is obvious that RHEA2 and RHEA3 exhibited superior hardness compared to the RHEA1 thin film due to their higher

δ values. The negligible improvement in the hardness of the RHEA2 in contrast to the RHEA3 can be related to the slight increase of the δ value.

Considering that the surface tribological properties and their function against rubbing counterparts play a crucial role in implant performance, the measured H and E values were used to calculate H/E and H^3/E^2 parameters. The H/E ratio manifests elastic strain to failure, and H^3/E^2 ratio indicates the material's resistance to plastic deformation under contact force [199]. The experimental results in this study demonstrate that depositing RHEA films on 316L remarkably enhanced its tribological performance, and both ratios for the RHEA3 specimen are higher than that of RHEA1, and RHEA2, resulting in excellent wear resistance.

Table 4.3. Mechanical behavior of the uncoated and PVD deposited substrates.

	H (GPa)	E (GPa)	H/E	H^3/E^2 (GPa)
316L	2.44 ± 0.18	195.62 ± 9.32	0.012	0.00038
RHEA1	12.23 ± 0.17	181.18± 1.3	0.067569	0.055837
RHEA2	17.29 ± 0.12	216.25± 1.9	0.079954	0.110528
RHEA3	17.25 ± 0.14	200.72± 1.2	0.085941	0.127405

4.3.3 Scratch Test

The corrosion and wear resistance of the coated metallic implant intimately depends on the adhesion strength between the coating and the substrate [200,201]. Poor levels of adhesion may lead to rapid worn off of the coating and subsequently accelerated deterioration of the substrate by the biological environment, which can remarkably diminish its durability and longevity [131,201,202]. Thus in this research, the scratch test was utilized to determine the adhesion strength of RHEA films on 316L substrate by analyzing FESEM images of scratch paths and measuring the load at which the film starts cracking and flaking. The FESEM micrographs of the tracks made by the scratch test on each coated specimen and the relevant profile of the load-scratch depth are presented in Figure 4. 6. An FESEM image and the accompanying load-scratch depth curves of RHEA coated specimens following the scratch test. In load-scratch depth curves, the critical load coincides with the abrupt change of the profile. The FESEM analysis and load-scratch depth curves indicate that the RHEA1 film on the 316L substrate begins to crack and delaminate at a critical load between 147 and 230 mN. Fluctuations in the load-scratch

depth curves of RHEA2 occur at 270-307 mN, indicating that the films start to crack and peel off the substrate. However, The RHEA3 film on the 316L substrate showed exceptional adhesion and resistance to scratching, with minimal delamination or flaking from the substrate, and only one instance of delamination was observed at around 300 mN. It is important to note that the characteristics and strength of interatomic forces have a critical impact on the adhesion strength between the deposited film and the substrate [203]. Since, in this research, the films and the substrate are composed of metallic materials, the electron transfer between them and, consequently, the generated metallic bonding governs the adhesion strength [203]. While the strength of the metallic bonding depends on the number of free or delocalized electrons, the Valance Electron Concentration (VEC) of the deposited films can strongly determine the adhesion strength between the film and the substrate. VEC is defined by [198]:

$$VEC = \sum_{i=1}^{n} c_i (VEC)_i \qquad \text{(Eq. 2)}$$

Where n is the number of constituent elements in RHEA film, ci is the atomic percentage of the ith element, and the (VEC)i is the VEC for the ith element. According to Eq.2, the VEC of the RHEA films can be calculated as 4, 6, and 6 for RHEA1, RHEA2, and RHEA3, respectively. Therefore the excellent adhesion properties of the RHEA2 and RHEA3 compared to the RHEA1 can be attributed to the higher VEC values of these films. On the other hand, the improved adhesion strength of the RHEA3, in contrast to the RHEA2, might be related to its tribological characteristics endorsed by H/E and H^3/E^2 parameters. As explained in the previous section, RHEA3, with higher values of H/E and H^3/E^2, indicated that this film has the potential to withstand the elastic strain and plastic deformation under the wearing force [204].

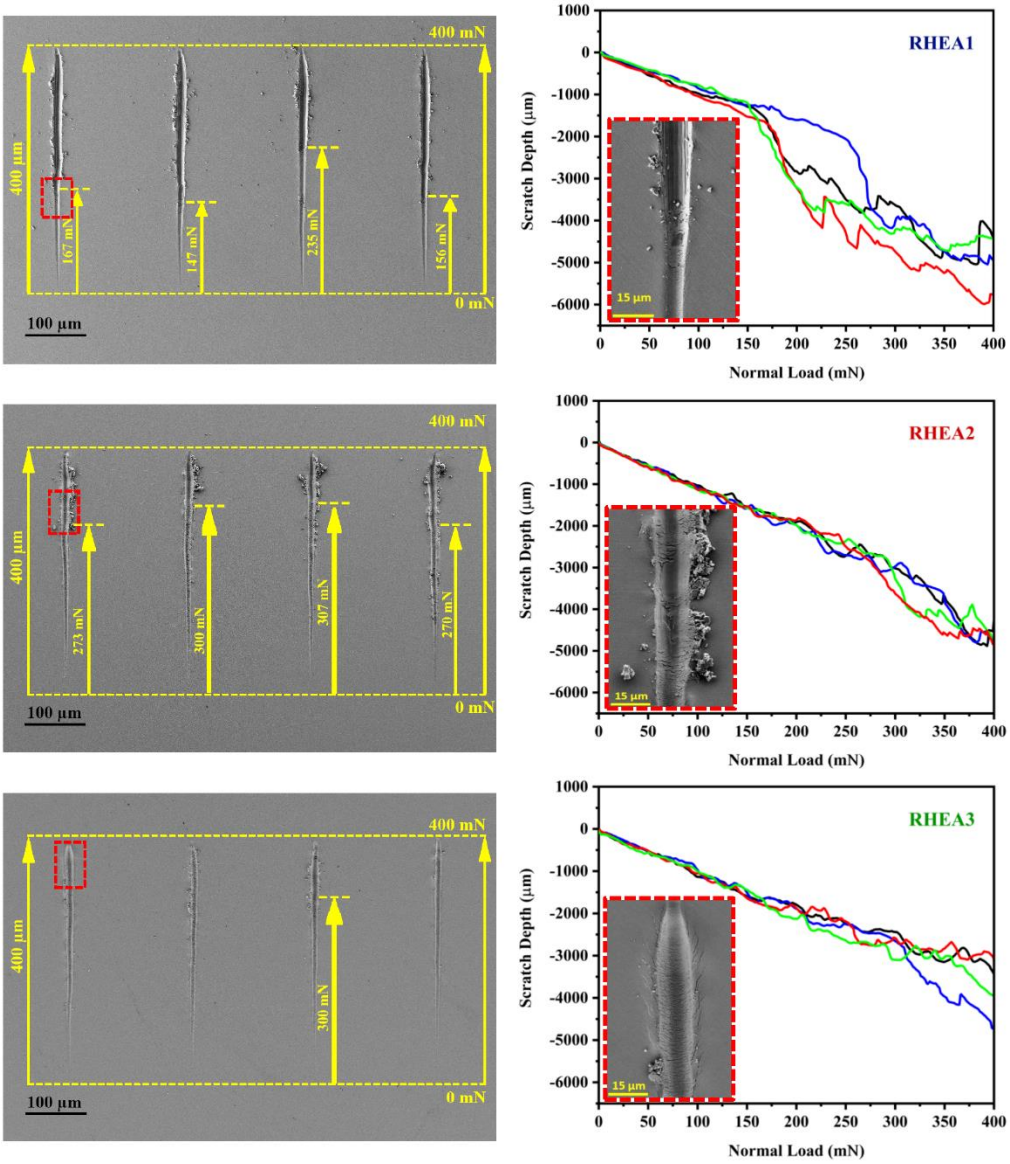

Figure 4. 6. An FESEM image and the accompanying load-scratch depth curves of RHEA coated specimens following the scratch test.

4.3.4 Biocorrosion Behavior

The Tafel curves of 316L, RHEA1, RHEA2, and RHEA3 specimens and corresponding FESEM micrographs after the corrosion tests are shown in Figure 4. 7. To simulate physiological conditions in the human body, all electrochemical tests were conducted in PBS solution at 37 ± 1 °C and at the scan rate of 1 mV/s. Figure 4. 7 depicts FESEM images of the uncoated and coated specimens after the biocorrosion test, and these images are provided to observe the films' surface corrosion behavior and pitting formation. As can be seen in Figure 4. 7, a higher number of pits were generated on the

surface of the uncoated 316L specimens compared to the RHEA coated specimens. The diameter of the pit traces on the uncoated 316L specimens is in the range of 5 to 50 μm. Even though the number of pitting holes generated on the coated 316L specimens has been significantly reduced, their size was increased. In Table 4.4, the listed parameters were calculated using the data presented in Figure 4. 7. The corrosion current density and the corrosion potential are described by Icorr and Ecorr. In order to obtain Icorr, the linear region in the vicinity of Ecorr was extrapolated from Tafel curves. As seen in Figure 4. 7 and Table 4.4, RHEA coated specimens showed higher potentials and lower current density compared to uncoated 316L indicating enhanced corrosion resistance. The uncoated 316L with Ecorr of −206.68 mV and Icorr of 1.68 μA/cm^2, exhibited inferior biocorrosion behavior in the PBS solution compared to coated specimens.

The pitting corrosion susceptibility of the uncoated and coated specimens was interpreted using the Tafel plots alongside the surface FESEM micrographs presented in Figure 4. 7 and also data given in Table 4.4. The results indicate that the deposition of RHEA film and altering its composition can significantly enhance the pitting potential (Ep) and reach the maximum value of 879.4 mV in the RHEA3 specimen.

Based on Stern-Geary's equation (Eq. 3), the polarization resistance (Rp) of examined specimens listed in Table 4.4 was determined [205].

$$I_{corr} = (\beta_A.\beta_C)/(R_p 2.303(\beta_A + \beta_C)) \qquad \text{(Eq. 3)}$$

In this equation, β_A (anodic slope) and β_C (cathodic slopes) were obtained from the slopes of the Tafel curves. As shown in Table 4.4, the Rp of RHEA coated specimens are remarkably greater than uncoated 316L substrate, and among the deposited films, RHEA3 exhibited the highest Rp (234E03) owing to its excellent adhesion strength to the 316L substrate.

Since the higher corrosion rate (CR) of implants, defined as their deterioration rate in biological environments (μm/year), incredibly limits their clinical use, it is essential to evaluate this parameter in the corrosion studies [193,206]. Therefore in this research CR of examined specimens was calculated based on corrosion current density given in Table 4.4. The presented data exhibits that the CR values of coated specimens are 8.4 to 10.2 orders of magnitude lower than those of uncoated 316L substrates.

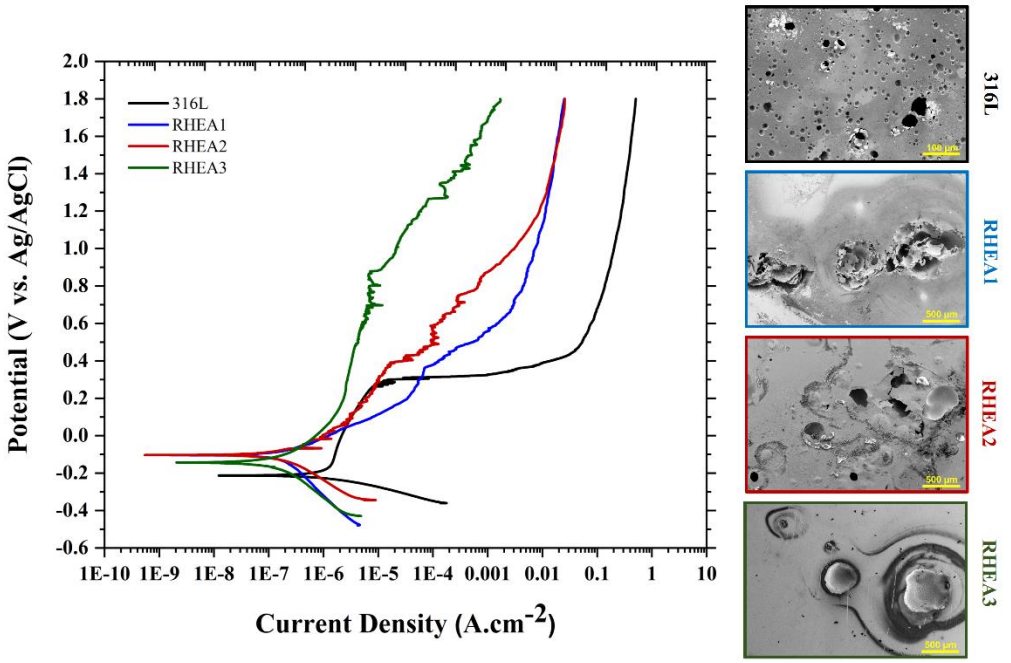

Figure 4. 7. Tafel curves of uncoated 316L and RHEA coated specimens obtained at 37 ± 1 °C in PBS solution and corresponding surface FESEM images of specimens after subjecting to the corrosion test.

Table 4.4. Obtained and calculated electrochemical parameters of uncoated 316L and RHEA coated specimens driven from Tafel curves.

	E_{corr} (mV)	I_{corr} (μA/cm^2)	E_{pit} (mV)	β_a (mV)	β_c (mV)	CR (×10^{-3}mm/year)	P	P_e (%)	R_p (×10^{3}Ωcm^2)
316L	-206.68	1.68	281.1	967.7	162.1	12.93	---	---	35.88
RHEA1	-101.27	0.211	362.3	165.7	212.6	1.525	0.146	87.5	191.63
RHEA2	-103.15	0.198	389.7	199.7	171.6	1.409	0.139	88.2	202.40
RHEA3	-143.94	0.187	879.4	208.3	196.9	1.263	0.132	88.9	235.03

Another parameter that effectively determines the electrochemical behavior of the magnetron sputtered coatings are pores, pinholes, and microcracks which can be intrinsically developed during the process. Thus in this work, to understand the importance of these defects on the corrosion resistance of coated specimens, Elsener's empirical equation (Eq. 4) is used to estimate the overall porosity of a corroded specimen [193,206].

$$P = \left(\frac{Rps}{Rp}\right) \times 10^{-\frac{\Delta Ei-o}{\beta a}} \qquad \text{(Eq. 4)}$$

In this equation, Rp represents the polarization resistance of the coated specimens, Rps is the polarization resistance of the uncoated substrate, ΔEi−0 signifies the difference in Ecorr values between the coating and substrate, and βa represents the anodic Tafel slope for the uncoated substrate. The calculated results in Table 4.4 revealed that the P value indicating the generated porosity in the coatings after the corrosion tests were slightly lower in the RHEA3 compared to RHEA1 and RHEA2 specimens.

Furthermore, the protective efficiency (Pe) of the deposited coatings is the other crucial aspect in evaluating the corrosion properties of the specimens that can be calculated through Eq. 5 as follow [193,206]:

$$P_e = \left(1 - \frac{icorr.\ coating}{icorr.\ substrate}\right).100 \quad \text{(Eq. 5)}$$

Where icorr. substrate is the corrosion current density of the uncoated substrate and icorr. coating is the corrosion current density of the deposited specimens. Based on a comparison of the calculated Pe values given in Table 4.4, the RHEA3 film poses the best protection efficiency. Considering the electrochemical values obtained through the corrosion tests demonstrated that RHEA3 with the lowest P (0.132) and the highest Pe (88.9%) possess excellent biocorrosion protectivity for 316L substrate.

4.3.5 Post-Corrosion Chemical Analysis

In order to identify the quantity of dissolved Cr and Ni ions in the PBS solution following the biocorrosion experiments, ICP-MS was utilized, and the results are presented in Figure 4. 8. It is clear that depositing RHEA films on the 316L substrate can diminish the amount of released Ni and Cr ions into the biological environment, and the best protectivity was obtained for the RHEA3 coated specimen. Depositing $Ti_{1.5}ZrTa_{0.5}Nb_{0.5}W_{0.5}$ RHEA on 316L substrate has decreased the Ni and Cr ions up to 92%. This result is in accordance with the protective efficiency (P_e) of RHEA3, mentioned in Table 4.4, and the FESEM observations after the corrosion test, which was depicted in Figure 4. 7.

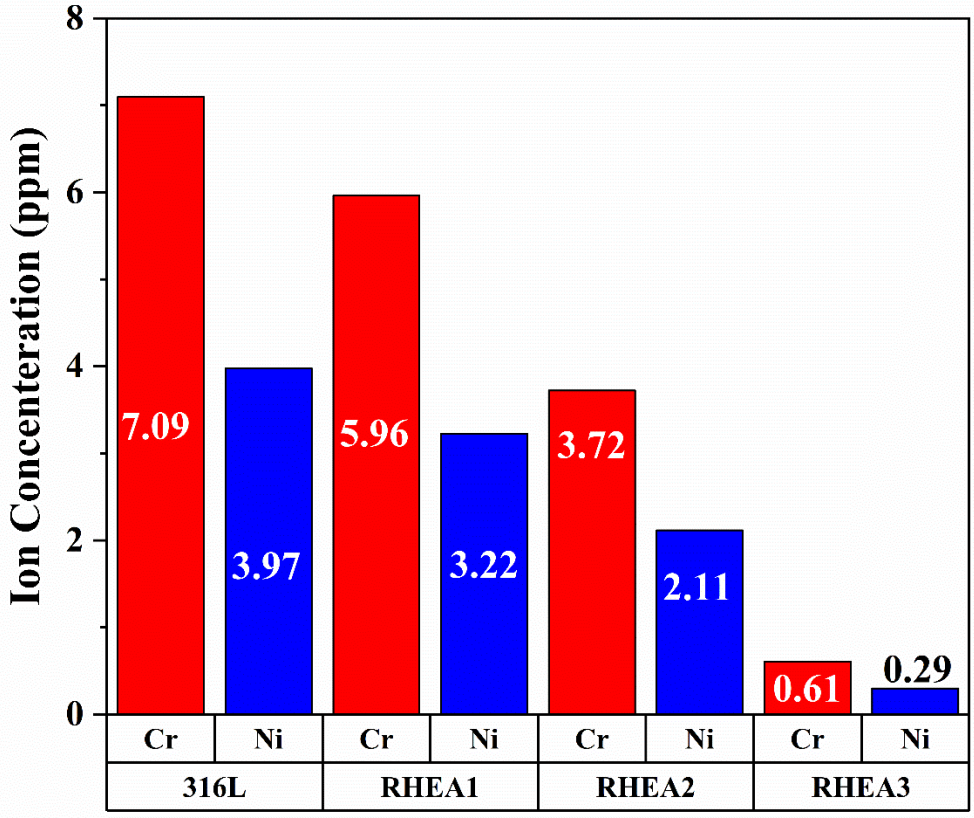

Figure 4. 8. The ion concentration of Ni and Cr after corrosion test of uncoated substrates and RHEA coated specimens.

4.3.6 In-vitro Cytotoxicity and Cell Adhesion

C2C12 cells were utilized to evaluate the biocompatibility and cell adhesion to the substrates, and the results were compared with the extensively used 316L as a control biomaterial. Figure 4. 9a showed no significant cytotoxicity regarding sample coatings compared to either control or 316L samples. To further confirm the cell viability, a calcein-AM/propidium iodide (PI) staining was utilized. No dead (red) cells were observed in the cells attached to the samples proving the high biocompatibility of the prepared specimens (Figure 4. 9b). The cell attachment to the samples was investigated using confocal microscopy and SEM after 72 h of cell seeding on the samples. The C2C12 cells were attached and spread onto the samples' surface, indicating great biocompatibility and cell proliferation, as shown in Figure 4. 9b. Taken together, coating 316L substrate with RHEA1, RHEA2, and RHEA3 not only enhanced electrochemical and mechanical properties, also improved the biocompatibility and cell proliferation that might make the prepared specimens promising candidates for bioapplications. The presence of native oxides of the constituent elements generated on the outermost surface

of the deposited RHEA thin films could improve their biocompatibility and osteointegration properties since the biological reactions take place at the surface of implants. Developed TiO_2 and ZrO_2 do not denature proteins, making them suitable for initial cell adhesion and tissue growth. Additionally, it has been demonstrated that coatings containing Ta, have excellent biocompatibility and corrosion resistance due to the formation of a self-passivating and stable Ta_2O_5 layer in a wide range of potential-pH [138,207].

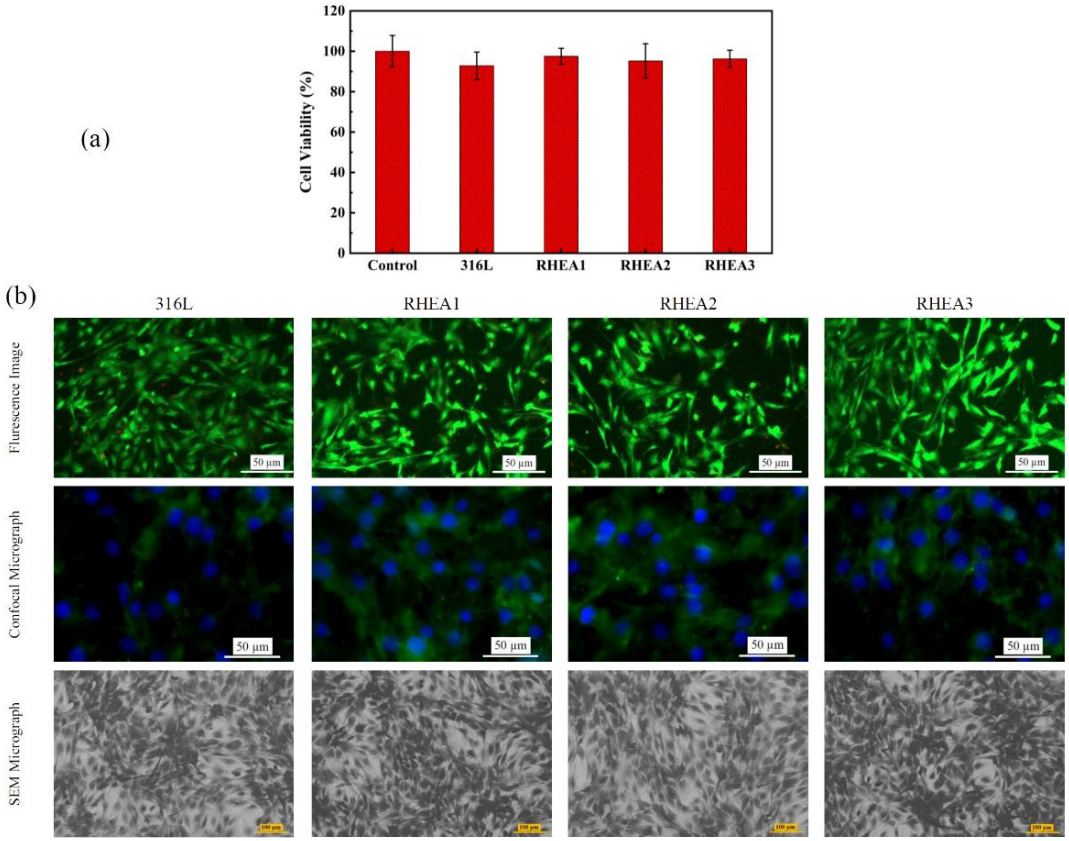

Figure 4. 9. (a) Quantitative analysis of cell viability after 72 h cultivation and (b) live/dead staining, confocal, and SEM micrograph of C2C12 cell incubated for 72 h onto 316L substrate and RHEA-coated specimens.

4.4 Conclusion

In this study, the structural characteristics, mechanical performance, corrosion resistance in biological environments, and in vitro biocompatibility of uncoated 316L substrate and $Ti_{1.5}ZrTa_{0.5}Nb_{0.5}Hf_{0.5}$, $Ti_{1.5}ZrTa_{0.5}Nb_{0.5}Mo_{0.5}$, and $Ti_{1.5}ZrTa_{0.5}Nb_{0.5}W_{0.5}$ RHEA films deposited versions were examined. The results suggest that RHEA3 may be a suitable protective coating for 316L biomaterials, and the key findings of this research are as follows:

• The RHEA films deposited had an amorphous structure with the granular features having a size ranging from a few to several hundreds of nanometres. The superficial surfaces of the deposited films were composed of elements in their oxide and/or sub-oxide forms. The smoothness and uniformity of the surface of the deposited films were supported by the roughness values, which were found to be in the same range and lower than 4 nm.

• The process of depositing RHEA films onto the surface of the 316L substrate has been found to improve the wettability of the substrate. The results obtained were within the desired range, which is essential for bone regeneration on metallic implants.

• The RHEA coated specimens exhibited significant improvement in hardness values compared to the uncoated 316L substrate, and the hardness of RHEA2 and RHEA3 was significantly higher than that of RHEA1. In addition, applying RHEA films to 316L significantly improves its tribological performance, and the RHEA3 specimen exhibited the highest level of wear resistance.

• The scratch tests demonstrated that while the RHEA1 and RHEA2 started to crack and peel off the substrate at a critical load of 147 to 230 mN and 270 to 307 mN, respectively, RHEA3 exhibited exceptional adhesion and resistance to scratching with minimal delamination.

• Electrochemical experiments in PBS solution revealed that applying RHEA films to a 316L substrate remarkably improved its biocorrosion resistance in terms of Ep, Rp, and Pe, with the highest values seen in the RHEA3 specimen. Furthermore, the data showed that the CR and P of the coated specimens are lower than those of uncoated 316L substrates, with the lowest values observed in the RHEA3 specimen.

• According to ICP-MS results, applying RHEA films to a 316L substrate reduced the amount of Ni and Cr ions released into the PBS during the biocorrosion testing. The

RHEA3 coated specimen was found to provide the best protection, decreasing the release of Ni and Cr ions by up to 92%.

• The in vitro cytotoxicity assessment of the examined specimens using C2C12 muscle myoblast cells revealed that RHEAs films did not induce any cytotoxic response, and good proliferation of the attached cells was observed.

CHAPTER 5

INVESTIGATION OF MICROSTRUCTURE, MECHANICAL PROPERTIES, AND BIOCORROSION BEHAVIOR OF $Ti_{1.5}ZrTa_{0.5}Nb_{0.5}W_{0.5}$ REFRACTORY HIGH-ENTROPY ALLOY FILM DOPED WITH Ag NANOPARTICLES

The majority of this chapter has been published in *Surfaces and Interfaces 28 (2022) 101617*. The original manuscript has been rearranged to conform to the format requirements of the dissertation.

5.1 Introduction

Life expectancy alterations as well as variation of population lifestyle, especially in the industrial nations, resulting in a significant increment of demands for implants, a trend that is most likely to continue for years [208]. Metallic biomaterials such as 316L, CoCrMo, and Ti6Al4V present immense potential for load-bearing applications, e.g., hip and knee prosthesis, due to their excellent formability and mechanical properties [209–211]. Among these alloys, Ti6Al4V is the most frequently used metallic implant in total hip replacements for substitution of damaged bone and treating arthritic hip joints due to its low elastic modulus decreasing the bone resorption caused by the stress shielding effect [212,213]. While Ti6Al4V is well-known for good biocompatibility and corrosion resistance, long-term usage of this popular alloy has raised serious concerns owing to aluminum and vanadium ions release [175,214,215]. As aluminum ion inhibits bone growth and possibly cause Alzheimer's disease, detrimental vanadium ion and vanadium oxide (V_2O_5) are known as toxic chemicals since they possess a high potential for cytotoxicity effect [175,216,217].

Therefore, preventing the toxic metal ions from being released is becoming the main challenge regarding the safety of implants in the human body. A variety of methods have been proposed to fabricate favorable coatings over the implants, which not only aid in holding the excellent bulk features during a long-life cycle but also inhibit or delay the release of the toxic ions [208,210,218–221].

Another most frequent clinical complication in implant rehabilitation which critically affects the integration between implants and surrounding tissues is the generation of bacterial biofilms on the implant surface [182,222,223]. It has been reported that the infection rates range from 0.5% to 3.0 % in total joint hip arthroplasties and 2 % to 30 % in external fixation [223–225]. Even though all medical cautions are taken during surgery and antibiotics are administered, unfortunately, contaminations present in the hospitals' environment and surgery devices can lead to bacterial infection during and after implantation and finally implant failure [226,227]. Several scientific experiments revealed that antibiotics have no significant effects in preventing implant-related infections because of decreasing blood circulation around the implant and consequently the deficiencies of antibiotics around it [228]. On the other, higher antibiotics are usually used in therapy compared to the actual required dose for pathogenic annihilation, and then

antibiotics surplus can generate harmful effects [229]. In addition, it has been demonstrated that the number of bacteria stems which are becoming resistant to antibiotics is increasing, and antibiotics cannot always fight the proliferation of bacteria on implants surfaces [229,230]. Therefore, it is highly essential to prevent bacterial infections by enhancing the antibacterial ability of implants by surface modification via applying a coating on them which contains antibacterial agents without affecting bulk mechanical properties.

Some metallic ions, including silver (Ag), copper (Cu), and zinc (Zn), have been found to exhibit antibacterial and biocompatible properties [224,231]. Ag has long been recognized to have significant bactericide properties and has gained increasing interest due to its broad antibacterial range, non-cytotoxicity at appropriate dosages, and good stability [231,232]. Even though a number of chemical forms of Ag are known to reveal antimicrobial activities, the clinical investigations demonstrated that at the same Ag concentration, the antimicrobial efficiency of the Ag nanoparticles (Ag NPs) is much higher than that of Ag ions (Ag^+) provided by $AgNO_3$, Ag_2O and $AgC_2H_3O_2$ [231,233–238]. However, the amount of the Ag NPs doped in the coating should be concerned since its dose-dependent manner may induce toxicity, inflammation, and oxidative stresses in human cells [235,236,239]. Previous works in this field have shown that promising bactericide properties with minimum cytotoxicity have been achieved in the surface of metallic implants, which contain 1 to 9 at% Ag dopants [223,240]. It is also worthwhile to note that the coatings doped with antibacterial agents must have excellent biocompatibility, optimum modulus of elasticity, higher hardness, and corrosion resistance within the application-specific tissue or body fluids, as well as good adhesion with the substrate deposited on them. By taking into account the needs for meeting such demands all at once, the deposition of biometallic films onto metallic substrates manifests itself as a viable option. High entropy alloys (HEAs), newly developed materials with non-equimolar or equimolar compositions, have recently gained attention because of their remarkable mechanical and physical properties along with high corrosion resistance [12,151,241–243]. Even though the bulk HEAs, including non-toxic refractory elements like Ta, Nb, Ti, Zr, Hf, W, and Mo, has been investigated as a new class of metallic biomaterials in the literature, refractory high-entropy alloys (RHEA) coating for biomedical applications is rare studied [93,99,150,151,184,206,244].

Meanwhile, the effect of embedding antibacterial agents in the physical and mechanical properties of RHEA coatings has not been systematically investigated. Since recent ongoing studies have demonstrated that Ag NPs-doped coating on orthopedic implants represents a promising approach to prevent implant-associated infections, this research was initiated to explore the microstructure, mechanical properties, and electrochemical behavior of RHEA coating doped with 9 at% Ag NPs by magnetron sputtering process [226,227,236,245,246]. This deposition technique became quite popular due to providing a uniform thickness of the coating, good adhesion, and easy control of the film composition and structure.

5.2 Experimental Methods

5.2.1 Target and Substrate Preparation

Non-equimolar $Ti_{1.5}ZrTa_{0.5}Nb_{0.5}W_{0.5}$ RHEA, with dimensions of 6.3 mm and 50.8mm as thickness and diameter, respectively, was used for depositing 1-1.2 μm thick films on commercially available Ti6Al4V substrates, and Si (100) wafers. Preparation of the target with nominal composition mentioned in Table 1 was done using arc melting of elements with a purity of 99.9% in the presence of highly pure argon (Ar) atmosphere; the melting process was repeated at least five times in order to enhance the chemical homogeneity. To further ensure low residual oxygen in the furnace chamber, 50 g of commercially pure titanium (CP-Ti) was remelted three times prior to the synthesis of the target to act as an oxygen-getter. Then the produced target was homogenized at 1000 °C for 12 h under the vacuum conditions. Through an X-ray fluorescence analyzer (XRF, Bruker S8 Tiger), the actual composition of the prepared target was determined, and the results are reported in Table 5. 1.

Table 5. 1. The nominal and actual chemical composition of the used target (at% and wt%)

	Ti		Zr		Ta		Nb		W	
	at%	wt%	at%	wt%	at%	wt%	at%	wt%	at%	wt%
Nominal	37.50	18.33	25.00	23.27	12.50	23.09	12.50	11.85	12.50	23.46
Actual	37.45	18.31	25.10	23.36	12.44	22.97	12.45	11.80	12.56	23.56

In order to dope silver (Ag) nanoparticles, the RHEA target was amended with circular holes that were filled with nuggets of Ag by utilizing a mechanical press. These holes were machined in the circumference of the highest sputter erosion area of the target. The number of Ag-filled holes used during the deposition process was altered to embed desired doses of the Ag nanoparticles (9 at%) in the structure of the RHEA film. The undoped and Ag-doped RHEA films deposited on the substrates were designated as RHEA, and RHEA-9Ag NPs, respectively.

For preparing the substrates, disc-shaped Ti6Al4V specimens with dimensions of 10 mm diameter and 1 mm thickness were cut from a rod by electro-discharge machining (EDM). The specimens were abraded by SiC sandpapers; this process was followed by polishing in the presence of alumina slurry (0.30 μm) to the mirror-like appearance. The polished specimens were ultrasonicated successively in acetone and ethanol and then rinsed with deionized water prior to deposition of the films.

5.2.2 Film Deposition Process

Nanovak (NVTS-400, Nanovak, Ankara, Turkey) magnetron sputtering was utilized to deposit undoped and Ag-doped RHEA films on the Ti6Al4V substrates and silicon wafers. Cross-sectional investigations and XRD analyses were performed on coated silicon wafers due to convenience in specimen preparation and improving the signal-to-noise ratio. Deposition of the films took place in an Ar atmosphere without substrate bias after heating the specimens up to 200 °C at the power of 120 W. The base pressure of the chamber was kept under 1×10^{-5} Pa, while the flow of Ar was maintained at 12 standard cubic centimeters per minute (SCCM) during the sputtering. In order to achieve a clean and uncontaminated sample surface, first, the target was subjected to a pre-sputtering process for almost 20 minutes using Ar plasma, and then the shutter placed between the specimens and the gun was opened

5.2.3 Microstructural and Mechanical Characterization

D8 Advanced X-ray diffractometer (XRD, Bruker) with a Cu K□ radiation was exploited for analyzing the phase structure of the Ti6Al4V substrate. Grazing incidence X-ray diffraction (GIXRD) was carried out where the range of acquisition angle was between

10° and 80°, incidence angle was 2°, and the scan speed was set to 0.6°/min at a step of 0.02°.

The surface morphology and cross-sectional investigations of the coated specimens were carried out through the field emission scanning electron microscope (FESEM, Zeiss, Ultra Plus), and also for the elemental analysis, an energy dispersive X-ray spectrometer (EDS) was utilized.

The chemical state of the constituent elements and composition profile along the depth of the deposited films were characterized by Thermo Fisher Scientific K-Alpha X-ray photoelectron spectroscopy (XPS) with a source of monochromatic Al Kα (1486.6 eV). The etching process was carried out over a 400 µm×400 µm area of the films using a rastered 4 keV Ar+ ion beam with the etching rate of 0.25 nm/s. The C1s peak of hydrocarbon at 284.6 eV binding energy was utilized as a reference for correcting the charging shifts in each spectrum.

Operated in tapping mode, an atomic force microscope (AFM, Brucker, Dimension Icon) was exploited for investigating the surface topography and phase contrast of the examined specimens.

The mechanical properties of the Ti6Al4V substrate and the deposited films were evaluated by utilizing an Agilent G200 nanoindentation that uses a Berkovich diamond as the indenter; nanoindentation tests were taken place at a continuous applied load of 3 mN as well as 5 seconds pause at the peak load and loading-unloading rate of 0.3 mN/s. Through the Oliver-Pharr method and loading-unloading curves, H and E parameters (as in hardness and elastic modulus, respectively) were determined. By controlling the indenter's penetration at approximately 1/10 of the films' thickness during the test, the influence of the substrate on the measurements was prevented. An average of 20 measurements was reported as the final H and E values of specimens with respect to standard deviation.

The surface wettability of the uncoated and coated specimens was studied by using sessile drop testing (DataPhysics, OCA 20) to measure the contact angle of droplets at room temperature. All specimens were cleaned up using a bath of acetone and ethanol, and later they were rinsed using deionized water and dried before the measurement. Droplets of phosphate buffer saline (PBS) were dropped over each specimen three times. Through a high-resolution camera, the static angles of droplets were recorded and determined five

seconds after dropping the PBS droplet. Table 5. 2 exhibits the composition and pH of the used PBS solution.

Table 5. 2. The composition and pH value of the used PBS solution

Ingredients	Amount of ingredients (g/l)	pH
NaCl	8.00	7.4±0.05
KH_2PO_4	0.24	
KCl	0.20	
$Na_2HPO_4.7H_2O$	2.19	

5.2.4 Biocorrosion Test

In order to observe the biocorrosion behavior of the uncoated and coated specimens when inserted into the human body, a potentiodynamic corrosion test in PBS solution was done by a three-electrode electrochemical cell using a potentiostat/galvanostat equipment (Biologic Science Instrument, VSP-300). Specimens placed in the cylindrical sample holder with a fixed exposed area were connected to the potentiostat/galvanostat as the working electrode, the platinum spiral wire was used as the counter electrode of the electrochemical cell, and an Ag/AgCl was placed in the electrolyte as the reference electrode. By utilizing a thermostatic bath during the tests, the temperature of the PBS remained constant at 37±1 ºC. Initially, specimens were placed in PBS for almost 1 hour, so that open circuit potential (OCP) reached a stable level. Later, potentiodynamic polarization tests were performed at a starting potential of 0.3 V (vs. EOCP) up to the final potential of 1.8 V (vs. ERef) with 1 mV/s as the scan rate. The reproducibility of data was confirmed by repeating at least five measurements. The corrosion current density, potential, and also corrosion resistance of each specimen were obtained by Tafel extrapolation. Electrochemical impedance spectroscopy (EIS) evaluations were carried out within 100 kHz - 10 mHz range and the sinusoidal perturbing signal of 10 mV at OCP. Before the EIS test, the specimens were also immersed in PBS solutions at 37±1 °C for 1

hour. The impedance data were analyzed by ZMan software, and the appropriate equivalent circuits were estimated. By considering the structure and shape of the electrode and its impedance response, the equivalent circuits of the specimens/solution system were simulated. Agilent 7700x inductively coupled plasma mass spectrometry (ICPMS) was used to determine the amount of Ag released from the Ag-doped specimens after the corrosion tests.

5.3 Results and Discussion

5.3.1 Microstructural Characterisation

In Figure 5. 1, GIXRD and XRD patterns of the Ti6Al4V, RHEA, and RHEA-9Ag NPs films deposited on a silicon wafer are presented. Figure 5. 1(a) explicitly reveals that the majority of Ti6Al4V substrate's structure is composed of α-HCP with a minor β-BCC phase. The observed broad peaks without any distinguished sharp diffraction pattern in Figure 5. 1(b, c) indicates that the deposited films are fully amorphous structure. The development of the amorphous films during the magnetron sputtering process can be attributed to the governing thermodynamic and kinetic rules indicative of low enthalpy, high entropy, long-range diffusion, and the difference in atomic dimensions of the constituent elements, all of which encourage the glass-forming ability of HEAs [160,184,247]. Accordingly, the available literature has pointed out the quenching-like effect of the sputtering process on the development of the films with amorphous nature; it was inferred that the temperature difference between the sputtered layer and the substrate would suppress the crystallization of the film, and as a consequence, it results in the development of amorphous films [157,164,184].

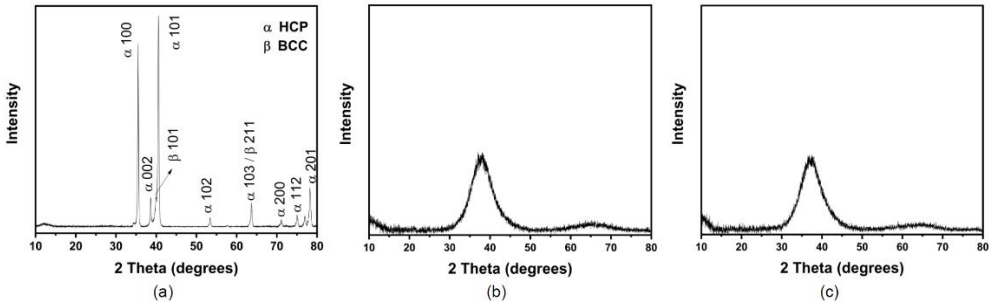

Figure 5. 1. (a) XRD pattern of Ti6Al4V substrate, GIXRD patterns of (b) RHEA and (c) RHEA-9Ag NPs specimens.

The cross-sectional FESEM micrographs of RHEA and RHEA-9Ag NPs films deposited on silicon wafers are presented in Figure 5. 2. As it is obvious, a compact and smooth film of undoped and Ag-doped RHEA with a thickness of about 1.10 m was developed on the substrates.

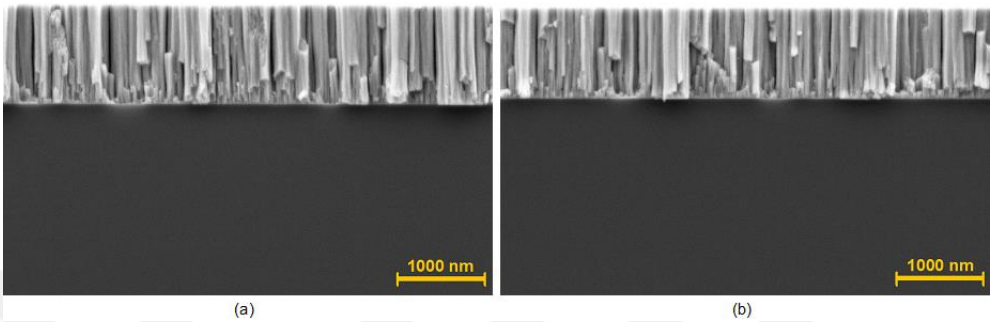

Figure 5. 2. Cross-sectional FESEM image of (a) RHEA and (b) RHEA-9Ag NPs films with silicon wafer as the substrate.

The surface morphology and chemical composition of the undoped and Ag-doped RHEA coated silicon wafers, obtained from FESEM-EDS, along with the corresponding spectra, are delineated in Figure 5. 3 and Figure 5. 4. As it is evident from the higher magnification images inserted in the upper left corner of Figure 5. 3, semi-spherical Ag nanoparticles in the Ag-doped specimen were uniformly distributed on the surface. Moreover, a continuous and cauliflower-like morphology of RHEA can be seen in Figure 5. 3 for both undoped and Ag-doped specimens. From the literature, the cauliflower-like grains in the most of metallic films are composed of many clusters which their sizes differ from several tens to hundreds of nanometers [160,162]. The surface morphology of deposited films was found dense, smooth without any voids or defects. Despite the amorphous nature of the sputtered films, grain boundaries can be detected when surface views of these films are investigated (Figure 5. 4). Such intrinsic grain boundaries within the amorphous coatings are the density-deficient regions that are generated by the void network's growth inside the structure [165,166]. Moreover, as it is seen in Figure 5. 4, some microcracks can be detected along the observed grain boundaries. The emergence of internal stresses while the films are being deposited promotes the development of these microcracks in the deposited layers [202,248,249].

The spectrum and chemical composition of RHEA and RHEA-9Ag NPs specimens obtained by EDS measurements from the surface and at three different regions with the

area of 2 µm × 2 µm of deposited films on the silicon wafer are given in Figure 5. 3. EDS spectrums of the RHEA specimen display signals of Ti, Zr, Ta, Nb, and W without any significant difference between the chemical composition of the deposited film and the used target. On the other hand, for RHEA-9Ag NPs, the existence of Ag signal confirms that Ag nanoparticles have been successfully embedded and homogenously distributed in the structure of the deposited film. Furthermore, detailed EDS point analyses were performed on RHEA-9Ag NPs over the film and also Ag nanoparticles, and the results are presented in Figure 5. 4. According to the results, the content of Ag in the structure of the film is about 9 at% which clarifies the presence of the Ag as an atomic form in the microstructure. However, the amount of the detected Ag on the white semi-spherical particle is about 14 at% which is higher than its amount in the film. Since the white particles are very small and during EDS analyses, the energy spectrum of other constituent elements can also be detected from its beneath, obtaining the actual amount of Ag in these white particles is impractical. Overall, it can be concluded that in the developed film, the constituent elements and the Ag nanoparticles were uniformly distributed throughout the microstructure.

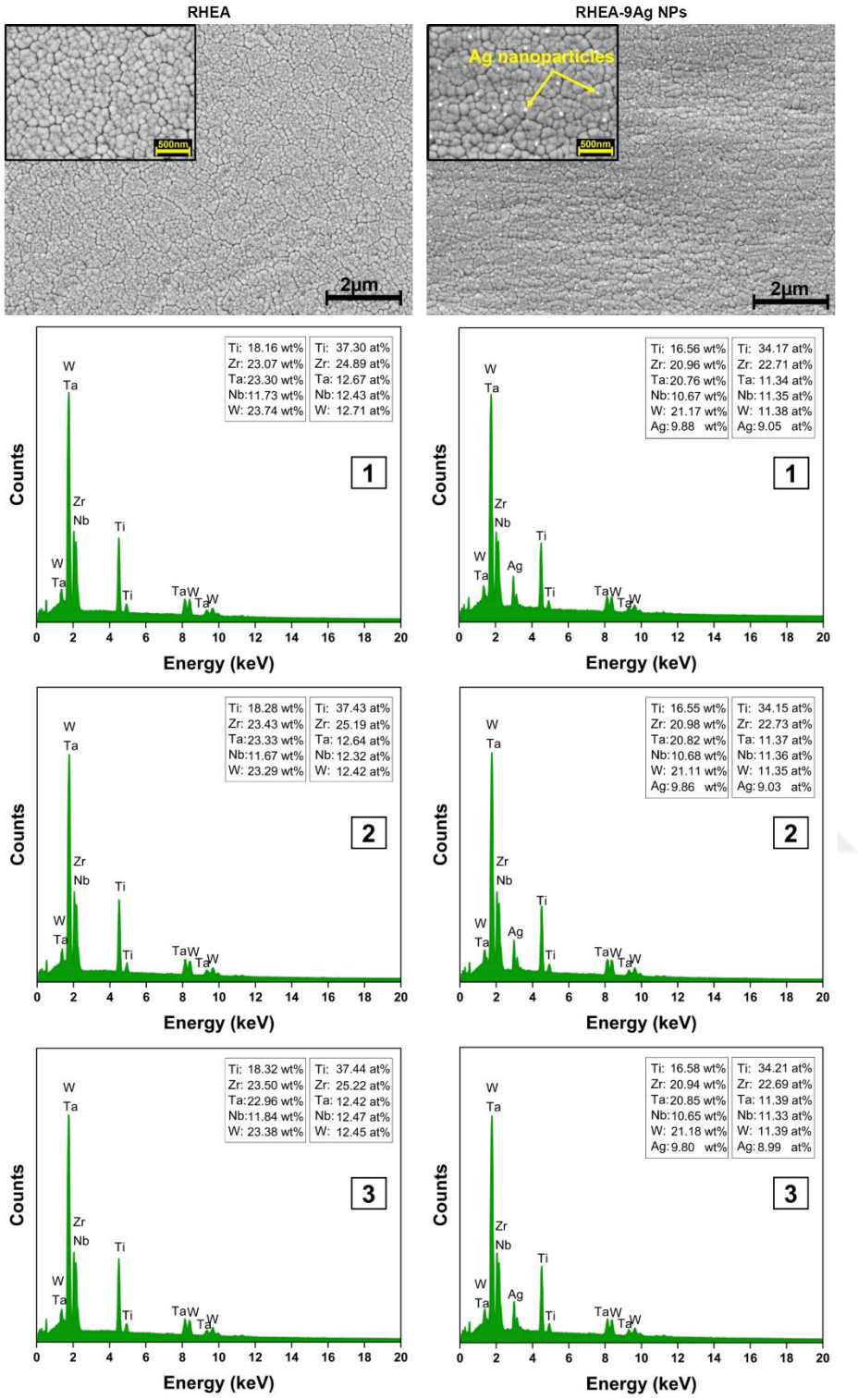

Figure 5. 3. Surface view FESEM micrographs and EDS characterizations obtained from the surface of left: undoped and right: Ag-doped RHEA films deposited on the silicon wafer.

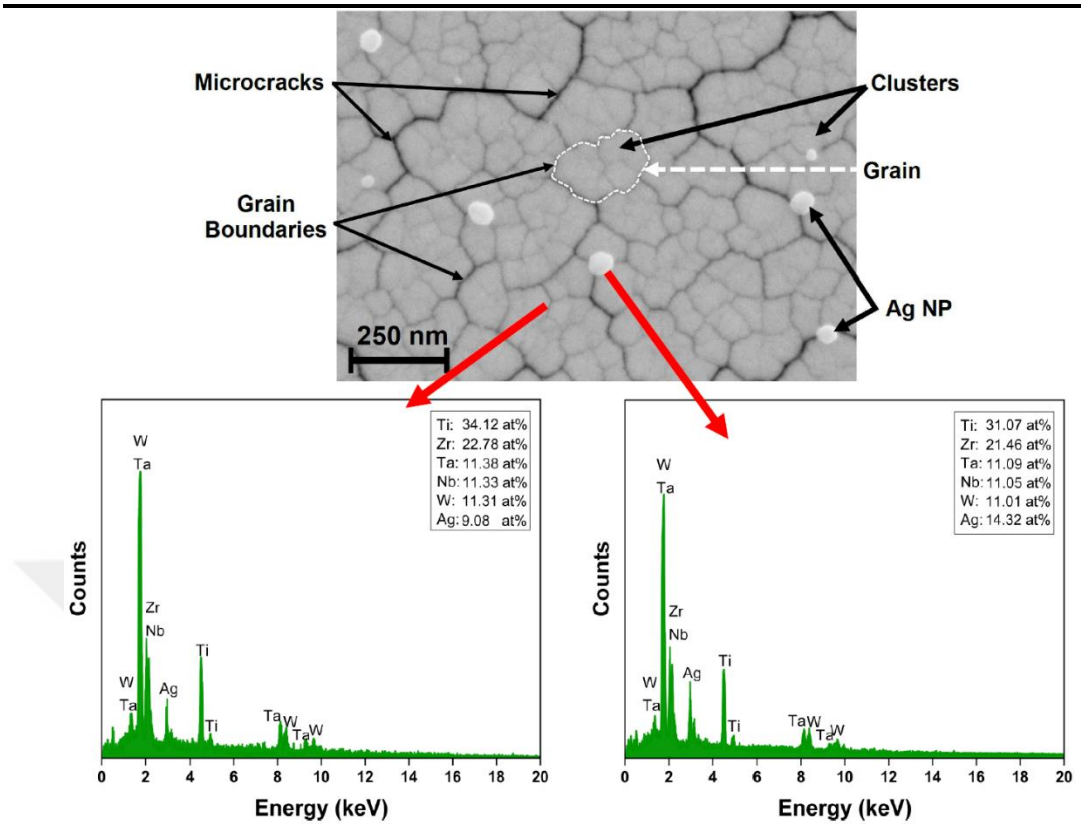

Figure 5. 4. High magnification FESEM micrographs and EDS characterizations obtained from the surface of Ag-doped RHEA films deposited on the silicon wafer.

The chemical state and composition of the constituent elements of the undoped and Ag-doped RHEA films were investigated in different depths. The etching process was done by ion bombardment (4 keV Ar^{+}) in 10 cycles for 400 sec during each cycle. The XPS spectra acquired from the outermost surface and the depth of 500 nm of the RHRA and RHEA-9Ag NPs specimens are given in Figure 5. 5 and Figure 5. 6. As it is evident from these figures, due to surface oxidation in the open environment, the XPS data collected from the surface of examined specimens revealed that the constituent elements of films are presented as their oxides and/or sub-oxides form. According to the obtained XPS spectrum given in Figure 5. 5 for RHEA specimen, available Ti peaks are related to TiO_2 oxide at 458.2eV and 464.0 eV. In Zr XPS spectra, while peaks at 182.1 and 184.4 belong to ZrO_2, the observed peaks at 178.8 eV and 181.1 eV are indicative of Zr sub-oxide. The sub-oxide formation was also observed in the XPS spectra of Ta, Nb, and W. In the case of Ta, peaks at 27.4 eV and 25.7 eV are associated to Ta_2O_5, and peaks at 22.2 eV and 24.0 eV are related to the formation of its sub-oxide. In the XPS spectrum of Nb, peaks at 206.7 eV and 209.5 eV belong to Nb_2O_5, and peaks at 202.2 eV and 204.2 eV are related to the formation of its sub-oxide. At XPS spectra of W, peaks at 34.9 eV and

37.1 eV are corresponding to WO_3, and peaks at 30.7 eV and 32.4 eV are correlated to the sub-oxide form of W. Owing to their high affinity to react with oxygen, the appearance of refractory metal oxide peaks is a common occurrence. For the outermost surface of the RHEA-9Ag NPs specimen, in addition to the oxides and sub-oxides of constituent elements revealed in the RHEA specimen, the detected Ag peaks confirm its presence and embedding in the structure of the deposited films. According to its spectra, while peaks at 374.1 eV and 368.1 eV represent metallic Ag, the peaks at 373.3 eV and 367.3 eV are matching to its oxide state (Ag_2O). It is worthwhile to mention that the shoulder identified at the binding energy of 365.5 eV is fitted to Nb $3P_{3/2}$, which exists as a Nb_2O_5.

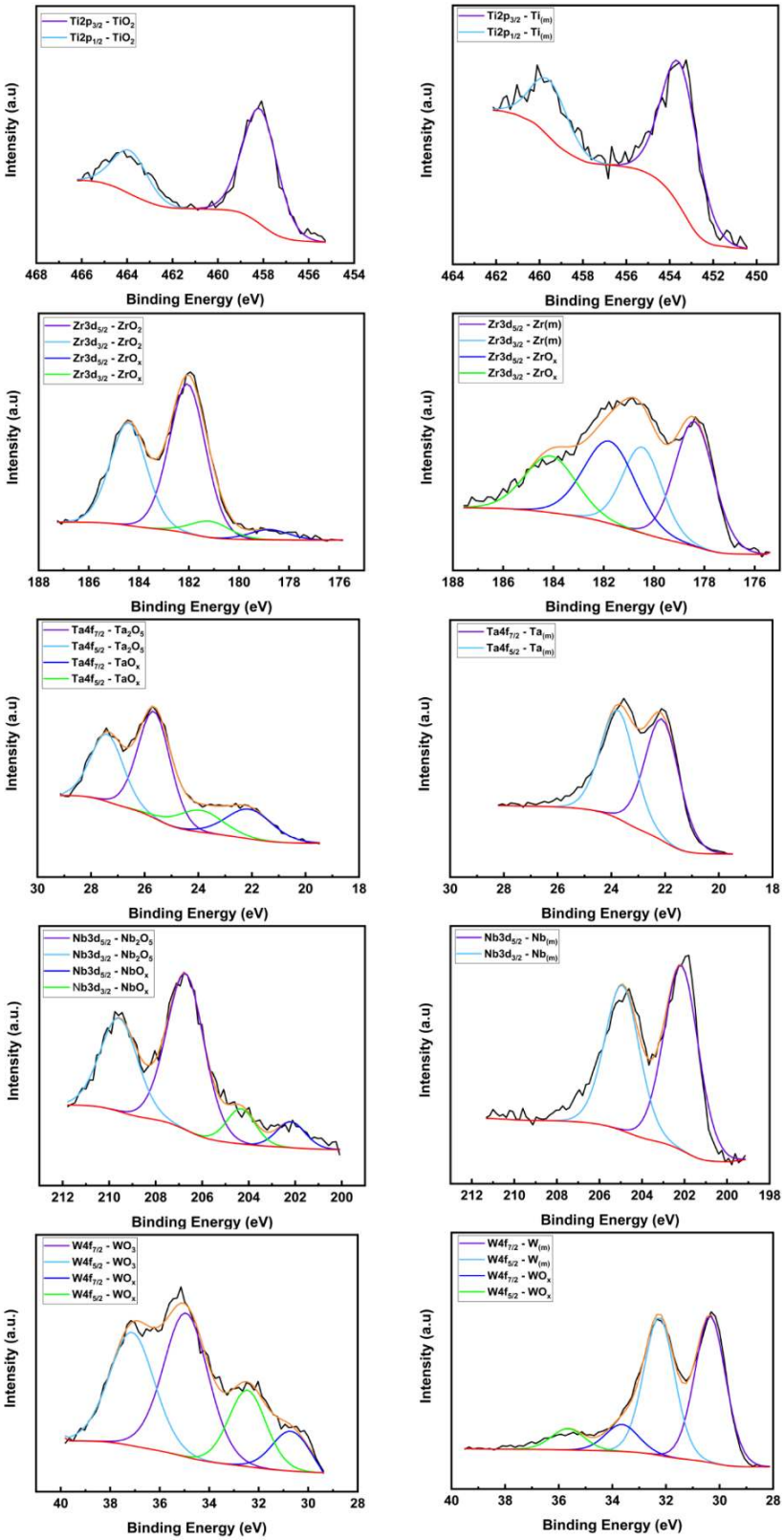

Figure 5. 5. The obtained XPS spectra for left: the RHEA film before etching and right: the RHEA film after etching.

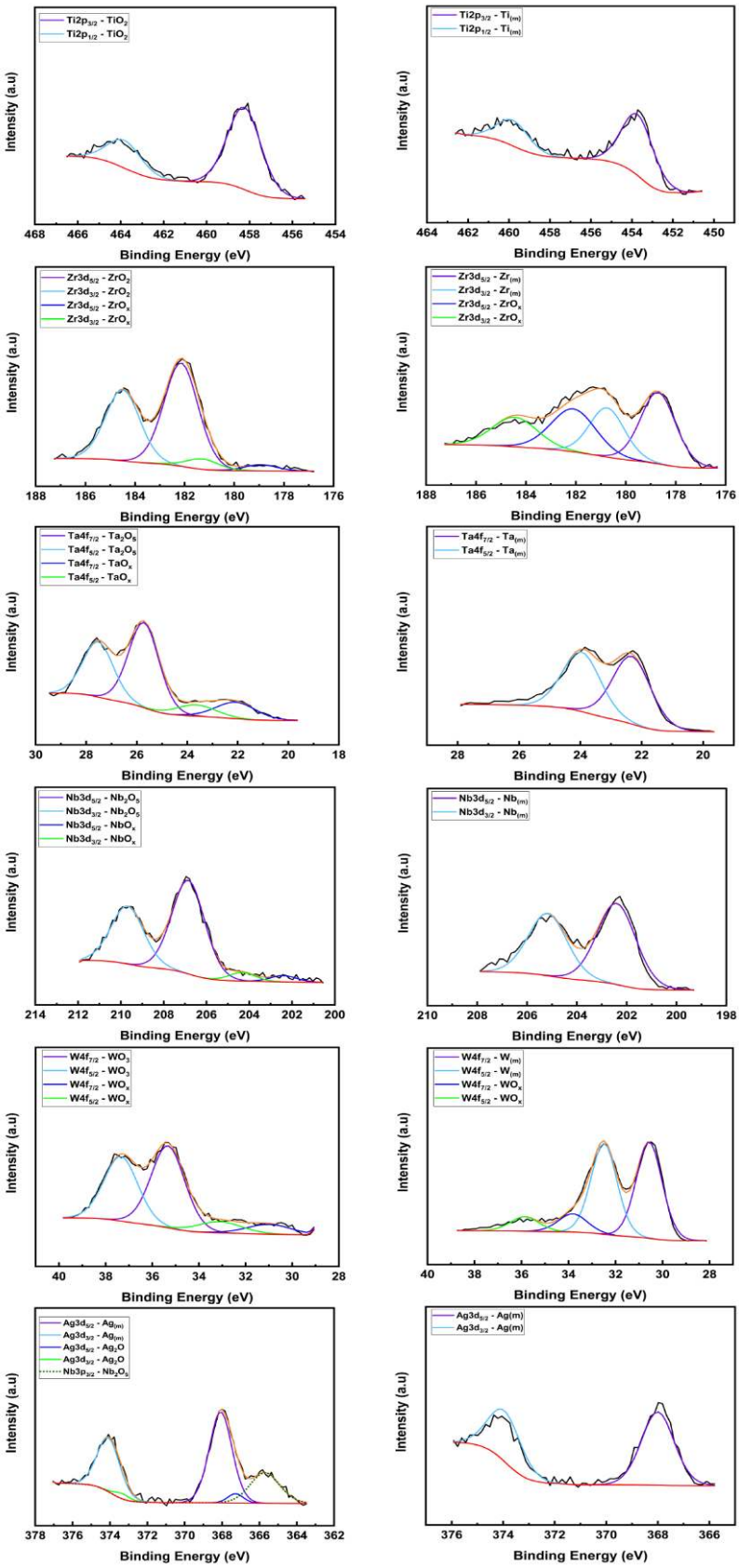

Figure 5. 6. The obtained XPS spectra for left: the RHEA-9Ag NPs film before etching and right: the RHEA-9Ag NPs film after etching.

Further XPS studies followed by etching the examined specimens revealed that the constituent elements are present in metallic form at all etching depths, and almost identical spectra and chemical composition were obtained. As it is obvious from Figure 5. 5 and Figure 5. 6, in RHEA and RHEA-9Ag NPs specimens and at the etched depth of 500 nm, peaks at 453.7 eV and 469.7 eV are related to metallic Ti. In addition, only metallic forms of Ta (22.5 eV and 24.1 eV) and Nb (202.1 eV and 204.9 eV) for both undoped and Ag-doped specimens, as well as metallic Ag (367.9 eV and 374.1 eV) for Ag-doped film were found in XPS spectra. It is noticeable that in the case of Zr and W, besides their dominant metallic peaks, signals of ZrO_x and WO_x were detected in their spectra. Despite employing high purity Ar and lowering the pressure in the PVD chamber to the appropriate value, the strong oxygen affinity of Zr and W resulted in the evolution of a minor amount of their sub-oxide throughout the deposited films [184,250].

To confirm the distribution of elements across the whole film thickness, XPS depth profiling was conducted on RHEA and RHEA-9Ag NPs specimens, and the results are given in Figure 5. 7. Fairly large amounts of oxygen atoms were detected on the outermost surface of the deposited films and significantly decreased after etching. While the amount of oxygen was reported higher than 50 at% at the outermost surfaces, after etching along the film thickness, its content abruptly decreased to less than 3 at%. A higher amount of oxygen at the surface resulted from the atmospheric oxidation of the constituent elements. Also, depth profiling analysis revealed a relatively uniform distribution of the Ti, Zr, Ta, Nb, and W elements in different etching depths. In addition, the depth profile survey confirmed the presence of Ag nanoparticles in the intended compositional amount (9 at%.) at all studied depths.

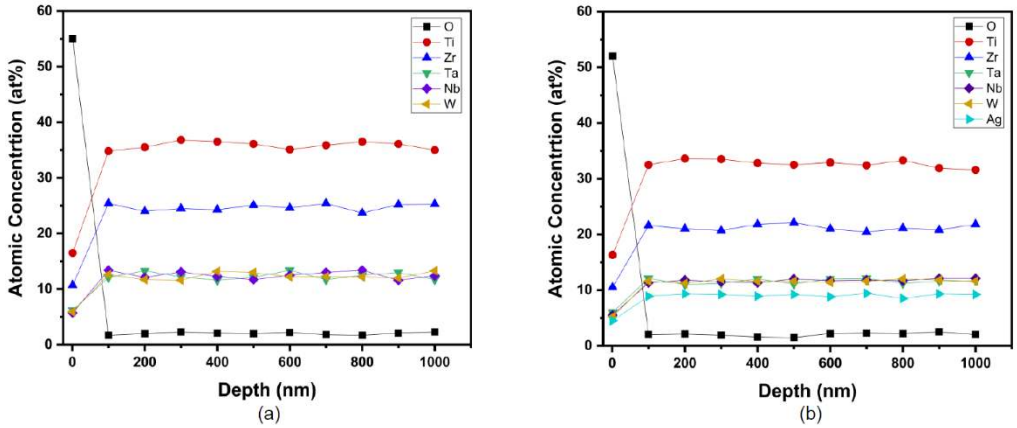

Figure 5. 7. XPS depth concentration profiles of RHEA and RHEA-9Ag NPs specimens.

The surface topography and phase images of the uncoated substrate, undoped and Ag-doped RHEAs coated specimens were observed by AFM, which was operated in the tapping mode over the area of the 5 μm × 5 μm and depicted in Figure 5. 8. Ti6Al4V substrate's surface contains scratch marks that are created during the mechanical polishing process. Also, cauliflower-like and homogenous structures are observed for RHEA and RHEA-9Ag NPs specimens. Average roughness (R_a) values for Ti6Al4V, RHEA, and RHEA-9Ag NPs specimens were reported 2.51±0.18 nm, 4.66±0.50 nm, and 5.71±0.50 nm, respectively. Through the deposition of the RHEA layer and the subsequent formation of cauliflower-like structures, the roughness of the substrate is slightly increased. Also, due to the formation and development of Ag nanoparticles, the roughness values of the Ag-doped specimen slightly increased compared with the undoped one. In phase imaging, contrast is caused by the local alterations of tip energy which are dissipated during the tip fluctuation over the sample's surface [251,252]. With this in mind, any second phase was not detected for Ti6Al4V and RHEA specimens. Furthermore, uniformly distributed spherical particles on the images of RHEA-9Ag NP specimen are related to the existence of Ag nanoparticles which are clearly detected by a variation of the phase.

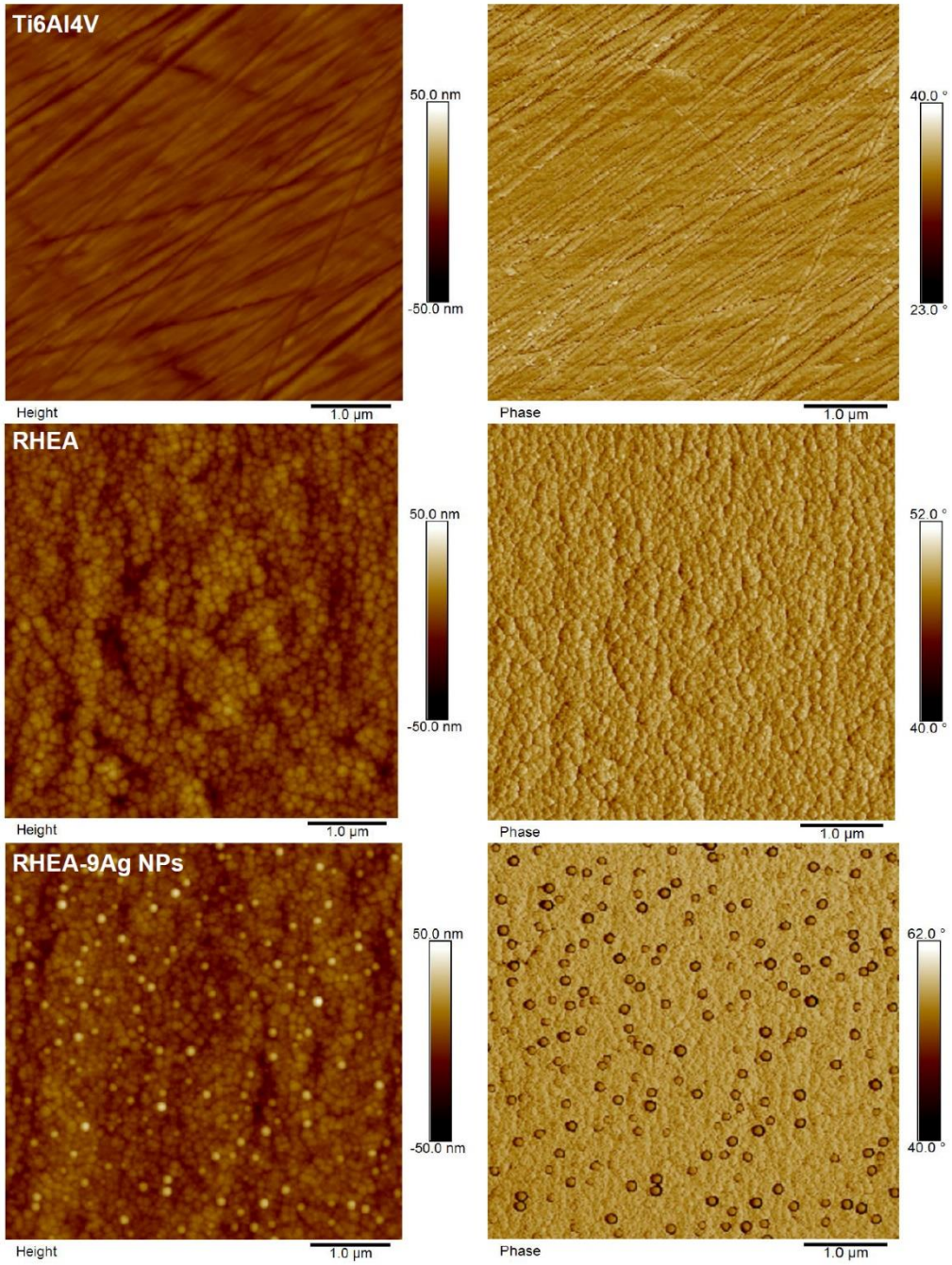

Figure 5. 8. Left: Topography and right: phase AFM images of the examined specimen.

The surface wettability of specimens was evaluated through the sessile drop method and a syringe containing PBS in which the liquid is dropped on their surface; after that, the image of PBS droplet showing the solid-liquid-air interfaces was captured, and its contact angle (CA) was recorded. Liquid droplet tends to preserve its spherical form on a hydrophobic surface rather than spreading over the surface in order to minimize its surface area. On the contrary, on a surface with high solid and liquid attraction, the droplet is spread open over the surface owing to low interfacial tension [195]. Figure 5. 9 depicts

states of PBS droplets on the specimens as well as their CAs. As seen from Figure 5. 9, RHEA coated specimen demonstrates a smaller CA when compared to the uncoated Ti6Al4V specimen, and RHEA-9Ag NPs specimen show larger contact angle compared to undoped RHEA film. The contact angle increased by embedding Ag nanoparticles in the structure. Accumulation of Ag atoms and the creation of the semi-spherical nanoparticles resulted in an increase in hydrophobicity and contact angle in comparison with undoped specimens [253]. It is well known in the literature that surface roughness and morphology have an important effect on surface wettability, where increasing the superficial roughness can lead to a decrease in the wettability and consequently rising CA value [254]. As demonstrated in Figure 5. 8, the roughness of the Ag-doped specimen was increased due to the presence of Ag nanoparticles on the surface, which is in good agreement with the increment CA of RHEA- 9Ag NPs to 63.10°. It is worth mentioning that surface wettability plays a crucial role in implant-bone interaction of orthopedic implants such as artificial hip joints, knee join, and bone plates by promoting the growth of bone-forming cells. It has been demonstrated that the favorable CAs values for the bone regeneration process are typically in the range of 35°–80° [196].

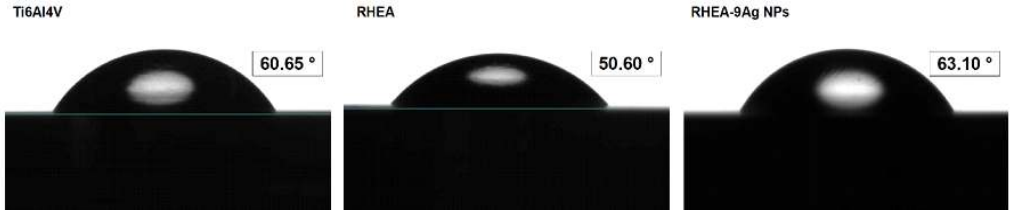

Figure 5. 9. Photographs of a PBS drops and their contact angles measured on the surface of Ti6Al4V, RHEA, and RHEA-9 Ag NPs.

5.3.2 Mechanical Properties

Mechanical properties of Ti6Al4V, RHEA, and RHEA-9Ag NPs specimens in terms of elastic modulus (E) and hardness (H) were successfully measured by nanoindentation tester according to the loading-unloading plots (Figure 5. 10 (a)) and utilizing the Oliver-Pharr method. As it is presented in Figure 5. 10 (b, c, d), the obtained results indicate that H values of Ti6Al4V, RHEA, and RHEA-9Ag NPs specimens are about 4.9±0.11 GPa, 18±0.19 GPa, and 16±0.14 GPa, respectively. Also, average E values of specimens are reported as 150±2.25 GPa, 210±1.53 GPa, and 200±1.37 GPa for Ti6Al4V, RHEA, and RHEA-9Ag, respectively. The results showed that in comparison to the Ti6Al4V, coated specimens manifested remarkable enhancements in H and E values. Generally, superior

improvement in H values of RHEAs films originates from the dense amorphous structure of RHEAs films [167]. This dense structure impedes shear band motion due to slip toward different grain orientations [184,255]. However, nanoindentation measurements exhibited that the RHEA-9Ag NPs specimen has a lower value of H and E compared with the RHEA specimen. Since Ag nanoparticles are known as soft metallic substance, their incorporation in the structure of the deposited films can result in a decrease in the mechanical properties [256].

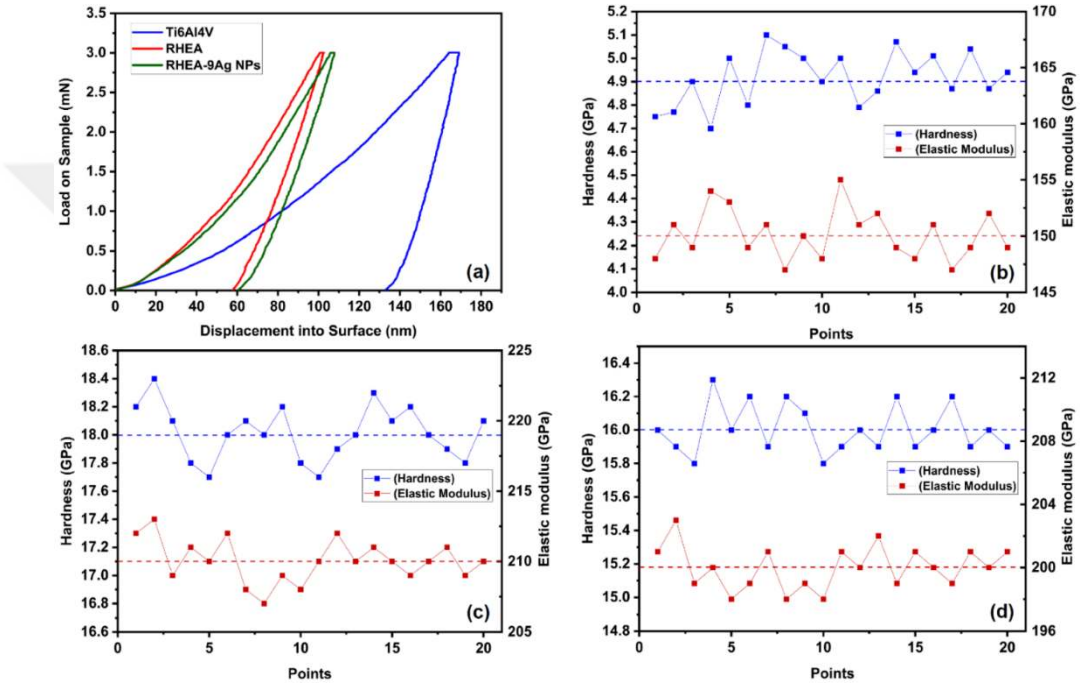

Figure 5. 10. Results of the nanoindentation measurements: a) load-unloading curves and H and E values of (b) Ti6Al4V, (c) RHAE film, and (d) RHEA-9Ag NPs film.

5.3.3 Electrochemica Measurements

Biocorrosion Behavior

The potentiodynamic polarization curves of Ti6Al4V, RHEA, and RHEA-9Ag NPs specimens are illustrated in Figure 5. 11 All electrochemical tests were done at 1 mV/s scan rate by immersion of specimens in the PBS solution at 37±1 °C in order to simulate the human body condition. The listed parameters in Table 5. 3 are calculated by using the data from the illustrated curves in Figure 5. 11. Icorr and Ecorr, represent the corrosion current density and corrosion potential, respectively. Icorr was obtained by extrapolating the linear region of Tafel plots in the vicinity of Ecorr. From the performed tests and

obtained parameters, the corrosion behavior of all specimens could be estimated in the biological environment.

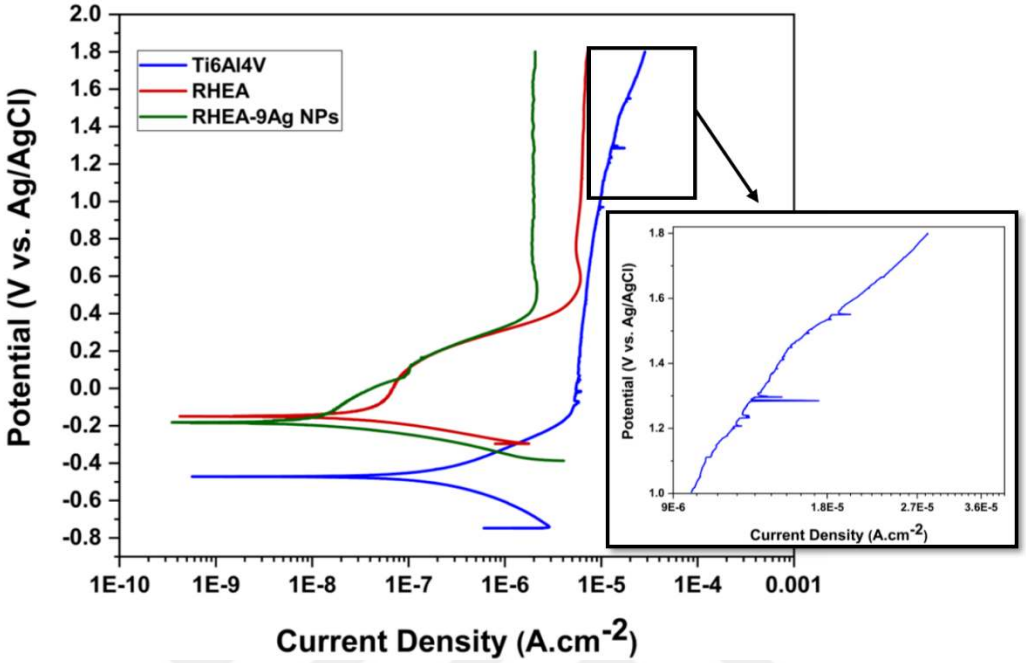

Figure 5. 11. Potentiodynamic curves of Ti6Al4V, RHEA and RHEA-9Ag NPs specimens obtained at 37±1 °C in PBS solution.

As seen from Figure 5. 11, even though current fluctuations appear in Ti6Al4V specimen at potentials values higher than 1.4 V, the RHEA and RHEA-9Ag NPs specimens demonstrated a continuous passive plateau without any pitting effects. These fluctuations in Ti6Al4V examined specimen denote a supreme resistance against surface pitting, as they called the metastable pitting. Furthermore, from Table 5. 3. Corrosion-related parameters obtained and calculated for Ti6Al4V, RHEA, and RHEA-9Ag NPs specimens from potentiodynamic tests at 37±1 °C in PBS electrolyte., the Icorr values of RHEA and RHEA-9Ag NPs coated specimens are lower than the uncoated Ti6Al4V substrate. The polarization resistance (R_p) of examined specimens (listed in Table 5. 3) are obtained by using the well-known Stern-Geary equation:

$$I_{corr} = (\beta_A.\beta_C)/(R_p 2.303(\beta_A + \beta_C)) \qquad \text{(Eq. 1)}$$

While β_A and β_C are calculated using the slopes of the Tafel branches and called cathodic and anodic slopes, respectively. As can be seen in Table 5. 3, the polarization resistance of coated specimens is higher than uncoated substrate owing to the excellent adhesion strength between undoped and Ag-doped RHEA films and the Ti6Al4V substrate [184].

The corrosion rate, also known as the rate of mass loss or the penetration rate of the corrosive solution into the coating, is obtained by using the corrosion current density and the following equation according to the ASTM G 102 [206]:

$$CR = \frac{K.Icorr.EW}{\rho} \qquad \text{(Eq. 2)}$$

Whereas CR is considered as the corrosion rate (mm/year); I_{corr} is the corrosion current density ($\mu A/cm^2$); ρ is the density of coating (g/cm^3); K is the constant for converting units (3.27×10^{-3} mm.g/ μA.cm.year); and finally, EW is the equivalent weight. It should be noted that the value of EW is calculated for coating based on the ASTM G 102 (1999) standard. By comparing the corrosion rate of the deposited specimens with that of the uncoated Ti6Al4V alloy (Table 5. 3), it is revealed that both RHEA and RHEA-9Ag NPs specimens possess lower CR values, and as a consequence, they demonstrate higher corrosion resistance. As it is obvious from Table 5. 3, the CR values of coated specimens are 2.3 to 2.8 orders of magnitude lower than that of the uncoated Ti6Al4V substrate.

The resistance against the corrosion phenomenon of the thin films prepared through the PVD technique mainly depends on the existence of discussed defects like microcracks, pinholes, and pores which occur while or after the sputtering process and can help the initiation of the pitting corrosion. Such pits occur where the passive film contains discontinuity in which the breakdown process takes place easily when it is exposed to an aggressive environment. Thereby, the evaluation of the porosity and pits are required to fully understand the corrosion mechanism of the specimens. The most common method in determining the total porosity of a corroded sample is Elsener's empirical equation [206,257]:

$$P = \left(\frac{Rps}{Rp}\right) \times 10^{-\frac{\Delta Ei-0}{\beta a}} \qquad \text{(Eq. 3)}$$

Where R_p and R_{ps} are regarded as the polarization resistance of the coated specimens and uncoated substrate, respectively, ΔE_{i-0} is the difference in E_{corr} values of the substrate and coated specimens, and βa is only the measured anodic Tafel slope obtained for the uncoated substrate. Accordingly, the calculated results are also listed in Table 5. 3.

For the RHEA-9Ag NPs specimen, the P value, denoting porosity, is lower than that for RHEA. The P value decreased with embedding Ag nanoparticles which indicates that the formation of a dense microstructure effectively enhanced the resistance of the surface against the corrosive media.

In addition, the deposited coatings' protective efficiency (P_e), which is another important factor in determining the corrosion behavior of the films, are calculated using Eq. (4):

$$P_e = (1 - \frac{icorr.\ coating}{icorr.\ substrate}).100 \quad \text{(Eq. 4)}$$

Where $i_{corr.\ substrate}$ and $i_{corr.\ coating}$ values are the corrosion current densities of the uncoated substrate and coated specimens, respectively [206,258]. Simply comparing the calculated P_e values point out that Ag-doped film has the highest protective efficiency. This fact confirms the results of the porosity (P) calculation; hence, the film with the lower porosity after the corrosion test (0.077) possesses higher protective efficiency (55.6%). All results reveal the fact that Ag nanoparticles are respectable corrosion inhibitors, and their presence can slightly affect the corrosion parameters [259].

Table 5. 3. Corrosion-related parameters obtained and calculated for Ti6Al4V, RHEA, and RHEA-9Ag NPs specimens from potentiodynamic tests at 37±1 °C in PBS electrolyte.

	E_{corr} (mV)	I_{corr} ($\mu A/cm^2$)	β_a (mV)	β_c (mV)	CR ($\times 10^{-3}$mm/year)	P	P_e (%)	R_p (Ωcm^2)
Ti6Al4V	-461.99	0.16	342.7	117.4	1.41	---	---	237E03
RHEA	-160.12	0.089	329.5	77.6	0.60	0.101	44.3	306E03
RHEA-9Ag NPs	-190.09	0.071	283.1	112.3	0.50	0.077	55.6	492E03

FESEM micrographs of the corroded uncoated and coated specimens are depicted in Figure 5. 12. These pictures are provided after the corrosion tests to evaluate the corrosion behavior and pit formation on the films' surface. While only a limited number of pitting cavities can be detected on the uncoated Ti6Al4V specimen's surface, it can be clearly seen from Figure 5. 12 (b, c) that there is no pit on the surface of RHEA and RHEA-9Ag NPs specimens. In these specimens, the chemical attack that results in metal deterioration did not occur because of the high adhesion strength of the deposited films to the substrate [184]. This is also in good agreement with the P value in Table 5. 3, which demonstrates that the possibility of the pit formation is very low or negligible.

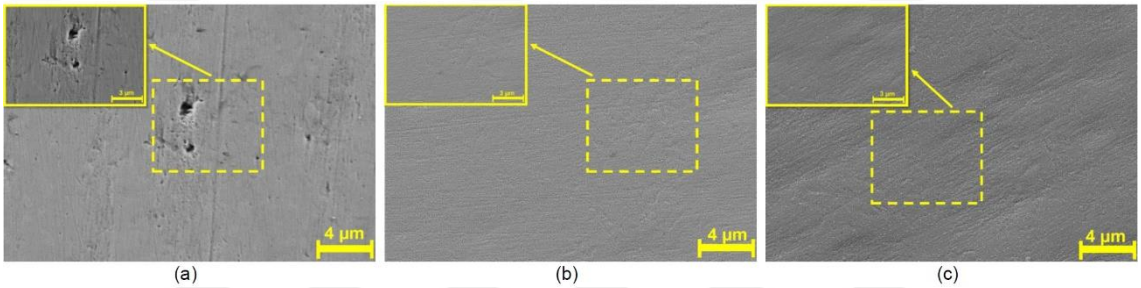

Figure 5. 12. FESEM images of (a) Ti6Al4V, (b) RHEA, and (c) RHEA-9Ag NPs specimens after subjecting to the corrosion test in PBS electrolyte at 37±1 °C.

Electrochenical Impedance Spectroscopy (EIS)

More detailed analyses on the corrosion resistance of Ti6Al4V, RHEA, and RHEA-9Ag NPs specimens are done by using EIS tests within the frequency range of 100 kHz to 10 mHz in PBS solution. The EIS results are depicted in different plots of Bode, Bode-phase, and Nyquist as shown in Figure 5. 13. According to these results, the value of impedance at the lowest frequency is indicative of specimens' total resistance. In general, a large diameter in the Nyquist semicircle and broad peak of the Bode-phase curves as well as a high |Z| value in the Bode plots, denote a better corrosion resistance of the specimens.

The proposed electrical equivalent circuit in Figure 5. 14 consists of only one time constant, which is based on the one slope-Bode plots and Bode-phase curves with single peaks. Such circuits have also been used by other reports [260,261]. This circuit is comprised of a constant phase element (CPE), a solution resistance (R_S), and a polarization resistance (R_P). In order to achieve a more accurate fitting, presence of surface roughness, and capacitive/resistive behavior of the simulated element, the CPE is

considered instead of a pure capacitor [262]. Additionally, the deviation from the perfect peak in the Bode-phase curves of the tested specimens (which usually occurs at 90 ° and is an indicator of pure capacitor) proves the need for using a CPE in the circuit. The impedance of CPE is defined as:

$$ZCPE= \frac{1}{(j\omega)^{n}Y0} \qquad \text{(Eq. 5)}$$

While ω is the angular frequency, Y0 denotes the general admittance function, and also the parameter n shows the phase shift with the values of 0 to 1 [263]. If n becomes equal to 1, the constant phase element behaves like a pure capacitor, and if n = 0, this element becomes a pure resistor [264]. Considering the discussed parameters, the calculation of double-layer capacitance (C_{dl}) is obtained from the presented equation:

$$C_{dl}=Y_0^{1-n} \times R_p^{(1-n)/n} \qquad \text{(Eq. 6)}$$

Moreover, the total electrochemical impedance with respect to the proposed electrical equivalent circuit of the specimens is defined by:

$$Z= Rs + Rp/(1+(j\omega Y_0)^{n}) \qquad \text{(Eq. 7)}$$

According to the aforementioned details, the values of parameters in the equivalent circuit are presented in Table 5. 4 by utilizing the ZMan software package with an average error of less than 6%. The presented EIS test results are in good agreement with the polarization test findings.

The Ag-doped specimen has higher polarization resistance in comparison to undoped and uncoated specimens. Table 5. 4 explicitly proves that the RHEA-9Ag NPs specimen has a much higher Rp of 4.93E5 $\Omega.cm^2$ compared to Ti6Al4V, RHEA, which is in good agreement with the achieved result of Rp from the polarization curve. This finding indicates the corrosion behavior's enhancement through the deposition of RHEA and doping the Ag nanoparticles.

The reported n in Table 5. 4 can also show the level of depression in the Nyquist plot semicircles, surface roughness and defects, and CPE deviation from a pure capacitor. For Ti6Al4V, RHEA, and RHEA-9Ag NPs specimens, n changes slightly after film deposition and embedding silver nano-particles, which is in good agreement with roughness changing. Considering this change, the Ti6Al4V specimen is highly prone to the attack of corrosive agents, which resulted in slight pitting traces. By considering similarities of roughness and n parameter in both Ag-doped and undoped specimens, lower Cdl of the RHEA-9Ag NPs represents the reduction of the active area, which

confirms the proper shielding effect of the deposited films. Furthermore, the ICP-MS analysis was conducted on the PBS solutions after the corrosion tests for identifying the amount of released Ag ions from the surface of the RHEA-9Ag NPs specimen. The results demonstrated that there was no release of Ag ions in the PBS solution, which is in good agreement with the obtained results of the biocorrosion tests (Table 5. 3). This condition is necessary for the biocompatibility of the medical implants since the uncontrolled release of the Ag could decrease the cell viability of surrounding tissues [233].

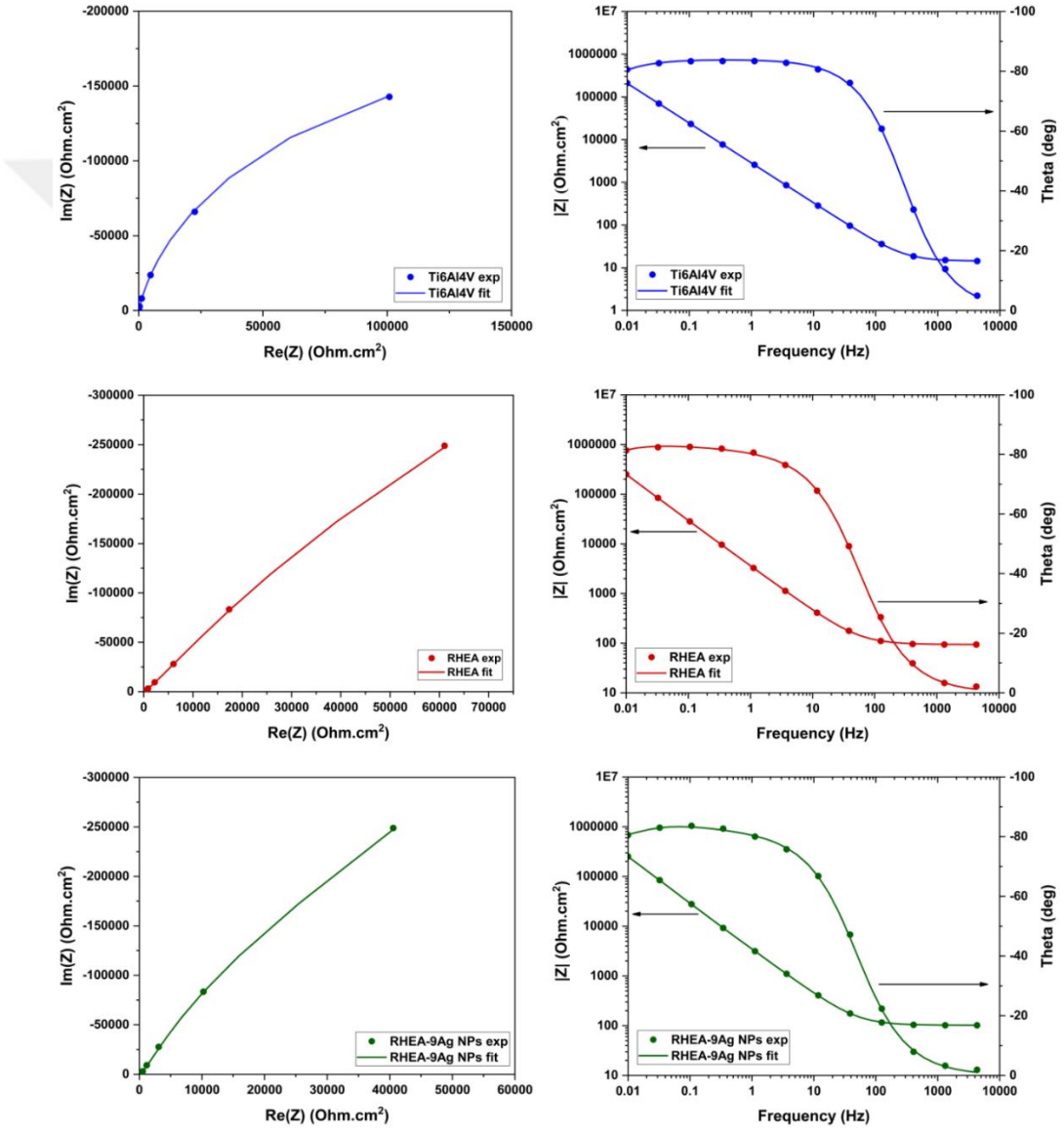

Figure 5. 13. Nyquist and Bode Phase plots of Ti6Al4V, RHEA and RHEA-9Ag NPs specimens at open circuit potential with 10 mV as the amplitude of sinusoidal potential running from 100 kHz to 10 mHz at 37±1 °C in the PBS solution.

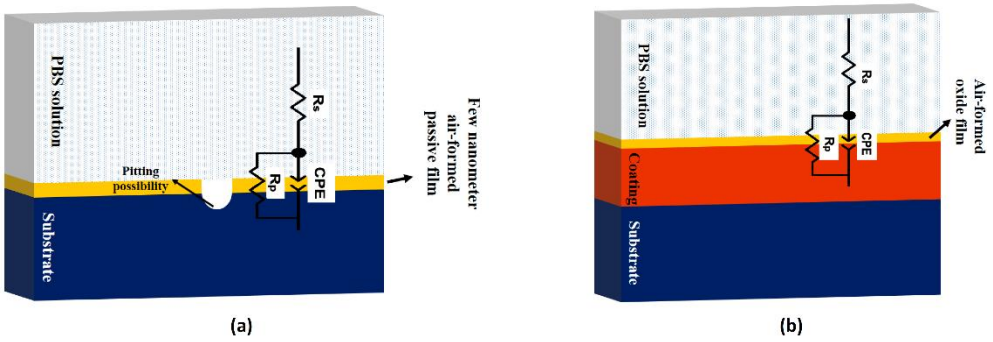

Figure 5. 14. Equivalent electrical circuit for (a) Ti6Al4V (b) RHEA and RHEA-9Ag specimens tested at 37±1 °C in the PBS solution.

Table 5. 4. Equivalent circuit elements values of Ti6Al4V, RHEA and RHEA-9Ag specimens for EIS

	Rs (Ωcm^2)	CPE ($\mu\Omega^{-1}S^n cm^{-2}$)	n	R_P (Ωcm^2)	C_{dl} ($\mu F.cm^{-2}$)
Ti6Al4V	19.33	3.25E-4	0.89	2.38E5	1.91
RHEA	19.79	3.9E-4	0.91	3.07E5	1.72
RHEA-9Ag NPs	20.91	2.52E-4	0.92	4.93E5	1.61

5.4 Conslusion

In this research, the microstructure, mechanical properties, and electrochemical behavior of Ti6Al4Vsubstrate, undoped and Ag-doped non-equimolar $Ti_{1.5}ZrTa_{0.5}Nb_{0.5}W_{0.5}$ RHEA films deposited on Ti6Al4V substrate by RF magnetron sputtering were investigated. Overall, the microstructural findings, outstanding mechanical properties, and biocorrosion behavior of examined specimens revealed that Ag nanoparticles could be successfully doped in the structure of the RHEA films and might satisfy the requirements for biomedical applications. The outcomes achieved in this study can be stated in particular as follows:

The amorphous undoped and Ag-doped RHEA film with cauliflower-like morphology were deposited on the substrates. The constituent elements, including Ti, Zr, Ta, Nb, and W as well as Ag dopant in the form of semi-spherical nanoparticles, were uniformly distributed in the structure of the developed films.

According to the nanoindentation test results, coated specimens exhibited a significant improvement in surface mechanical properties in terms of H and E. While the H and E values of coated specimens were reported between 16±0.14 GPa to 18±0.19 GPa and 200±1.37 GPa to 210±1.53 GPa, respectively, the H and E values of the uncoated Ti6Al4V substrate were measured 4.9±0.11 GPa and 150±2.25 GPa, respectively. The dense amorphous structure of RHEAs films contributes to enhancement in mechanical characteristics.

The roughness and contact angle values of the coated specimens increased with the addition of Ag nanoparticles. In comparison to an undoped specimen, the accumulation of Ag nanoparticles and the development of semi-spherical Ag nanoparticles resulted in an increase in roughness and subsequently contact angle.

The biocorrosion tests revealed that while the current fluctuation occurs in Ti6Al4V substrate at higher potentials, a constant passive plateau without pitting effect was noted in the RHEA and RHEA-9Ag NP specimens. This result is in good agreement with the obtained Icorr and calculated CR, and Rp values which demonstrate improvement in the electrochemical behavior of coated specimens. RHEA-9Ag NPs with CR value of 0.50×10^{-3} mm/year and Pe value of 55.6% exhibited the positive effect of embedding Ag nanoparticles on the biocorrosion behavior of RHEA film.

The EIS results revealed that the lowest Cdl value (1.61 $\mu F.cm^{-2}$) and the highest Rp value (4.93E5 $\Omega.cm^2$) were achieved in the RHEA-9Ag NPs specimen. These results confirm the anti-corrosive behavior of Ag nanoparticles and the protective feature of the deposited film.

CHAPTER 6

IN VITRO ANTIBACTERIAL AND CYTOTOXICITY ASSESSMENT OF MAGNETRON SPUTTERED $Ti_{1.5}ZrTa_{0.5}Nb_{0.5}W_{0.5}$ REFRACTORY HIGH-ENTROPY ALLOY DOPED WITH Ag NANOPARTICLES

The majority of this chapter has been published in *Vacuum 203 (2022) 111286*. The original manuscript has been rearranged to conform to the format requirements of the dissertation.

6.1 Introduction

Patients receiving orthopedic implants could experience serious life-threatening complications from implant-related infections after surgery [231,236]. Mainly these infections are caused by hospital environments and healthcare facilities rather than by the patient's health situation at the time of admission [227,265]. Hospital-acquired infection is responsible for 40-70 % of prosthetic implant infections, which is the primary cause of implant failure [266]. Infection rates in whole hip joint replacement range from 0.5 to 3.0 %, while external fixation infection rates range from 2 to 30 % [227]. Previous studies suggest that the number of patients who suffer from hospital-acquired infections increases as the number of implantations grows annually [231,266]. Treatment of such infections is not only expensive from both a societal and financial perspective but also leads to the emergence of drug-resistant bacteria, increasing mortality and morbidity [226,231]. As a result, the development of implants having inherent antibacterial properties on their surfaces for preventing implant-related infections attracted particular attention [233]. Using implants with good antibacterial capability will diminish infection rates during surgery and allow the implant to perform a bactericidal role in the human body, which will reduce the chances of postoperative infections [267]. Thus, the development of surface coatings containing antibacterial agents has been considered as an excellent alternative to control and prevent bacteria growth on the surface of the implants [232]. Due to its broad range of antibacterial activity against both Gram-negative and Gram-positive bacteria, silver nanoparticles (Ag NPs) are regarded as a potential biocide for use in the biomedical industries [232,233,268]. The precise bactericidal mechanism (s) of Ag NPs is still unknown; however, free metal ion toxicity resulting from the dissolution of Ag^+ from the NPs' surface could be a possibility [246,267,269]. Therefore, the concentration of antimicrobial agents released from or immobilized on the implant's surface should be controlled since high levels of the antibacterial agents may result in local toxicity in surrounding tissues [236,267,270,271]. Even though implant coatings releasing antibacterial agents may be beneficial, their drawbacks, such as the limited and uncontrolled release of the antibacterial agents, encouraged researchers to develop stable and durable antibacterial coatings lasting over the lifetime of an implant [233,272].

Our previous work [193] indicates excellent mechanical properties and resistance to biocorrosion of non-equimolar $Ti_{1.5}ZrTa_{0.5}Nb_{0.5}W_{0.5}$ RHEAs, particularly the possibility of controllable and homogeneous doping of Ag nanoparticles in its structure. In this study,

we assessed the antibacterial property and biocompatibility of RHEA film doped with 9 at% Ag NPs. The antibacterial property was tested on P. Aeruginosa and S.Aureus, which are common bacteria found in contaminated surfaces and the hospitals' environment [230,237]. Such contaminations may lead to infection incidences of the implants and severe health problems in patients. Biocompatibility of the Ag NP doped RHEA film was confirmed using C2C12 mouse muscle myoblast cells.

6.2 Materials and Methods

6.2.1 Thin Film Deposition Process

The 1-1.1 µm thick films of undoped and Ag nanoparticles doped $Ti_{1.5}ZrTa_{0.5}Nb_{0.5}W_{0.5}$ RHEA films were deposited on the Si (100) wafers and Ti6Al4V substrates utilizing the radio frequency (RF) magnetron sputtering technique. By electro-discharge machining (EDM), round-shaped Ti6Al4V substrates with a diameter of 10 mm and a thickness of 1 mm were cut from a rod followed by grinding and polishing processes to get a mirror-like finished surface. Before the deposition process, the prepared specimens were sonicated successively in acetone and ethanol and then washed with deionized water. $Ti_{1.5}ZrTa_{0.5}Nb_{0.5}W_{0.5}$ RHEA target was prepared in an arc-melting furnace under the argon atmosphere and then subjected to remelting and flipping to ensure chemical homogeneity. The chemical composition of the prepared target, deposition parameters, and the method of doping desired amount of the Ag nanoparticles (9 at%) have been described in Ref. [193]. The undoped and Ag nanoparticles doped RHEA films deposited specimens were named RHEA and RHEA-9Ag NPs, respectively.

6.2.2 Microstructural Characteisation

Using a field emission scanning electron microscope (FESEM, Zeiss, Ultra Plus) equipped with an energy dispersive X-ray spectrometer (EDS), the surface morphology of the coated specimens and the chemical composition of the deposited films were analyzed. The phase and the distribution of the constituent elements in the deposited films were studied by a high-resolution transmission electron microscope (HRTEM, Hitachi, HF5000). For this purpose, specimens were prepared using a focused ion beam and electron beam system (FIB, Hitachi, NX5000 ETHOS).

Surface free energy (SFE) of the uncoated and coated specimens were analyzed with the sessile drop technique (Attension Theta Optical Tensiometer, Biolin Scientific), and measurements were repeated at least three times for each specimen to ensure accuracy. The dispersive component of the SFE analyses was diiodomethane, and the polar components were formamide and DI water. The Owens-Wendt (OW) theoretical method was applied to the recorded contact angles as following equation [273]:

$$\gamma_l(1 + cos\,\theta) = 2\sqrt{\gamma_s^d}\gamma_l^d + 2\sqrt{\gamma_s^p}\gamma_l^p \qquad \text{(Eq.1)}$$

Where γ_l represents liquid free energy, γ_s represents solid free energy, d signifies dispersive components, and p signifies polar components [274].

6.2.3 Antibacterial Assessment

The antibacterial efficacy of the examined specimens was evaluated by the bacterial counting method using Gram-negative Pseudomonas Aeruginosa (P.Aeruginosa) ATCC 15442 and gram-positive Staphylococcus Aureus (S.Aureus) ATCC 23235 bacteria. Uncoated Ti6Al4V and undoped RHEA coated specimens were used as a control to assess the effect of doping Ag nanoparticles in the deposited films. Before the tests, all specimens were sterilized under ultraviolet (UV) light for 30 minutes. In this method, 3 mL overnight cultures of bacteria were grown in an appropriate growth medium. P.aeruginosa and S.aureus were grown in tryptic soy broth (TSB) and nutrient broth (NB), respectively, at 37 °C on a shaker incubator (175 rpm) overnight. Pre-sterilized specimens were placed onto the agar plates containing the appropriate growth medium. Overnight bacterial suspensions were diluted 10-6 by their growth medium, and 10 µl portions of diluted bacteria suspension were placed on all control and test specimens in triplicate, followed by adding a thin and sterile glass slide to cover the surfaces. Using glass slides provides close contact of the inoculum and the specimens by spreading it over their entire surface area. 150 µl growth medium solution was plated around the specimens on agar Petri-dish to keep the medium humid, and then plates were placed into the oven at 37 °C for 6 h incubation. Afterward, all covered specimens were dropped into the 1 ml mediums, and solutions were mixed vigorously with vortex for 10 sec. Subsequently, 100 µl of these solutions were spread on the growth plates, then incubated overnight at 37 °C. The

antimicrobial activity of the examined specimens was evaluated by counting survived microorganisms and calculating their reduction compared to their initial concentrations on control surfaces.

6.2.4 Cytocompatibility

For biocompatibility tests, the specimens were sterilized by first washing them with ethanol (3 times) and then using UV light at room temperature for 6 h. Then, adherent C2C12 mouse muscle myoblast cells (50,000 cells/well) were seeded onto the specimens in a 24-well plate and incubated at 37 ℃ under 5% CO2 for 72 h. After removing the medium and washing them with PBS, the cytotoxicity was determined using MTT as described in previous works [275]. Results were analyzed by GraphPad Prism 8 software used with one-way ANOVA with Tukey's comparison test. Statistical significance was expressed as mean ± standard deviation ($p < 0.05$). A live/dead test was conducted to further assess cytotoxicity according to the manufacturer's protocol. Fluorescence micrographs were captured from a fluorescence microscope (Zeiss Axio observer Z1). Cells were also seeded onto specimens as described above to monitor the cells under microscopy. The media was removed after 72 h, and the cells were subsequently rinsed using PBS. In the next step, the cells were fixated with 4% paraformaldehyde for 20 minutes. A nuclear staining dye, DAPI, was added to incubate the cells for a further 15 minutes. Phalloidin was also used to visualize the actin filaments at 2 µg/mL for 15 min at dark. Rewashing the cells three times with PBS were performed to remove unbound dyes. The fixed cell specimens were studied using a confocal microscope (Leica dmi8/SP8) with two different filters for DAPI (λex: 325-375 nm and λem: 435-485 nm) and FITC (λex: 495 nm and λem: 516 nm). ImageJ was used to merge and process the images.

6.3 Results and Discussion

6.3.1 Crystal Structure

Figure 6. 1 (a, b) shows the surface morphology of undoped and Ag nanoparticles doped RHEA films deposited on Ti6Al4V substrate. Expectedly, semi-spherical Ag nanoparticles were evenly dispersed on the surface of the RHEA-9Ag NPs specimen, and both undoped and Ag nanoparticles doped specimens display a cauliflower-like

morphology [184,193]. The deposited films were smooth without any evidence of defects or voids. Figure 6. 1(c, d) shows the cross-sectional bright-field TEM image of the RHEA and RHEA-9Ag NPs film deposited on the silicon wafer. A uniform and fully dense structure film of undoped and Ag-doped RHEA with a thickness of about 1.02 µm have been formed on the substrates. From the higher magnification image of the cross-section of the Ag-doped specimen, inset in Figure 6. 1c, it is apparent that Ag nanoparticles successfully doped in the surface of the deposited film. The average sizes of the semi-spherical shaped nanoparticles dispersed on the surface of the RHEA-9Ag NPs film determined through FESEM micrograph (Figure 6. 1b) and TEM image (Figure 6. 1d) and were found to vary between 40 to 70 nm. The images in Figure 6. 1(e, f) are the selected area electron diffraction (SAED) patterns, which show a region containing a maze-like pattern without any local lattice fringes; in other words, only one diffuse halo and no crystalline spot could be observed, corresponding to an amorphous structure [276].

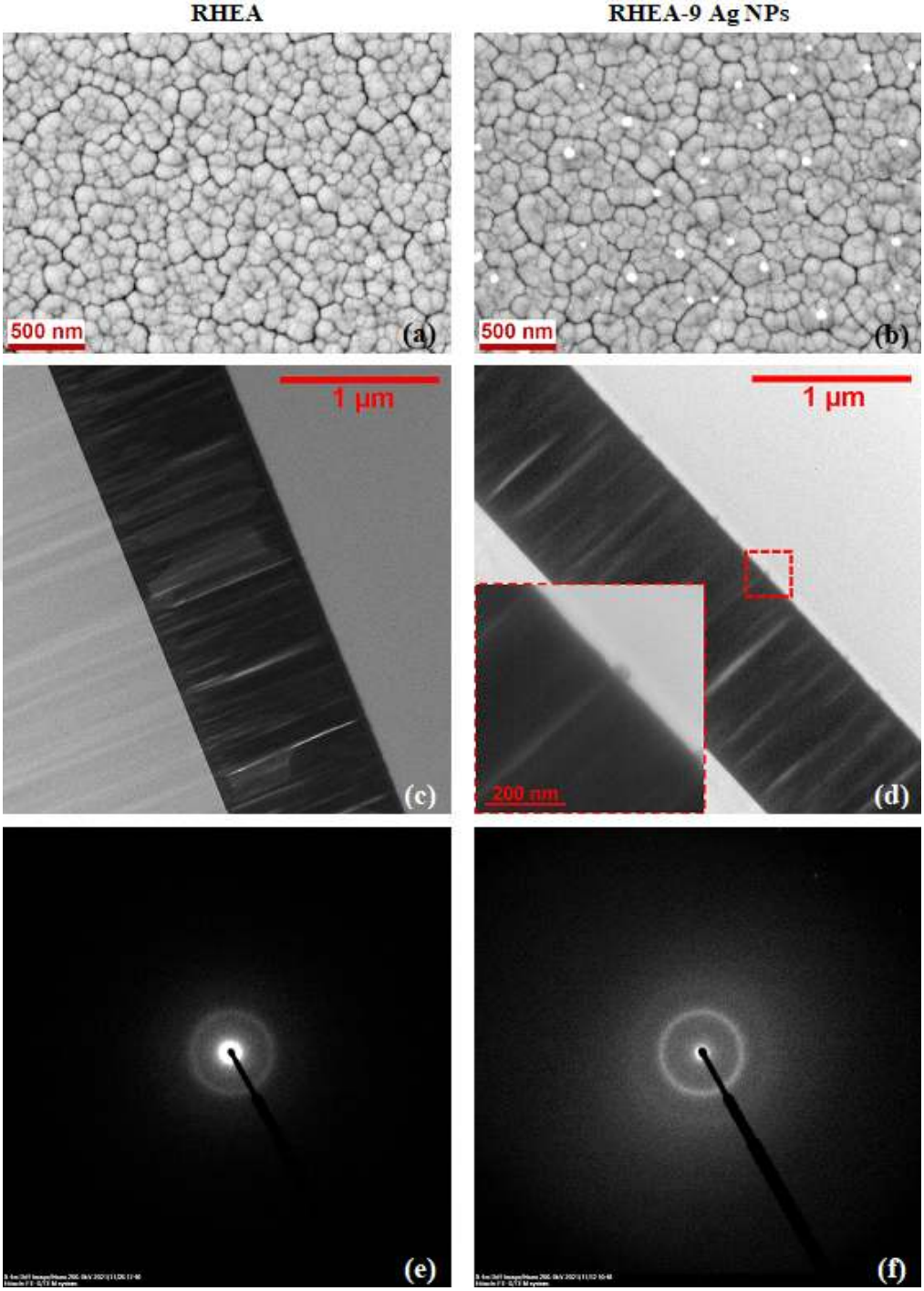

Figure 6. 1. (a, b) Surface view FESEM micrograph of undoped and Ag nanoparticles doped RHEA films deposited on Ti6Al4V substrate, (c, d) cross-sectional bright-field TEM images, and (e, f) SAED pattern of undoped and Ag nanoparticles doped RHEA films deposited on the silicon wafer.

Table 6. 1 presents the SEM-EDS analyses performed at the different regions of the coated silicon wafers. The results indicated that the chemical composition of the RHEA

film was quite close to the nominal and actual composition of the target, and Ag was presented at the desired amount, as reported in the previous work [193].

Table 6. 1. The chemical composition of RHEA and RHEA-9Ag NPs films deposited on the silicon wafer (at% and wt%).

	Ti		Zr		Ta		Nb		W		Ag	
	at%	wt%	at%	wt%	at%	wt%	at%	wt%	at%	wt%	at%	wt%
RHEA	37.56 ± 0.19	18.36 ± 0.09	25.09 ± 0.16	25.36 ± 0.16	12.56 ± 0.11	23.20 ± 0.20	12.31 ± 0.07	11.67 ± 0.06	12.48 ± 0.10	23.41 ± 0.18	---	---
RHEA-9Ag NPs	34.19 ± 0.21	16.57 ± 0.09	22.71 ± 0.18	20.96 ± 0.16	11.36 ± 0.09	20.80 ± 0.16	11.35 ± 0.11	10.67 ± 0.10	11.38 ± 0.10	21.17 ± 0.19	9.05 ± 0.05	9.83 ± 0.06

A TEM-EDS mapping analysis presented in Figure 6. 2 revealed that the constituent elements, including Ti, Zr, Ta, Nb, W, and Ag, are uniformly dispersed through the

deposited film. Furthermore, the outermost apparent semi-spherical Ag nanoparticles confirm the successful attachment and anchoring of the dopant agent on the surface of the coated specimen.

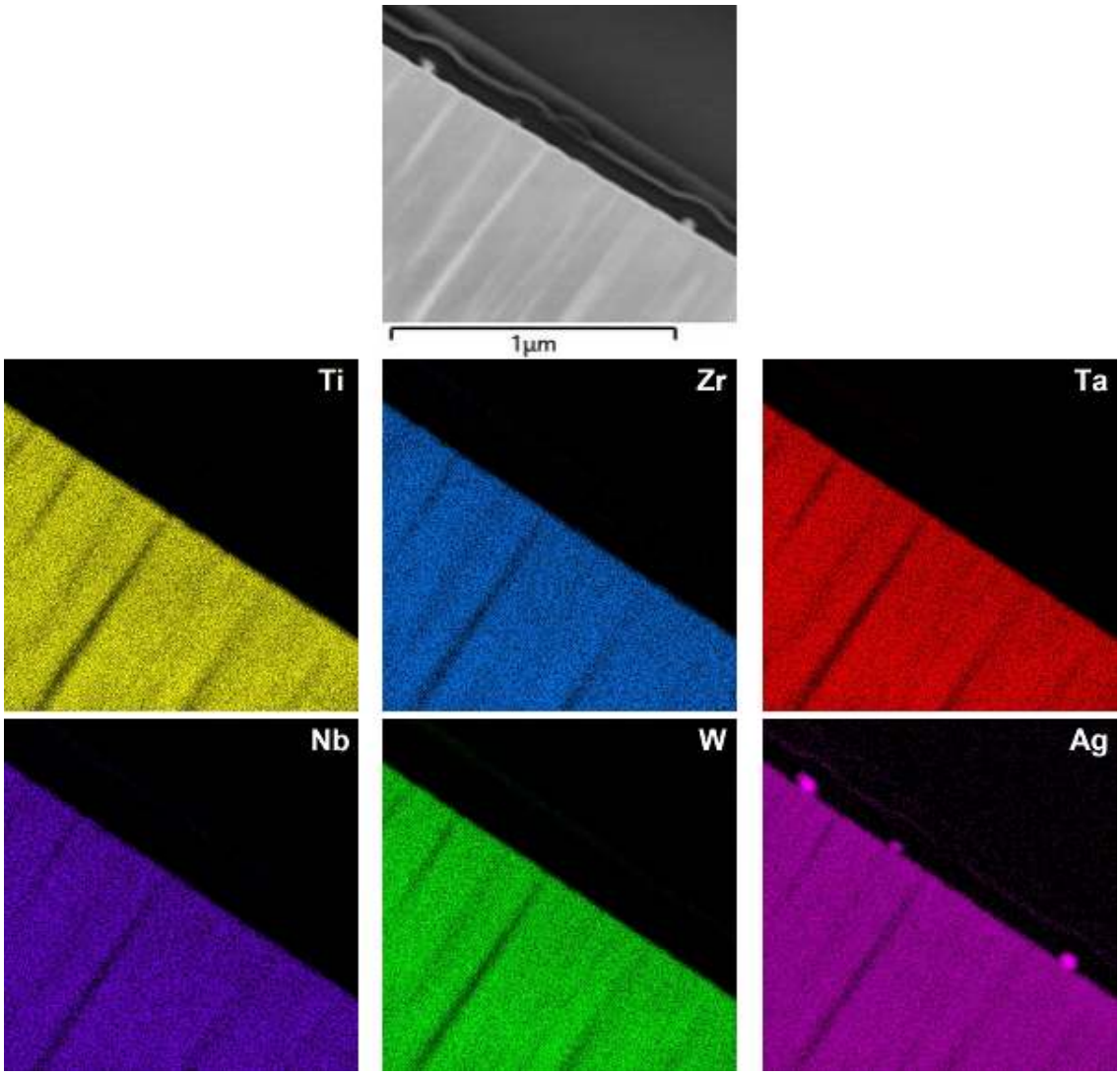

Figure 6. 2. TEM-EDS elemental mapping of RHEA-9Ag NPs film deposited on silicon wafer.

The SFE values of the uncoated Ti6Al4V, RHEA, and RHEA-9Ag NPs coated specimens were measured as 45.36, 54.94, and 43.05 mJ/m2, respectively, which is in good agreement with the wettability results reported in the previous work [193]. The inverse relationship of SFE and roughness values because of the presence of doped nanoparticles onto the surface of the specimens has been discussed in the literature [277]. Coating Ti6Al4V substrate with RHEA film increased the SFE, which caused a decrease in contact angle (CA). However, the dopping of the Ag nanoparticles on the surface decreased the SFE value of the RHEA-9Ag NPs specimen. The SFE and hydrophilicity

of implant surfaces have been reported to affect protein adsorption and cell adhesion after implantation, and in general, it has been demonstrated that cells prefer to grow on surfaces that possess higher SFE values [278–280].

6.3.2 Antibacterial Performance

Antibacterial performance of RHEA-9Ag NPs films deposited on Ti6Al4V was tested against P. Aeruginosa and S. Aureus in comparison with the control groups (Ti6Al4V and RHEA) is presented in Figure 6. 3. After 6 h incubation of the specimens with these bacteria, a large number of bacteria colonies were found on the uncoated Ti6Al4V substrate, and RHEA coated specimen. In contrast, only a few bacteria were observed on RHEA-9Ag NPs, indicating that doping Ag NPs could effectively decrease the number of viable bacteria colonies on the surface of RHEA films (Figure 6. 3a).

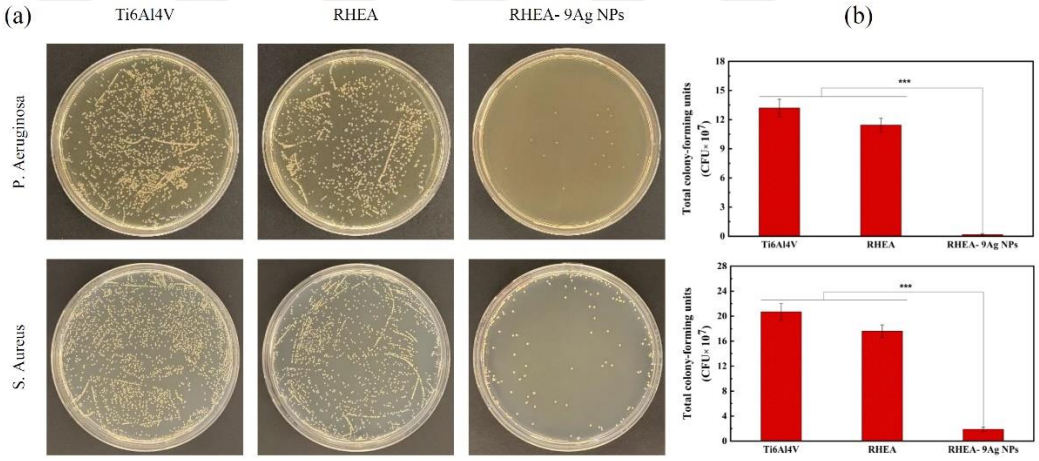

Figure 6. 3. (a) Colony forming units (CFU) of viable P. Aeruginosa and S. Aureus bacteria on Ti6Al4V substrate, RHEA, and RHEA-9Ag NPs specimens and (b) corresponding total CFU (*** $p < 0.001$).

As it is obvious in Figure 6. 3b the total colony forming units (CFU) of P.Aeruginosa on Ti6Al4V, RHEA coated and RHEA-9Ag NPs coated Ti6Al4V were 13.2×107, 11.45×107, and 0.19×107 CFU, respectively. Also, CFU of S.Aureus was found as 20.7×107, 17.6×107, and 1.89×107 for Ti6Al4V, RHEA, RHEA-9Ag NPs, respectively. As a result, the antibacterial efficacy of RHEA-9Ag NPs against P. Aeruginosa and S. Aureus was determined to be 98.5 % and 90.9 %, respectively. Hence, cumulative data suggest that the doping of 9 at% Ag nanoparticles can remarkably enhance the antibacterial activity of RHEA film against both Gram-negative and Gram-positive bacteria. Although the antibacterial mechanism of Ag NPs dopant remains unclear and in

debate, it is generally agreed that Ag+ cations released from their surface can penetrate through the cell wall, change DNA molecules into a condensed form, leading to the loss of their replication function, and at the same time react with thiol groups in proteins, which causes damage or even death of the bacteria [281–283].

6.3.3 Cytotoxicity

The cytotoxicity of the specimens on healthy cells is critical in practice. This was determined using C2C12 cells incubated on the specimens for 72 h using standard MTT assay (Figure 6. 4a). Although the viability of the cells incubated on Ti6Al4V decreased to about 80%, no significant toxicity was observed in any of the specimens indicating high biocompatibility of the prepared specimens. To further confirm the biocompatibility of the specimens, a calcein-AM/propidium iodide (PI) staining was used where green and red fluorescence indicates live and dead cells, respectively. Despite a few dead cells observed on Ti6Al4V, all cells were alive on RHEA, and RHEA-9Ag NPs coated Ti6Al4V (Figure 6. 4b). In addition, fluorescent and confocal microscopy images, as well as SEM images, indicate the uniform distribution of the cells on all three specimens and healthy cell morphology (Figure 6. 4b). Ag is known as an antibacterial agent; however, it may cause significant cytotoxicity to healthy cells at high concentrations [284,285]. Here, RHEA-9Ag NPs, containing 9 at% Ag, did not cause significant toxicity. These results suggest that coating of Ti6Al4V with a film of RHEA-9Ag NPs poses no significant toxicity to healthy cells but offers a strong antibacterial function.

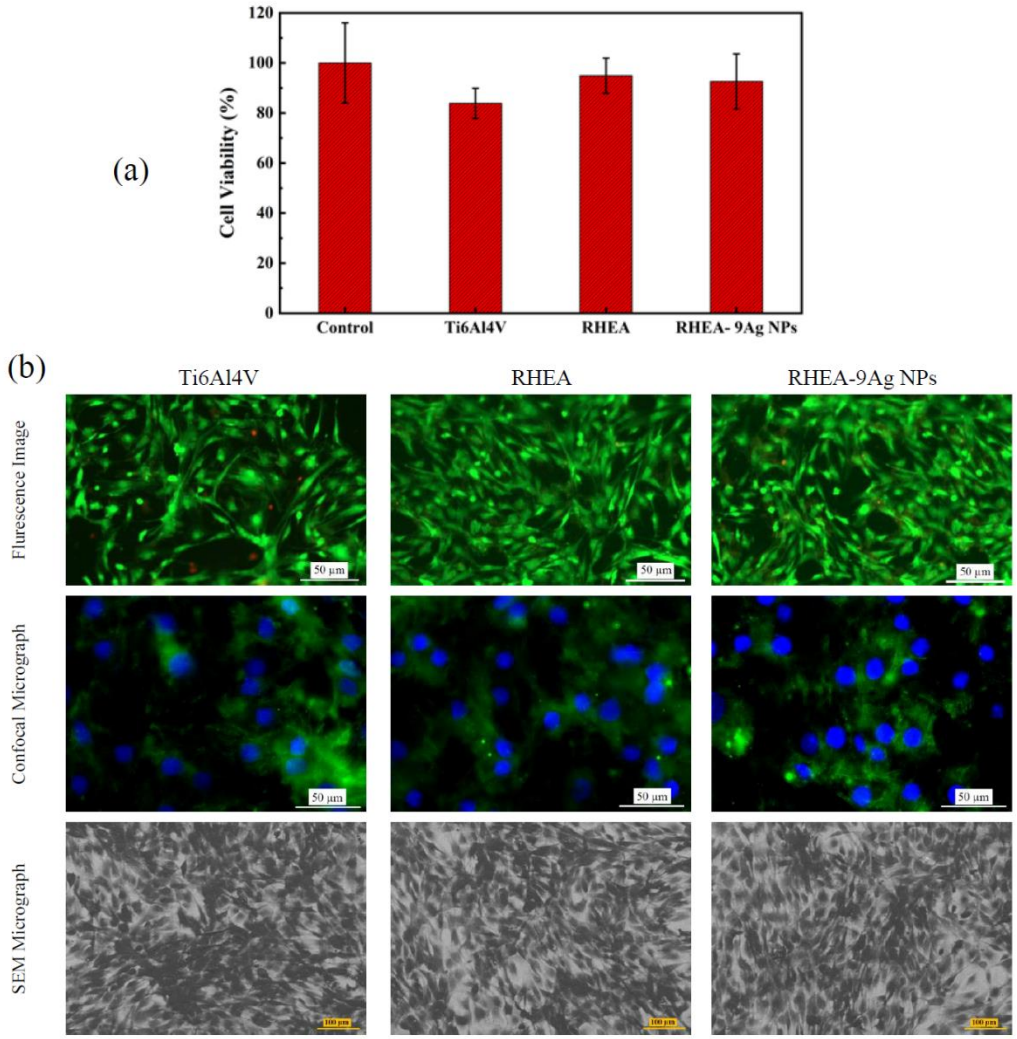

Figure 6. 4. (a) Quantitative analysis of cell viability after 72 h cultivation and (b) live/dead staining, confocal and SEM micrograph of C2C12 cell incubated for 72 h onto Ti6Al4V substrate, RHEA, and RHEA-9Ag NPs specimens.

6.4 Conclusion

In conclusion, a novel Ag NPs doped $Ti_{1.5}ZrTa_{0.5}Nb_{0.5}W_{0.5}$ RHEA film composed of biocompatible elements and 9 at% Ag was successfully deposited on the Ti6Al4V substrate as an antibacterial film. The amorphous structure of the undoped and Ag nanoparticles doped films was determined through microstructural evaluations. The RHEA-9Ag NPs coated specimen exhibited strong antibacterial activity against both Gram-negative and Gram-positive bacteria. The in vitro biocompatibility assessment of the examined specimens using C2C12 muscle myoblast cells on the specimen for 72 h revealed that both undoped and Ag nanoparticles doped films are non-cytotoxic and even safer than the Ti6Al4V alloy. The excellent antibacterial activity and cell proliferation ability, as well as superior mechanical properties and biocorrosion behavior demonstrated in the previous research [16], prove the great potential of Ag nanoparticles doped RHEA films as a biocompatible antibacterial coating for metallic implants.

CHAPTER 7

EXPLORING THE ROLE OF MO AND MN IN IMPROVING THE OER AND HER PERFORMANCE OF CoCuFeNi-BASED HIGH-ENTROPY ALLOYS

The majority of this chapter has been published in *ACS Appl. Energy Mater. 2024, 7, 6, 2423–2435*. The original manuscript has been rearranged to conform to the format requirements of the dissertation.

7.1 Introduction

In the current century, the rapid population growth and technological innovations led to an unprecedented increase in the consumption of conventional fossil fuels, presenting significant environmental challenges. This surge in demand exacerbates the threat of environmental degradation, underscoring the urgent need to transition towards greener and more sustainable energy sources. Consequently, we have to explore and adopt viable alternatives to fossil fuels to mitigate these environmental risks and ensure a sustainable future [286–288]. Overall water splitting is a solution and has been studied extensively to contribute to the hydrogen economy as an alternative to fossil fuels [289]. As a result of its high energy density, high abundance, and zero carbon footprint, hydrogen has been considered the ideal and potential alternative energy carrier to fossil fuels to date [290,291]. Furthermore, hydrogen enables the storage of renewable electricity as chemical bonds [292]. The overall water splitting is realized by reduction of water at the cathode, the hydrogen evolution reaction (HER) and oxidation of water at the anode, the oxygen evolution reaction (OER) [293]. In order to be successful, this process requires the fabrication of cheap, efficient, long-lasting, and scalable electrocatalysts [294]. Thus, there is a tremendous work to develop low-cost catalysts for overall water splitting, specifically in an alkaline media. Transition metal (TM) nitrides, carbides, oxides, and hydroxides have thus been evaluated as replacements for Pt/C as a benchmark for HER catalysts and RuO_2/IrO_2 as a benchmark for OER catalysts [295,296]. However, development of a bifunctional electrode, which can carry out both HER and OER in an alkaline media is a very challenging.

Transition metal-based electrochemical catalysts have garnered significant attention for their role in the anodic OER during water electrolysis. These catalysts, particularly alloys of iron (Fe), nickel (Ni), and cobalt (Co), owe their high efficiency to superior adsorption properties facilitated by the combined sites on the alloy surfaces. Consequently, these transition metal alloys have been effectively employed as highly efficient OER electrocatalysts [297,298]. In addition to improving mechanical properties, immunity to corrosion, and catalytic efficiency, combining and alloying dissimilar metals can result in a broad range of beneficial physical and chemical characteristics [193,299].

Recent research efforts have concentrated on creating catalysts that do not rely on expensive noble metals, aiming for affordability. An ideal catalyst, formulated from cheap transition metals, is anticipated to achieve a metal-hydrogen (M-H) bond strength

that rivals that of platinum (Pt). This expectation is supported by the "volcano plot," which demonstrates that a catalyst's effectiveness in the hydrogen evolution reaction (HER) increases with the strength of the M-H bond [300]. Due to the weak bonding between metals like Co and Cu with H, researchers focused on the combination of such metals with class I Mo or Nb atoms that bond H strongly. The multicomponent alloy materials like NiMoCo are expected to have high catalytic activity due to the synergistic effects and partially filled d orbitals [301–304]. Through the incorporation of different elements with Mo, the electrochemical efficacy of the catalyst undergoes modification as a consequence of the ligand effect stemming from the creation of heteroatomic bonds, as well as the strain effect resulting from the adjustment in bond length, thus facilitating the catalytic process [305]. Nonetheless, despite their high electrochemistry, most transition metals have limited corrosion resistance, which restricts these materials' usability as electrocatalysts in basic and acidic media [306,307].

There is a recently developed category of metallic materials identified as High-entropy alloys (HEAs). They are composed of solid solutions of five or more elements in equiatomic or near-equiatomic proportions [122,184,308]. The characteristics of HEAs are influenced by the high entropy effect, cocktail effect, and lattice distortion effects, which can be strategically manipulated to enhance catalytic activity. This involves tuning the composition, combining catalytically active metals, and controlling the electronic structure, particularly the d-band center, to optimize surface energy and promote selective reactivity in catalytic reactions [309,310]. The fascinating properties of HEAs, such as their strength and hardness, resistance to wear, stability under heat, and corrosion resistance, have recently attracted considerable attention for various applications [311–314]. Preparation and manufacturing methods used for manufacturing HEAs play a significant role in their superior properties. At the same time, with the various manufacturing methods for preparing HEAs, mechanical alloying (MA) is an option for preparing HEAs obtaining crystalline HEAs that are homogeneous at room temperature [315,316].

In this work, CoCuFeNi, CoCuFeNiMn, CoCuFeNiMo, CoCuFeNiMn$Mo_{0.5}$ CoCuFeNiMnMo, and CoCuFeNiMn$Mo_{1.5}$ high-entropy alloy powders were prepared via the mechanical alloying method for catalyzing OER and HER. An electrochemical test in 1 M KOH indicates that HEA with the highest Mo amount exhibits greater OER performance. On the other hand, HEA with the lowest Mo amount exhibits the best HER

activity, like smaller overpotential and outstanding stability, similar to nanostructured catalysts.

7.2 Materials and Methods

7.2.1 Synthesis of Electrocatalysts:

Homogenous equiatomic and non-equiatomic CoCuFeNi, CoCuFeNiMn, CoCuFeNiMo, $CoCuFeNiMnMo_{0.5}$ CoCuFeNiMnMo, and $CoCuFeNiMnMo_{1.5}$ high-entropy alloy powders were synthesized via mechanical alloying (MA) using elemental metal powders with 99.9% purity. A high-speed planetary ball mill (RestchTM PM 200) for 10 hours at 400 rpm with a ball-to-powder weight ratio (BPR) of 10:1 was used in this MA experiment. Mixtures were prepared and filled in mills in a glove box under an argon atmosphere to avoid oxidation throughout the ball milling process.

As can be seen in Table 7. 1, X-Ray Fluorescence (XRF) technique (BrukerTM S8 TIGER) was used to measure the chemical composition of synthesized powders, confirming that all elements specified for the composition are present with negligible differences from the nominal composition.

Table 7. 1. XRF measured the chemical composition of the synthesized powders.

	Co		Cu		Fe		Ni		Mn		Mo	
	at%	wt%	at%	wt%	at%	wt%	at%	wt%	at%	wt%	at%	wt%
CoCuFeNi	24.75± 0.20	24.61± 0.43	24.44± 0.23	26.20± 0.53	24.86± 0.24	23.42± 0.48	25.53± 0.24	25.53± 0.51	---	---	---	---
CoCuFeNiMn	19.27± 0.19	19.42± 0.58	19.60± 0.18	21.3± 0.60	20.66± 0.18	19.73± 0.52	20.13± 0.21	20.2± 0.61	20.34± 0.22	19.11± 0.60	---	---
CoCuFeNiMo	19.49± 0.22	17.18± 0.58	19.68± 0.21	18.7± 0.60	20.35± 0.27	17± 0.66	20.39± 0.23	17.9± 0.61	---	---	20.09± 0.06	28.84± 0.26
CoCuFeNiMnMo$_{0.5}$	17.41± 0.18	16.6± 0.63	18.00± 0.16	18.5± 0.62	18.48± 0.18	16.7± 0.61	18.32± 0.19	17.4± 0.65	18.67± 0.21	16.6± 0.71	9.11± 0.07	14.14± 0.35
CoCuFeNiMnMo	16.05± 0.18	14.6± 0.68	16.42± 0.16	16.1± 0.65	17.17± 0.19	14.8± 0.69	16.89± 0.18	15.3± 0.68	16.75± 0.23	14.2± 0.81	16.71± 0.05	24.75± 0.27
CoCuFeNiMnMo$_{1.5}$	14.70± 0.18	12.9± 0.74	15.01± 0.15	14.2± 0.69	15.88± 0.20	13.2± 0.76	15.79± 0.17	13.8± 0.72	15.16± 0.24	12.4± 0.92	23.45± 0.03	32.92± 0.23

7.2.2 Microstructural Characterization:

Crystal structures of ball-milled powders were analyzed using a Bruker D8 Advance X-ray diffractometer (XRD) equipped with a Cu Kα radiation (λ = 1.5405 Å) in the range of 2θ=15–90°. Rietveld refinement was performed by using TOPAS Academics V5 software. The broadening of profiles related to strain was modeled using the Gaussian function, while the broadening associated with particle size was represented by the Lorentzian function. Zeiss Ultra Plus was used for field emission scanning electron microscope (FESEM) images. The microstructure and crystallinity of the samples and the distribution of the constituent elements in the mechanically alloyed specimens were investigated via an aberration-corrected high-resolution transmission electron microscope (HRTEM, Hitachi, HF5000), employing energy-dispersive spectroscopy (EDS) at an acceleration voltage of 200 kV. To analyze X-ray photoelectron spectroscopy (XPS), A Thermo Scientific K-Alpha X-Ray photoelectron spectrometer with an Al Kα monochromator source (1486.6 eV) was utilized. Avantage 5.9 software was used for fitting the data. All spectra were corrected with respect to a C1s peak at 284.5 eV.

7.2.3 Electrochemical Measurements:

The linear sweep voltammetry (LSV) tests were carried out via a three-electrode system on a Biologic VSP Potentiostat to analyze the electrochemical properties of ball-milled electrocatalyst powders where a Hg/HgO electrode and platinum sheet were used as reference and counter electrodes, respectively, in 1M KOH medium. The experiment utilized a glassy carbon (GC) electrode with a diameter of three millimeters as the working electrode. To prepare the catalyst ink, 870 µL of ethylene glycol was mixed with 130 µL of a 1 wt.% Nafion solution. Into this mixture, 5 mg of catalyst powder was introduced and subjected to ultrasonic treatment for 60 minutes to ensure uniform distribution. Subsequently, 3 µL of this evenly mixed catalyst ink was applied to the surface of a pre-cleaned GC electrode. The electrode, with the ink applied, was then left to dry at 60°C for 6 hours in an air atmosphere. The LSV curves were recorded between 1.2 and 1.8 V (versus RHE) and 0.0 and -1.0 V (versus RHE) for OER and HER experiments, respectively. For OER, all measurements were conducted in the electrolyte saturated with Oxygen (O_2) to maintain the O_2/H_2O stability and equilibrium at 1.23 V vs. RHE. Catalytic activities were evaluated at the potential at the current density of 10

$mA.cm^{-2}$. Measured potentials vs. Hg/HgO electrode were converted to potentials vs. Reversible Hydrogen Electrode (RHE) using ERHE = EHg/HgO + 0.059 pH + 0.098. The stability test was carried out with a Rotating Disc Electrode (RDE). The sample on an RDE was prepared by using the same ink as explained above. The stability of electrocatalysts was tested with the chronopotentiometry method at 10 $mA.cm^{-2}$ under a rotation speed of 1600 rpm. For electrochemical impedance spectroscopy (EIS) measurements, a sinusoidal potential of 10 mV was applied in a frequency range between 100 kHz and 0.1 Hz. Cyclic Voltammetry (CV) tests were used to determine the double-layer capacitance parameter (Cdl) to estimate the electrochemically active surface area (ECSA). CV experiments were carried out at five different scanning rates (10, 20, 40, 60, and 80 $mV.s^{-1}$) across a potential region of 1.1-1.2 V (vs. RHE).

The turnover frequency (TOF) was calculated at the overpotential of 380 mV with the following equation:

$$TOF = \frac{jA}{4F\frac{m}{M}} \qquad \text{Eq.1}$$

where j refers to current density ($mA.cm^{-2}$) at the specified overpotential, A represents the working electrode's surface area, F shows the faraday constant (96485 C mol^{-1}), m is the weight of the catalyst, and M indicates the molecular weight of the mechanically alloyed HEA catalyst [317].

The overall water-splitting reaction was conducted in a two-cell configuration, utilizing a graphite electrode (GE) as the catalyst substrate. The electrolyte used in the experiment was a 1.0 M solution of KOH. The anode and cathode electrodes were prepared by dropping the ink (the same ink prepared for the GC electrode) onto the GE to cover an area of 0.5 cm × 0.3 cm. A gas chromatography instrument (GC-2014 SHIMADZU with 3-valve manual sampling port, Molecular Sieve 5A column), Ar as carrier gas, was utilized to quantify the hydrogen (H_2) and oxygen (O_2) gases produced. The cell was connected to the sampling port of GC and constantly fed with Ar gas at 25 ml/min to carry the products to the GC. The volume of the sampling port was 0.5 ml. The gaseous products were monitored every 20 minutes by applying a current density of 20 $mA.cm^{-2}$ to the two-electrode cell, which was carefully sealed for 120 minutes. The Faradaic efficiency of the hydrogen evolution reaction (HER) was calculated using Eq. 2:

FE = (nexp)/(Q/nF) Eq.2

Where nexp shows the number of H_2 moles created at 20 $mA.cm^{-2}$ current density, Q is the total charge generated, n refers to the number of electrons exchanged, which equals 2 for HER, and F is the Faraday's constant (96485 $C.mol^{-1}$) [318].

After the completion of long-term stability experiments, the 1M KOH electrolyte employed was subjected to analysis using inductively coupled plasma mass spectrometry (ICP-MS, Agilent 7700x) in order to determine the levels of constituent element ions that were released.

7.3 Results and discussion

7.3.1 Characterization of the Mechanically alloyed powders:

Figure 7. 1 shows the XRD patterns of the mechanically alloyed CoCuFeNi, CoCuFeNiMn, CoCuFeNiMo, $CoCuFeNiMnMo_{0.5}$ CoCuFeNiMnMo, and $CoCuFeNiMnMo_{1.5}$ powders. As it is seen in Figure 7. 1, a single-phase FCC structure was achieved for CoCuFeNi and CoCuFeNiMn. However, CoCuFeNiMo, $CoCuFeNiMnMo_{0.5}$ CoCuFeNiMnMo, and $CoCuFeNiMnMo_{1.5}$ alloys are composed of a mixture of FCC and BCC phases. The positions of the diffraction peaks for the FCC phase are approximately at 2θ= 44°,53°, and 75°. Also, the positions for BCC phases are at approximately 2θ= 39°,58°, and 75°.

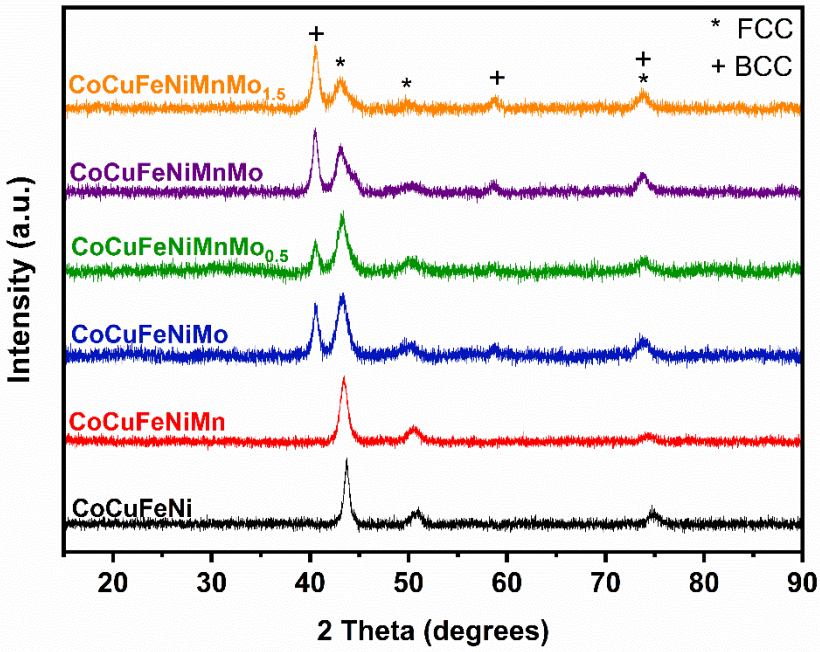

Figure 7. 1. X-ray diffraction patterns of the mechanically alloyed CoCuFeNi, CoCuFeNiMn, CoCuFeNiMo, $CoCuFeNiMnMo_{0.5}$ CoCuFeNiMnMo, and $CoCuFeNiMnMo_{1.5}$ powders.

In traditional solid solutions, the rules of formation are guided by the characteristics of alloys composed of one or two principal elements. According to Hume-Rothery's rule, factors such as the size difference between atoms, electronegativity, the spatial arrangement of atoms or ions within a crystal structure, and valency are pivotal in the formation of solid solutions. However, the formation process of simple solid solutions in HEAs diverges from these established patterns seen in conventional alloys [319]. According to Guo et al., other factors in addition to mixing entropy (ΔSmix), including valence electron concentration (VEC), mixing enthalpy (ΔHmix), and atomic size difference (δ), is also useful in predicting the formation of solid solutions in HEAs [161,320]. ΔSmix, ΔHmix, δ, and VEC can be defined as:

$$\Delta Smix = -R \sum_{i=1}^{n} C_i \ln C_i \qquad \text{Eq.3}$$

$$\Delta Hmix = \sum_{i=1, i\neq j}^{n} 4\Delta H_{ij}^{mix} C_i C_J \qquad \text{Eq.4}$$

$$\delta = 100\sqrt{\sum_{i=1}^{n} C_i(1 - r_i/r)^2} \qquad \text{Eq.5}$$

$$VEC = \sum_{i=1}^{n} c_i (VEC)_i \qquad \text{Eq.6}$$

In the above equations, R represents the gas constant (8.314 J (K mol)$^{-1}$), the components i_{th} and j_{th} are represented by C_i and C_j, respectively, as molar percentages, $\sum_{i=1}^{n} C_i = 1$ and ΔH_{ij}^{mix} is the enthalpy of mixing between components ith and jth, r_i and $(VEC)_i$ are the atomic radius and the VEC of the ith component, respectively [321]. The basic properties of mechanically alloyed HEAs are calculated by Eqs. (3)– (6) and listed in Table 7. 2

According to Guo et al., solid solutions can form in HEAs when

-22 ≤ ΔHmix ≤ 7 kJ.mol-1, 0 ≤ δ ≤ 8.5, and 11 ≤ ΔSmix ≤ 19.5 J/(K·mol) [198]. Based on these findings and the calculations presented in Table 2, solid solutions are most likely to form in mechanically alloyed powders.

It is important to note that a value of VEC less than 6.87 will stabilize a BCC solid solution; a value of VEC between 6.87 and 8.0 will create a two-phase FCC+BCC solid

solution, and a value of VEC greater than 8 will stabilize an FCC solid solution [198,249]. According to the calculated VEC values in Table 7. 2, VEC values decreased with the increasing Mo content. Based on the above-mentioned VEC rule, CoCuFeNi, and CoCuFeNiMn powders, with VEC values of 9.5 and 9, respectively, exhibited FCC structure. However, as Guo et al. mentioned [161], there could be some exceptions for the crystal structure with certain compositions. Cichooki et al. have argued that in HEAs with a Mo content above 10 at%, a mixed structure (FCC + BCC) may co-exist [322], which correlates with our results.

Table 7. 2. The parameters of ΔS, ΔH, δ, and VEC for mechanically alloyed CoCuFeNi, CoCuFeNiMn, CoCuFeNiMo, $CoCuFeNiMnMo_{0.5}$ CoCuFeNiMnMo, and $CoCuFeNiMnMo_{1.5}$ powders.

	VEC	**ΔS_{mix} J/(K·mol)**	**ΔH_{mix} (kJ/mol)**	**δ**
CoCuFeNi	9.5	11.52	5	4.63
CoCuFeNiMn	9	13.38	1.76	4.61
CoCuFeNiMo	8.8	13.38	4	4.76
$CoCuFeNiMnMo_{0.5}$	8.7	14.69	2.11	4.62
CoCuFeNiMnMo	8.5	14.91	2.33	4.54
$CoCuFeNiMnMo_{1.5}$	8.3	14.78	2.46	4.44

In all mechanically alloyed CoCuFeNi, CoCuFeNiMn, CoCuFeNiMo, $CoCuFeNiMnMo_{0.5}$ CoCuFeNiMnMo, and $CoCuFeNiMnMo_{1.5}$ powders, percentage of crystallinity, phases (BCC or FCC), percentage of phases, space groups, Crystallite size, lattice strain, and lattice parameter were determined by Rietveld refinement analysis and the results were given in . The goodness of fit parameter ($\chi 2$) for the Rietveld refinement was between 2.3-2.8, which is a typical value for optimal fitting. As given in Table 7. 3, the addition of Mo results in the formation of the BCC structure. In addition, the amount of BCC structure increased as the amount of Mo increased in the structure [322,323].

Table 7. 3. Some microstructural characteristics for the mechanically alloyed CoCuFeNi, CoCuFeNiMn, CoCuFeNiMo, $CoCuFeNiMnMo_{0.5}$ CoCuFeNiMnMo, and $CoCuFeNiMnMo_{1.5}$ powders obtained by Rietveld refinement.

	Crystallinity (C) Amorphous (A)	Structure	Amount	Space group	Crystallite Size (nm)	Lattice Strain (%)	a (A°)
CoCuFeNi	99.4% (C) 0.6% (A)	FCC	100%	Fm-3m	15.5± 0.71	0.05± 0.01	3.6422± 0.0041
CoCuFeNiMn	99.8% (C) 0.2% (A)	FCC	100%	Fm-3m	20.5± 0.75	1.11± 0.07	3.6431± 0.0037
CoCuFeNiMo	99.96% (C)	FCC	76.94%± 0.23	Fm-3m	14.7± 0.53	1.12± 0.09	3.6458± 0.0019
	0.04% (A)	BCC	23.06%± 0.14	Im-3m	19.8± 0.66	0.987± 0.02	3.1523± 0.0014
$CoCuFeNiMnMo_{0.5}$	95.75% (C)	FCC	88.97%± 0.43	Fm-3m	8.2± 0.14	2.3± 0.09	3.6188± 0.0058
	4.25% (A)	BCC	11.03%± 0.20	Im-3m	42.1± 0.82	0.3± 0.05	3.1345± 0.0011
CoCuFeNiMnMo	94.79% (C)	FCC	77.42%± 0.37	Fm-3m	9.8± 0.18	1.91± 0.04	3.6346± 0.0025
	5.21% (A)	BCC	22.58%± 0.17	Im-3m	22.9± 0.73	0.809± 0.03	3.1519± 0.0012
$CoCuFeNiMnMo_{1.5}$	93.7% (C)	FCC	71.60%± 0.38	Fm-3m	13.3± 0.41	1.28± 0.07	3.6099± 0.0072
	6.3% (A)	BCC	28.40%± 0.22	Im-3m	15.1± 0.58	1.23± 0.07	3.1427± 0.0021

7.3.2 Morphology of the Mechanically alloyed powders

The evolution of the shape of mechanically alloyed powder after 10 hours of high-energy ball milling was followed by SEM in Figure 7. 2. As is visible in Figure 7. 2, the mechanically alloyed powders have a plate-like structure with a large aspect ratio. More specifically, all the mechanically alloyed powders become more and more anisotropic and can be qualified as "flakes" as evidenced by higher magnification SEM images [324,325]. The composition of mechanically alloyed HEAs does not influence the final shape of powders.

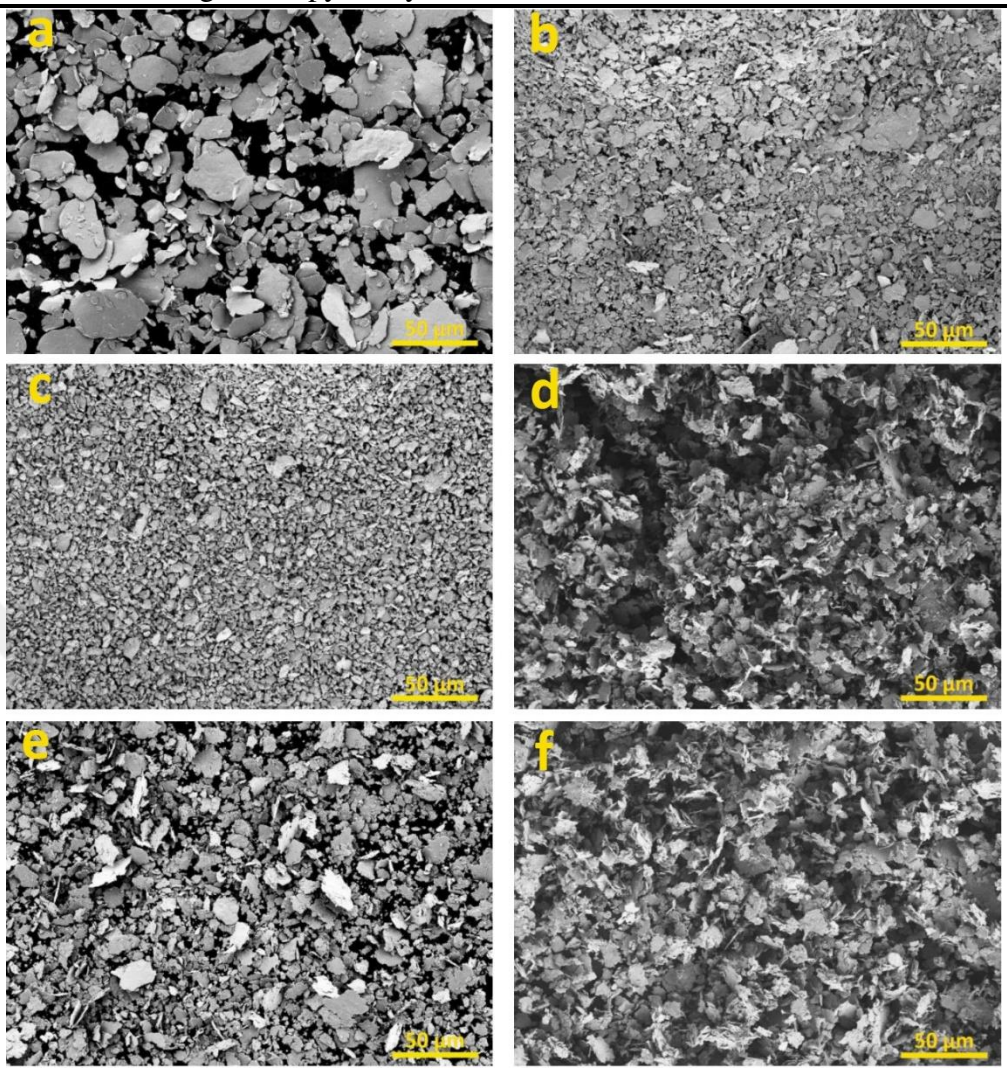

Figure 7. 2. FESEM images of a) CoCuFeNi, b) CoCuFeNiMn, c) CoCuFeNiMo, d) $CoCuFeNiMnMo_{0.5}$, e) CoCuFeNiMnMo, and f) $CoCuFeNiMnMo_{1.5}$ powders.

High-resolution TEM (HRTEM) images of the $CoCuFeNiMnMo_{0.5}$ and $CoCuFeNiMnMo_{1.5}$ are given in Figure 7. 3, Figure 7. 4, respectively. The selected area electron diffraction (SAED) patterns are also given to identify the crystalline structure of the mechanically alloyed HEAs [326]. The SAED pattern can be assigned to both BCC and FCC in accordance with the XRD results. As is obvious in Figure 7. 3b, for $CoCuFeNiMnMo_{0.5}$, the lattice fringes display an interplanar spacing of 0.210 nm and 0.189 nm, corresponding to the (111) crystal plane and (200) crystal plane of the HEA respectively.

According to Figure 7. 4b, the lattice fringes for $CoCuFeNiMnMo_{1.5}$ show an interplanar spacing of 0.222 nm and 0.208 nm, which correspond to the (110) and (111) crystal planes of the HEA.

Elemental EDS mapping of the $CoCuFeNiMnMo_{0.5}$ and $CoCuFeNiMnMo_{1.5}$ samples confirms that six elements, Co (yellow), Cu (violet), Fe (orange), Ni (red), Mn (green), and Mo (cyan) are homogeneously distributed over the selected particle area as depicted in Figure 7. 3c and Figure 7. 4c. It may be claimed that during the mechanical alloying process, the diffusion of the constituent elements into the structure and the consequent high-entropy effect causes the constituent elements to distribute uniformly with no separation of phases [118].

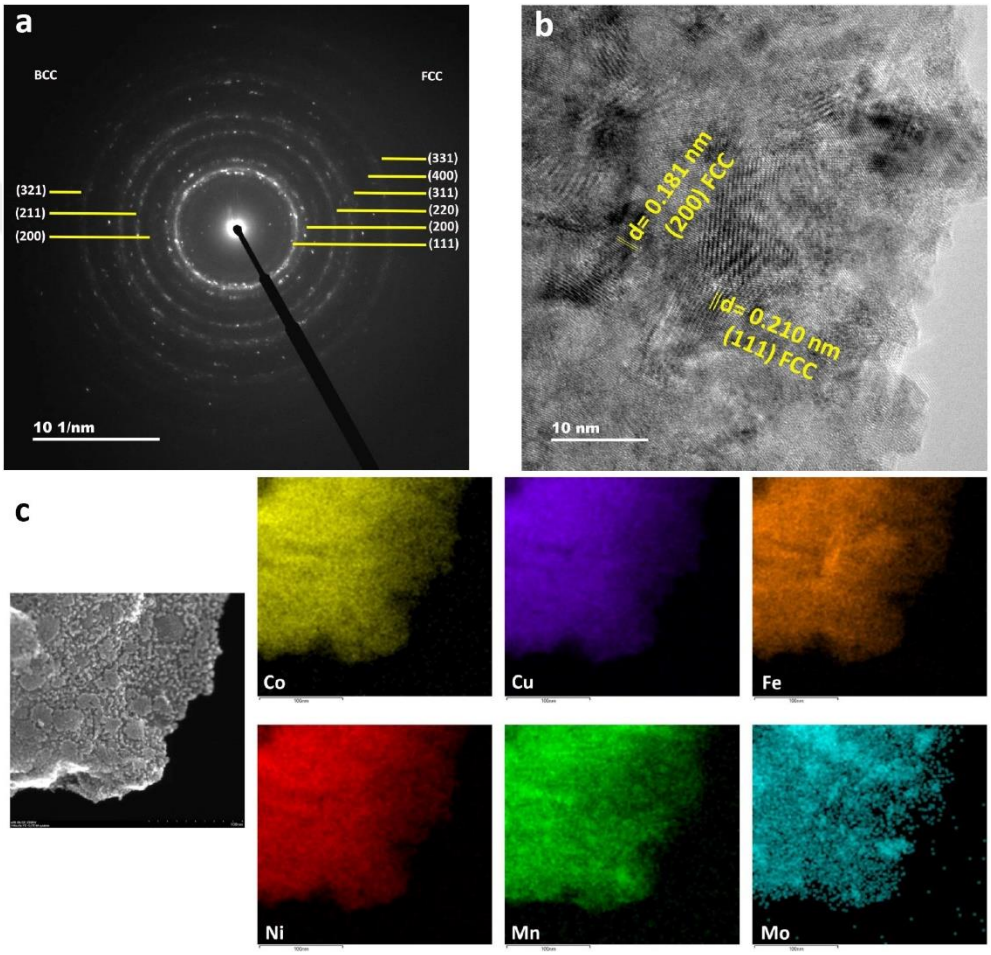

Figure 7. 3. For the $CoCuFeNiMnMo_{0.5}$ sample, a) SAED pattern, b) HRTEM image, and c) TEM-EDS elemental mapping.

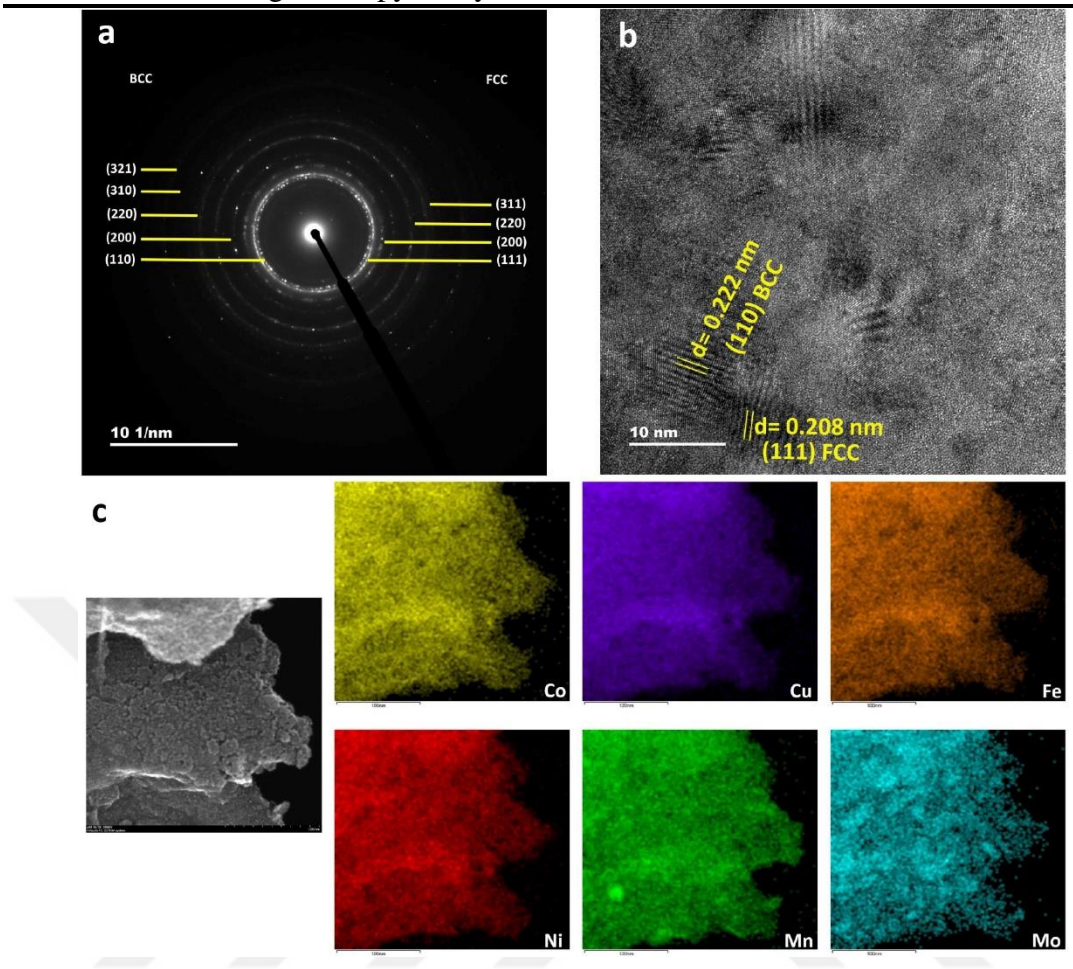

Figure 7. 4. For the $CoCuFeNiMnMo_{1.5}$ sample, a) SAED pattern, b) HRTEM image, and c) TEM-EDS elemental mapping.

7.3.3 XPS Study

The electrocatalytic activity of a catalyst is directly related to its surface chemistry; therefore, the oxidation levels of the HEA catalysts were analyzed using XPS [327]. The XPS data of the specimens and their fitted graphs can be found in Figure 7. 5, Figure 7. 6, Figure 7. 7, Figure 7. 8, Figure 7. 9, and Figure 7. 10. The Co 2p spectrum can be studied in three pairs of doublets: a doublet at Co 2p3/2 at 778.05 ± 0.05 eV representing metallic Co, and two spin-orbit peaks with Co 2p3/2 at 780 ± 0.1 eV and satellites at 785.8 ± 0.1 than can be attributed to CoO. For the Cu element, in the Cu 2p spectra, Cu 2p 3/2 and Cu 2p 1/2 are detected at 932.5 ± 0.2 eV and 952.2 ± 0.1 eV, which correspond to metallic Cu. While Cu 2p 3/2 and Cu 2p 1/2 are observed at 934.8 ± 0.1 eV and 954.3 ± 0.2 eV, which correspond to Cu^{2+}, and satellites at 943.7 ± 0.2 eV. For Fe 2p spectrums, the two noticeable peaks are detected, which can be attributed to metallic Fe (Fe 2p 3/2

at 707.3 ± 0.1 eV and Fe 2p 1/2 at 720.3 eV) and Fe^{2+} (Fe 2p 3/2 at 712.1 eV and Fe 2p 1/2 at 724.8 ± 0.1). The Ni 2p spectrums indicate the metallic Ni at 825.8 ± 0.1 eV for Ni 2p3/2, but the peak at 855.6 ± 0.3 eV for Ni 2p 3/2 confirms the existence of NiO and a satellite at 861.1 ± 0.2. In the Mn 2p spectra, metallic Mn at 641.6 ± 0.2 eV and different oxidation states are obvious. In the case of Mo, the Mo 3d spectrums are split into two peaks at 227.9 ± 0.1 eV and 232.1 ± 0.1 eV, and accordingly, they are in agreement with the properties of metallic Mo and MoO_3, respectively. The introduction of Mo into multiatomic structures and HEAs containing Fe, Ni, Cu, and Co results in a slight shift in the XPS peaks of these metals [118,317,328–330]. The shift is evidence of electron transfer between the atoms on the surface, which may favor the adsorption of reaction intermediates on reactive sites at the surface. Higher valence state metals on the surface supply active sites with favorable electronic structures. We have not observed a significant shift in peak positions, but there is an apparent decrease in the intensities of Ni^0, Fe^0, Cu^0, and Co^0 peaks relative to the peaks corresponding to the higher oxidation state of these metals after the incorporation of Mn and Mo atoms into the HEA structure, which is evidence of strong electronic interaction between these metals. Mo exists in its metallic and +6 state. The latter is important for the optimization of the electronic structure at the surface. XPS analysis also shows that oxygen is present on the surface of HEAs. The existence of oxides on the surface of the HEA electrodes can clearly be attributed to the oxidization of HEA electrodes in the air. [184,326] The peaks of O 1s at 529.8, 531.2, and 533.1 eV in XPS spectra correspond to the characteristics of metal oxide, metal hydroxide, and adsorbed H_2O. The broader and featureless O 1s peak after the incorporation of Mo into the structure can be assigned to the variety of M-OH bonds on the surface of Mo-containing HEAs.

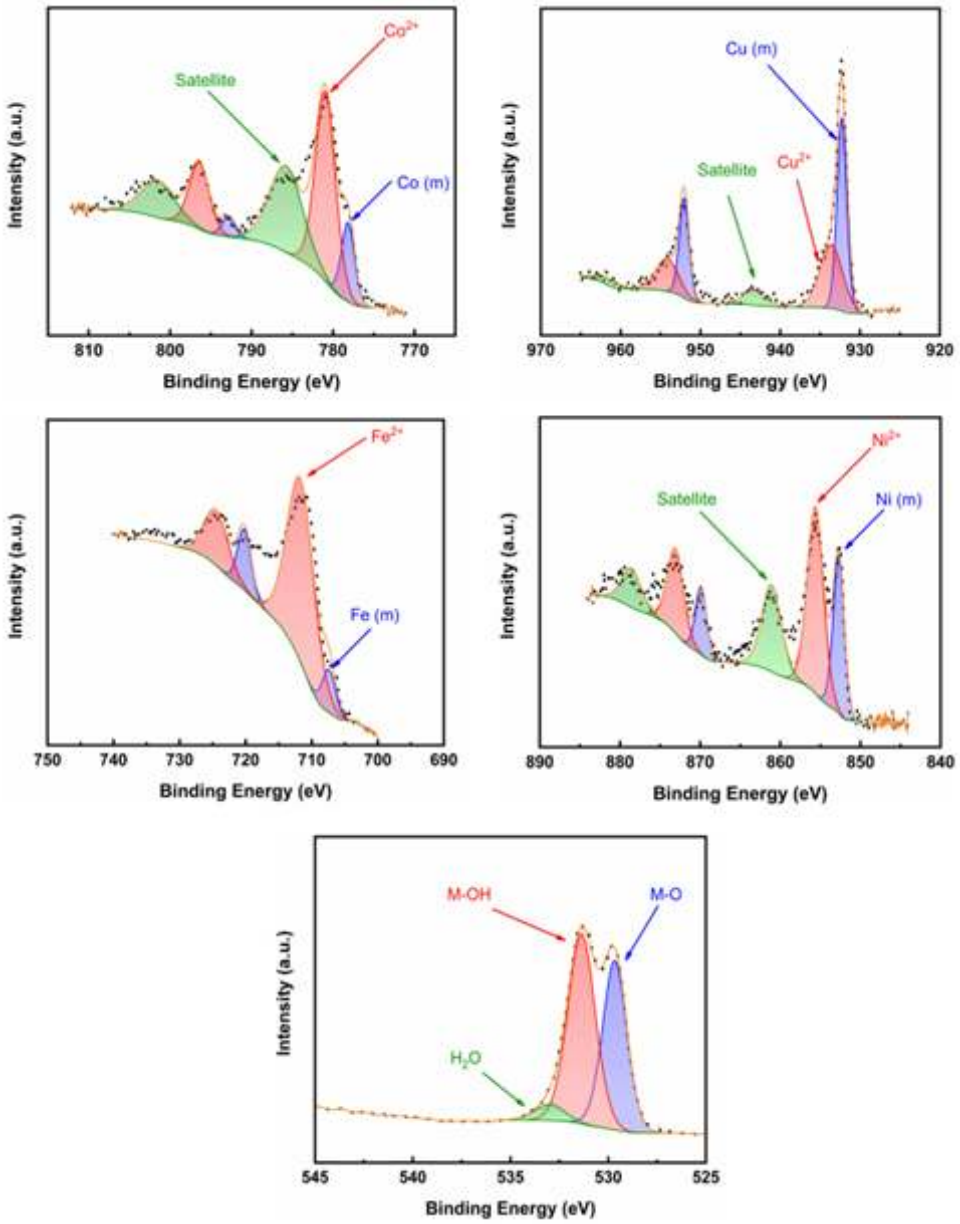

Figure 7. 5. XPS spectra of constituent elements for mechanically alloyed CoCuFeNi HEA

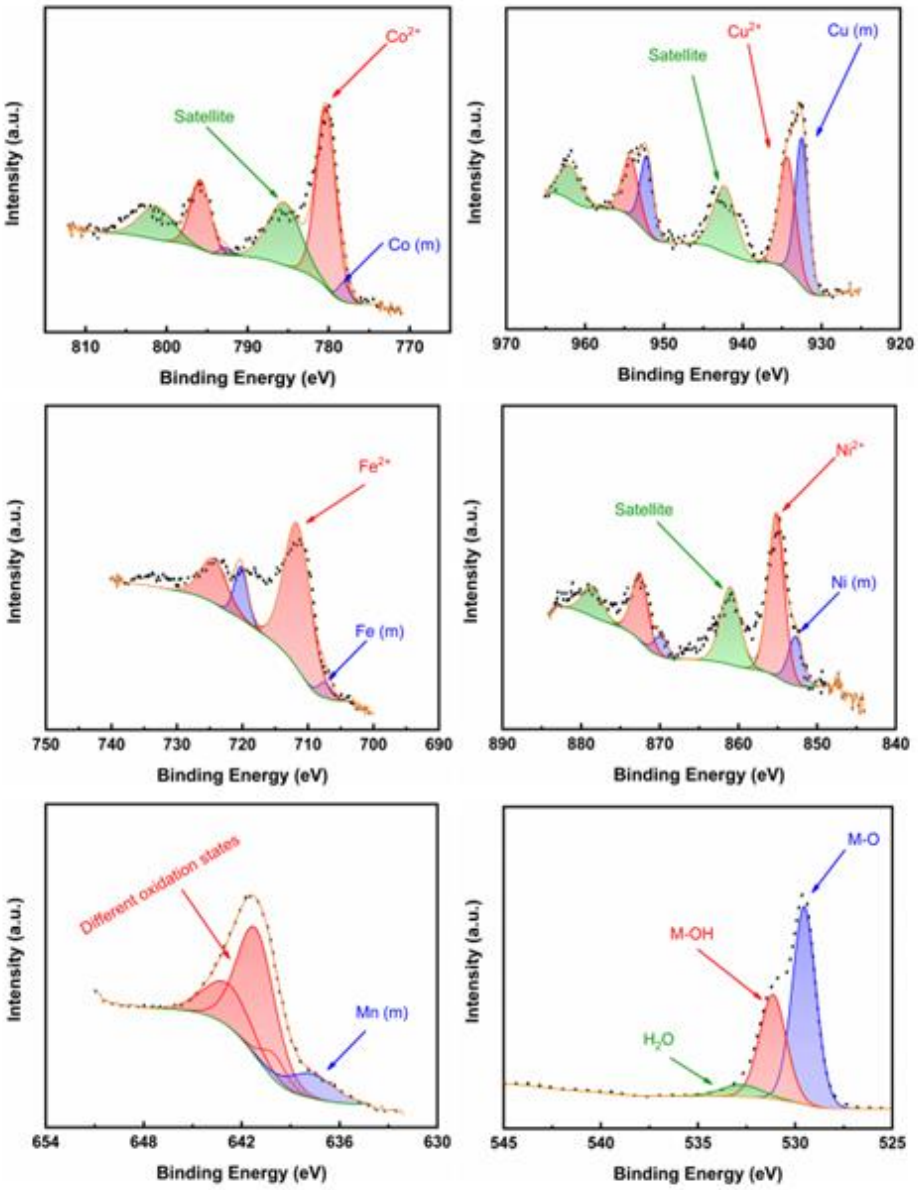

Figure 7. 6. XPS spectra of constituent elements for mechanically alloyed CoCuFeNiMn HEA

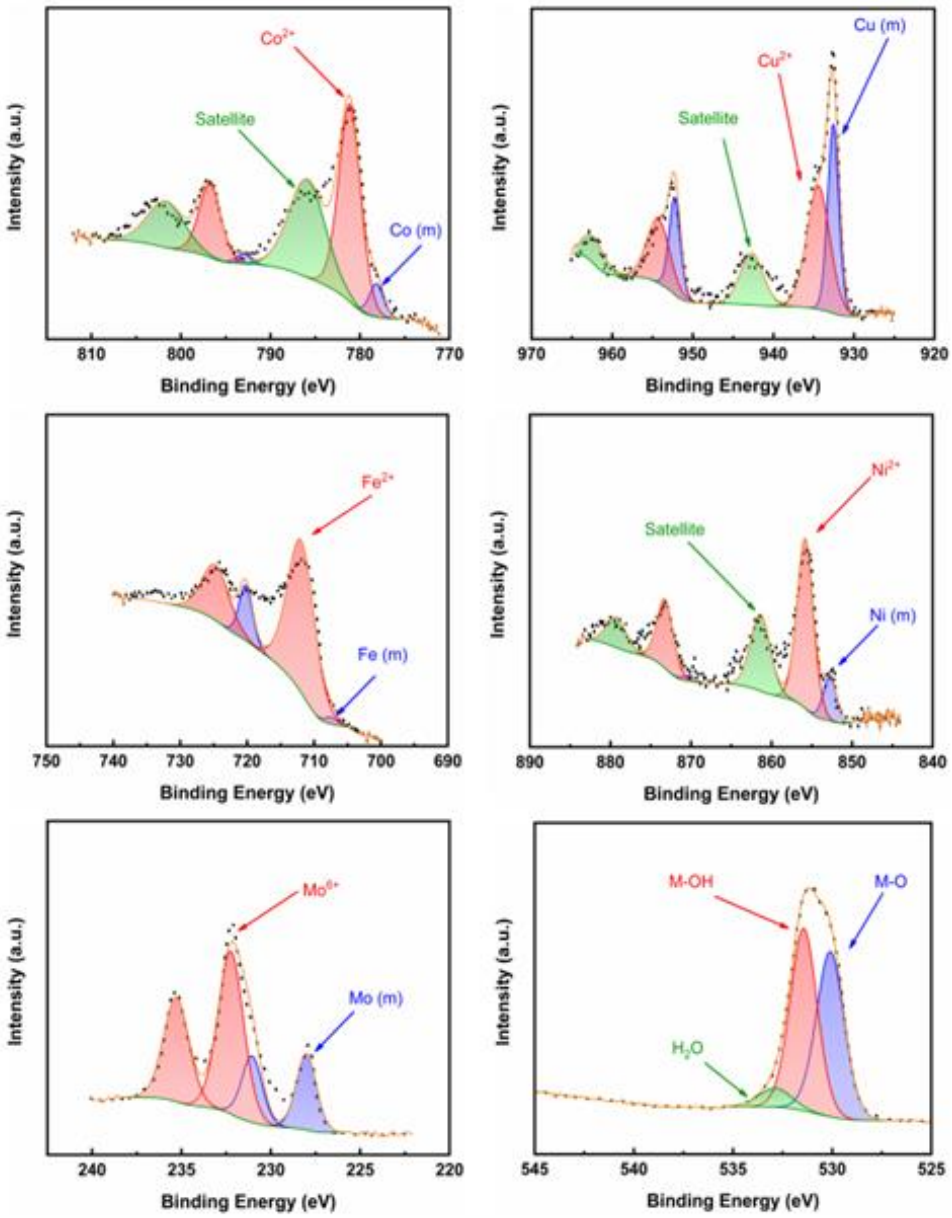

Figure 7. 7. XPS spectra of constituent elements for mechanically alloyed CoCuFeNiMo HEA

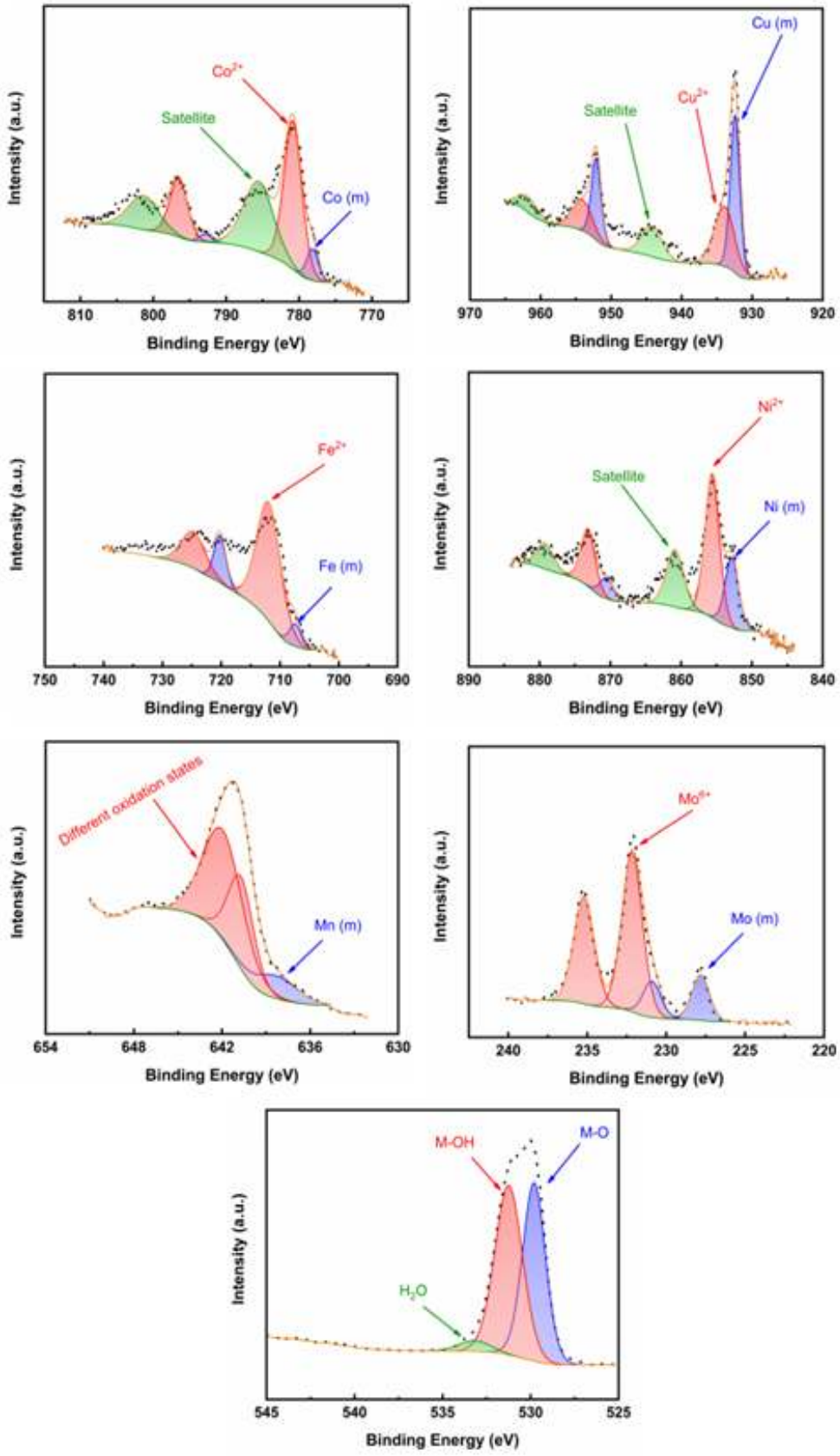

Figure 7. 8. XPS spectra of constituent elements for mechanically alloyed $CoCuFeNiMnMo_{0.5}$ HEA

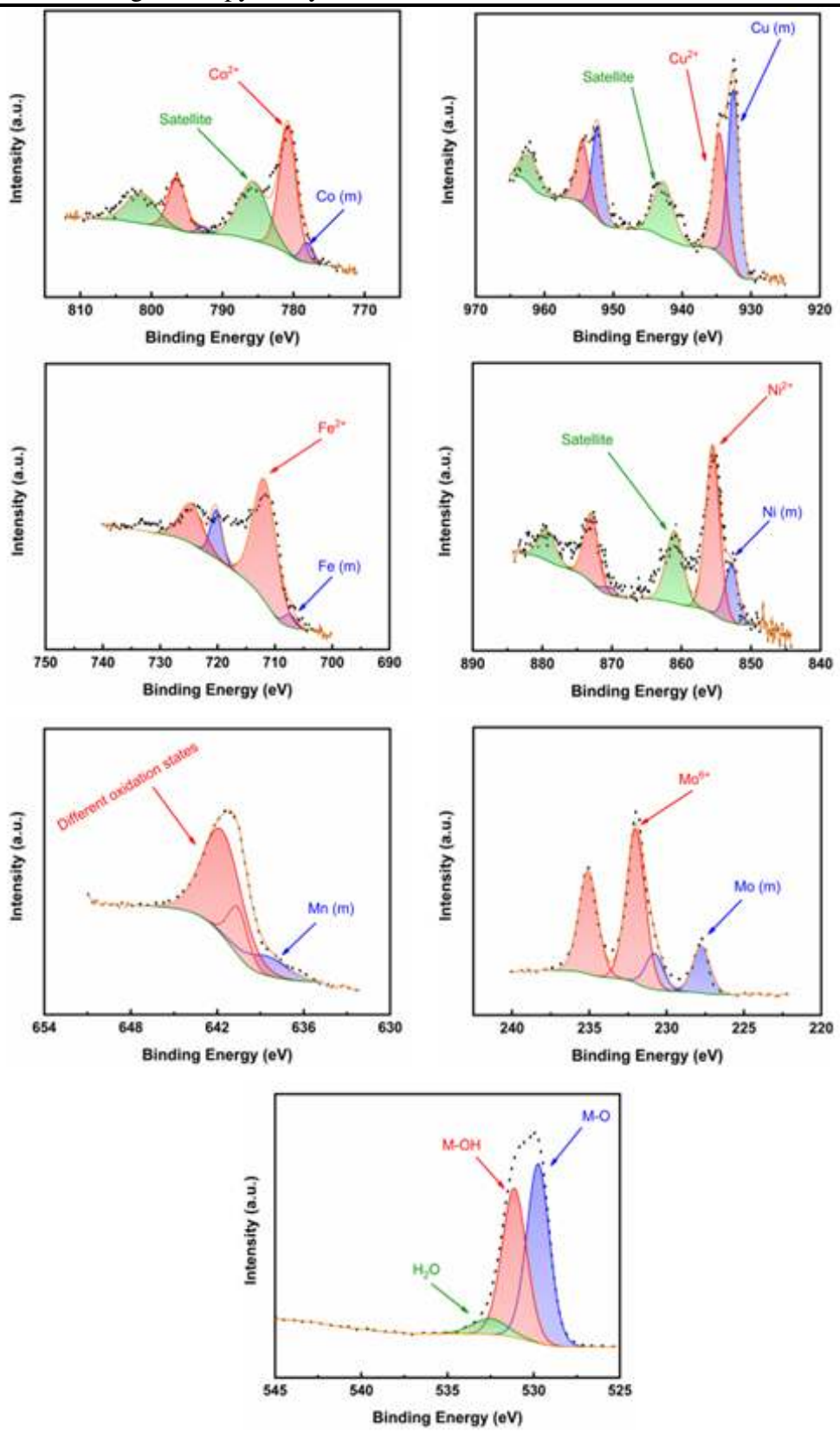

Figure 7. 9. XPS spectra of constituent elements for mechanically alloyed CoCuFeNiMnMo HEA

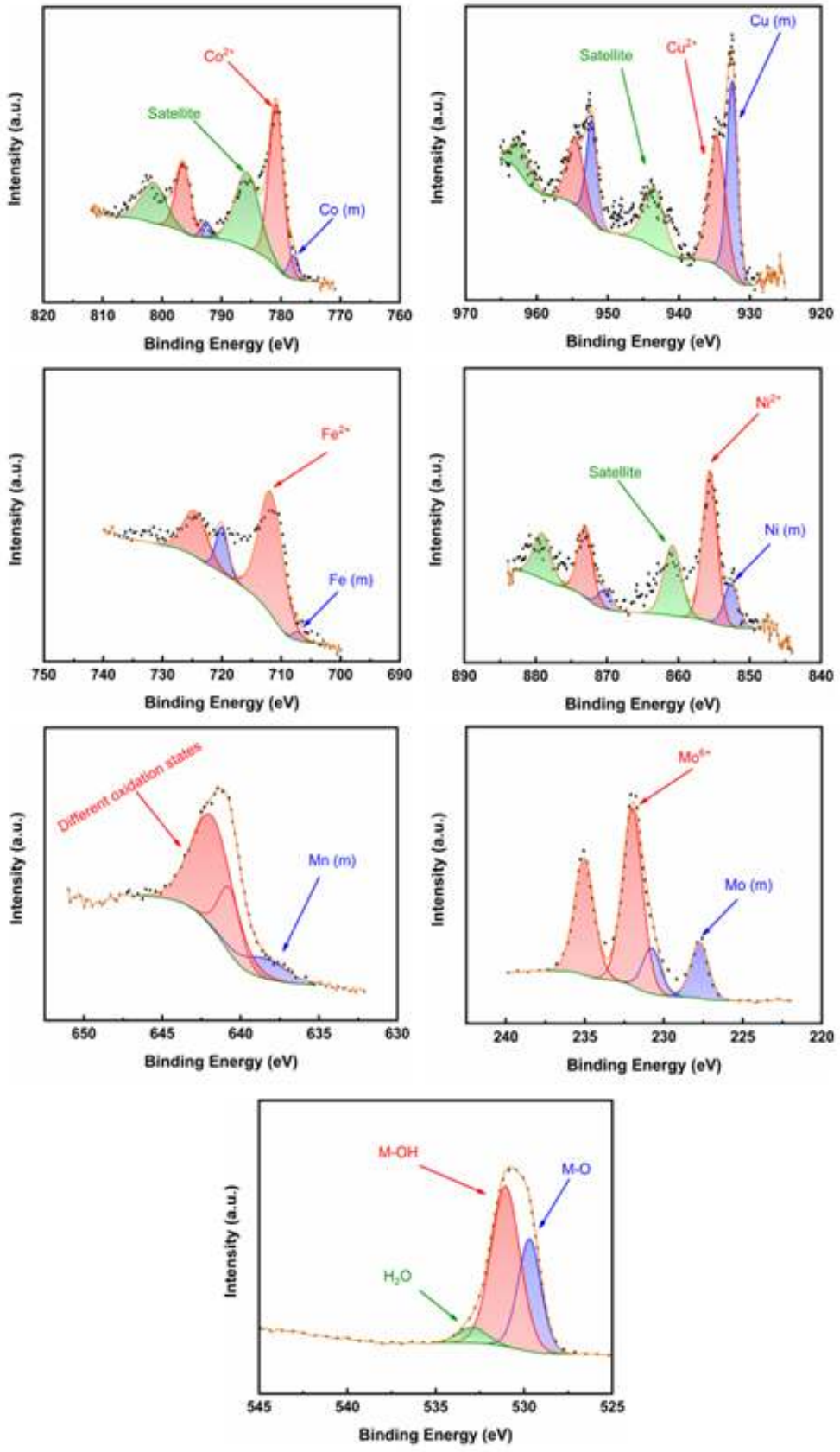

Figure 7. 10. XPS spectra of constituent elements for mechanically alloyed $CoCuFeNiMnMo_{1.5}$ HEA

7.3.4 OER Activity

OER performance of the mechanically alloyed samples was evaluated in 1 M KOH electrolyte saturated with O_2. As shown in Figure 7. 11a, A linear sweep voltammetry (LSV) measurement was performed at a scan rate of 10 $mV.s^{-1}$. In order to gain a comprehensive understanding of OER mechanisms, Tafel plots of OER reactions were plotted against the current density as the required overpotential. To determine the OER kinetics, the slopes of these plots are taken into account. Figure 7. 11b shows the Tafel slope of mechanically alloyed HEAs. Tafel slope is obtained from the LSV curve by:

$$\eta = a + b\log j \qquad \text{Eq.7}$$

ŋ, j, and b represent the overpotential, corresponding current density, and Tafel slope, respectively.

A summary of the overpotentials and slopes of the Tafel curves for the electrocatalysts is shown in Figure 7. 11c. As it was shown in Figure 7. 11c, the overpotential to achieve 10 $mA.cm^{-2}$ current density was 480 ± 12 mV, 420 ± 10 mV, 410 ± 14 mV, 395 ± 12 mV, and 375 ± 15 mV for CoCuFeNiMn, CoCuFeNiMo, $CoCuFeNiMnMo_{0.5}$ CoCuFeNiMnMo, and $CoCuFeNiMnMo_{1.5}$, respectively. Also, the equimolar CoCuFeNiMo electrocatalyst exhibits a smaller Tafel slope of 61 mV/decade compared to the other mechanically alloyed HEA electrocatalysts. When the OER gets underway and potential is applied, the surface - already saturated with adsorbed intermediates - contributes to a decrease in the OER process's kinetic rate. Subsequently, there's an escalation in the value of the Tafel slope. This electrochemical behavior was also observed in the literature [331]. For $CoCuFeNiMnMo_{1.5}$ electrocatalyst, long-term electrolysis stability (Figure 7. 11d) was investigated at the current density of 10 $mA.cm^{-2}$, HEA electrode displayed a stable overpotential for 72h. Remarkably, the outcome of the ICP-MS examination conducted after 72 hours revealed that the presence of dissolved Co, Cu, and Mo ions in the electrolyte was extremely low, and no detection of other elements was observed. The experiments revealed that the insertion of Mo into the CoCuFeNi enhances the OER activity. On the other side, the contribution of Mn in the structure and producing equimolar CoCuFeNiMn HEA results in the slightest improvement in the OER performance. Due to this, other factors, such as electronic effects and cocktail effects, are potentially more effective for performance improvement than the High-entropy effect [332,333]. Incorporation of Mo into the HEA structures

results in the change in the electronic state of surface atoms, which favors the adsorption of intermediate spaces on the catalyst surface.

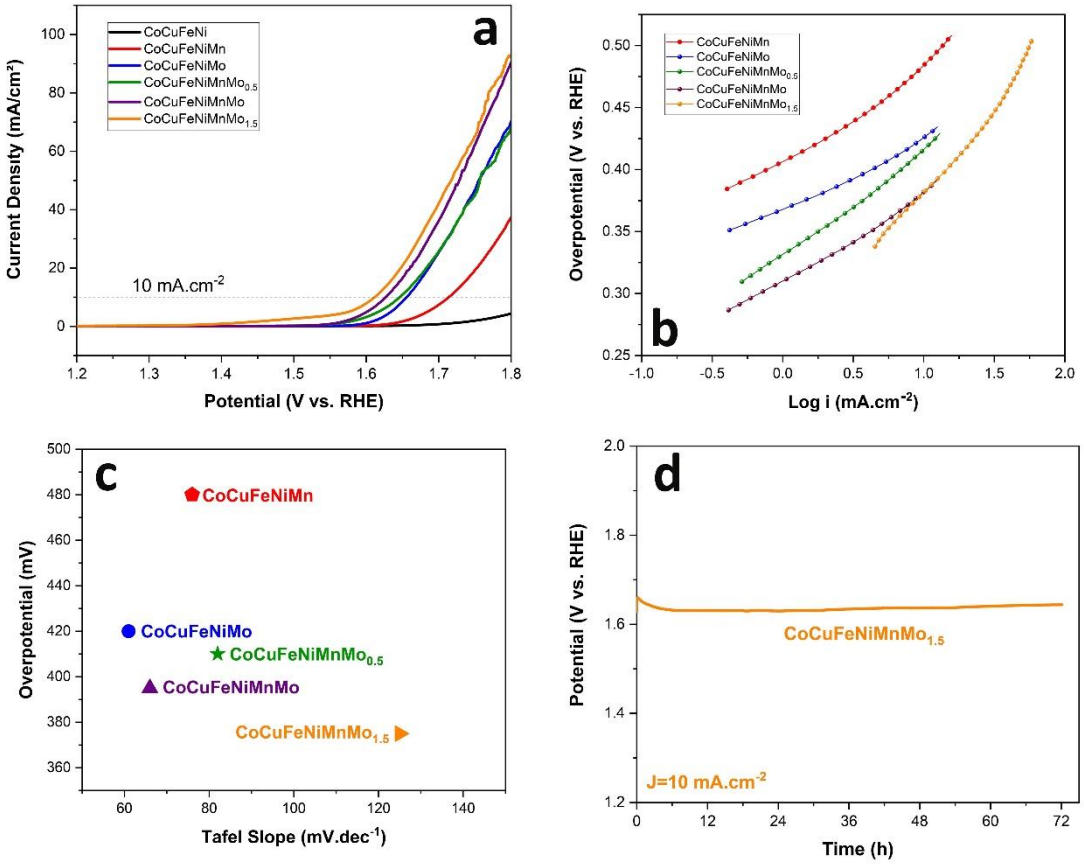

Figure 7. 11. Electrochemical investigations for OER in 1.0 M KOH. a) The LSV curves of different catalysts (results are not IR-corrected), b) corresponding Tafel slopes, c) Tafel slope compared to overpotential, and d) chronopotentiometry stability test.

The OER performance of the $CoCuFeNiMnMo_{1.5}$ catalyst was found to be superior to that of other transition metal-based electrocatalysts, as reported in Table 7. 4 and Figure 7. 12. Additionally, Table 7. 4 presents a comparative analysis of the overpotential for the OER between the synthesized HEA and commercially employed electrocatalysts, as well as the state-of-the-art noble metal system. This evidence highlights the potential of HEA as a viable option for electrocatalytic applications.

Table 7. 4. Summary of OER activity of HEAs in this and previous studies

Composition	Structural feature	Overpotential at 10 mA.cm^{-2}	Tafel slope/ (mV·dec^{-1})	Electrolyte	Ref
$CoCuFeNiMnMo_{1.5}$	Ball mill powders	375 ± 15 mV	140	1.0 M KOH	This work
Co-Fe-Ga-Ni-Zn	Nanoparticles	370 mV	71	1.0 M KOH	[334]
HEO $(Co, Cu, Fe, Mn, Ni)_3O_4$	Nanoparticles	400	76.7	1.0 M KOH	[335]
$(Mn_{0.19}Fe_{0.19}Ni_{0.19}Cr_{0.18}Zn_{0.18})_3O_4$	Nanoparticles	413	----	1.0 M KOH	[336]
$(Mn_{0.19}Fe_{0.19}Ni_{0.19}Cr_{0.18}Co_{0.19})_3O_4$	Nanoparticles	386	---	1.0 M KOH	[336]
MnFeCoNi	Ball mill powders	377	99.6	1.0 M KOH	[337]
CoFeLaNiPt	Nanoparticles	377 ± 4 mV	---	0.1 M KOH	[338]
NiO	Nanoparticles	576	236	1.0 M KOH	[339]
Ni_3Fe alloy	Mesoporous	372	75	0.1 M KOH	[340]
20% Ru/C	---	390	---	0.1 M KOH	[341]
IrO_2	----	340	116	1.0 M KOH	[342]
RuO2	----	370	66	1.0 M KOH	[343]

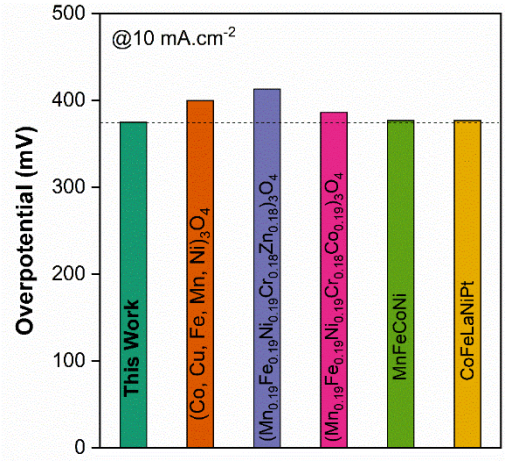

Figure 7. 12. Summary of OER activity of HEAs in this and previous studies

7.3.5 HER Activity

Similar to OER, the catalyst powders for HER were loaded on the GC electrodes, and a negative potential window was generated in 1 M KOH. An illustration of the relevant LSV curves and their Tafel slopes can be found in Figure 7. 13a and Figure 7. 13b. Figure 7. 13c summarizes the overpotentials and Tafel slopes of mechanically alloyed electrocatalysts specimens. According to this Figure, the overpotential for attaining -10 $mA.cm^{-2}$ current density was 605 ± 10 mV, 445 ± 14 mV, 286 ± 11 mV, 275 ± 12 mV, 315 ± 14 mV, and 385 ± 13 mV for CoCuFeN, CoCuFeNiMn, CoCuFeNiMo, $CoCuFeNiMnMo_{0.5}$, CoCuFeNiMnMo, and $CoCuFeNiMnMo_{1.5}$, respectively. The results show that the overpotential for CoCuFeNiMnMo0.5 (275 ± 12 mV) was much smaller than that of CoCuFeNi, demonstrating that this composition is beneficial for the best electrocatalytic performance.

As can be seen in Figure 7. 13c, the plotted Tafel slopes for mechanically alloyed catalysts show a correlation between current density and overpotential, which can be used to study the HER kinetics and eventually to determine its mechanism. In theory, the Volmer adsorption and desorption processes in an alkali solution follow two paths:

$$\text{Volmer step: } H_2O + e^- \rightarrow OH^- + H_{ad}$$

$$\text{Heyrovsky step: } H_2O + e^- + H_{ad} \rightarrow OH^- + H_2$$

In alkaline media, Had represents hydrogen adsorption.

According to the Volmer adsorption process, hydrogen binds to the catalyst in alkaline media, followed by the Heyrovsky step that desorbs it.

Tafel slopes in the Volmer-Heyrovsky mechanism are typically within the range of 40-120 $mV.dec^{-1}$ [344]. As reported in Figure 6c, the Tafel slope of CoCuFeNiMo is 125 $mV \cdot dec^{-1}$, showing that the CoCuFeNiMo catalyst has the most rapid kinetics in HER. For the $CoCuFeNiMnMo_{0.5}$ electrocatalyst, long-term electrolysis stability was investigated (Figure 7. 13d) at the current density of 10 $mA.cm^{-2}$, and the $CoCuFeNiMnMo_{0.5}$ HEA electrode displayed a stable overpotential for 72 h.

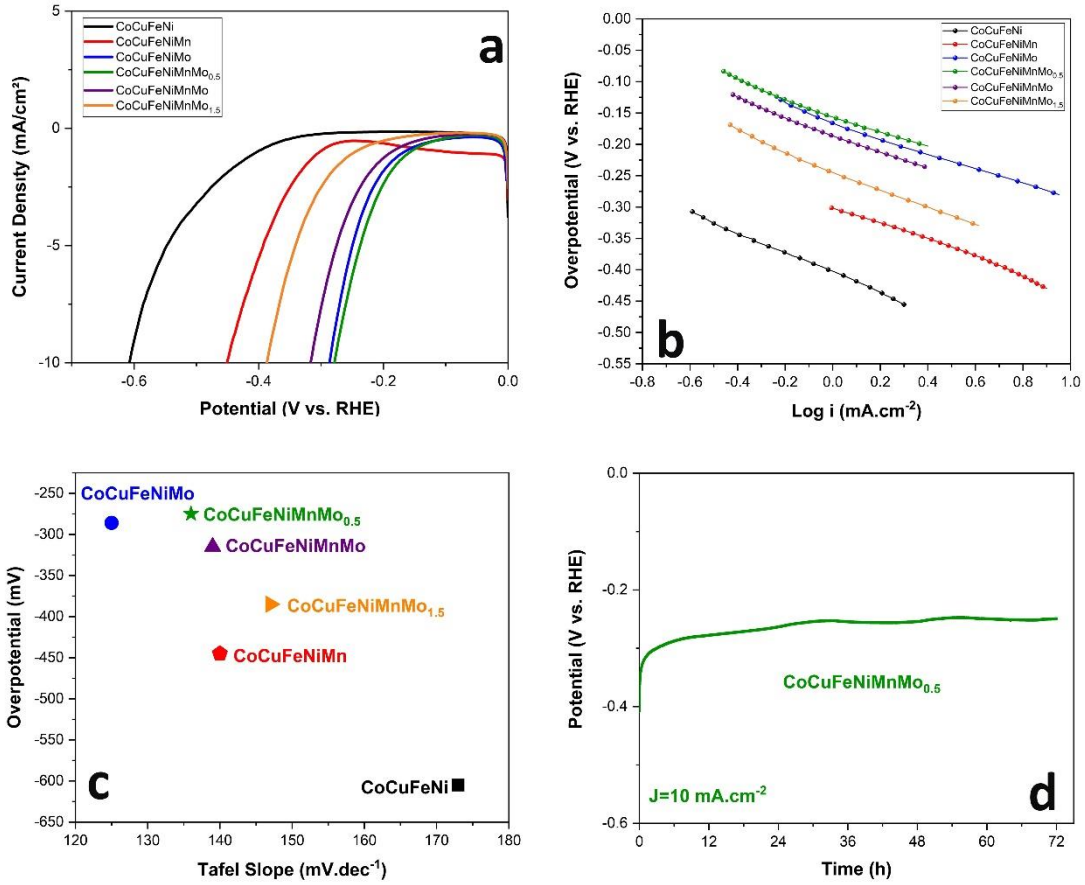

Figure 7. 13. Electrochemical investigations for HER in 1.0 M KOH. a) The LSV curves of different catalysts (results are not IR-corrected), b) corresponding Tafel slopes, c) Tafel slope compared to overpotential, and d) chronopotentiometry stability test.

Finally, Figure 7. 14 compares LSV curves for HER potential region before and immediately after the stability test. The LSV curves showed little overpotential increase at -10 mA.cm^{-2} from 278 mV to 311 mV (89% retention) after 72 h. Notably, the results of the ICP-MS analysis performed after 72 hours indicated that the levels of Co, Cu, and Mo ions dissolved in the electrolyte were exceptionally minimal, and no evidence of other elements was found. The remarkable catalytic characteristics of high-entropy alloys could be explained by the electronic effects resulting from the particular atomic configuration and structure, as well as the synergic effect, which is commonly known as the "cocktail effect" in HEAs [118,345].

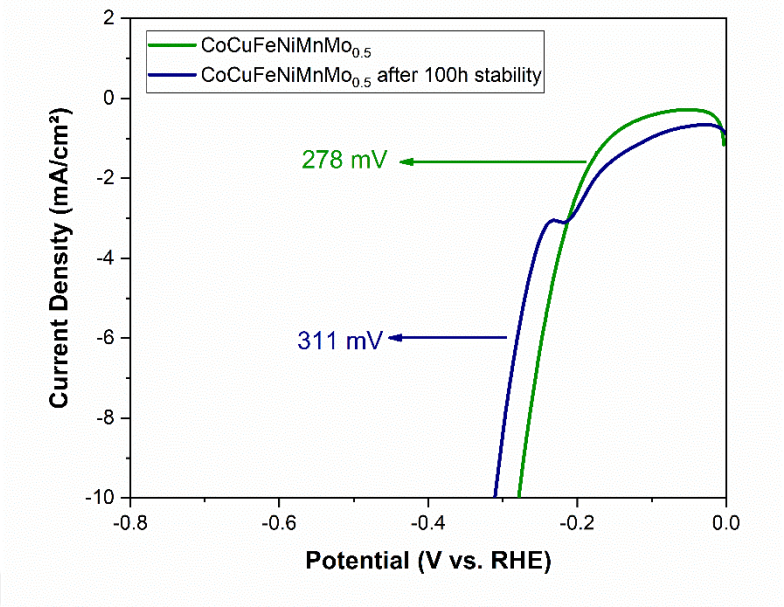

Figure 7. 14. LSV curves for $CoCuFeNiMnMo_{0.5}$ HEA electrode before and after 72-h stability test.

The HER performance of the $CoCuFeNiMnMo_{0.5}$ is better than that of other transition metal-based electrocatalysts, as shown in Table 7. 5 and Figure 7. 15.

Additionally, an examination was conducted to assess the impact of employing various counter electrodes on the overpotential of OER and HER. Two optimal samples for HER and OER were selected, and the Pt counter electrode was substituted with a pure graphite electrode. The outcomes depicted in Figure 7. 16 indicated that altering the counter electrode does not influence the overpotential for HER and OER.

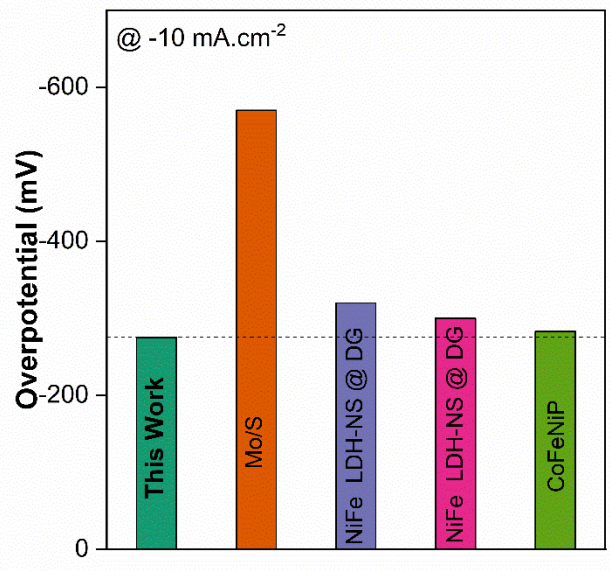

Figure 7. 15. Summary of HER activity of HEAs in this and previous studies

Table 7. 5. Summary of HER activity of HEAs in this and previous studies

Composition	Structural feature	Overpotential at 10 mA.cm^{-2}	Tafel slope/ (mV·dec^{-1})	Electrolyte	Ref
$CoCuFeNiMnMo_{0.5}$	Ball mill powders	275 ± 12 mV	136	1.0 M KOH	This work
CoCuFeNiMo	Ball mill powders	286 ± 11 mV	125	1.0 M KOH	This work
NiCoFeP	Nanoparticles	283 mV	----	1.0 M KOH	[129]
NiFe LDH-NS @ DG	Pyrolysis	300 mV	110	1.0 M KOH	[346]
Co_9S_8@NC	----	400 mV	154.1	1.0 M KOH	[347]
Mo/S	Anodic deposition	570 mv	----	1.0 M NaOH	[348]
Pt	---	100 mv	----	1.0 M NaOH	[349]

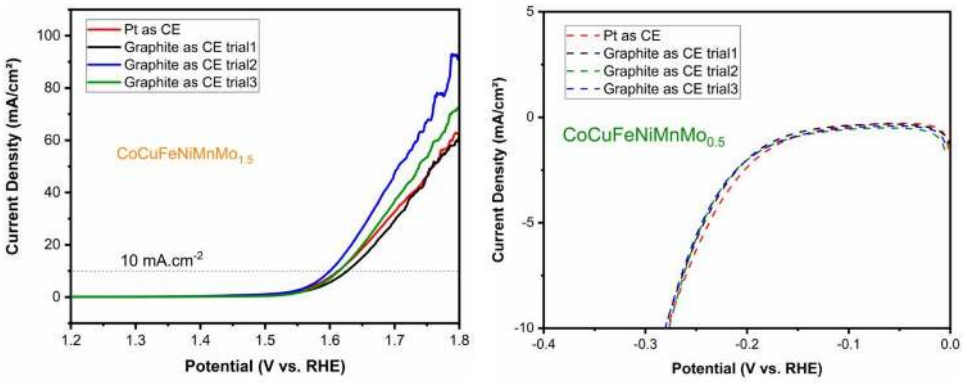

Figure 7. 16. LSV curves for OER and HER show the difference between using Pt and pure Graphite as counter electrodes.

7.3.6 Surface Analysis of the HEA electrode

The electrochemically active surface area (ECSA) was estimated with the double-layer capacitance (C_{dl}) method. In order to examine the ECSA, CVs at five different scan rates in the range of 10 - 80 mV/s) were conducted in the potential range of 1.1-1.2V. The corresponding CVs are depicted in Figure 7. 17. ECSA was calculated from the following equation:

$$ECSA = C_{dl}/C_s \quad \text{Eq.8}$$

in which C_s represent the sample's specific capacitance, and Cdl is the double-layer capacitance estimated from the i_c vs. ν plot according to the equation:

$$i_c = \nu C_{dl} \qquad \text{Eq.9}$$

where i_c is the charging current and ν is the scan rate.

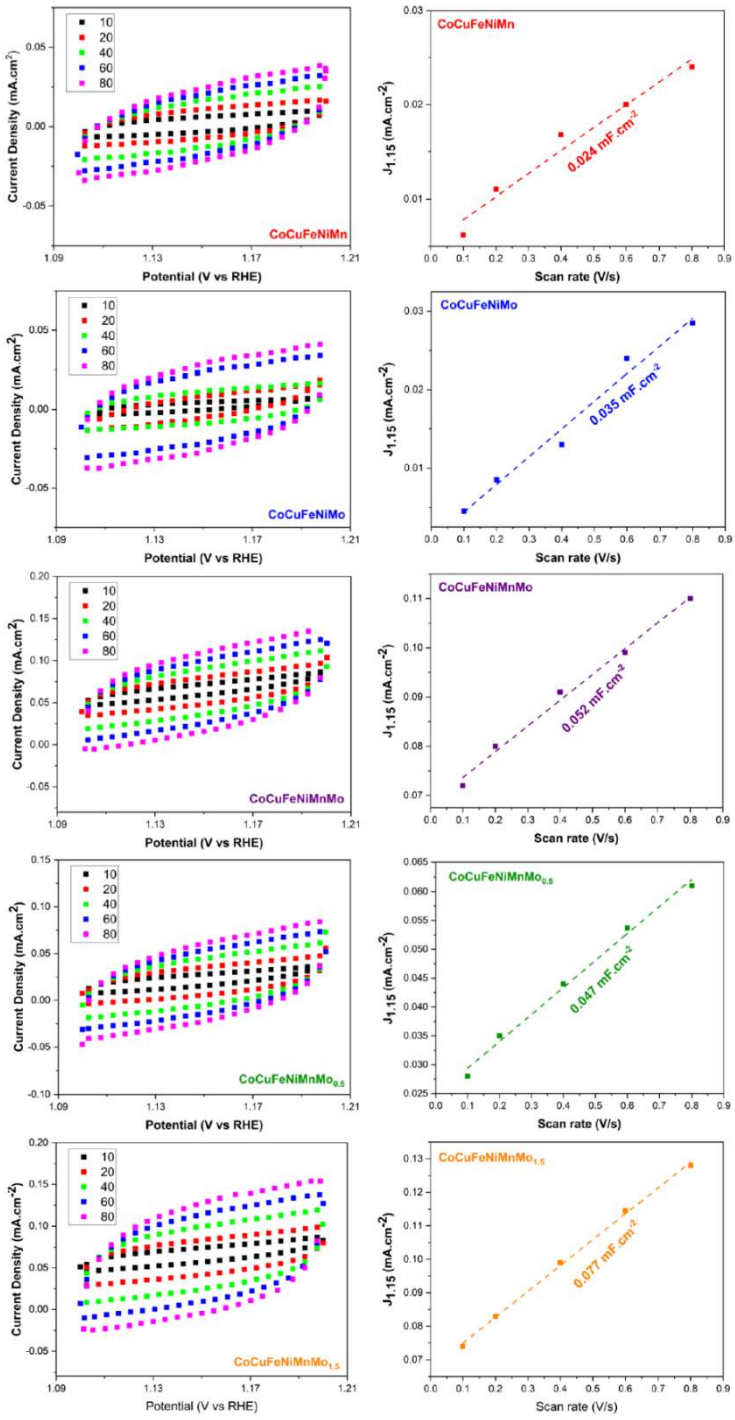

Figure 7. 17. Left: Cyclic voltammetry of HEA powders measured at different scan rate (10-80 mV s-1), and Right the linear plot of capacitive current densities vs. scan rate.

It has been previously indicated that C_s equals 0.040 mF.cm^{-2} in 1 M KOH solution [350]. From Figure 7. 17, the calculated C_{dl} value for CoCuFeNiMnMo$_{1.5}$ is 0.077 mF.cm^{-2}, which is larger than the obtained results for CoCuFeNiMnMo and CoCuFeNiMnMo$_{0.5}$ (0.052 and 0.047 mF.cm^{-2}, respectively). Calculated ECSA values for the mechanically alloyed HEA electrocatalysts were 1.925, 1.3, and 1.175 for CoCuFeNiMnMo$_{1.5}$, CoCuFeNiMnMo, and CoCuFeNiMnMo$_{0.5}$, respectively, as presented in Figure 7. 18a. It has been demonstrated that an increase in the concentration of Mo (molybdenum) leads to a corresponding increase in the ECSA. This, in turn, results in enhanced catalytic activity for the OER due to the larger ECSA [121]. Also, TOF demonstrates the same order, and TOF of the CoCuFeNiMnMo$_{1.5}$ catalyst presents a higher value of 0.004 s^{-1} at the overpotential of 380 mV and increased 2 times compared to the TOF value of CoCuFeNiMnMo$_{0.5}$, which was 0.002 S^{-1}.

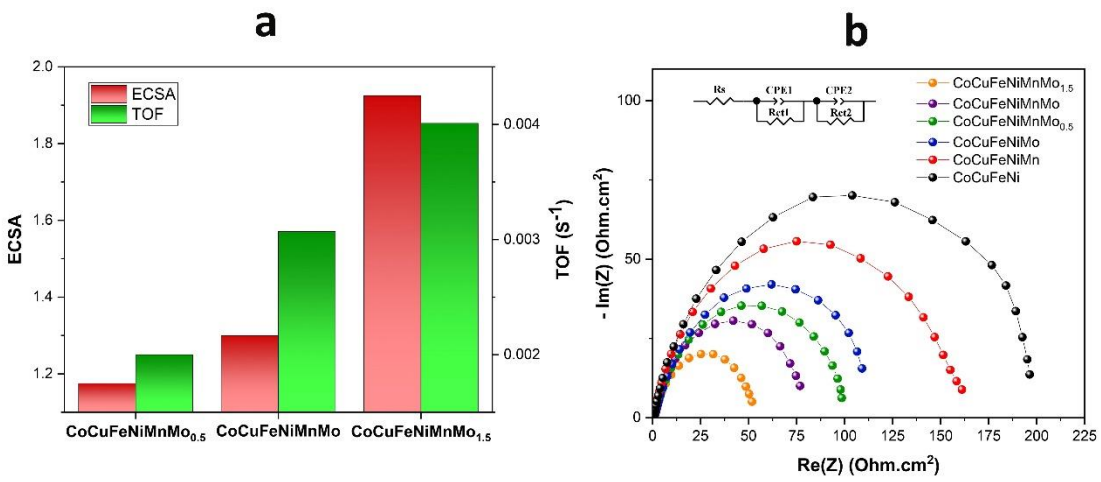

Figure 7. 18. a) ECSA and TOF values of CoCuFeNiMnMo$_{0.5}$, CoCuFeNiMnMo, and CoCuFeNiMnMo$_{1.5}$ and b) EIS Nyquist spectra of produced powders

The EIS technique was used to analyze the interfacial behavior of HEA electrodes, and the impact of constituent elements on the EIS was investigated and presented in Figure 7. 18b. In this case, the high-frequency resistance indicates the solution resistance (R_s), while the arc radius of the Nyquist plot represents the charge transfer resistance (R_{ct}) [351,352]. Obviously, the CoCuFeNiMnMo$_{1.5}$ electrode had a lower R_s of 0.51 Ω.cm^2 and R_{ct} of 57.6 Ω.cm^2 than the other HEA electrodes, which could be ascribed to the developed rate of the charge transfer and conversion of intermediates. Also, CoCuFeNiMnMo and CoCuFeNiMnMo$_{0.5}$ exhibited small R_{ct} values of 86.8 Ω.cm^2 and

107.7 $\Omega.cm^2$, respectively. The detailed results of EIS test can be find in Table 7. 6. These findings are consistent with the LSV curves for OER in Figure 7. 11a as well as ESCA and TOF values in Figure 7. 18a.

Table 7. 6. Equivalent circuit elements values of HEA specimens for EIS.

	Rs (Ωcm^2)	CPE1 ($\mu\Omega^{-1}S^n cm^{-2}$)	n	R1 (Ωcm^2)	CPE2 ($\mu\Omega^{-1}S^n cm^{-2}$)	n	R2 (Ωcm^2)
CoCuFeNi	0.68	6.84E-4	0.80	13.4	5.63E-4	0.84	193.1
CoCuFeNiMn	0.69	4.27E-4	0.81	10.5	9.65E-4	0.83	144
CoCuFeNiMo	0.65	1.91E-4	0.83	8.7	7.78E-4	0.81	118.1
$CoCuFeNiMnMo_{0.5}$	0.64	3.21E-4	0.82	7.2	7.96E-4	0.81	100.5
CoCuFeNiMnMo	0.55	6.49E-4	0.83	6.1	2.41E-4	0.83	80.7
$CoCuFeNiMnMo_{1.5}$	0.51	6.54E-4	0.83	4.5	2.27E-4	0.82	53.1

7.3.7 Overall water splitting

For overall water splitting, as seen in Figure 7. 20a, a chronopotentiometric stability test for $CoCuFeNiMnMo_{1.5}$ ‖ $CoCuFeNiMnMo_{0.5}$ was performed at a current density of 20 $mA.cm^{-2}$ for 12 h in 1 M KOH. Also, the chronopotentiometry stability test for GE ‖ GE was done (Figure 7. 19a) at the same condition, and after 1h, the current density was continuously decreased. As it is evident from the Figure 7. 19b, the $CoCuFeNiMnMo_{1.5}$ ‖ $CoCuFeNiMnMo_{0.5}$ electrolyzer requires a 1.76 V cell voltage to achieve the 10 $mA.cm^{-2}$ current density. In the end, a well-sealed cell was used for quantitatively collecting the H_2 gas generated at 20 $mA.cm^{-2}$. A comparison was made between the measured H_2 and theoretical values based on the supplied charges (Figure 7. 20b). As shown in Figure 7. 20b, there is a reasonable correlation between the measured and theoretical amounts of H_2 gas. Therefore, Eq. 2 can be used to calculate the Faradaic efficiency. By so doing, over 80% of the Faradaic efficiency can be reached for H_2 (Figure 7. 20c).

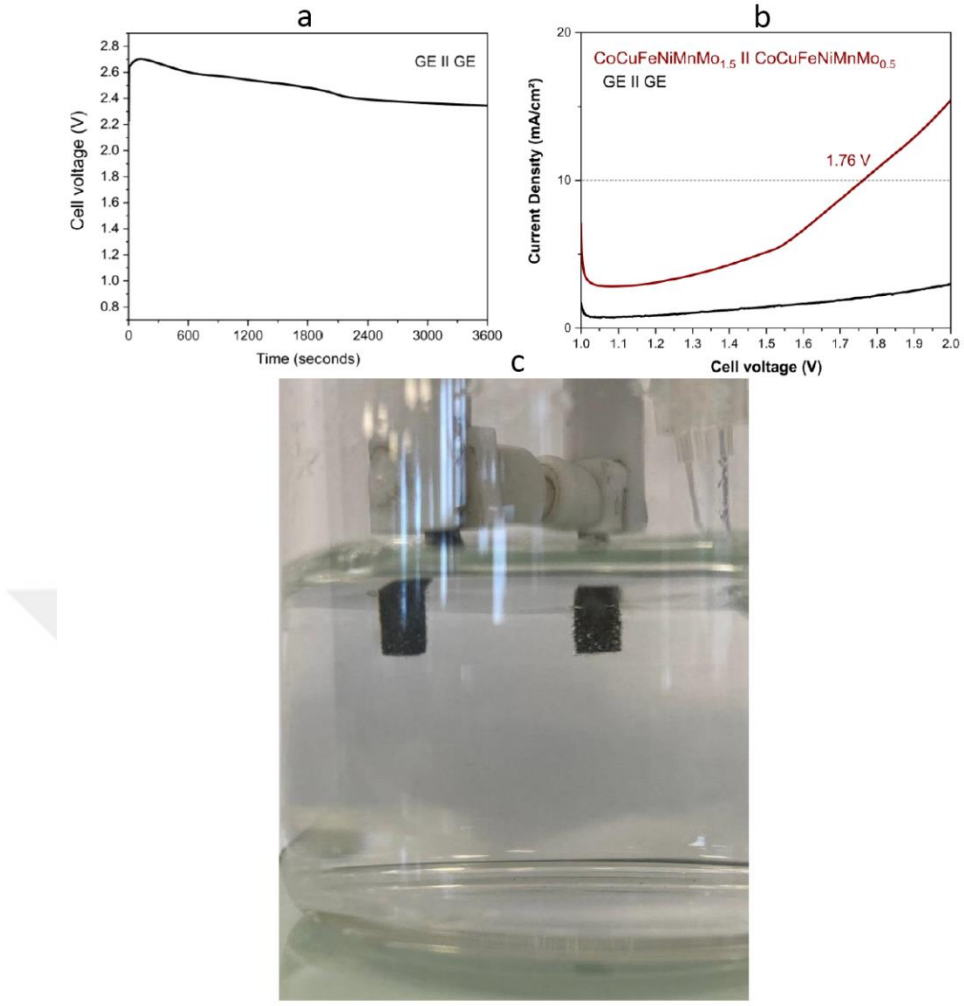

Figure 7. 19. a) Chronopotentiometric investigations of two-electrode overall water-splitting cells, b) Polarization curves of $CoCuFeNiMnMo_{0.5}$ and $CoCuFeNiMnMo_{1.5}$ catalysts used as the cathode (−) and anode (+), respectively, in a two-electrode cell recorded on GE substrate. (GE‖GE couples polarization curves for the sake of comparison) c) A digital photograph of two-electrode cell used in this work showing the evolution of H_2.

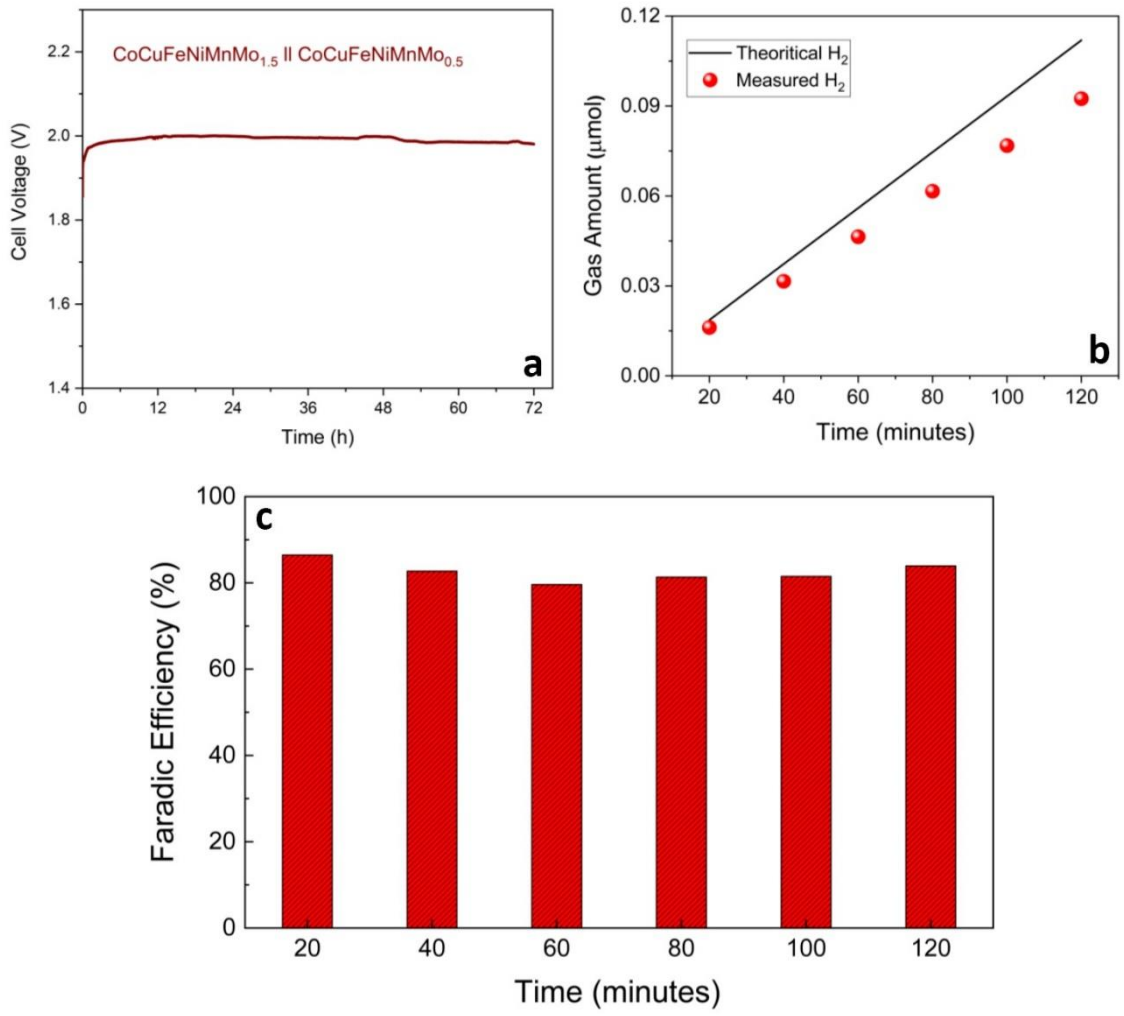

Figure 7. 20. Electrochemical investigations of two-electrode overall water-splitting cells. a) Chronopotentiometric curves of $CoCuFeNiMnMo_{1.5}$ ǁ $CoCuFeNiMnMo_{0.5}$, b) Theoretical and experimental H_2 production as a function of the work times for the overall water-splitting process, c) Faradic Efficiency of Produced H_2 gas.

7.4 Conclusion

The characterization and phase study show that mechanically alloyed powders without Mo content are composed of a single FCC phase while adding Mo leads to a mixture of FCC and BCC phases. The OER and HER activity of mechanically alloyed samples of HEAs were evaluated in a 1 M KOH electrolyte. It was found that the insertion of Mo into the CoCuFeNi structure of the HEAs improved the OER activity, while the contribution of Mn did not significantly improve the OER performance. In addition, it was found that the $CoCuFeNiMnMo_{0.5}$ HEA had the best electrocatalytic performance for the HER, with a lower overpotential than the other HEA samples. The ECSA of

various mechanically alloyed HEA electrocatalysts was calculated by measuring their Cdl using CV at different scan rates. It was found that the ECSA values for the HEA electrocatalysts were in the order of $CoCuFeNiMnMo_{1.5}$ > CoCuFeNiMnMo > $CoCuFeNiMnMo_{0.5}$. The EIS technique was used to analyze the interfacial behavior of the HEA electrodes and showed that the $CoCuFeNiMnMo_{1.5}$ electrode had lower high-frequency resistance (indicating the solution resistance, Rs) and charge transfer resistance (Rct) values compared to the other HEA electrodes, which could be attributed to its improved charge transfer and conversion of intermediates. The cell voltage required to achieve a current density of 10 $mA.cm^{-2}$ was measured and found to be 1.76 V for the electrolyzer with $CoCuFeNiMnMo_{1.5}$ ‖ $CoCuFeNiMnMo_{0.5}$ electrodes. The results showed a reasonable correlation between the measured and theoretical amounts of H_2 gas, indicating that the Faradaic efficiency of the electrolysis reaction was over 80%. This research offers a wealth of empirical and theoretical insights that can be applied in the development of CoCuFeNi-based HEA electrocatalysts. The simplicity and efficiency of the fabrication process, in addition to the inexpensive nature of the Co, Cu, Fe, Ni, Mn, and Mo elements utilized, make this material a promising and cost-effective option for electrochemical water splitting.

CHAPTER 8

CONCLUSION

In this doctoral dissertation, a comprehensive exploration was conducted on the characteristics and potential applications of High Entropy Alloys (HEAs), particularly focusing on their suitability as coatings for biomedical implants and their efficacy as electrocatalysts. The study spanned five main chapters, each delving into different facets of HEAs, including their microstructure, mechanical properties, electrochemical behavior, biocompatibility, and catalytic performance. This conclusion synthesizes the key findings from each chapter to present a cohesive understanding of the research.

The third chapter explored the deposition of non-equimolar $Ti_{1.5}Ta_{0.5}Hf_{0.5}Nb_{0.5}Zr$ RHEA films on 316L, CoCrMo, and Ti6Al4V substrates using RF magnetron sputtering. This investigation aimed to evaluate the suitability of RHEA films as alternative coatings for metallic biomaterials. Observations showed that the RHEA films presented a dense, smooth, and cauliflower-like appearance with an amorphous configuration. Despite being amorphous, the films exhibited grain boundaries, which were formed by the expansion of the void network. The mechanical attributes of the substrates significantly improved following the application of the RHEA films, evidenced by marked increases in hardness levels. Scratch test outcomes revealed the RHEA film's superior adhesion on the Ti6Al4V substrate, showcasing enhanced resistance to cracking and delamination in comparison to other substrates. Corrosion tests in PBS solution indicated that the RHEA-coated Ti6Al4V substrate displayed a consistent passive plateau without pitting, signifying improved corrosion resistance. Further validation came from EIS results, which indicated that the RHEA-coated Ti6Al4V sample possessed the highest charge transfer resistance, suggesting outstanding adhesion at the film/substrate interface and enhanced corrosion resistance in PBS solution.

In the fourth chapter, attention was turned to the structural attributes, mechanical properties, corrosion resistance, and biocompatibility of uncoated 316L substrates and various RHEA films. The research underscored the viability of RHEA3 as an effective protective coating for 316L biomaterials. The RHEA films applied exhibited an amorphous structure with granular features of varying sizes. The surface layers of these films consisted of elements in their oxide and/or sub-oxide states. The smoothness and consistency of the film surfaces were corroborated by roughness measurements, which were all below 4 nm. The deposition of RHEA films on 316L substrates enhanced their wettability, crucial for bone integration on metallic implants. The RHEA-coated specimens demonstrated marked improvements in hardness, with RHEA2 and RHEA3

showing significantly higher values than RHEA1. The application of RHEA films notably enhanced the tribological behavior of 316L, with RHEA3 exhibiting the greatest wear resistance. Scratch testing indicated that RHEA1 and RHEA2 began to crack and peel off at a critical load, whereas RHEA3 showed superior adhesion and scratch resistance with minimal delamination. Electrochemical tests in PBS solution showed that RHEA films significantly boosted the biocorrosion resistance of 316L substrates, with RHEA3 achieving the highest resistance. ICP-MS analysis confirmed that RHEA coatings reduced the release of Ni and Cr ions into the PBS during biocorrosion tests, with the RHEA3 coated specimen reducing these ion releases by up to 92%. In vitro cytotoxicity tests using C2C12 muscle myoblast cells indicated that the RHEA films were non-cytotoxic and supported healthy cell proliferation.

The fifth chapter delved into the microstructure, mechanical properties, and electrochemical behavior of Ti6Al4V substrates, both undoped and Ag-doped with non-equimolar $Ti_{1.5}ZrTa_{0.5}Nb_{0.5}W_{0.5}$ RHEA films applied via RF magnetron sputtering. The study confirmed that Ag nanoparticles could be effectively incorporated into the structure of the RHEA films, meeting the criteria for biomedical use. Both undoped and Ag-doped RHEA films, displaying a cauliflower-like morphology, were deposited on the substrates. The constituent elements—Ti, Zr, Ta, Nb, and W—along with the Ag dopant in the form of semi-spherical nanoparticles, were evenly dispersed throughout the film structures. Nanoindentation tests showed that the coated specimens significantly improved in terms of surface mechanical properties, including hardness and elastic modulus. The dense amorphous structure of the RHEA films contributed to this enhancement in mechanical characteristics. The addition of Ag nanoparticles increased both the roughness and the contact angle of the coated specimens. Compared to the undoped films, the presence of semi-spherical Ag nanoparticles led to higher roughness and, consequently, increased contact angle. Biocorrosion tests indicated that while fluctuations in current were observed at higher potentials in the Ti6Al4V substrate, a constant passive plateau without pitting was noted in both the RHEA and RHEA-9Ag NP specimens. This finding aligns with the corrosion current, corrosion rate, and polarization resistance measurements, all of which pointed to improved electrochemical behavior in the coated specimens. Specifically, the RHEA-9Ag NPs displayed better corrosion rate and polarization efficiency, underscoring the beneficial impact of embedding Ag nanoparticles on the biocorrosion resistance of the RHEA film. EIS results confirmed that the RHEA-9Ag NPs

specimen achieved the lowest double-layer capacitance and the highest polarization resistance, validating the anti-corrosive properties of Ag nanoparticles and the protective capability of the deposited film.

The sixth chapter discussed the creation of a novel Ag nanoparticles doped $Ti_{1.5}ZrTa_{0.5}Nb_{0.5}W_{0.5}$ RHEA film, composed of biocompatible elements and containing 9 atomic percent Ag, which was successfully deposited on a Ti6Al4V substrate to serve as an antibacterial coating. Microstructural evaluations confirmed the amorphous structure of both the undoped and Ag-doped films. The RHEA-9Ag NPs coated specimen demonstrated potent antibacterial activity against both Gram-negative and Gram-positive bacteria. An in vitro biocompatibility assessment using C2C12 muscle myoblast cells cultured on the specimens for 72 hours showed that both the undoped and Ag-doped films were non-cytotoxic and proved to be even safer than the Ti6Al4V alloy itself. The outstanding antibacterial activity, along with the cell proliferation capabilities, superior mechanical properties, and improved biocorrosion behavior established in previous studies, highlight the significant potential of Ag nanoparticles doped RHEA films as a biocompatible antibacterial coating for metallic implants.

In the seventh chapter, the characterization and phase analysis revealed that mechanically alloyed powders without Mo consist solely of a FCC phase, whereas the inclusion of Mo results in a blend of FCC and BCC phases. The OER and HER activities of the HEAs were evaluated in a 1 M KOH electrolyte. It was discovered that integrating Mo into the CoCuFeNi structure of the HEAs enhanced the OER activity, although the addition of Mn did not significantly boost the OER performance. Furthermore, the $CoCuFeNiMnMo_{0.5}$ HEA demonstrated superior electrocatalytic performance for the HER, achieving a lower overpotential compared to other HEA samples. ECSA of various mechanically alloyed HEA electrocatalysts was determined by measuring their Cdl using CV at varying scan rates. The ECSA values were ranked as follows: $CoCuFeNiMnMo_{1.5}$ > CoCuFeNiMnMo > $CoCuFeNiMnMo_{0.5}$. EIS was employed to assess the interfacial behavior of the HEA electrodes, indicating that the $CoCuFeNiMnMo_{1.5}$ electrode exhibited lower high-frequency resistance (solution resistance, Rs) and charge transfer resistance (Rct) compared to other HEA electrodes, suggesting enhanced charge transfer and conversion of intermediates. The cell voltage necessary to achieve a current density of 10 $mA.cm^{-2}$ was measured at 1.76 V for the electrolyzer equipped with $CoCuFeNiMnMo_{1.5}$ ‖ $CoCuFeNiMnMo_{0.5}$ electrodes. The results demonstrated a

reasonable agreement between the measured and theoretical amounts of hydrogen gas, confirming that the Faradaic efficiency of the electrolysis reaction exceeded 80%. This chapter offers substantial experimental insights that can guide the development of CoCuFeNi-based HEA electrocatalysts. The straightforward and efficient fabrication process, coupled with the affordable nature of the elements used (Co, Cu, Fe, Ni, Mn, and Mo), positions this material as a viable and cost-effective alternative for electrochemical water splitting applications.

In conclusion, this thesis has provided a comprehensive investigation into the potential of HEAs as alternative coatings for metallic biomaterials and as efficient electrocatalysts for energy conversion processes. Through a series of experimental studies, it was demonstrated that HEA films could enhance the mechanical properties, biocompatibility, and corrosion resistance of metallic substrates, making them suitable for biomedical applications. Additionally, the research explored the electrocatalytic performance of mechanically alloyed HEA samples, highlighting their potential in improving the efficiency of electrochemical water splitting. The findings contribute to the advancement of HEA research and offer valuable insights for the development of novel materials with enhanced properties for biomedical and energy-related applications.

BIBLIOGRAPHY

[1] Y. Zhang, Y.J. Zhou, J.P. Lin, G.L. Chen, P.K. Liaw, Solid-solution phase formation rules for multi-component alloys, Adv Eng Mater 10 (2008) 534–538. https://doi.org/10.1002/adem.200700240.

[2] J.W. Yeh, S.K. Chen, S.J. Lin, J.Y. Gan, T.S. Chin, T.T. Shun, C.H. Tsau, S.Y. Chang, Nanostructured high-entropy alloys with multiple principal elements: Novel alloy design concepts and outcomes, Adv Eng Mater 6 (2004) 299–303. https://doi.org/10.1002/adem.200300567.

[3] B. He, Y. Zu, Y. Mei, Design of advanced electrocatalysts for the high-entropy alloys: Principle, progress, and perspective, J Alloys Compd 958 (2023) 170479. https://doi.org/10.1016/j.jallcom.2023.170479.

[4] E.P. George, D. Raabe, R.O. Ritchie, High-entropy alloys, Nat Rev Mater 4 (2019) 515–534. https://doi.org/10.1038/s41578-019-0121-4.

[5] Y. Sun, S. Dai, High-entropy materials for catalysis: A new frontier, 2021. https://www.science.org.

[6] Y. Ma, Y. Ma, Q. Wang, S. Schweidler, M. Botros, T. Fu, H. Hahn, T. Brezesinski, B. Breitung, High-entropy energy materials: Challenges and new opportunities, Energy Environ Sci 14 (2021) 2883–2905. https://doi.org/10.1039/d1ee00505g.

[7] S.A. Lee, J. Bu, J. Lee, H.W. Jang, High-Entropy Nanomaterials for Advanced Electrocatalysis, Small Science 3 (2023). https://doi.org/10.1002/smsc.202200109.

[8] B. Cantor, I.T.H. Chang, P. Knight, A.J.B. Vincent, Microstructural development in equiatomic multicomponent alloys, Materials Science and Engineering A 375–377 (2004) 213–218. https://doi.org/10.1016/j.msea.2003.10.257.

[9] Z.U. Arif, M.Y. Khalid, A. Al Rashid, E. ur Rehman, M. Atif, Laser deposition of high-entropy alloys: A comprehensive review, Opt Laser Technol 145 (2022). https://doi.org/10.1016/j.optlastec.2021.107447.

[10] D.B. Miracle, O.N. Senkov, A critical review of high entropy alloys and related concepts, Acta Mater 122 (2017) 448–511. https://doi.org/10.1016/j.actamat.2016.08.081.

[11] Y. Yao, J. Chen, R. Niu, Z. Zhao, X. Wang, High-Entropy Materials: Features for Lithium–Sulfur Battery Applications, Metals (Basel) 13 (2023). https://doi.org/10.3390/met13050833.

[12] Y. Zhang, T.T. Zuo, Z. Tang, M.C. Gao, K.A. Dahmen, P.K. Liaw, Z.P. Lu, Microstructures and properties of high-entropy alloys, Prog Mater Sci 61 (2014) 1–93. https://doi.org/10.1016/j.pmatsci.2013.10.001.

[13] L.J. Santodonato, Y. Zhang, M. Feygenson, C.M. Parish, M.C. Gao, R.J.K. Weber, J.C. Neuefeind, Z. Tang, P.K. Liaw, Deviation from high-entropy configurations in the atomic distributions of a multi-principal-element alloy, Nat Commun 6 (2015). https://doi.org/10.1038/ncomms6964.

[14] Y. Zou, S. Maiti, W. Steurer, R. Spolenak, Size-dependent plasticity in an Nb25Mo25Ta25W25 refractory high-entropy alloy, Acta Mater 65 (2014) 85–97. https://doi.org/10.1016/J.ACTAMAT.2013.11.049.

[15] C.W. Tsai, Y.L. Chen, M.H. Tsai, J.W. Yeh, T.T. Shun, S.K. Chen, Deformation and annealing behaviors of high-entropy alloy Al0.5CoCrCuFeNi, J Alloys Compd 486 (2009) 427–435. https://doi.org/10.1016/J.JALLCOM.2009.06.182.

[16] W.H. Liu, Y. Wu, J.Y. He, T.G. Nieh, Z.P. Lu, Grain growth and the Hall–Petch relationship in a high-entropy FeCrNiCoMn alloy, Scr Mater 68 (2013) 526–529. https://doi.org/10.1016/J.SCRIPTAMAT.2012.12.002.

[17] X. Wang, W. Guo, Y. Fu, High-entropy alloys: Emerging materials for advanced functional applications, J Mater Chem A Mater 9 (2021) 663–701. https://doi.org/10.1039/d0ta09601f.

[18] Y. Brif, M. Thomas, I. Todd, The use of high-entropy alloys in additive manufacturing, Scr Mater 99 (2015) 93–96. https://doi.org/10.1016/J.SCRIPTAMAT.2014.11.037.

[19] P.D. Jablonski, J.J. Licavoli, M.C. Gao, J.A. Hawk, Manufacturing of High Entropy Alloys, JOM 67 (2015) 2278–2287. https://doi.org/10.1007/s11837-015-1540-3.

[20] Y.J. Jia, H.N. Chen, X.D. Liang, Microstructure and wear resistance of CoCrNbNiW high-entropy alloy coating prepared by laser melting deposition, Rare Metals 38 (2019) 1153–1159. https://doi.org/10.1007/s12598-019-01342-y.

[21] K.Y. Tsai, M.H. Tsai, J.W. Yeh, Sluggish diffusion in Co-Cr-Fe-Mn-Ni high-entropy alloys, Acta Mater 61 (2013) 4887–4897. https://doi.org/10.1016/j.actamat.2013.04.058.

[22] S. Varalakshmi, G. Appa Rao, M. Kamaraj, B.S. Murty, Hot consolidation and mechanical properties of nanocrystalline equiatomic AlFeTiCrZnCu high entropy

alloy after mechanical alloying, J Mater Sci 45 (2010) 5158–5163. https://doi.org/10.1007/s10853-010-4246-5.

[23] W. Ji, Z. Fu, W. Wang, H. Wang, J. Zhang, Y. Wang, F. Zhang, Mechanical alloying synthesis and spark plasma sintering consolidation of CoCrFeNiAl high-entropy alloy, J Alloys Compd 589 (2014) 61–66. https://doi.org/10.1016/J.JALLCOM.2013.11.146.

[24] S. Calderon Velasco, A. Cavaleiro, S. Carvalho, Functional properties of ceramic-Ag nanocomposite coatings produced by magnetron sputtering, Prog Mater Sci 84 (2016) 158–191. https://doi.org/10.1016/J.PMATSCI.2016.09.005.

[25] S. Varalakshmi, M. Kamaraj, B.S. Murty, Synthesis and characterization of nanocrystalline AlFeTiCrZnCu high entropy solid solution by mechanical alloying, J Alloys Compd 460 (2008) 253–257. https://doi.org/10.1016/J.JALLCOM.2007.05.104.

[26] C. Suryanarayana, Mechanical Alloying: A Novel Technique to Synthesize Advanced Materials, Research 2019 (2019). https://doi.org/10.34133/2019/4219812.

[27] B. Zhang, Y. Duan, Y. Cui, G. Ma, T. Wang, X. Dong, A new mechanism for improving electromagnetic properties based on tunable crystallographic structures of FeCoNiSi: XAl0.4 high entropy alloy powders, RSC Adv 8 (2018) 14936–14946. https://doi.org/10.1039/c8ra01762j.

[28] V. Shivam, J. Basu, Y. Shadangi, M.K. Singh, N.K. Mukhopadhyay, Mechano-chemical synthesis, thermal stability and phase evolution in AlCoCrFeNiMn high entropy alloy, J Alloys Compd 757 (2018) 87–97. https://doi.org/10.1016/J.JALLCOM.2018.05.057.

[29] C. Kursun, M. Gogebakan, E. Uludag, M.S. Bozgeyik, F.S. Uludag, Structural, electrical and magnetic properties of Nd – A – CoO3 (A = Sr, Ca) Perovskite Powders by Mechanical Alloying, Sci Rep 8 (2018). https://doi.org/10.1038/s41598-018-31458-7.

[30] Z. Szklarz, J. Lekki, P. Bobrowski, M.B. Szklarz, Ł. Rogal, The effect of SiC nanoparticles addition on the electrochemical response of mechanically alloyed CoCrFeMnNi high entropy alloy, Mater Chem Phys 215 (2018) 385–392. https://doi.org/10.1016/J.MATCHEMPHYS.2018.05.056.

[31] F. Alijani, M. Reihanian, K. Gheisari, Study on phase formation in magnetic FeCoNiMnV high entropy alloy produced by mechanical alloying, J Alloys Compd 773 (2019) 623–630. https://doi.org/10.1016/J.JALLCOM.2018.09.204.

[32] R.B. Mane, B.B. Panigrahi, Effect of alloying order on non-isothermal sintering kinetics of mechanically alloyed high entropy alloy powders, Mater Lett 217 (2018) 131–134. https://doi.org/10.1016/J.MATLET.2018.01.092.

[33] M. Murali, S.P.K. Babu, B.J. Krishna, A. Vallimanalan, Synthesis and characterization of AlCoCrCuFeZnx high-entropy alloy by mechanical alloying, Progress in Natural Science: Materials International 26 (2016) 380–384. https://doi.org/10.1016/J.PNSC.2016.06.008.

[34] N.A. Khan, RF Magnetron Sputtered AlCoCrCu 0.5 FeNi High Entropy Alloy (HEA) and High Entropy Ceramic (HEC) Thin Films, 2021.

[35] J. Cieslak, J. Tobola, K. Berent, M. Marciszko, Phase composition of AlxFeNiCrCo high entropy alloys prepared by sintering and arc-melting methods, J Alloys Compd 740 (2018) 264–272. https://doi.org/10.1016/J.JALLCOM.2017.12.333.

[36] Y. Chen, S. Zhu, X. Wang, B. Yang, Z. Ren, G. Han, S. Wen, The strength-ductility balance of Al0·4CoCu0.6NiTix (x≤1.0) and Al0·4CoCu0·6NiSi0.2Tix (x≤0.5) high entropy alloys by regulating the proportion of Ti and improving the cooling rate, Vacuum 155 (2018) 270–279. https://doi.org/10.1016/J.VACUUM.2018.06.020.

[37] P. Zhang, Y. Li, Z. Chen, J. Zhang, B. Shen, Oxidation response of a vacuum arc melted NbZrTiCrAl refractory high entropy alloy at 800–1200 °C, Vacuum 162 (2019) 20–27. https://doi.org/10.1016/J.VACUUM.2019.01.026.

[38] X.H. Yan, J.S. Li, W.R. Zhang, Y. Zhang, A brief review of high-entropy films, Mater Chem Phys 210 (2018) 12–19. https://doi.org/10.1016/J.MATCHEMPHYS.2017.07.078.

[39] M.D. Cropper, Thin films of AlCrFeCoNiCu high-entropy alloy by pulsed laser deposition, Appl Surf Sci 455 (2018) 153–159. https://doi.org/10.1016/J.APSUSC.2018.05.172.

[40] S. Chuhan, Microstructure, Mechanical Properties, Scratch Responses and Wear Behaviours of Transition Metal Nitride and High Entropy Alloy Coatings, (n.d.). https://doi.org/10.26190/unsworks/22205.

[41] F. Sanchette, C. Ducros, T. Schmitt, P. Steyer, A. Billard, Nanostructured hard coatings deposited by cathodic arc deposition: From concepts to applications, Surf Coat Technol 205 (2011) 5444–5453. https://doi.org/10.1016/J.SURFCOAT.2011.06.015.

[42] J.M. Lackner, W. Waldhauser, R. Berghauser, R. Ebner, B. Major, T. Schöberl, Structural, mechanical and tribological investigations of pulsed laser deposited titanium nitride coatings, Thin Solid Films 453–454 (2004) 195–202. https://doi.org/10.1016/J.TSF.2003.11.106.

[43] P.J. Kelly, R.D. Arnell, Magnetron sputtering: a review of recent developments and applications, Vacuum 56 (2000) 159–172. https://doi.org/10.1016/S0042-207X(99)00189-X.

[44] I. Safi, Recent aspects concerning DC reactive magnetron sputtering of thin films: a review, Surf Coat Technol 127 (2000) 203–218. https://doi.org/10.1016/S0257-8972(00)00566-1.

[45] W.D. Sproul, P.J. Rudnik, M.E. Graham, S.L. Rohde, High rate reactive sputtering in an opposed cathode closed-field unbalanced magnetron sputtering system, Surf Coat Technol 43–44 (1990) 270–278. https://doi.org/10.1016/0257-8972(90)90080-V.

[46] Q. Xing, H. Wang, M. Chen, Z. Chen, R. Li, P. Jin, Y. Zhang, Mechanical properties and corrosion resistance of NbTiAlSiZrNx high-entropy films prepared by RF magnetron sputtering, Entropy 21 (2019). https://doi.org/10.3390/e21040396.

[47] F. Lukác, P. Hruška, S. Cichon, T. Vlasák, J. Cížek, T. Kmjec, O. Melikhova, M. Butterling, M.O. Liedke, A. Wagner, Defects in thin layers of high entropy alloy HfNbTaTiZr, Acta Phys Pol A 137 (2020) 219–221. https://doi.org/10.12693/APhysPolA.137.219.

[48] S. Chen, Z. Cai, Z. Lu, J. Pu, R. Chen, S. Zheng, C. Mao, S. Chen, Tribo-corrosion behavior of VAlTiCrCu high-entropy alloy film, Mater Charact 157 (2019) 109887. https://doi.org/10.1016/J.MATCHAR.2019.109887.

[49] W.B. Liao, H. Zhang, Z.Y. Liu, P.F. Li, J.J. Huang, C.Y. Yu, Y. Lu, High strength and deformation mechanisms of Al0.3CoCrFeNi high-entropy alloy thin films fabricated by magnetron sputtering, Entropy 21 (2019). https://doi.org/10.3390/e21020146.

[50] N. Tüten, D. Canadinc, A. Motallebzadeh, B. Bal, Microstructure and tribological properties of TiTaHfNbZr high entropy alloy coatings deposited on Ti6Al4V substrates, Intermetallics (Barking) 105 (2019) 99–106. https://doi.org/10.1016/J.INTERMET.2018.11.015.

[51] X. Yu, J. Wang, L. Wang, W. Huang, Fabrication and characterization of CrNbSiTiZr high-entropy alloy films by radio-frequency magnetron sputtering via tuning substrate bias, Surf Coat Technol 412 (2021) 127074. https://doi.org/10.1016/J.SURFCOAT.2021.127074.

[52] W. Zhang, R. Tang, Z.B. Yang, C.H. Liu, H. Chang, J.J. Yang, J.L. Liao, Y.Y. Yang, N. Liu, Preparation, structure, and properties of an AlCrMoNbZr high-entropy alloy coating for accident-tolerant fuel cladding, Surf Coat Technol 347 (2018) 13–19. https://doi.org/10.1016/J.SURFCOAT.2018.04.037.

[53] N. Behravan, A. Farhadizadeh, S. Ghasemi, A. Khademi, H. Shojaei, H. Ghomi, The pressure dependence of structure and composition of sputtered AlCrSiTiMoO high entropy thin film, J Alloys Compd 852 (2021) 156421. https://doi.org/10.1016/J.JALLCOM.2020.156421.

[54] W.H. Kao, Y.L. Su, J.H. Horng, H.M. Wu, Effects of carbon doping on mechanical, tribological, structural, anti-corrosion and anti-glass-sticking properties of CrNbSiTaZr high entropy alloy coatings, Thin Solid Films 717 (2021) 138448. https://doi.org/10.1016/J.TSF.2020.138448.

[55] P.K. Huang, J.W. Yeh, Effects of nitrogen content on structure and mechanical properties of multi-element (AlCrNbSiTiV)N coating, Surf Coat Technol 203 (2009) 1891–1896. https://doi.org/10.1016/J.SURFCOAT.2009.01.016.

[56] S. PalDey, S.C. Deevi, Single layer and multilayer wear resistant coatings of (Ti,Al)N: a review, Materials Science and Engineering: A 342 (2003) 58–79. https://doi.org/10.1016/S0921-5093(02)00259-9.

[57] P.C. Wo, X.L. Zhao, P.R. Munroe, Z.F. Zhou, K.Y. Li, D. Habibi, Z.H. Xie, Extremely hard, damage-tolerant ceramic coatings with functionally graded, periodically varying architecture, Acta Mater 61 (2013) 193–204. https://doi.org/10.1016/J.ACTAMAT.2012.09.049.

[58] Y.W. Lin, J.H. Huang, G.P. Yu, Effect of nitrogen flow rate on properties of nanostructured TiZrN thin films produced by radio frequency magnetron sputtering, Thin Solid Films 518 (2010) 7308–7311. https://doi.org/10.1016/J.TSF.2010.04.099.

[59] A. Singh, P. Kuppusami, S. Khan, C. Sudha, R. Thirumurugesan, R. Ramaseshan, R. Divakar, E. Mohandas, S. Dash, Influence of nitrogen flow rate on microstructural and nanomechanical properties of Zr–N thin films prepared by pulsed DC magnetron sputtering, Appl Surf Sci 280 (2013) 117–123. https://doi.org/10.1016/J.APSUSC.2013.04.107.

[60] J.A. Thornton, INFLUENCE OF APPARATUS GEOMETRY AND DEPOSITION CONDITIONS ON THE STRUCTURE AND TOPOGRAPHY OF THICK SPUTTERED COATINGS., in: J Vac Sci Technol, 1974: pp. 666–670. https://doi.org/10.1116/1.1312732.

[61] P.B. Barna, M. Adamik, Fundamental structure forming phenomena of polycrystalline films and the structure zone models, Thin Solid Films 317 (1998) 27–33. https://doi.org/10.1016/S0040-6090(97)00503-8.

[62] P.R. Willmott, J.R. Huber, RMP Colloquia Pulsed laser vaporization and deposition, n.d.

[63] X.J. Hua, P. Hu, H.R. Xing, J.Y. Han, S.W. Ge, S.L. Li, C.J. He, K.S. Wang, C.J. Cui, Development and Property Tuning of Refractory High-Entropy Alloys: A Review, The Chinese Society for Metals, 2022. https://doi.org/10.1007/s40195-022-01382-x.

[64] O.N. Senkov, G.B. Wilks, D.B. Miracle, C.P. Chuang, P.K. Liaw, Refractory high-entropy alloys, Intermetallics (Barking) 18 (2010) 1758–1765. https://doi.org/10.1016/j.intermet.2010.05.014.

[65] O.N. Senkov, G.B. Wilks, J.M. Scott, D.B. Miracle, Mechanical properties of Nb25Mo25Ta25W25 and V20Nb20Mo20Ta20W20 refractory high entropy alloys, Intermetallics (Barking) 19 (2011) 698–706. https://doi.org/10.1016/J.INTERMET.2011.01.004.

[66] G.M. Karthik, P. Asghari-Rad, P. Sathiyamoorthi, A. Zargaran, E.S. Kim, T.S. Kim, H.S. Kim, Architectured multi-metal CoCrFeMnNi-Inconel 718 lamellar composite by high-pressure torsion, Scr Mater 195 (2021) 113722. https://doi.org/10.1016/J.SCRIPTAMAT.2021.113722.

[67] M. Li, Q. Chen, X. Cui, X. Peng, G. Huang, Evaluation of corrosion resistance of the single-phase light refractory high entropy alloy TiCrVNb0.5Al0.5 in chloride environment, J Alloys Compd 857 (2021) 158278. https://doi.org/10.1016/J.JALLCOM.2020.158278.

[68] M. Feuerbacher, T. Lienig, C. Thomas, A single-phase bcc high-entropy alloy in the refractory Zr-Nb-Ti-V-Hf system, Scr Mater 152 (2018) 40–43. https://doi.org/10.1016/J.SCRIPTAMAT.2018.04.009.

[69] E. Fazakas, V. Zadorozhnyy, L.K. Varga, A. Inoue, D. V. Louzguine-Luzgin, F. Tian, L. Vitos, Experimental and theoretical study of Ti20Zr20Hf20Nb20X20 (X = V or Cr) refractory high-entropy alloys, Int J Refract Metals Hard Mater 47 (2014) 131–138. https://doi.org/10.1016/J.IJRMHM.2014.07.009.

[70] J. Málek, J. Zýka, F. Lukáč, M. Vilémová, T. Vlasák, J. Čížek, O. Melikhova, A. Macháčková, H.S. Kim, The effect of processing route on properties of HfNbTaTiZr high entropy alloy, Materials 12 (2019). https://doi.org/10.3390/ma12234022.

[71] P.K. Sarswat, S. Sarkar, A. Murali, W. Huang, W. Tan, M.L. Free, Additive manufactured new hybrid high entropy alloys derived from the AlCoFeNiSmTiVZr system, Appl Surf Sci 476 (2019) 242–258. https://doi.org/10.1016/J.APSUSC.2018.12.300.

[72] B. Kang, J. Lee, H.J. Ryu, S.H. Hong, Ultra-high strength WNbMoTaV high-entropy alloys with fine grain structure fabricated by powder metallurgical process, Materials Science and Engineering: A 712 (2018) 616–624. https://doi.org/10.1016/J.MSEA.2017.12.021.

[73] Y. Long, X. Liang, K. Su, H. Peng, X. Li, A fine-grained NbMoTaWVCr refractory high-entropy alloy with ultra-high strength: Microstructural evolution and mechanical properties, J Alloys Compd 780 (2019) 607–617. https://doi.org/10.1016/J.JALLCOM.2018.11.318.

[74] W. Xiong, A.X.Y. Guo, S. Zhan, C.T. Liu, S.C. Cao, Refractory high-entropy alloys: A focused review of preparation methods and properties, J Mater Sci Technol 142 (2023) 196–215. https://doi.org/10.1016/j.jmst.2022.08.046.

[75] N.N. Guo, L. Wang, L.S. Luo, X.Z. Li, R.R. Chen, Y.Q. Su, J.J. Guo, H.Z. Fu, Hot deformation characteristics and dynamic recrystallization of the MoNbHfZrTi refractory high-entropy alloy, Materials Science and Engineering: A 651 (2016) 698–707. https://doi.org/10.1016/J.MSEA.2015.10.113.

[76] J. Yi, S. Tang, C. Zhang, M. Xu, L. Yang, L. Wang, L. Zeng, Microstructure and Mechanical Properties of a New Refractory Equiatomic CrHfNbTaTi High-Entropy Alloy, JOM 73 (2021) 934–940. https://doi.org/10.1007/s11837-020-04557-y.

[77] W. Guo, B. Liu, Y. Liu, T. Li, A. Fu, Q. Fang, Y. Nie, Microstructures and mechanical properties of ductile NbTaTiV refractory high entropy alloy prepared by powder metallurgy, J Alloys Compd 776 (2019) 428–436. https://doi.org/10.1016/J.JALLCOM.2018.10.230.

[78] Y. Cao, Y. Liu, Y. Li, B. Liu, A. Fu, Y. Nie, Precipitation behavior and mechanical properties of a hot-worked TiNbTa0.5ZrAl0.5 refractory high entropy alloy, Int J Refract Metals Hard Mater 86 (2020) 105132. https://doi.org/10.1016/J.IJRMHM.2019.105132.

[79] B. Kang, J. Lee, H.J. Ryu, S.H. Hong, Microstructure, mechanical property and Hall-Petch relationship of a light-weight refractory Al0.1CrNbVMo high entropy alloy fabricated by powder metallurgical process, J Alloys Compd 767 (2018) 1012–1021. https://doi.org/10.1016/J.JALLCOM.2018.07.145.

[80] S.K. Bachani, C.J. Wang, B.S. Lou, L.C. Chang, J.W. Lee, Microstructural characterization, mechanical property and corrosion behavior of VNbMoTaWAl refractory high entropy alloy coatings: Effect of Al content, Surf Coat Technol 403 (2020) 126351. https://doi.org/10.1016/J.SURFCOAT.2020.126351.

[81] S. Alvi, D. M. Jarzabek, M. Gilzad Kohan, D. Hedman, P. Jenczyk, M. Maria Natile, A. Vomiero, F. Akhtar, Synthesis and Mechanical Characterization of a CuMoTaWV High-Entropy Film by Magnetron Sputtering, ACS Applied Materials & Interfaces 12 (2020) 21070–21079. https://doi.org/10.1021/acsami.0c02156.

[82] T.G. de Oliveira, D.V. Fagundes, P. Capellato, D. Sachs, A.A.A.P. da Silva, A Review of Biomaterials Based on High-Entropy Alloys, Metals (Basel) 12 (2022) 1–20. https://doi.org/10.3390/met12111940.

[83] B. Ghiban, G. Popescu, C. Lazar, L. Rosu, I. Constantin, M. Olaru, B. Carlan, Corrosion Behaviour in Human Stimulation Media of a High Entropy Titan-Based Alloy, in: IOP Conf Ser Mater Sci Eng, Institute of Physics Publishing, 2018. https://doi.org/10.1088/1757-899X/374/1/012004.

[84] N. Ma, S. Liu, W. Liu, L. Xie, D. Wei, L. Wang, L. Li, B. Zhao, Y. Wang, Research Progress of Titanium-Based High Entropy Alloy: Methods, Properties, and Applications, Front Bioeng Biotechnol 8 (2020) 1–18. https://doi.org/10.3389/fbioe.2020.603522.

[85] M. Khodaei, F. Nejatidanesh, M.J. Shirani, S. Iyengar, H. Sina, A. Valanezhad, O. Savabi, Optimum temperature and chlorine ion concentration for hydrogen

peroxide treatment of titanium dental implant material, Journal of Materials Research and Technology 9 (2020) 13312–13319. https://doi.org/10.1016/J.JMRT.2020.09.040.

[86] Y.W. Cui, L.Y. Chen, P. Qin, R. Li, Q. Zang, J. Peng, L. Zhang, S. Lu, L. Wang, L.C. Zhang, Metastable pitting corrosion behavior of laser powder bed fusion produced Ti-6Al-4V in Hank's solution, Corros Sci 203 (2022) 110333. https://doi.org/10.1016/J.CORSCI.2022.110333.

[87] J. Feng, Y. Tang, J. Liu, P. Zhang, C. Liu, L. Wang, Bio-high entropy alloys: Progress, challenges, and opportunities, Front Bioeng Biotechnol 10 (2022) 1–26. https://doi.org/10.3389/fbioe.2022.977282.

[88] M. Gu, Y. Gong, X. Wu, Y. Dong, G.L. Wang, Surface polarization of BiOI to boost photoelectrochemical signal transduction for high-performance bioassays, Chemical Communications 58 (2022) 4651–4654. https://doi.org/10.1039/d2cc00019a.

[89] S. Zheng, J. Li, J. Zhang, K. Jiang, X. Liu, C. Chang, X. Wang, Effect of Si addition on the electrochemical corrosion and passivation behavior of Fe-Cr-Mo-C-B-Ni-P metallic glasses, J Non Cryst Solids 493 (2018) 33–40. https://doi.org/10.1016/J.JNONCRYSOL.2018.04.036.

[90] E.H. Hwang, J.S. Park, H.G. Seong, S.J. Kim, Analysis on surface film formed on high-strength carbon steels in acidic phosphate solution and its relationship with localized corrosion in a 3.5% NaCl solution, Journal of Materials Research and Technology 8 (2019) 1419–1426. https://doi.org/10.1016/J.JMRT.2018.10.007.

[91] Q.T. Song, J. Xu, (TiZrNbTa)90Mo10 high-entropy alloy: Electrochemical behavior and passive film characterization under exposure to Ringer's solution, Corros Sci 167 (2020). https://doi.org/10.1016/j.corsci.2020.108513.

[92] C.B. Aksoy, D. Canadinc, M.B. Yagci, Assessment of Ni ion release from TiTaHfNbZr high entropy alloy coated NiTi shape memory substrates in artificial saliva and gastric fluid, Mater Chem Phys 236 (2019) 121802. https://doi.org/10.1016/J.MATCHEMPHYS.2019.121802.

[93] S.P. Wang, J. Xu, TiZrNbTaMo high-entropy alloy designed for orthopedic implants: As-cast microstructure and mechanical properties, Materials Science and Engineering: C 73 (2017) 80–89. https://doi.org/10.1016/J.MSEC.2016.12.057.

[94] C.H. Yang, Y.T. Wang, W.F. Tsai, C.F. Ai, M.C. Lin, H.H. Huang, Effect of oxygen plasma immersion ion implantation treatment on corrosion resistance and

cell adhesion of titanium surface, Clin Oral Implants Res 22 (2011) 1426–1432. https://doi.org/10.1111/j.1600-0501.2010.02132.x.

[95] M. Rincic Mlinaric, K. Durgo, V. Katic, S. Spalj, Cytotoxicity and oxidative stress induced by nickel and titanium ions from dental alloys on cells of gastrointestinal tract, Toxicol Appl Pharmacol 383 (2019) 114784. https://doi.org/10.1016/J.TAAP.2019.114784.

[96] T. Hori, T. Nagase, M. Todai, A. Matsugaki, T. Nakano, Development of non-equiatomic Ti-Nb-Ta-Zr-Mo high-entropy alloys for metallic biomaterials, Scr Mater 172 (2019) 83–87. https://doi.org/10.1016/J.SCRIPTAMAT.2019.07.011.

[97] T. Nagase, Y. Iijima, A. Matsugaki, K. Ameyama, T. Nakano, Design and fabrication of Ti–Zr-Hf-Cr-Mo and Ti–Zr-Hf-Co-Cr-Mo high-entropy alloys as metallic biomaterials, Materials Science and Engineering: C 107 (2020) 110322. https://doi.org/10.1016/J.MSEC.2019.110322.

[98] P. Edalati, R. Floriano, Y. Tang, A. Mohammadi, K.D. Pereira, A.D. Luchessi, K. Edalati, Ultrahigh hardness and biocompatibility of high-entropy alloy TiAlFeCoNi processed by high-pressure torsion, Materials Science and Engineering: C 112 (2020) 110908. https://doi.org/10.1016/J.MSEC.2020.110908.

[99] M. Todai, T. Nagase, T. Hori, A. Matsugaki, A. Sekita, T. Nakano, Novel TiNbTaZrMo high-entropy alloys for metallic biomaterials, Scr Mater 129 (2017) 65–68. https://doi.org/10.1016/J.SCRIPTAMAT.2016.10.028.

[100] W. Yang, S. Pang, Y. Liu, Q. Wang, P.K. Liaw, T. Zhang, Design and properties of novel Ti–Zr–Hf–Nb–Ta high-entropy alloys for biomedical applications, Intermetallics (Barking) 141 (2022) 107421. https://doi.org/10.1016/J.INTERMET.2021.107421.

[101] 2006-Industrial development of high-entropy alloys (P, (n.d.).

[102] Z. Ke, C. Yi, L. Zhang, Z.Y. He, J. Tan, Y. Jiang, Characterization of a new Ti-13Nb-13Zr-10Cu alloy with enhanced antibacterial activity for biomedical applications, Mater Lett 253 (2019) 335–338. https://doi.org/10.1016/J.MATLET.2019.07.008.

[103] M. B. Kosnik, M. Zwicky Hauschild, P. Fantke, Toward Assessing Absolute Environmental Sustainability of Chemical Pollution, Environmental Science & Technology 56 (2022) 4776–4787. https://doi.org/10.1021/acs.est.1c06098.

[104] X. Wang, H. Zhong, S. Xi, W.S.V. Lee, J. Xue, Understanding of Oxygen Redox in the Oxygen Evolution Reaction, Advanced Materials 34 (2022). https://doi.org/10.1002/adma.202107956.

[105] C. Li, H. Jang, M.G. Kim, L. Hou, X. Liu, J. Cho, Ru-incorporated oxygen-vacancy-enriched MoO2 electrocatalysts for hydrogen evolution reaction, Applied Catalysis B: Environment and Energy 307 (2022) 121204. https://doi.org/10.1016/J.APCATB.2022.121204.

[106] X.M. Liu, X. Cui, K. Dastafkan, H.F. Wang, C. Tang, C. Zhao, A. Chen, C. He, M. Han, Q. Zhang, Recent advances in spinel-type electrocatalysts for bifunctional oxygen reduction and oxygen evolution reactions, Journal of Energy Chemistry 53 (2021) 290–302. https://doi.org/10.1016/J.JECHEM.2020.04.012.

[107] Y. Liu, B. Hu, S. Wu, M. Wang, Z. Zhang, B. Cui, L. He, M. Du, Hierarchical nanocomposite electrocatalyst of bimetallic zeolitic imidazolate framework and MoS2 sheets for non-Pt methanol oxidation and water splitting, Appl Catal B 258 (2019) 117970. https://doi.org/10.1016/J.APCATB.2019.117970.

[108] Q. Zhang, J. Guan, Single-Atom Catalysts for Electrocatalytic Applications, Adv Funct Mater 30 (2020). https://doi.org/10.1002/adfm.202000768.

[109] K. Chu, H. Nan, Q. Li, Y. Guo, Y. Tian, W. Liu, Amorphous MoS3 enriched with sulfur vacancies for efficient electrocatalytic nitrogen reduction, Journal of Energy Chemistry 53 (2021) 132–138. https://doi.org/10.1016/J.JECHEM.2020.04.074.

[110] Z. Li, H. He, H. Cao, S. Sun, W. Diao, D. Gao, P. Lu, S. Zhang, Z. Guo, M. Li, R. Liu, D. Ren, C. Liu, Y. Zhang, Z. Yang, J. Jiang, G. Zhang, Atomic Co/Ni dual sites and Co/Ni alloy nanoparticles in N-doped porous Janus-like carbon frameworks for bifunctional oxygen electrocatalysis, Appl Catal B 240 (2019) 112–121. https://doi.org/10.1016/J.APCATB.2018.08.074.

[111] L. Trotochaud, S.W. Boettcher, Precise oxygen evolution catalysts: Status and opportunities, Scr Mater 74 (2014) 25–32. https://doi.org/10.1016/J.SCRIPTAMAT.2013.07.019.

[112] N.T. Suen, S.F. Hung, Q. Quan, N. Zhang, Y.J. Xu, H.M. Chen, Electrocatalysis for the oxygen evolution reaction: Recent development and future perspectives, Chem Soc Rev 46 (2017) 337–365. https://doi.org/10.1039/c6cs00328a.

[113] R.P. Forslund, W.G. Hardin, X. Rong, A.M. Abakumov, D. Filimonov, C.T. Alexander, J.T. Mefford, H. Iyer, A.M. Kolpak, K.P. Johnston, K.J. Stevenson, Exceptional electrocatalytic oxygen evolution via tunable charge transfer

interactions in La0.5Sr1.5Ni1−xFexO4±δ Ruddlesden-Popper oxides, Nat Commun 9 (2018). https://doi.org/10.1038/s41467-018-05600-y.

[114] X. Huo, H. Yu, B. Xing, X. Zuo, N. Zhang, Review of High Entropy Alloys Electrocatalysts for Hydrogen Evolution, Oxygen Evolution, and Oxygen Reduction Reaction, Chemical Record 22 (2022). https://doi.org/10.1002/tcr.202200175.

[115] Y. Zhao, M. Luo, S. Chu, M. Peng, B. Liu, Q. Wu, P. Liu, F.M.F. de Groot, Y. Tan, 3D nanoporous iridium-based alloy microwires for efficient oxygen evolution in acidic media, Nano Energy 59 (2019) 146–153. https://doi.org/10.1016/J.NANOEN.2019.02.020.

[116] J. You, R. Yao, W. Ji, Y. Zhao, Z. Wang, Research of high entropy alloys as electrocatalyst for oxygen evolution reaction, J Alloys Compd 908 (2022) 164669. https://doi.org/10.1016/j.jallcom.2022.164669.

[117] H.J. Qiu, G. Fang, Y. Wen, P. Liu, G. Xie, X. Liu, S. Sun, Nanoporous high-entropy alloys for highly stable and efficient catalysts, J Mater Chem A Mater 7 (2019) 6499–6506. https://doi.org/10.1039/c9ta00505f.

[118] H.-J. Qiu, G. Fang, J. Gao, Y. Wen, J. Lv, H. Li, G. Xie, X. Liu, S. Sun, Noble Metal-Free Nanoporous High-Entropy Alloys as Highly Efficient Electrocatalysts for Oxygen Evolution Reaction, ACS Mater Lett 1 (2019) 526–533. https://doi.org/10.1021/acsmaterialslett.9b00414.

[119] Z. Jin, J. Lv, H. Jia, W. Liu, H. Li, Z. Chen, X. Lin, G. Xie, X. Liu, S. Sun, H.J. Qiu, Nanoporous Al-Ni-Co-Ir-Mo High-Entropy Alloy for Record-High Water Splitting Activity in Acidic Environments, Small 15 (2019). https://doi.org/10.1002/smll.201904180.

[120] Z. Ding, J. Bian, S. Shuang, X. Liu, Y. Hu, C. Sun, Y. Yang, High Entropy Intermetallic–Oxide Core–Shell Nanostructure as Superb Oxygen Evolution Reaction Catalyst, Adv Sustain Syst 4 (2020). https://doi.org/10.1002/adsu.201900105.

[121] J. Tang, J.L. Xu, Z.G. Ye, X.B. Li, J.M. Luo, Microwave sintered porous CoCrFeNiMo high entropy alloy as an efficient electrocatalyst for alkaline oxygen evolution reaction, J Mater Sci Technol 79 (2021) 171–177. https://doi.org/10.1016/J.JMST.2020.10.079.

[122] H. Wang, R. Wei, X. Li, X. Ma, X. Hao, G. Guan, Nanostructured amorphous Fe29Co27Ni23Si9B12 high-entropy-alloy: an efficient electrocatalyst for oxygen

evolution reaction, J Mater Sci Technol 68 (2021) 191–198. https://doi.org/10.1016/J.JMST.2020.06.045.

[123] J. Su, R. Ge, Y. Dong, F. Hao, L. Chen, Recent progress in single-atom electrocatalysts: Concept, synthesis, and applications in clean energy conversion, J Mater Chem A Mater 6 (2018) 14025–14042. https://doi.org/10.1039/c8ta04064h.

[124] J. Zhu, L. Hu, P. Zhao, L.Y.S. Lee, K.Y. Wong, Recent Advances in Electrocatalytic Hydrogen Evolution Using Nanoparticles, Chem Rev 120 (2020) 851–918. https://doi.org/10.1021/acs.chemrev.9b00248.

[125] X. Zou, Y. Zhang, Noble metal-free hydrogen evolution catalysts for water splitting, Chem Soc Rev 44 (2015) 5148–5180. https://doi.org/10.1039/c4cs00448e.

[126] M.W. Glasscott, A.D. Pendergast, S. Goines, A.R. Bishop, A.T. Hoang, C. Renault, J.E. Dick, Electrosynthesis of high-entropy metallic glass nanoparticles for designer, multi-functional electrocatalysis, Nat Commun 10 (2019). https://doi.org/10.1038/s41467-019-10303-z.

[127] D. Zhang, Y. Shi, H. Zhao, W. Qi, X. Chen, T. Zhan, S. Li, B. Yang, M. Sun, J. Lai, B. Huang, L. Wang, The facile oil-phase synthesis of a multi-site synergistic high-entropy alloy to promote the alkaline hydrogen evolution reaction, J Mater Chem A Mater 9 (2021) 889–893. https://doi.org/10.1039/d0ta10574k.

[128] X. Wang, Q. Peng, X. Zhang, X. Lv, X. Wang, Y. Fu, Carbonaceous-assisted confinement synthesis of refractory high-entropy alloy nanocomposites and their application for seawater electrolysis, J Colloid Interface Sci 607 (2022) 1580–1588. https://doi.org/10.1016/J.JCIS.2021.08.201.

[129] D. Lai, Q. Kang, F. Gao, Q. Lu, High-entropy effect of a metal phosphide on enhanced overall water splitting performance, J Mater Chem A Mater 9 (2021) 17913–17922. https://doi.org/10.1039/d1ta04755h.

[130] I. Kopova, J. Stráský, P. Harcuba, M. Landa, M. Janeček, L. Bačákova, Newly developed Ti–Nb–Zr–Ta–Si–Fe biomedical beta titanium alloys with increased strength and enhanced biocompatibility, Materials Science and Engineering: C 60 (2016) 230–238. https://doi.org/10.1016/J.MSEC.2015.11.043.

[131] G.H. Zhao, R.E. Aune, N. Espallargas, Tribocorrosion studies of metallic biomaterials: The effect of plasma nitriding and DLC surface modifications, J

Mech Behav Biomed Mater 63 (2016) 100–114. https://doi.org/10.1016/J.JMBBM.2016.06.014.

[132] S.V. Muley, A.N. Vidvans, G.P. Chaudhari, S. Udainiya, An assessment of ultra fine grained 316L stainless steel for implant applications, Acta Biomater 30 (2016) 408–419. https://doi.org/10.1016/J.ACTBIO.2015.10.043.

[133] J. Zhao, D. Xu, M.B. Shahzad, Q. Kang, Y. Sun, Z. Sun, S. Zhang, L. Ren, C. Yang, K. Yang, Effect of surface passivation on corrosion resistance and antibacterial properties of Cu-bearing 316L stainless steel, Appl Surf Sci 386 (2016) 371–380. https://doi.org/10.1016/J.APSUSC.2016.06.036.

[134] M. Das, K. Bhattacharya, S.A. Dittrick, C. Mandal, V.K. Balla, T.S. Sampath Kumar, A. Bandyopadhyay, I. Manna, In situ synthesized TiB–TiN reinforced Ti6Al4V alloy composite coatings: Microstructure, tribological and in-vitro biocompatibility, J Mech Behav Biomed Mater 29 (2014) 259–271. https://doi.org/10.1016/J.JMBBM.2013.09.006.

[135] M. Jenko, M. Gorenšek, M. Godec, M. Hodnik, B.Š. Batič, Č. Donik, J.T. Grant, D. Dolinar, Surface chemistry and microstructure of metallic biomaterials for hip and knee endoprostheses, Appl Surf Sci 427 (2018) 584–593. https://doi.org/10.1016/J.APSUSC.2017.08.007.

[136] S. Mischler, A.I. Muñoz, Wear of CoCrMo alloys used in metal-on-metal hip joints: A tribocorrosion appraisal, Wear 297 (2013) 1081–1094. https://doi.org/10.1016/J.WEAR.2012.11.061.

[137] M. Geetha, A.K. Singh, R. Asokamani, A.K. Gogia, Ti based biomaterials, the ultimate choice for orthopaedic implants – A review, Prog Mater Sci 54 (2009) 397–425. https://doi.org/10.1016/J.PMATSCI.2008.06.004.

[138] M. Poorraeisi, A. Afshar, The study of electrodeposition of hydroxyapatite-ZrO2-TiO2 nanocomposite coatings on 316 stainless steel, Surf Coat Technol 339 (2018) 199–207. https://doi.org/10.1016/J.SURFCOAT.2018.02.030.

[139] C. Domínguez-Trujillo, E. Peón, E. Chicardi, H. Pérez, J.A. Rodríguez-Ortiz, J.J. Pavón, J. García-Couce, J.C. Galván, F. García-Moreno, Y. Torres, Sol-gel deposition of hydroxyapatite coatings on porous titanium for biomedical applications, Surf Coat Technol 333 (2018) 158–162. https://doi.org/10.1016/J.SURFCOAT.2017.10.079.

[140] C. Hübsch, P. Dellinger, H.J. Maier, F. Stemme, M. Bruns, M. Stiesch, L. Borchers, Protection of yttria-stabilized zirconia for dental applications by oxidic

PVD coating, Acta Biomater 11 (2015) 488–493. https://doi.org/10.1016/J.ACTBIO.2014.09.042.

[141] A.C. Hee, Y. Zhao, D. Choudhury, S. Ghosh, Q. Zhu, H. Zhu, Tribological behavior of hydrogenated diamond-like carbon on polished alumina substrate with chromium interlayer for biomedical application, Biotribology 7 (2016) 1–10. https://doi.org/10.1016/J.BIOTRI.2016.06.001.

[142] S. Sheikh, M.K. Bijaksana, A. Motallebzadeh, S. Shafeie, A. Lozinko, L. Gan, T.K. Tsao, U. Klement, D. Canadinc, H. Murakami, S. Guo, Accelerated oxidation in ductile refractory high-entropy alloys, Intermetallics (Barking) 97 (2018) 58–66. https://doi.org/10.1016/J.INTERMET.2018.04.001.

[143] M.H. Tsai, J.W. Yeh, High-entropy alloys: A critical review, Mater Res Lett 2 (2014) 107–123. https://doi.org/10.1080/21663831.2014.912690.

[144] Y.F. Ye, Q. Wang, J. Lu, C.T. Liu, Y. Yang, High-entropy alloy: challenges and prospects, Materials Today 19 (2016) 349–362. https://doi.org/10.1016/j.mattod.2015.11.026.

[145] K.G. Pradeep, C.C. Tasan, M.J. Yao, Y. Deng, H. Springer, D. Raabe, Non-equiatomic high entropy alloys: Approach towards rapid alloy screening and property-oriented design, Materials Science and Engineering A 648 (2015) 183–192. https://doi.org/10.1016/j.msea.2015.09.010.

[146] M. Wang, H. Cui, Y. Zhao, C. Wang, N. Wei, Y. Zhao, X. Zhang, Q. Song, A simple strategy for fabrication of an FCC-based complex concentrated alloy coating with hierarchical nanoprecipitates and enhanced mechanical properties, Mater Des 180 (2019) 107893. https://doi.org/10.1016/J.MATDES.2019.107893.

[147] M. Wang, H. Cui, Y. Zhao, C. Wang, N. Wei, X. Gao, Q. Song, Enhanced strength and ductility in a spark plasma sintered CoCrCu0·5NiAl0.5 high-entropy alloy via a double-step ball milling approach for processing powders, Materials Science and Engineering: A 762 (2019) 138071. https://doi.org/10.1016/J.MSEA.2019.138071.

[148] Y. Lu, X. Gao, L. Jiang, Z. Chen, T. Wang, J. Jie, H. Kang, Y. Zhang, S. Guo, H. Ruan, Y. Zhao, Z. Cao, T. Li, Directly cast bulk eutectic and near-eutectic high entropy alloys with balanced strength and ductility in a wide temperature range, Acta Mater 124 (2017) 143–150. https://doi.org/10.1016/J.ACTAMAT.2016.11.016.

[149] A. Hynowska, A. Blanquer, E. Pellicer, J. Fornell, S. Suriñach, M.D. Baró, S. González, E. Ibáñez, L. Barrios, C. Nogués, J. Sort, Novel Ti-Zr-Hf-Fe nanostructured alloy for biomedical applications, Materials 6 (2013) 4930–4945. https://doi.org/10.3390/ma6114930.

[150] G. Perumal, H. Singh Grewal, M. Pole, L. Vinod Kumar Reddy, S. Mukherjee, H. Singh, G. Manivasagam, H. Singh Arora, Enhanced Biocorrosion Resistance and Cellular Response of a Dual-Phase High Entropy Alloy through Reduced Elemental Heterogeneity, ACS Appl Bio Mater 3 (2020) 1233–1244. https://doi.org/10.1021/acsabm.9b01127.

[151] A. Motallebzadeh, N.S. Peighambardoust, S. Sheikh, H. Murakami, S. Guo, D. Canadinc, Microstructural, mechanical and electrochemical characterization of TiZrTaHfNb and Ti1.5ZrTa0.5Hf0.5Nb0.5 refractory high-entropy alloys for biomedical applications, Intermetallics (Barking) 113 (2019) 106572. https://doi.org/10.1016/J.INTERMET.2019.106572.

[152] T. Nagase, M. Todai, T. Hori, T. Nakano, Microstructure of equiatomic and non-equiatomic Ti-Nb-Ta-Zr-Mo high-entropy alloys for metallic biomaterials, J Alloys Compd 753 (2018) 412–421. https://doi.org/10.1016/J.JALLCOM.2018.04.082.

[153] A. Hynowska, A. Blanquer, E. Pellicer, J. Fornell, S. Suriñach, M.D. Baró, S. González, E. Ibáñez, L. Barrios, C. Nogués, J. Sort, Novel Ti-Zr-Hf-Fe nanostructured alloy for biomedical applications, Materials 6 (2013) 4930–4945. https://doi.org/10.3390/ma6114930.

[154] I. Basu, J.T.M. De Hosson, High entropy alloys: Ready to set sail?, Metals (Basel) 10 (2020). https://doi.org/10.3390/met10020194.

[155] D.B. Miracle, J.D. Miller, O.N. Senkov, C. Woodward, M.D. Uchic, J. Tiley, Exploration and development of high entropy alloys for structural applications, Entropy 16 (2014) 494–525. https://doi.org/10.3390/e16010494.

[156] W. Li, P. Liu, P.K. Liaw, Microstructures and properties of high-entropy alloy films and coatings: A review, Mater Res Lett 6 (2018) 199–229. https://doi.org/10.1080/21663831.2018.1434248.

[157] T.K. Chen, M.S. Wong, T.T. Shun, J.W. Yeh, Nanostructured nitride films of multi-element high-entropy alloys by reactive DC sputtering, Surf Coat Technol 200 (2005) 1361–1365. https://doi.org/10.1016/j.surfcoat.2005.08.081.

[158] N. Tüten, D. Canadinc, A. Motallebzadeh, B. Bal, Microstructure and tribological properties of TiTaHfNbZr high entropy alloy coatings deposited on Ti–6Al–4V substrates, Intermetallics (Barking) 105 (2019) 99–106. https://doi.org/10.1016/j.intermet.2018.11.015.

[159] O. V. Sobol', A.A. Andreev, V.F. Gorban', N.A. Krapivka, V.A. Stolbovoi, I. V. Serdyuk, V.E. Fil'chikov, Reproducibility of the single-phase structural state of the multielement high-entropy Ti-V-Zr-Nb-Hf system and related superhard nitrides formed by the vacuum-arc method, Technical Physics Letters 38 (2012) 616–619. https://doi.org/10.1134/S1063785012070127.

[160] B. Ren, Z. Shen, Z. Liu, Structure and mechanical properties of multi-element (AlCrMnMoNiZr)N x coatings by reactive magnetron sputtering, J Alloys Compd 560 (2013) 171–176. https://doi.org/10.1016/j.jallcom.2013.01.148.

[161] S. Guo, Phase selection rules for cast high entropy alloys: An overview, Materials Science and Technology (United Kingdom) 31 (2015) 1223–1230. https://doi.org/10.1179/1743284715Y.0000000018.

[162] B. Ren, Z.X. Liu, L. Shi, B. Cai, M.X. Wang, Structure and properties of (AlCrMnMoNiZrB 0.1)N x coatings prepared by reactive DC sputtering, Appl Surf Sci 257 (2011) 7172–7178. https://doi.org/10.1016/j.apsusc.2011.03.083.

[163] S.C. Liang, Z.C. Chang, D.C. Tsai, Y.C. Lin, H.S. Sung, M.J. Deng, F.S. Shieu, Effects of substrate temperature on the structure and mechanical properties of (TiVCrZrHf)N coatings, Appl Surf Sci 257 (2011) 7709–7713. https://doi.org/10.1016/J.APSUSC.2011.04.014.

[164] Y.Y. Chen, T. Duval, U.D. Hung, J.W. Yeh, H.C. Shih, Microstructure and electrochemical properties of high entropy alloys-a comparison with type-304 stainless steel, Corros Sci 47 (2005) 2257–2279. https://doi.org/10.1016/j.corsci.2004.11.008.

[165] S. Tsukimoto, M. Moriyama, M. Murakami, Microstructure of amorphous tantalum nitride thin films, Thin Solid Films 460 (2004) 222–226. https://doi.org/10.1016/j.tsf.2004.01.073.

[166] C.H. Tsau, Z.Y. Hwang, S.K. Chen, The Microstructures and Electrical Resistivity of (Al, Cr, Ti)FeCoNiOx High-Entropy Alloy Oxide Thin Films, Advances in Materials Science and Engineering 2015 (2015). https://doi.org/10.1155/2015/353140.

[167] L. Liu, J.B. Zhu, C. Hou, J.C. Li, Q. Jiang, Dense and smooth amorphous films of multicomponent FeCoNiCuVZrAl high-entropy alloy deposited by direct current magnetron sputtering, Mater Des 46 (2013) 675–679. https://doi.org/10.1016/j.matdes.2012.11.001.

[168] A. Motallebzadeh, M.B. Yagci, E. Bedir, C.B. Aksoy, D. Canadinc, Mechanical Properties of TiTaHfNbZr High-Entropy Alloy Coatings Deposited on NiTi Shape Memory Alloy Substrates, Metall Mater Trans A Phys Metall Mater Sci 49 (2018) 1992–1997. https://doi.org/10.1007/s11661-018-4605-4.

[169] S.Y. Chang, S.Y. Lin, Y.C. Huang, C.L. Wu, Mechanical properties, deformation behaviors and interface adhesion of (AlCrTaTiZr)Nx multi-component coatings, Surf Coat Technol 204 (2010) 3307–3314. https://doi.org/10.1016/j.surfcoat.2010.03.041.

[170] X.C. Zhang, B.S. Xu, H.D. Wang, Y. Jiang, Y.X. Wu, Modeling of thermal residual stresses in multilayer coatings with graded properties and compositions, Thin Solid Films 497 (2006) 223–231. https://doi.org/10.1016/j.tsf.2005.09.184.

[171] Y. Shi, B. Yang, X. Xie, J. Brechtl, K.A. Dahmen, P.K. Liaw, Corrosion of Al xCoCrFeNi high-entropy alloys: Al-content and potential scan-rate dependent pitting behavior, Corros Sci 119 (2017) 33–45. https://doi.org/10.1016/j.corsci.2017.02.019.

[172] C.H. Lai, M.H. Tsai, S.J. Lin, J.W. Yeh, Influence of substrate temperature on structure and mechanical, properties of multi-element (AlCrTaTiZr)N coatings, Surf Coat Technol 201 (2007) 6993–6998. https://doi.org/10.1016/j.surfcoat.2007.01.001.

[173] Andrzej Lasia, Electrochemical Impedance Spectroscopy and its Applications, n.d.

[174] A. Nouri, C. Wen, Introduction to surface coating and modification for metallic biomaterials, Surface Coating and Modification of Metallic Biomaterials (2015) 3–60. https://doi.org/10.1016/B978-1-78242-303-4.00001-6.

[175] N.S. Manam, W.S.W. Harun, D.N.A. Shri, S.A.C. Ghani, T. Kurniawan, M.H. Ismail, M.H.I. Ibrahim, Study of corrosion in biocompatible metals for implants: A review, J Alloys Compd 701 (2017) 698–715. https://doi.org/10.1016/j.jallcom.2017.01.196.

[176] H.F. Li, Y.F. Zheng, Recent advances in bulk metallic glasses for biomedical applications, Acta Biomater 36 (2016) 1–20. https://doi.org/10.1016/j.actbio.2016.03.047.

[177] S.P. Hannula, O. Söderberg, T. Jämsä, V.K. Lindroos, Shape Memory Alloys for Biomedical Applications, in: Materials in Clinical Applications VII, Trans Tech Publications Ltd, 2006: pp. 109–118. https://doi.org/10.4028/www.scientific.net/ast.49.109.

[178] A. Grill, Diamond-like carbon coatings as biocompatible materials—an overview, Diam Relat Mater 12 (2003) 166–170. https://doi.org/10.1016/S0925-9635(03)00018-9.

[179] G. Manivasagam, D. Dhinasekaran, A. Rajamanickam, Biomedical Implants: Corrosion and its Prevention-A Review, 2010.

[180] M.J. Yaszemski, Biomaterials in orthopedics, M. Dekker, 2004.

[181] E.K. Brooks, R.P. Brooks, M.T. Ehrensberger, Effects of simulated inflammation on the corrosion of 316L stainless steel, Materials Science and Engineering C 71 (2017) 200–205. https://doi.org/10.1016/j.msec.2016.10.012.

[182] F.G. Echeverrigaray, S. Echeverrigaray, A.P.L. Delamare, C.H. Wanke, C.A. Figueroa, I.J.R. Baumvol, C. Aguzzoli, Antibacterial properties obtained by low-energy silver implantation in stainless steel surfaces, Surf Coat Technol 307 (2016) 345–351. https://doi.org/10.1016/j.surfcoat.2016.09.005.

[183] A.A. Alamdari, M. Hashemkhani, S. Hendessi, P.T. Guner, H.Y. Acar, I.H. Kavakli, U. Unal, A. Motallebzadeh, In vitro antibacterial and cytotoxicity assessment of magnetron sputtered Ti1.5ZrTa0.5Nb0.5W0.5 refractory high-entropy alloy doped with Ag nanoparticles, Vacuum 203 (2022) 111286. https://doi.org/10.1016/J.VACUUM.2022.111286.

[184] N.S. Peighambardoust, A.A. Alamdari, U. Unal, A. Motallebzadeh, In vitro biocompatibility evaluation of Ti1.5ZrTa0.5Nb0.5Hf0.5 refractory high-entropy alloy film for orthopedic implants: Microstructural, mechanical properties and corrosion behavior, J Alloys Compd 883 (2021). https://doi.org/10.1016/j.jallcom.2021.160786.

[185] M.Y. He, Y.F. Shen, N. Jia, P.K. Liaw, C and N doping in high-entropy alloys: A pathway to achieve desired strength-ductility synergy, Appl Mater Today 25 (2021) 101162. https://doi.org/10.1016/J.APMT.2021.101162.

[186] T. Li, Y. Lu, Z. Li, T. Wang, T. Li, Hot deformation behavior and microstructure evolution of non-equimolar Ti2ZrHfV0.5Ta0.2 refractory high-entropy alloy, Intermetallics (Barking) 146 (2022) 107586. https://doi.org/10.1016/J.INTERMET.2022.107586.

[187] H. Jahangiri, Y. Morova, A. Asghari Alamdari, Z. Eroğlu, A. Sennaroğlu, S. Guo, O. Metin, A. Motallebzadeh, Femtosecond laser-mediated preparation of HfNbTaTiZr refractory high-entropy alloy nanoparticles for photothermal therapy applications: Influence of solvent and fluence, Intermetallics (Barking) 156 (2023) 107834. https://doi.org/10.1016/J.INTERMET.2023.107834.

[188] M. Calin, J. Vishnu, P. Thirathipviwat, M.M. Popa, M. Krautz, G. Manivasagam, A. Gebert, Tailoring biocompatible Ti-Zr-Nb-Hf-Si metallic glasses based on high-entropy alloys design approach, Materials Science and Engineering: C 121 (2021) 111733. https://doi.org/10.1016/J.MSEC.2020.111733.

[189] Z. Fu, W. Chen, H. Xiao, L. Zhou, D. Zhu, S. Yang, Fabrication and properties of nanocrystalline Co0.5FeNiCrTi0.5 high entropy alloy by MA–SPS technique, Mater Des 44 (2013) 535–539. https://doi.org/10.1016/J.MATDES.2012.08.048.

[190] T. Li, J. Miao, Y. Lu, T. Wang, T. Li, Effect of Zr on the as-cast microstructure and mechanical properties of lightweight Ti2VNbMoZrx refractory high-entropy alloys, Int J Refract Metals Hard Mater 103 (2022) 105762. https://doi.org/10.1016/J.IJRMHM.2021.105762.

[191] T. Li, W. Jiao, J. Miao, Y. Lu, E. Guo, T. Wang, T. Li, P.K. Liaw, A novel ZrNbMoTaW refractory high-entropy alloy with in-situ forming heterogeneous structure, Materials Science and Engineering: A 827 (2021) 142061. https://doi.org/10.1016/J.MSEA.2021.142061.

[192] A. Motallebzadeh, Evaluation of mechanical properties and in vitro biocompatibility of TiZrTaNbHf refractory high-entropy alloy film as an alternative coating for TiO2 layer on NiTi alloy, Surf Coat Technol 448 (2022) 128918. https://doi.org/10.1016/J.SURFCOAT.2022.128918.

[193] A.A. Alamdari, U. Unal, A. Motallebzadeh, Investigation of microstructure, mechanical properties, and biocorrosion behavior of Ti1.5ZrTa0.5Nb0.5W0.5 refractory high-entropy alloy film doped with Ag nanoparticles, Surfaces and Interfaces (2021) 101617. https://doi.org/10.1016/j.surfin.2021.101617.

[194] W. Weng, A. Biesiekierski, J. Lin, S. Ozan, Y. Li, C. Wen, Development of beta-type Ti-Nb-Zr-Mo alloys for orthopedic applications, Appl Mater Today 22 (2021) 100968. https://doi.org/10.1016/J.APMT.2021.100968.

[195] M. Alinezhadfar, S. Nasiri Khalil Abad, M. Mozammel, Multifunctional cobalt coating with exceptional amphiphobic properties: self-cleaning and corrosion

inhibition, Surfaces and Interfaces 21 (2020) 100744. https://doi.org/10.1016/j.surfin.2020.100744.

[196] R. Aqib, S. Kiani, S. Bano, A. Wadood, M.A. Ur Rehman, Ag–Sr doped mesoporous bioactive glass nanoparticles loaded chitosan/gelatin coating for orthopedic implants, Int J Appl Ceram Technol 18 (2021) 544–562. https://doi.org/10.1111/ijac.13702.

[197] C.H. Lai, S.J. Lin, J.W. Yeh, S.Y. Chang, Preparation and characterization of AlCrTaTiZr multi-element nitride coatings, Surf Coat Technol 201 (2006) 3275–3280. https://doi.org/10.1016/j.surfcoat.2006.06.048.

[198] S. Guo, C.T. Liu, Phase stability in high entropy alloys: Formation of solid-solution phase or amorphous phase, Progress in Natural Science: Materials International 21 (2011) 433–446. https://doi.org/10.1016/S1002-0071(12)60080-X.

[199] J.B. Cheng, X.B. Liang, B.S. Xu, Effect of Nb addition on the structure and mechanical behaviors of CoCrCuFeNi high-entropy alloy coatings, Surf Coat Technol 240 (2014) 184–190. https://doi.org/10.1016/j.surfcoat.2013.12.053.

[200] B. Henriques, M. Sampaio, M. Buciumeanu, J.C.M. Souza, J.R. Gomes, F. Silva, O. Carvalho, Laser surface structuring of Ti6Al4V substrates for adhesion enhancement in Ti6Al4V-PEEK joints, Materials Science and Engineering: C 79 (2017) 177–184. https://doi.org/10.1016/J.MSEC.2017.04.157.

[201] W. Li, D. Ming-hui, Z. Hong-sen, Z. Bin, Study on HfCxN1-x coatings deposited on biomedical AISI 316L by radio-frequency magnetron sputtering, J Alloys Compd 730 (2018) 219–227. https://doi.org/10.1016/J.JALLCOM.2017.09.289.

[202] C.A. Love, R.B. Cook, T.J. Harvey, P.A. Dearnley, R.J.K. Wood, Diamond like carbon coatings for potential application in biological implants - A review, in: Tribol Int, Elsevier Ltd, 2013: pp. 141–150. https://doi.org/10.1016/j.triboint.2012.09.006.

[203] K.L. Mittal, ADHESION MEASUREMENT OF THIN FILMS, C) Gordon and Breach Science Publishers Ltd, 1976.

[204] S. Peng, J. Xu, D. Hu, Z.H. Xie, P. Munroe, The impact of surface scratches on the corrosion behavior of nanocrystalline high entropy alloy coatings: Electrochemical experiments and first-principles study, Appl Mater Today 31 (2023) 101767. https://doi.org/10.1016/J.APMT.2023.101767.

[205] C.H. Lin, J.G. Duh, Corrosion behavior of (Ti-Al-Cr-Si-V)xNy coatings on mild steels derived from RF magnetron sputtering, Surf Coat Technol 203 (2008) 558–561. https://doi.org/10.1016/j.surfcoat.2008.04.067.

[206] V. Braic, M. Balaceanu, M. Braic, A. Vladescu, S. Panseri, A. Russo, Characterization of multi-principal-element (TiZrNbHfTa)N and (TiZrNbHfTa)C coatings for biomedical applications, J Mech Behav Biomed Mater 10 (2012) 197–205. https://doi.org/10.1016/j.jmbbm.2012.02.020.

[207] J. Xu, X. ke Bao, T. Fu, Y. Lyu, P. Munroe, Z.H. Xie, In vitro biocompatibility of a nanocrystalline β-Ta2O5 coating for orthopaedic implants, Ceram Int 44 (2018) 4660–4675. https://doi.org/10.1016/J.CERAMINT.2017.12.040.

[208] L. Bait, L. Azzouz, N. Madaoui, N. Saoula, Influence of substrate bias voltage on the properties of TiO2 deposited by radio-frequency magnetron sputtering on 304L for biomaterials applications, Appl Surf Sci 395 (2017) 72–77. https://doi.org/10.1016/J.APSUSC.2016.07.101.

[209] M. Sarraf, B.A. Razak, B. Nasiri-Tabrizi, A. Dabbagh, N.H.A. Kasim, W.J. Basirun, E. Bin Sulaiman, Nanomechanical properties, wear resistance and in-vitro characterization of Ta2O5 nanotubes coating on biomedical grade Ti–6Al–4V, J Mech Behav Biomed Mater 66 (2017) 159–171. https://doi.org/10.1016/j.jmbbm.2016.11.012.

[210] D. Pradhan, A.W. Wren, S.T. Misture, N.P. Mellott, Investigating the structure and biocompatibility of niobium and titanium oxides as coatings for orthopedic metallic implants, Materials Science and Engineering C 58 (2016) 918–926. https://doi.org/10.1016/j.msec.2015.09.059.

[211] V. Vadillo-Rodríguez, J.M. Bruque, A.M. Gallardo-Moreno, M.L. González-Martín, Surface-dependent mechanical stability of adsorbed human plasma fibronectin on Ti6Al4V: Domain unfolding and stepwise unraveling of single compact molecules, Langmuir 29 (2013) 8554–8560. https://doi.org/10.1021/la401776e.

[212] F. Bartolomeu, M.M. Costa, J.R. Gomes, N. Alves, C.S. Abreu, F.S. Silva, G. Miranda, Implant surface design for improved implant stability – A study on Ti6Al4V dense and cellular structures produced by Selective Laser Melting, Tribol Int 129 (2019) 272–282. https://doi.org/10.1016/j.triboint.2018.08.012.

[213] S. Ozan, J. Lin, Y. Li, R. Ipek, C. Wen, Development of Ti-Nb-Zr alloys with high elastic admissible strain for temporary orthopedic devices, Acta Biomater 20 (2015) 176–187. https://doi.org/10.1016/j.actbio.2015.03.023.

[214] M. Bartmanski, A. Zielinski, B. Majkowska-Marzec, G. Strugala, Effects of solution composition and electrophoretic deposition voltage on various properties of nanohydroxyapatite coatings on the Ti13Zr13Nb alloy, Ceram Int 44 (2018) 19236–19246. https://doi.org/10.1016/j.ceramint.2018.07.148.

[215] P.S. Nnamchi, C.S. Obayi, I. Todd, M.W. Rainforth, Mechanical and electrochemical characterisation of new Ti-Mo-Nb-Zr alloys for biomedical applications, J Mech Behav Biomed Mater 60 (2016) 68–77. https://doi.org/10.1016/j.jmbbm.2015.12.023.

[216] R. Banerjee, S. Nag, J. Stechschulte, H.L. Fraser, Strengthening mechanisms in Ti-Nb-Zr-Ta and Ti-Mo-Zr-Fe orthopaedic alloys, Biomaterials 25 (2004) 3413–3419. https://doi.org/10.1016/j.biomaterials.2003.10.041.

[217] S. Nag, R. Banerjee, H.L. Fraser, Microstructural evolution and strengthening mechanisms in Ti-Nb-Zr-Ta, Ti-Mo-Zr-Fe and Ti-15Mo biocompatible alloys, Materials Science and Engineering C 25 (2005) 357–362. https://doi.org/10.1016/j.msec.2004.12.013.

[218] A. Vladescu, S.C. Padmanabhan, F. Ak Azem, M. Braic, I. Titorencu, I. Birlik, M.A. Morris, V. Braic, Mechanical properties and biocompatibility of the sputtered Ti doped hydroxyapatite, J Mech Behav Biomed Mater 63 (2016) 314–325. https://doi.org/10.1016/j.jmbbm.2016.06.025.

[219] Y. Li, B. Yao, B.Y. Long, H.W. Tian, B. Wang, Preparation, characterization and mechanical properties of microarc oxidation coating formed on titanium in Al(OH) 3 colloidal solution, Appl Surf Sci 258 (2012) 5238–5243. https://doi.org/10.1016/j.apsusc.2012.01.170.

[220] H.A. Ching, D. Choudhury, M.J. Nine, N.A. Abu Osman, Effects of surface coating on reducing friction and wear of orthopaedic implants, Sci Technol Adv Mater 15 (2014) 1–21. https://doi.org/10.1088/1468-6996/15/1/014402.

[221] A.M.M. dos Santos, R.J.C. Batista, L.A.M. Martins, M. Ilha, M.Q. Vieira, D.R. Miquita, F.C.R. Guma, I.L. Müller, T.M. Manhabosco, Corrosion and cell viability studies of graphite-like hydrogenated amorphous carbon films deposited on bare and nitrided titanium alloy, Corros Sci 82 (2014) 297–303. https://doi.org/10.1016/j.corsci.2014.01.025.

[222] J.S. Fernandes, P. Gentile, R.A. Pires, R.L. Reis, P. V. Hatton, Multifunctional bioactive glass and glass-ceramic biomaterials with antibacterial properties for repair and regeneration of bone tissue, Acta Biomater 59 (2017) 2–11. https://doi.org/10.1016/j.actbio.2017.06.046.

[223] A. Ewald, S.K. Glückermann, R. Thull, U. Gbureck, Antimicrobial titanium/silver PVD coatings on titanium, Biomed Eng Online 5 (2006) 1–10. https://doi.org/10.1186/1475-925X-5-22.

[224] F. Hempel, B. Finke, C. Zietz, R. Bader, K.D. Weltmann, M. Polak, Antimicrobial surface modification of titanium substrates by means of plasma immersion ion implantation and deposition of copper, Surf Coat Technol 256 (2014) 52–58. https://doi.org/10.1016/j.surfcoat.2014.01.027.

[225] E. Zhang, X. Wang, M. Chen, B. Hou, Effect of the existing form of Cu element on the mechanical properties, bio-corrosion and antibacterial properties of Ti-Cu alloys for biomedical application, Materials Science and Engineering C 69 (2016) 1210–1221. https://doi.org/10.1016/j.msec.2016.08.033.

[226] K.G.U.R. Kumarasinghe, W.C.H. Silva, M.D.A. Fernando, L. Palliyaguru, P.S. Jayawardena, M. Shimomura, S.S.N. Fernando, T.D.C.P. Gunasekara, P.M. Jayaweera, One-pot reducing agent-free synthesis of silver nanoparticles/nitrocellulose composite surface coating with antimicrobial and antibiofilm activities, Biomed Res Int 2021 (2021) 1–16. https://doi.org/10.1155/2021/6666642.

[227] M. Cloutier, D. Mantovani, F. Rosei, Antibacterial Coatings: Challenges, Perspectives, and Opportunities, Trends Biotechnol 33 (2015) 637–652. https://doi.org/10.1016/j.tibtech.2015.09.002.

[228] K. Batebi, B. Abbasi Khazaei, A. Afshar, Characterization of sol-gel derived silver/fluor-hydroxyapatite composite coatings on titanium substrate, Surf Coat Technol 352 (2018) 522–528. https://doi.org/10.1016/j.surfcoat.2018.08.021.

[229] R. Parveen, P.K. Maiti, N. Murmu, A. Datta, Preparation of serum capped silver nanoparticles for selective killing of microbial cells sparing host cells, Sci Rep 11 (2021) 1–12. https://doi.org/10.1038/s41598-021-91031-7.

[230] E. Zhang, C. Liu, A new antibacterial Co-Cr-Mo-Cu alloy: Preparation, biocorrosion, mechanical and antibacterial property, Materials Science and Engineering C 69 (2016) 134–143. https://doi.org/10.1016/j.msec.2016.05.028.

[231] I.A.J. van Hengel, M.W.A.M. Tierolf, L.E. Fratila-apachitei, I. Apachitei, A.A. Zadpoor, Antibacterial titanium implants biofunctionalized by plasma electrolytic oxidation with silver, zinc, and copper: A systematic review, Int J Mol Sci 22 (2021). https://doi.org/10.3390/ijms22073800.

[232] M. Ramstedt, B. Ekstrand-Hammarström, A. V. Shchukarev, A. Bucht, L. Österlund, M. Welch, W.T.S. Huck, Bacterial and mammalian cell response to poly(3-sulfopropyl methacrylate) brushes loaded with silver halide salts, Biomaterials 30 (2009) 1524–1531. https://doi.org/10.1016/j.biomaterials.2008.12.008.

[233] S. Agnihotri, S. Mukherji, S. Mukherji, Immobilized silver nanoparticles enhance contact killing and show highest efficacy: Elucidation of the mechanism of bactericidal action of silver, Nanoscale 5 (2013) 7328–7340. https://doi.org/10.1039/c3nr00024a.

[234] L. Xin, J. Wang, Y. Wu, S. Guo, J. Tong, Increased oxidative stress and activated heat shock proteins in human cell lines by silver nanoparticles, Hum Exp Toxicol 34 (2015) 315–323. https://doi.org/10.1177/0960327114538988.

[235] X.F. Zhang, W. Shen, S. Gurunathan, Silver nanoparticle-mediated cellular responses in various cell lines: An in vitro model, Int J Mol Sci 17 (2016) 1–26. https://doi.org/10.3390/ijms17101603.

[236] S. Castiglioni, A. Cazzaniga, L. Locatelli, J.A.M. Maier, Silver nanoparticles in orthopedic applications: New insights on their effects on osteogenic cells, Nanomaterials 7 (2017). https://doi.org/10.3390/nano7060124.

[237] D.S. Mohamed, R.M.A. El-Baky, T. Sandle, S.A. Mandour, E.F. Ahmed, Antimicrobial activity of silver-treated bacteria against other multi-drug resistant pathogens in their environment, Antibiotics 9 (2020) 1–14. https://doi.org/10.3390/antibiotics9040181.

[238] D.K. Tiwari, J. Behari, P. Sen, Time and dose-dependent antimicrobial potential of Ag nanoparticles synthesized by top- down approach, Curr Sci 95 (2008) 647–655.

[239] S. Castiglioni, A. Cazzaniga, C. Perrotta, J.A.M. Maier, Silver nanoparticles-induced cytotoxicity requires ERK activation in human bladder carcinoma cells, Toxicol Lett 237 (2015) 237–243. https://doi.org/10.1016/j.toxlet.2015.06.1707.

[240] D. Cai, X. Zhao, L. Yang, R. Wang, G. Qin, D. fu Chen, E. Zhang, A novel biomedical titanium alloy with high antibacterial property and low elastic modulus, J Mater Sci Technol 81 (2021) 13–25. https://doi.org/10.1016/j.jmst.2021.01.015.

[241] A. Ghaderi, H. Moghanni, K. Dehghani, Microstructural Evolution and Mechanical Properties of Al0.5CoCrFeNi High-Entropy Alloy after Cold Rolling and Annealing Treatments, J Mater Eng Perform 30 (2021) 7817–7825. https://doi.org/10.1007/s11665-021-05886-y.

[242] Z. Zhou, L. Wang, X. Zhao, J. Wu, F. Zhang, J. Pi, Effects of W addition on the Corrosion Behaviors of FeCoNiCrMn High Entropy Alloy Composites in the 3.5 wt.% NaCl solution, Surfaces and Interfaces 23 (2021) 100956. https://doi.org/10.1016/J.SURFIN.2021.100956.

[243] S.N. Chen, Y.F. Zhang, Y.M. Zhao, W.Q. Yan, S. Wu, L. Chen, P. Pang, B. Liao, X.Y. Wu, X.P. Ouyang, Preparation and regulation of AlCrNiTiSi high entropy alloy coating by a multi-arc magnetic filter cathode vacuum arc system, Surfaces and Interfaces 26 (2021) 101400. https://doi.org/10.1016/J.SURFIN.2021.101400.

[244] G. Popescu, B. Ghiban, C.A. Popescu, L. Rosu, R. Truscă, I. Carcea, V. Soare, D. Dumitrescu, I. Constantin, M.T. Olaru, B.A. Carlan, New TiZrNbTaFe high entropy alloy used for medical applications, in: IOP Conf Ser Mater Sci Eng, Institute of Physics Publishing, 2018. https://doi.org/10.1088/1757-899X/400/2/022049.

[245] Y. Qing, L. Cheng, R. Li, G. Liu, Y. Zhang, X. Tang, J. Wang, H. Liu, Y. Qin, Potential antibacterial mechanism of silver nanoparticles and the optimization of orthopedic implants by advanced modification technologies, Int J Nanomedicine 13 (2018) 3311–3327. https://doi.org/10.2147/IJN.S165125.

[246] A. Besinis, T. De Peralta, R.D. Handy, Inhibition of biofilm formation and antibacterial properties of a silver nano-coating on human dentine, Nanotoxicology 8 (2014) 745–754. https://doi.org/10.3109/17435390.2013.825343.

[247] C.H. Lin, J.G. Duh, J.W. Yeh, Multi-component nitride coatings derived from Ti-Al-Cr-Si-V target in RF magnetron sputter, Surf Coat Technol 201 (2007) 6304–6308. https://doi.org/10.1016/j.surfcoat.2006.11.041.

[248] V. Soare, M. Burada, I. Constantin, D. Mitricə, V. Bədiliţə, A. Caragea, M. Târcolea, Electrochemical deposition and microstructural characterization of AlCrFeMnNi and AlCrCuFeMnNi high entropy alloy thin films, Appl Surf Sci 358 (2015) 533–539. https://doi.org/10.1016/j.apsusc.2015.07.142.

[249] A.D. Pogrebnjak, A.A. Bagdasaryan, I. V Yakushchenko, V.M. Beresnev, The structure and properties of high-entropy alloys and nitride coatings based on them, Russian Chemical Reviews 83 (2014) 1027–1061. https://doi.org/10.1070/rcr4407.

[250] Y. Zhang, J.-W. Yeh, J.F. Sun, J.P. Lin, K.-F. Yao, High-entropy alloys, Elsevier, 2015. https://doi.org/10.1155/2015/781303.

[251] F. Lavini, F. Cellini, M. Rejhon, J. Kunc, C. Berger, W. de Heer, E. Riedo, Atomic force microscopy phase imaging of epitaxial graphene films, Journal of Physics:Materials 3 (2020). https://doi.org/10.1088/2515-7639/ab7a02.

[252] C. Guyot, M. Voué, Intrinsic optical properties of Ag-doped poly-(vinyl alcohol) nanocomposites: an analysis of the film thickness effect on the plasmonic resonance parameters, Appl Phys A Mater Sci Process 126 (2020) 1–13. https://doi.org/10.1007/s00339-020-04055-7.

[253] S. Kasraei, M. Azarsina, Addition of silver nanoparticles reduces the wettability of methacrylate and silorane-based composites, Braz Oral Res 26 (2012) 505–510. https://doi.org/10.1590/S1806-83242012000600004.

[254] M. Alinezhadfar, M. Mozammel, Effect of Pre-treatment on Roughness and Hydrophobicity of Electro-Etched Steel with Improved Corrosion Resistance, J Mater Eng Perform 29 (2020) 5950–5958. https://doi.org/10.1007/s11665-020-05074-4.

[255] C. Te Lee, W.H. Cho, M.H. Shiao, C.N. Hsiao, K.S. Tang, C.C. Jaing, Effects of DC bias on the microstructure, residual stress and hardness properties of TiVCrZrTaN films by reactive RF magnetron sputtering, in: Procedia Eng, Elsevier Ltd, 2012: pp. 316–321. https://doi.org/10.1016/j.proeng.2012.03.046.

[256] S. Mahdavi, A. Asghari-Alamdari, M. Zolola-Meibodi, Effect of alumina particle size on characteristics, corrosion, and tribological behavior of Co/Al2O3 composite coatings, Ceram Int 46 (2020) 5351–5359. https://doi.org/10.1016/j.ceramint.2019.10.289.

[257] B. Elsener, A. Rota, H. Böhni, Impedance Study on the Corrosion of PVD and CVD Titanium Nitride Coatings, Materials Science Forum 44–45 (1989) 29–38. https://doi.org/10.4028/www.scientific.net/msf.44-45.29.

[258] K. Nozawa, K. Aramaki, One- and two-dimensional polymer films of modified alkanethiol monolayers for preventing iron from corrosion, Corros Sci 41 (1999) 57–73. https://doi.org/10.1016/S0010-938X(98)00048-1.

[259] O.A. Olaseinde, O.F. Olarenwaju, S.T. Mohammed, Effect of Silver Nanoparticles on the Corrosion Behaviour of Mild Steel and 316 Austenitic Stainless Steel in 0.5 M H2SO4, European Journal of Engineering Research and Science 4 (2019) 4–10. https://doi.org/10.24018/ejers.2019.4.4.1039.

[260] B. Burnat, M. Walkowiak-Przybyło, T. Błaszczyk, L. Klimek, Corrosion behaviour of polished and sandblasted titanium alloys in PBS solution, Acta Bioeng Biomech 15 (2013) 87–95. https://doi.org/10.5277/abb130111.

[261] E. Rahimi, R. Offoiach, K. Baert, H. Terryn, M. Lekka, L. Fedrizzi, Role of phosphate, calcium species and hydrogen peroxide on albumin protein adsorption on surface oxide of Ti6Al4V alloy, Materialia (Oxf) 15 (2021). https://doi.org/10.1016/j.mtla.2020.100988.

[262] A. Toosinezhad, M. Alinezhadfar, S. Mahdavi, Cobalt/graphene electrodeposits: Characteristics, tribological behavior, and corrosion properties, Surf Coat Technol 385 (2020) 125418. https://doi.org/10.1016/j.surfcoat.2020.125418.

[263] A. Popova, S. Raicheva, E. Sokolova, M. Christov, Frequency dispersion of the interfacial impedance at mild steel corrosion in acid media in the presence of benzimidazole derivatives, Langmuir 12 (1996) 2083–2089. https://doi.org/10.1021/la950148+.

[264] H. Torbati-Sarraf, S.A. Torbati-Sarraf, A. Poursaee, T.G. Langdon, Electrochemical behavior of a magnesium ZK60 alloy processed by high-pressure torsion, Corros Sci 154 (2019) 90–100. https://doi.org/10.1016/j.corsci.2019.04.006.

[265] T. Schmitz, F. Warmuth, E. Werner, C. Hertl, J. Groll, U. Gbureck, C. Moseke, Physical and chemical characterization of Ag-doped Ti coatings produced by magnetron sputtering of modular targets, Materials Science and Engineering: C 44 (2014) 126–131. https://doi.org/10.1016/J.MSEC.2014.08.024.

[266] A. Hasan, V. Saxena, L.M. Pandey, Surface Functionalization of Ti6Al4V via Self-assembled Monolayers for Improved Protein Adsorption and Fibroblast Adhesion, Langmuir 34 (2018) 3494–3506. https://doi.org/10.1021/acs.langmuir.7b03152.

[267] A. Besinis, T. De Peralta, R.D. Handy, The antibacterial effects of silver, titanium dioxide and silica dioxide nanoparticles compared to the dental disinfectant chlorhexidine on Streptococcus mutans using a suite of bioassays, Nanotoxicology 8 (2014) 1–16. https://doi.org/10.3109/17435390.2012.742935.

[268] J. Wang, X. Gong, J. Hai, T. Li, Synthesis of silver–hydroxyapatite composite with improved antibacterial properties, Vacuum 152 (2018) 132–137. https://doi.org/10.1016/J.VACUUM.2018.03.015.

[269] P.A. Zapata, M. Larrea, L. Tamayo, F.M. Rabagliati, M.I. Azócar, M. Páez, Polyethylene / silver-nano fi ber composites : A material for antibacterial fi lms, 69 (2016) 1282–1289.

[270] S. Momeni, W. Tillmann, Influence of Ag on antibacterial performance, microstructure and phase transformation of NiTi shape memory alloy coatings, Vacuum 164 (2019) 242–245. https://doi.org/10.1016/J.VACUUM.2019.02.051.

[271] S. Mei, H. Wang, W. Wang, L. Tong, H. Pan, C. Ruan, Q. Ma, M. Liu, H. Yang, L. Zhang, Y. Cheng, Y. Zhang, L. Zhao, P.K. Chu, Antibacterial effects and biocompatibility of titanium surfaces with graded silver incorporation in titania nanotubes, Biomaterials 35 (2014) 4255–4265. https://doi.org/10.1016/J.BIOMATERIALS.2014.02.005.

[272] Y. Qiao, X. Liu, Biocompatible Coating, Elsevier, 2014. https://doi.org/10.1016/B978-0-08-096532-1.00418-0.

[273] H. Miyajima, G. Awadzi, F. Ozer, F.K. Mante, Effect of surface physico-chemico-biological modifications of titanium on critical and theoretical surface free energy, Appl Surf Sci 470 (2019) 386–394. https://doi.org/10.1016/J.APSUSC.2018.11.133.

[274] F. Rupp, R.A. Gittens, L. Scheideler, A. Marmur, B.D. Boyan, Z. Schwartz, J. Geis-Gerstorfer, A review on the wettability of dental implant surfaces I: Theoretical and experimental aspects, Acta Biomater 10 (2014) 2894–2906. https://doi.org/10.1016/J.ACTBIO.2014.02.040.

[275] M. Hashemkhani, A. Muti, A. Sennaroğlu, H. Yagci Acar, Multimodal image-guided folic acid targeted Ag-based quantum dots for the combination of selective methotrexate delivery and photothermal therapy, J Photochem Photobiol B 213 (2020) 112082. https://doi.org/10.1016/J.JPHOTOBIOL.2020.112082.

[276] J. Yang, K. Shi, Q. Chen, W. Zhang, C. Zhu, Z. Ning, J. Liao, Y. Yang, N. Liu, J. Yang, Effect of Au-ion irradiation on the surface morphology, microstructure and mechanical properties of amorphous AlCrFeMoTi HEA coating, Surf Coat Technol 418 (2021) 127252. https://doi.org/10.1016/J.SURFCOAT.2021.127252.

[277] M. Shaker, E. Salahinejad, A combined criterion of surface free energy and roughness to predict the wettability of non-ideal low-energy surfaces, Prog Org Coat 119 (2018) 123–126. https://doi.org/10.1016/J.PORGCOAT.2018.02.028.

[278] D.E. MacDonald, N. Deo, B. Markovic, M. Stranick, P. Somasundaran, Adsorption and dissolution behavior of human plasma fibronectin on thermally and chemically modified titanium dioxide particles, Biomaterials 23 (2002) 1269–1279. https://doi.org/10.1016/S0142-9612(01)00317-9.

[279] F. Rupp, L. Scheideier, N. Olshanska, M. De Wild, M. Wieland, J. Geis-Gerstorfer, Enhancing surface free energy and hydrophilicity through chemical modification of microstructured titanium implant surfaces, J Biomed Mater Res A 76 (2006) 323–334. https://doi.org/10.1002/jbm.a.30518.

[280] B. Majhy, P. Priyadarshini, A.K. Sen, Effect of surface energy and roughness on cell adhesion and growth-facile surface modification for enhanced cell culture, RSC Adv 11 (2021) 15467–15476. https://doi.org/10.1039/d1ra02402g.

[281] M. López-Heras, I.G. Theodorou, B.F. Leo, M.P. Ryan, A.E. Porter, Towards understanding the antibacterial activity of Ag nanoparticles: Electron microscopy in the analysis of the materials-biology interface in the lung, Environ Sci Nano 2 (2015) 312–326. https://doi.org/10.1039/c5en00051c.

[282] T.C. Dakal, A. Kumar, R.S. Majumdar, V. Yadav, Mechanistic basis of antimicrobial actions of silver nanoparticles, Front Microbiol 7 (2016). https://doi.org/10.3389/fmicb.2016.01831.

[283] Y.N. Slavin, J. Asnis, U.O. Häfeli, H. Bach, Metal nanoparticles: Understanding the mechanisms behind antibacterial activity, J Nanobiotechnology 15 (2017). https://doi.org/10.1186/s12951-017-0308-z.

[284] C. Liao, Y. Li, S.C. Tjong, Bactericidal and cytotoxic properties of silver nanoparticles, Int J Mol Sci 20 (2019). https://doi.org/10.3390/ijms20020449.

[285] M. Akter, M.T. Sikder, M.M. Rahman, A.K.M.A. Ullah, K.F.B. Hossain, S. Banik, T. Hosokawa, T. Saito, M. Kurasaki, A systematic review on silver nanoparticles-induced cytotoxicity: Physicochemical properties and perspectives, J Adv Res 9 (2018) 1–16. https://doi.org/10.1016/J.JARE.2017.10.008.

[286] S. Apak, E. Atay, G. Tuncer, Renewable hydrogen energy and energy efficiency in Turkey in the 21st century, Int J Hydrogen Energy 42 (2017) 2446–2452. https://doi.org/10.1016/J.IJHYDENE.2016.05.043.

[287] B. Xiong, L. Chen, J. Shi, Anion-Containing Noble-Metal-Free Bifunctional Electrocatalysts for Overall Water Splitting, ACS Catal 8 (2018) 3688–3707. https://doi.org/10.1021/acscatal.7b04286.

[288] S.D. Ghadge, O. I. Velikokhatnyi, M. K. Datta, P. M. Shanthi, S. Tan, K. Damodaran, P. N. Kumta, Experimental and Theoretical Validation of High Efficiency and Robust Electrocatalytic Response of One-Dimensional (1D) (Mn,Ir)O2:10F Nanorods for the Oxygen Evolution Reaction in PEM-Based Water Electrolysis, ACS Catal 9 (2019) 2134–2157. https://doi.org/10.1021/acscatal.8b02901.

[289] Y. Zhu, G. Chen, X. Xu, G. Yang, M. Liu, Z. Shao, Enhancing Electrocatalytic Activity for Hydrogen Evolution by Strongly Coupled Molybdenum Nitride@Nitrogen-Doped Carbon Porous Nano-Octahedrons, ACS Catal 7 (2017) 3540–3547. https://doi.org/10.1021/acscatal.7b00120.

[290] T. Feng, Q. Zeng, S. Lu, M. Yang, S. Tao, Y. Chen, Y. Zhao, B. Yang, Morphological and Interfacial Engineering of Cobalt-Based Electrocatalysts by Carbon Dots for Enhanced Water Splitting, ACS Sustainable Chemistry & Engineering 7 (2019) 7047–7057. https://doi.org/10.1021/acssuschemeng.8b06832.

[291] J. Yu, Q. He, G. Yang, W. Zhou, Z. Shao, M. Ni, Recent Advances and Prospective in Ruthenium-Based Materials for Electrochemical Water Splitting, ACS Catal 9 (2019) 9973–10011. https://doi.org/10.1021/acscatal.9b02457.

[292] J. Marie Vianney Nsanzimana, R. Dangol, V. Reddu, S. Duo, Y. Peng, K. Ngoc Dinh, Z. Huang, Q. Yan, X. Wang, Facile Synthesis of Amorphous Ternary Metal Borides–Reduced Graphene Oxide Hybrid with Superior Oxygen Evolution Activity, ACS Applied Materials & Interfaces 11 (2018) 846–855. https://doi.org/10.1021/acsami.8b17836.

[293] S. Anantharaj, S. Rao Ede, K. Sakthikumar, K. Karthick, S. Mishra, S. Kundu, Recent Trends and Perspectives in Electrochemical Water Splitting with an Emphasis on Sulfide, Selenide, and Phosphide Catalysts of Fe, Co, and Ni: A Review, ACS Catal 6 (2016) 8069–8097. https://doi.org/10.1021/acscatal.6b02479.

[294] P. Zhang, M. Wang, Y. Yang, T. Yao, H. Han, L. Sun, Electroless plated Ni–Bx films as highly active electrocatalysts for hydrogen production from water over a

wide pH range, Nano Energy 19 (2016) 98–107. https://doi.org/10.1016/J.NANOEN.2015.11.020.

[295] W. Han, M. Li, Y. Ma, J. Yang, Cobalt-Based Metal-Organic Frameworks and Their Derivatives for Hydrogen Evolution Reaction, Front Chem 8 (2020) 1–18. https://doi.org/10.3389/fchem.2020.592915.

[296] S. Chamani, M. Khatamian, N. Sadat Peighambardoust, U. Aydemir, Microwave-Assisted Auto-Combustion Synthesis of Binary/Ternary CoxNi1−xFerrite for Electrochemical Hydrogen and Oxygen Evolution, ACS Omega 6 (2021) 33024–33032. https://doi.org/10.1021/acsomega.1c05183.

[297] Z. Jin, L. Zhang, Performance of Ni-Cu bimetallic co-catalyst g-C3N4 nanosheets for improving hydrogen evolution, J Mater Sci Technol 49 (2020) 144–156. https://doi.org/10.1016/J.JMST.2020.02.025.

[298] W. Li, Q. Hu, Y. Liu, M. Zhang, J. Wang, X. Han, C. Zhong, W. Hu, Y. Deng, Powder metallurgy synthesis of porous Ni-Fe alloy for oxygen evolution reaction and overall water splitting, J Mater Sci Technol 37 (2020) 154–160. https://doi.org/10.1016/J.JMST.2019.06.021.

[299] M.S. Lal, R. Sundara, High Entropy Oxides—A Cost-Effective Catalyst for the Growth of High Yield Carbon Nanotubes and Their Energy Applications, ACS Applied Materials & Interfaces 11 (2019) 30846–30857. https://doi.org/10.1021/acsami.9b08794.

[300] M.M. Jaksic, Hypo–hyper-d-electronic interactive nature of synergism in catalysis and electrocatalysis for hydrogen reactions, Electrochim Acta 45 (2000) 4085–4099. https://doi.org/10.1016/S0013-4686(00)00525-9.

[301] M. Schalenbach, F.D. Speck, M. Ledendecker, O. Kasian, D. Goehl, A.M. Mingers, B. Breitbach, H. Springer, S. Cherevko, K.J.J. Mayrhofer, Nickel-molybdenum alloy catalysts for the hydrogen evolution reaction: Activity and stability revised, Electrochim Acta 259 (2018) 1154–1161. https://doi.org/10.1016/J.ELECTACTA.2017.11.069.

[302] N.R. Elezović, V.D. Jović, N. V. Krstajić, Kinetics of the hydrogen evolution reaction on Fe–Mo film deposited on mild steel support in alkaline solution, Electrochim Acta 50 (2005) 5594–5601. https://doi.org/10.1016/J.ELECTACTA.2005.03.037.

[303] S.M. Kim, S.H. Jin, Y.J. Lee, M.H. Lee, Design of Nickel Electrodes by Electrodeposition: Effect of Internal Stress on Hydrogen Evolution Reaction in

Alkaline Solutions, Electrochim Acta 252 (2017) 67–75. https://doi.org/10.1016/J.ELECTACTA.2017.08.157.

[304] B. Yazici, G. Tatli, H. Galip, M. Erbil, Investigation of suitable cathodes for the production of hydrogen gas by electrolysis, Int J Hydrogen Energy 20 (1995) 957–965. https://doi.org/10.1016/0360-3199(95)00032-9.

[305] X. Qian, J. Fang, J. Xia, G. He, H. Chen, Recent progress and perspective on molybdenum-based electrocatalysts for water electrolysis, Int J Hydrogen Energy 48 (2023) 26084–26106. https://doi.org/10.1016/J.IJHYDENE.2023.03.228.

[306] C. Canales, A.F. Olea, L. Gidi, R. Arce, G. Ramírez, Enhanced light-induced hydrogen evolution reaction by supramolecular systems of cobalt(II) and copper(II) octaethylporphyrins on glassy carbon electrodes, Electrochim Acta 258 (2017) 850–857. https://doi.org/10.1016/J.ELECTACTA.2017.11.135.

[307] S. Cherevko, S. Geiger, O. Kasian, N. Kulyk, J.P. Grote, A. Savan, B.R. Shrestha, S. Merzlikin, B. Breitbach, A. Ludwig, K.J.J. Mayrhofer, Oxygen and hydrogen evolution reactions on Ru, RuO2, Ir, and IrO2 thin film electrodes in acidic and alkaline electrolytes: A comparative study on activity and stability, Catal Today 262 (2016) 170–180. https://doi.org/10.1016/J.CATTOD.2015.08.014.

[308] J. Huang, P. Wang, P. Li, H. Yin, D. Wang, Regulating electrolytic Fe0.5CoNiCuZnx high entropy alloy electrodes for oxygen evolution reactions in alkaline solution, J Mater Sci Technol 93 (2021) 110–118. https://doi.org/10.1016/j.jmst.2021.03.046.

[309] Y. Xin, S. Li, Y. Qian, W. Zhu, H. Yuan, P. Jiang, R. Guo, L. Wang, High-Entropy Alloys as a Platform for Catalysis: Progress, Challenges, and Opportunities, ACS Catal 10 (2020) 11280–11306. https://doi.org/10.1021/acscatal.0c03617.

[310] Y. Zhang, D. Wang, S. Wang, High-Entropy Alloys for Electrocatalysis: Design, Characterization, and Applications, Small 18 (2022) 1–22. https://doi.org/10.1002/smll.202104339.

[311] K.B. Zhang, Z.Y. Fu, J.Y. Zhang, W.M. Wang, S.W. Lee, K. Niihara, Annealing effects on structure and mechanical properties of CoCrFeNiTiAlx high-entropy alloys, in: IOP Conf Ser Mater Sci Eng, 2011. https://doi.org/10.1088/1757-899X/20/1/012009.

[312] C.W. Tsai, M.H. Tsai, J.W. Yeh, C.C. Yang, Effect of temperature on mechanical properties of Al0.5CoCrCuFeNi wrought alloy, J Alloys Compd 490 (2010) 160–165. https://doi.org/10.1016/j.jallcom.2009.10.088.

[313] Y.F. Kao, T.J. Chen, S.K. Chen, J.W. Yeh, Microstructure and mechanical property of as-cast, -homogenized, and -deformed AlxCoCrFeNi ($0 \leq x \leq 2$) high-entropy alloys, J Alloys Compd 488 (2009) 57–64. https://doi.org/10.1016/j.jallcom.2009.08.090.

[314] X.R. Wang, Z.Q. Wang, P. He, T.S. Lin, Y. Shi, Microstructure and wear properties of CuNiSiTiZr high-entropy alloy coatings on TC11 titanium alloy produced by electrospark - computer numerical control deposition process, Surf Coat Technol 283 (2015) 156–161. https://doi.org/10.1016/j.surfcoat.2015.10.013.

[315] S. Varalakshmi, M. Kamaraj, B.S. Murty, Processing and properties of nanocrystalline CuNiCoZnAlTi high entropy alloys by mechanical alloying, Materials Science and Engineering A 527 (2010) 1027–1030. https://doi.org/10.1016/j.msea.2009.09.019.

[316] K.K. Alaneme, M.O. Bodunrin, S.R. Oke, Processing, alloy composition and phase transition effect on the mechanical and corrosion properties of high entropy alloys: A review, Journal of Materials Research and Technology 5 (2016) 384–393. https://doi.org/10.1016/j.jmrt.2016.03.004.

[317] Y. Mei, Y. Feng, C. Zhang, Y. Zhang, Q. Qi, J. Hu, High-Entropy Alloy with Mo-Coordination as Efficient Electrocatalyst for Oxygen Evolution Reaction, ACS Catal 12 (2022) 10808–10817. https://doi.org/10.1021/acscatal.2c02604.

[318] N. Sadat Peighambardoust, E. Hatipoglu, U. Aydemir, Structure-Induced Catalytic Activity of Nickel- and Cobalt-Substituted Layered MoB2 toward Hydrogen Evolution, ACS Sustainable Chemistry & Engineering 10 (2022) 15909–15925. https://doi.org/10.1021/acssuschemeng.2c05251.

[319] S. Zhang, C.L. Wu, C.H. Zhang, M. Guan, J.Z. Tan, Laser surface alloying of FeCoCrAlNi high-entropy alloy on 304 stainless steel to enhance corrosion and cavitation erosion resistance, Opt Laser Technol 84 (2016) 23–31. https://doi.org/10.1016/j.optlastec.2016.04.011.

[320] Z. Wang, X. Wang, H. Yue, G. Shi, S. Wang, Microstructure, thermodynamics and compressive properties of AlCoCrCuMn-x (x=Fe, Ti) high-entropy alloys, Materials Science and Engineering A 627 (2015) 391–398. https://doi.org/10.1016/j.msea.2015.01.002.

[321] S. Sheikh, S. Shafeie, Q. Hu, J. Ahlström, C. Persson, J. Veselý, J. Zýka, U. Klement, S. Guo, Alloy design for intrinsically ductile refractory high-entropy alloys, J Appl Phys 120 (2016). https://doi.org/10.1063/1.4966659.

[322] K. Cichocki, P. Bała, T. Kozieł, G. Cios, N. Schell, K. Muszka, Effect of Mo on Phase Stability and Properties in FeMnNiCo High-Entropy Alloys, Metall Mater Trans A Phys Metall Mater Sci 53 (2022) 1749–1760. https://doi.org/10.1007/s11661-022-06629-x.

[323] X. Yao, J. Wei, T. Li, Effects of Mo Element on Microstructure and Mechanical Properties of CoCrFeMnNi High Entropy Alloys, IOP Conf Ser Mater Sci Eng 585 (2019). https://doi.org/10.1088/1757-899X/585/1/012019.

[324] T. Varol, A. Canakci, S. Ozkaya, F. Erdemir, Determining the effect of flake matrix size and Al2O3 content on microstructure and mechanical properties of Al2O3 nanoparticle reinforced Al matrix composites, Particulate Science and Technology 36 (2018) 312–323. https://doi.org/10.1080/02726351.2016.1248259.

[325] B. Madavali, J.H. Lee, J.K. Lee, K.Y. Cho, S. Challapalli, S.J. Hong, Effects of atmosphere and milling time on the coarsening of copper powders during mechanical milling, Powder Technol 256 (2014) 251–256. https://doi.org/10.1016/J.POWTEC.2014.02.019.

[326] H. Zhang, Y. Pan, Y.Z. He, Synthesis and characterization of FeCoNiCrCu high-entropy alloy coating by laser cladding, Mater Des 32 (2011) 1910–1915. https://doi.org/10.1016/j.matdes.2010.12.001.

[327] M. Einert, M. Mellin, N. Bahadorani, C. Dietz, S. Lauterbach, J.P. Hofmann, Mesoporous High-Entropy Oxide Thin Films: Electrocatalytic Water Oxidation on High-Surface-Area Spinel (Cr0.2Mn0.2Fe0.2Co0.2Ni0.2)3O4 Electrodes, ACS Appl Energy Mater 5 (2022) 717–730. https://doi.org/10.1021/acsaem.1c03190.

[328] T. Zhang, H.F. Zhao, K.Y. Wang, Z.J. Chen, L. Li, J. Peng, X. Peng, Y.J. Huang, H. Bin Yu, Three factors make bulk high-entropy alloys as effective electrocatalysts for oxygen evolution, Materials Futures 2 (2023). https://doi.org/10.1088/2752-5724/aceef3.

[329] Z. Wang, J. Qu, Y. He, T. Xiong, Z. Huang, F. Wang, M.S. Balogun, Exceptional alkaline hydrogen evolution by molybdenum-oxide-nitride-based electrocatalysts with fast water-dissociation and hydrogen-adsorption kinetics, Mater Chem Front 7 (2023) 2683–2692. https://doi.org/10.1039/d2qm01349e.

[330] W. Wang, Y.Z. Lu, X. Lu, A porous high-entropy alloy for high-efficient oxygen evolution reaction, Rare Metals 42 (2023) 2174–2181. https://doi.org/10.1007/s12598-022-02255-z.

[331] E. Sadeghi, N. Sadat Peighambardoust, U. Aydemir, Tailoring the Morphology of Cost-Effective Vanadium Diboride Through Cobalt Substitution for Highly Efficient Alkaline Water Oxidation, Inorg Chem 60 (2021) 19457–19466. https://doi.org/10.1021/acs.inorgchem.1c03374.

[332] G. Zhang, K. Ming, J. Kang, Q. Huang, Z. Zhang, X. Zheng, X. Bi, High entropy alloy as a highly active and stable electrocatalyst for hydrogen evolution reaction, Electrochim Acta 279 (2018) 19–23. https://doi.org/10.1016/j.electacta.2018.05.035.

[333] F. Calle-Vallejo, O. A. Díaz-Morales, M. J. Kolb, M. T. M. Koper, Why Is Bulk Thermochemistry a Good Descriptor for the Electrocatalytic Activity of Transition Metal Oxides?, ACS Catal 5 (2015) 869–873. https://doi.org/10.1021/cs5016657.

[334] L. Sharma, N.K. Katiyar, A. Parui, R. Das, R. Kumar, C.S. Tiwary, A.K. Singh, A. Halder, K. Biswas, Low-cost high entropy alloy (HEA) for high-efficiency oxygen evolution reaction (OER), Nano Res 15 (2022) 4799–4806. https://doi.org/10.1007/s12274-021-3802-4.

[335] D. Wang, Z. Liu, S. Du, Y. Zhang, H. Li, Z. Xiao, W. Chen, R. Chen, Y. Wang, Y. Zou, S. Wang, Low-temperature synthesis of small-sized high-entropy oxides for water oxidation, J Mater Chem A Mater 7 (2019) 24211–24216. https://doi.org/10.1039/c9ta08740k.

[336] D. Stenzel, B. Zhou, C. Okafor, M.V. Kante, L. Lin, G. Melinte, T. Bergfeldt, M. Botros, H. Hahn, B. Breitung, S. Schweidler, High-entropy spinel-structure oxides as oxygen evolution reaction electrocatalyst, Front Energy Res 10 (2022). https://doi.org/10.3389/fenrg.2022.942314.

[337] W. Dai, T. Lu, Y. Pan, Novel and promising electrocatalyst for oxygen evolution reaction based on MnFeCoNi high entropy alloy, J Power Sources 430 (2019) 104–111. https://doi.org/10.1016/J.JPOWSOUR.2019.05.030.

[338] M.W. Glasscott, A.D. Pendergast, S. Goines, A.R. Bishop, A.T. Hoang, C. Renault, J.E. Dick, Electrosynthesis of high-entropy metallic glass nanoparticles for designer, multi-functional electrocatalysis, Nat Commun 10 (2019). https://doi.org/10.1038/s41467-019-10303-z.

[339] A. Kumar, S. Bhattacharyya, Porous NiFe-Oxide Nanocubes as Bifunctional Electrocatalysts for Efficient Water-Splitting, ACS Applied Materials & Interfaces 9 (2017) 41906–41915. https://doi.org/10.1021/acsami.7b14096.

[340] G. Fu, Z. Cui, Y. Chen, L. Xu, Y. Tang, J.B. Goodenough, Hierarchically mesoporous nickel-iron nitride as a cost-efficient and highly durable electrocatalyst for Zn-air battery, Nano Energy 39 (2017) 77–85. https://doi.org/10.1016/j.nanoen.2017.06.029.

[341] Y. Gorlin, T. F. Jaramillo, A Bifunctional Nonprecious Metal Catalyst for Oxygen Reduction and Water Oxidation, J Am Chem Soc 132 (2010) 13612–13614. https://doi.org/10.1021/ja104587v.

[342] S. Duan, S. Chen, T. Wang, S. Li, J. Liu, J. Liang, H. Xie, J. Han, S. Jiao, R. Cao, H.L. Wang, Q. Li, Elemental selenium enables enhanced water oxidation electrocatalysis of NiFe layered double hydroxides, Nanoscale 11 (2019) 17376–17383. https://doi.org/10.1039/c9nr06169j.

[343] Z. Liu, H. Tan, D. Liu, X. Liu, J. Xin, J. Xie, M. Zhao, L. Song, L. Dai, H. Liu, Promotion of Overall Water Splitting Activity Over a Wide pH Range by Interfacial Electrical Effects of Metallic NiCo-nitrides Nanoparticle/NiCo 2 O 4 Nanoflake/graphite Fibers, Advanced Science 6 (2019). https://doi.org/10.1002/advs.201801829.

[344] B. Mete, N.S. Peighambardoust, S. Aydin, E. Sadeghi, U. Aydemir, Metal-substituted zirconium diboride (Zr1-xTMxB2; TM = Ni, Co, and Fe) as low-cost and high-performance bifunctional electrocatalyst for water splitting, Electrochim Acta 389 (2021) 138789. https://doi.org/10.1016/J.ELECTACTA.2021.138789.

[345] M.Y. Gao, C. Yang, Q.B. Zhang, Y.W. Yu, Y.X. Hua, Y. Li, P. Dong, Electrochemical fabrication of porous Ni-Cu alloy nanosheets with high catalytic activity for hydrogen evolution, Electrochim Acta 215 (2016) 609–616. https://doi.org/10.1016/J.ELECTACTA.2016.08.145.

[346] Y. Jia, L. Zhang, G. Gao, H. Chen, B. Wang, J. Zhou, M.T. Soo, M. Hong, X. Yan, G. Qian, J. Zou, A. Du, X. Yao, A Heterostructure Coupling of Exfoliated Ni–Fe Hydroxide Nanosheet and Defective Graphene as a Bifunctional Electrocatalyst for Overall Water Splitting, Advanced Materials 29 (2017). https://doi.org/10.1002/adma.201700017.

[347] R. Liu, H. Zhang, X. Zhang, T. Wu, H. Zhao, G. Wang, Co9S8@N,P-doped porous carbon electrocatalyst using biomass-derived carbon nanodots as a precursor for overall water splitting in alkaline media, RSC Adv 7 (2017) 19181–19188. https://doi.org/10.1039/c7ra01798g.

[348] D. Merki, S. Fierro, H. Vrubel, X. Hu, Amorphous molybdenum sulfide films as catalysts for electrochemical hydrogen production in water, Chem Sci 2 (2011) 1262–1267. https://doi.org/10.1039/c1sc00117e.

[349] C. C. L. McCrory, S. Jung, I. M. Ferrer, S. M. Chatman, J. C. Peters, T. F. Jaramillo, Benchmarking Hydrogen Evolving Reaction and Oxygen Evolving Reaction Electrocatalysts for Solar Water Splitting Devices, J Am Chem Soc 137 (2015) 4347–4357. https://doi.org/10.1021/ja510442p.

[350] J. Tang, J.L. Xu, Z.G. Ye, Y.C. Ma, X.B. Li, J.M. Luo, Y.Z. Huang, Synthesis of flower-like cobalt, nickel phosphates grown on the surface of porous high entropy alloy for efficient oxygen evolution, J Alloys Compd 885 (2021). https://doi.org/10.1016/j.jallcom.2021.160995.

[351] K. Huang, D. Peng, Z. Yao, J. Xia, B. Zhang, H. Liu, Z. Chen, F. Wu, J. Wu, Y. Huang, Cathodic plasma driven self-assembly of HEAs dendrites by pure single FCC FeCoNiMnCu nanoparticles as high efficient electrocatalysts for OER, Chemical Engineering Journal 425 (2021). https://doi.org/10.1016/j.cej.2021.131533.

[352] P. Ma, M. Zhao, L. Zhang, H. Wang, J. Gu, Y. Sun, W. Ji, Z. Fu, Self- supported high-entropy alloy electrocatalyst for highly efficient H2 evolution in acid condition, Journal of Materiomics 6 (2020) 736–742. https://doi.org/10.1016/j.jmat.2020.06.001.